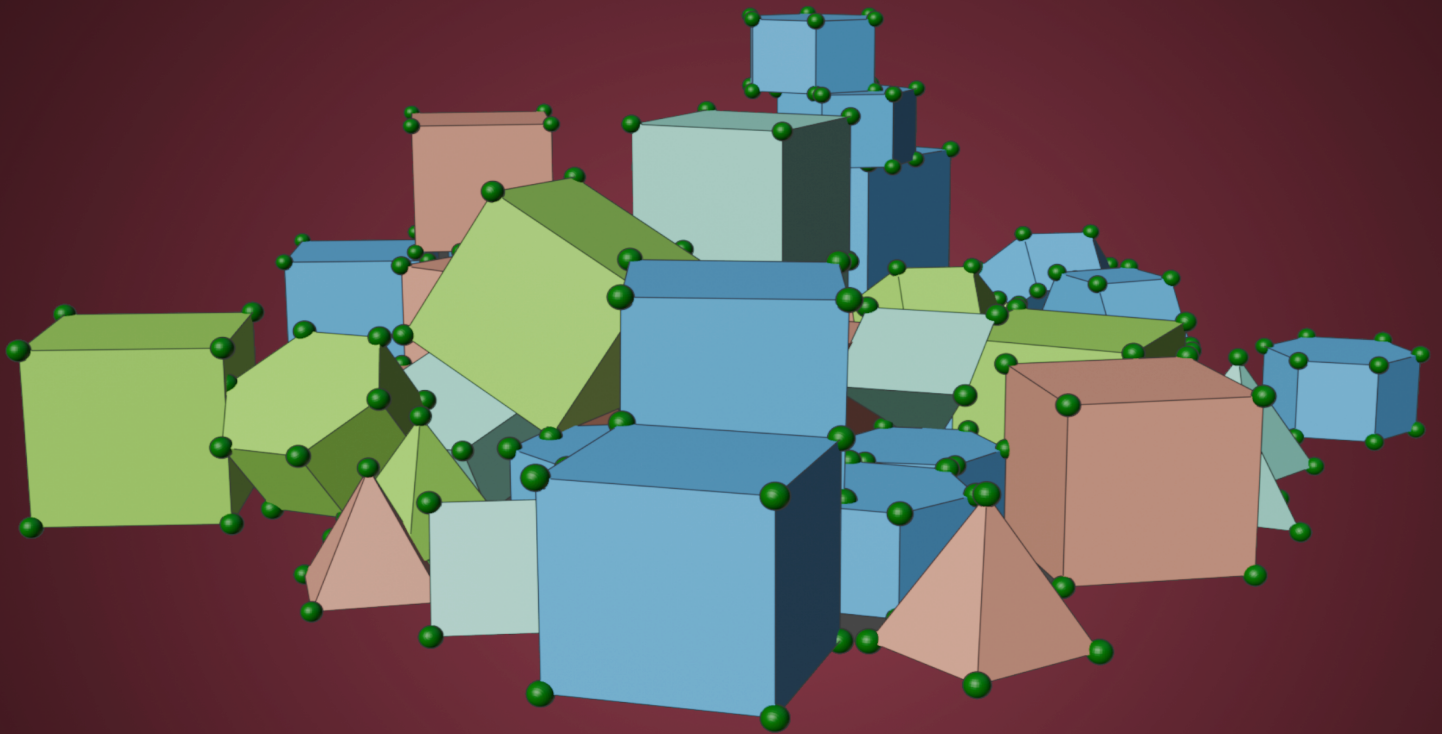


# Building Blocks for Cluster Mott Insulators

From Elementary Models  
to Potential Realizations



---

Vaishnavi Jayakumar

•

Dissertation



# Building blocks for cluster Mott insulators: From elementary models to potential realizations

**Inaugural-Dissertation**

zur

Erlangung des Doktorgrades

der Mathematisch-Naturwissenschaftlichen Fakultät

der Universität zu Köln

vorgelegt von

**Vaishnavi Jayakumar**

aus Bangalore, Indien



Köln 2024



**Berichterstatter:**

Prof. Dr. Simon Trebst,  
Institute for Theoretical Physics,  
University of Cologne, Germany.

apl. Prof. Dr. Ralf Bulla,  
Institute for Theoretical Physics,  
University of Cologne, Germany.

Prof. Ciarán Hickey,  
School of Physics,  
University College Dublin, Ireland.

**Datum der Abgabe der Dissertation :** 1. Juli 2024

**Tag der mündlichen Prüfung:** 5. September 2024

Die vorliegende Dissertation wurde von der Mathematisch-Naturwissenschaftlichen Fakultät der Universität zu Köln angenommen.



ಸಾಧನ ಶರೀರವಿದು,  
ನೀ ದಯದಿ ಕೊಟ್ಟದ್ದು,  
ಸಾಧಾರಣವಲ್ಲ ಸಾಧುಪ್ರಿಯನೇ

ಓದಿದೆನು ಎಲ್ಲಣ್ಣ, ಕಲ್ಲಣ್ಣ ಎನುತಲಿ  
ಸ್ವಾಧ್ಯಾಯವು ಎನಗೆ ಪಗಡೆ ಪಂಜಿ  
ಸಾಧಿಸಿ ಈ ಪರಿಯ ಧನವನ್ನು ಕೂಡ್ಡಾಕಿ  
ಮೋದಿ ಸಿರಿ ಹಯವದನ ನಾನಿನ್ನ ಮರೆತೆ

ಪಾತಕಿಗಳನೊಡನಾಡಿ ನಾನಿನ್ನ  
ಪೂತಾಬ್ಜಪದ ಭಜಿಸದೆ ಹೋದೆ ನಾ  
ಪಾತಕವೆಣಿಸದೆ ಸೀತಾರಮಣ  
ಜಗನ್ನಾಥವಿಠಲನ ಗೀತಾಮೃತವ ನುಡಿಸು



# Abstract

The Hubbard model is a paradigmatic model in condensed matter physics, which provides a rich playground for investigating the physics of a wide range of strongly correlated electronic systems. The core principle of the Hubbard model is the competition between Coulomb repulsions and hoppings. An important limit in the model is the Mott insulating regime, which is realized in the strong interaction limit. As a result, electrons get localized on single atomic sites at half-filling. In this thesis, we investigate extensions of this idea to cluster Mott insulators. These are special materials where electrons are now localized on clusters of sites. We use the theoretical framework that we develop to explore the physics of real cluster Mott materials.

To that end, in a first study, we construct and study the cluster Hubbard model on a plethora of different clusters. We propose a new selection rule, called the cluster Hund's rule, which provides guidelines as to which states qualify as ground states in the pure interaction limit of the cluster Hubbard Hamiltonian. Using a combination of analytical insights and exact diagonalization, we conducted a comprehensive investigation of the emergent degrees of freedom in clusters of different geometries and fillings. This study helped us understand how these cluster Mott degrees of freedom respond to the interplay of strong correlations and hopping.

In a second study, we investigated the cause of the observed magnetic signatures in  $\text{Ba}_4\text{LiIr}_3\text{O}_{12}$ . This material hosts iridium dimers, and was expected to be non-magnetic since it possesses completely filled shells. Using insights from our previous study, we were able to detect non-trivial ground state degeneracies called non-Kramers doublets as the reason behind the observed magnetism of the material. Hence, we established  $\text{Ba}_4\text{LiIr}_3\text{O}_{12}$  as the first cluster Mott material whose physics is driven by non-Kramers doublets.

Having constructed this theoretical framework so far, we used it in our third study to investigate real materials which host trimer clusters – hexagonal perovskites of the form  $\text{A}_4\text{BM}_3\text{O}_{12}$ , and considered different fillings of  $3d$  to  $5d$  transition-metal “M” ions. Through a systematic treatment, we verified the observed magnetic moments for a wide variety of trimer materials. In addition, we also obtained the composition of magnetic moments in different directions. We use this study to propose ground state properties and phase diagrams for materials that are likely to be synthesized in the future.



# Contents

<b>1</b>	<b>Introduction</b>	<b>13</b>
<b>I</b>	<b>Theoretical Foundations</b>	<b>17</b>
<b>2</b>	<b>Localization of electrons in solids</b>	<b>19</b>
2.1	Oxidation states and valency . . . . .	21
2.1.1	Hybridization and coordination bonds . . . . .	23
2.1.2	Mixed oxidation states . . . . .	23
2.2	Role of relativistic effects in the atom . . . . .	26
2.2.1	Coupling schemes . . . . .	28
2.2.2	Racah parameters . . . . .	29
2.3	Conclusion . . . . .	31
<b>3</b>	<b>Exact diagonalization</b>	<b>33</b>
3.1	Constructing the Hamiltonian matrix . . . . .	33
3.2	Block diagonalization of the Hamiltonian matrix . . . . .	35
3.2.1	Computer storage of states . . . . .	36
3.3	Jordan-Wigner strings . . . . .	38
3.4	Krylov space techniques and the Lanczos method . . . . .	40
3.4.1	The Lanczos routine . . . . .	41
3.4.2	Conclusion . . . . .	43
<b>II</b>	<b>Building Blocks for Cluster Mott Insulators</b>	<b>45</b>
<b>4</b>	<b>Localization of electrons on clusters</b>	<b>47</b>
4.1	Cluster Mott materials . . . . .	47
4.1.1	Structural clusters . . . . .	48
4.1.2	Emergent clusters . . . . .	51
4.2	Hamiltonian considerations . . . . .	53
4.2.1	Intra-cluster hopping and molecular orbitals . . . . .	54
4.2.2	Intra-cluster interactions . . . . .	56
4.2.3	Cluster Hund's rules . . . . .	57

4.3	Conclusion	60
<b>5</b>	<b>Single orbital Hubbard model</b>	<b>61</b>
5.1	Molecular orbital levels	61
5.1.1	Interaction Hamiltonian	62
5.1.2	Results	63
5.2	Conclusion	65
<b>6</b>	<b>Multiorbital Hubbard model</b>	<b>67</b>
6.1	Two orbitals per site	67
6.1.1	Molecular orbital levels	67
6.1.2	Interaction Hamiltonian	68
6.1.3	Some select phase diagrams	68
6.2	Three orbitals per site	80
6.2.1	Molecular orbital levels	80
6.2.2	Interaction Hamiltonian	80
6.2.3	Some select phase diagrams	80
6.3	Conclusion	85
<b>III</b>	<b>Candidate Cluster Mott Insulator Materials</b>	<b>87</b>
<b>7</b>	<b>The transition metal ion</b>	<b>89</b>
7.1	Crystal field splitting	90
7.1.1	Octahedral crystal fields	90
7.1.2	Tetrahedral crystal fields	93
7.1.3	Effect of ligand fields in multi-electron systems	96
7.2	Spin-orbit coupling	98
7.2.1	T-P equivalence	99
7.2.2	Energy splitting due to SOC	101
7.2.3	Effect of SOC on magnetic moments	101
7.2.4	Contributions to the susceptibility	103
7.3	Conclusion	104
<b>8</b>	<b>Non-Kramers doublets in <math>\text{Ba}_4\text{LiIr}_3\text{O}_{12}</math></b>	<b>105</b>
8.1	The dimer compound $\text{Ba}_4\text{LiIr}_3\text{O}_{12}$	105
8.1.1	Experimental observations	107
8.2	Kramers vs non-Kramers degeneracies	108
8.2.1	Interpreting degeneracies in the presence of SOC	109
8.3	Non-Kramers degeneracies in $\text{Ba}_4\text{LiIr}_3\text{O}_{12}$	111
8.4	Non-Kramers degeneracies in other materials	115
8.5	Conclusion	116

---

<b>9</b>	<b>Properties of materials with <math>M_3O_{12}</math> trimer clusters</b>	<b>119</b>
9.1	Survey of materials . . . . .	119
9.2	Structure and Hamiltonian particulars . . . . .	122
9.2.1	Interactions and hopping . . . . .	123
9.2.2	Crystal fields and spin-orbit coupling . . . . .	125
9.2.3	Parameter selection . . . . .	126
9.3	Single-particle sector and molecular orbitals . . . . .	126
9.3.1	Zero SOC . . . . .	126
9.3.2	Non-zero SOC . . . . .	128
9.4	Phase diagrams and effective moments for select fillings . . . . .	128
9.4.1	$n_f = 11$ electrons . . . . .	129
9.4.2	$n_f = 13$ electrons . . . . .	132
9.4.3	$n_f = 14$ electrons . . . . .	135
9.4.4	$n_f = 15$ electrons . . . . .	136
9.4.5	Manganese, $n_f = 10$ electrons . . . . .	138
9.5	Conclusion . . . . .	139
<b>10</b>	<b>General concluding remarks</b>	<b>141</b>
	<b>Appendices</b>	<b>143</b>
<b>A</b>	<b>Group theory essentials and character tables</b>	<b>147</b>
A.1	Groups and crystal point groups . . . . .	147
A.1.1	Point groups . . . . .	148
A.2	Representations of groups . . . . .	149
A.3	Characters of a representation . . . . .	150
A.3.1	Nomenclature of irreducible representations: Mulliken notation . . . . .	151
A.4	Character tables of point groups . . . . .	151
<b>B</b>	<b>The periodic table</b>	<b>155</b>
	<b>Bibliography</b>	<b>155</b>
	<b>Acknowledgements</b>	<b>171</b>



Philip Anderson, being one of the physicists who revolutionized the study of strongly correlated systems at large, also had many words of wisdom to impart, which perfectly and beautifully encapsulated the essence and intuition behind many developments in condensed matter physics in the latter half of the 20th century. One of the cornerstones of his contributions was towards the concept of localization. In his Nobel lecture [1], he found inspiration in the unlikeliest of sources, Lewis Carroll’s *Alice in Wonderland* – “Now here, you see, it takes all the running you can do, to keep in the same place”. This sentence aptly captures why physicists are fascinated with electrons in solids.

In fact, the Nobel Prize in Physics in 1977 was all about different figurative manifestations of the phrase “all the running”, to keep electrons in the same place. On one hand, Anderson pioneered the concept of Anderson localization [2], a phenomenon that exemplifies the vital role of disorder in the movement of electrons, and has, over the decades, become ubiquitous in a variety of condensed matter systems [3–15].

On the other hand, the second Nobel laureate of 1977, Sir Neville Mott, focused on a different facet of “all the running”. He introduced the concept of a Mott insulating phase, a phenomenon that exemplifies the role of interactions between electrons, in localizing them [16]. To close the loop, the third Nobel laureate, John Van Vleck, studied their manifestations in terms of magnetic signatures [17]. Ever since then, one of the major trajectories of condensed matter physics has been to understand localization and its consequences in many-body problems.

While one half of the story in this thesis is about localization, especially of the nature that Sir Mott championed, the second half of the story also finds motivation from another of Anderson’s adages of wisdom: “More is different” [18]. In the spirit of Anderson’s essay, one can pose the question: How can Mott insulators be used as a playground to study new physics?” What would “more” mean in such a context? What would “different” mean in such a context?

The playground that a Mott insulator provides has previously been explored theoretically and experimentally. This has led to many important developments, such as insights into the Hubbard model on various lattices [19, 20], Kitaev physics and quantum spin liquids [21–26], high- $T_c$  superconductivity [27], charge density waves [28, 29], quantum criticality [30], and valence bond solids [31], to name a few.

In this thesis, we study the newest addition to the playground, by exploring extensions to the

concept of a Mott insulator: We add additional orbitals to every site, while also considering clusters of sites embedded on a larger lattice. These “cluster” Mott insulators have been subject to enthusiastic scrutiny, with various techniques such as RIXS [32–34] and DFT/DMFT, among others [35], used to explore an ever-growing list of cluster Mott materials that are being synthesized.

However, there exists very little theoretical perspective on the properties of cluster Mott insulators and, more importantly, on the vastly different behaviors that materials in the same family sometimes display [36–40]. Through the course of the thesis, we follow a bottom-up approach to building an understanding of cluster Mott materials. We start with toy models that capture core interactions within and between clusters in a material, and later apply them in the context of real cluster Mott candidate materials, while also trying to understand some new physics that emerges along the way. We employ a blend of theoretical and numerical approaches to gain insights into the comprehensive study we embarked upon.

In **Chapter 2**, we provide a brief overview of localization and Mott insulators. We discuss the factors that determine the pull and push of electrons in a real crystal. We will also briefly touch upon how these can be denoted using different measures and languages, such as bonding and oxidation states.

In **Chapter 3**, we discuss the core numerical machinery that went into the story – exact diagonalization. In this chapter, we discuss the need for such a technique in the field of strongly-correlated systems, and also explain how to mitigate the numerical obstacle of dealing with very large eigenvalue problems.

**Chapter 4** focuses on the concept of a cluster. We begin with a brief survey of different clusters that are hosted by various materials, and various materials that have been synthesized so far, which have hosted such clusters. We then establish some core theoretical foundations for a cluster Mott insulator. Here, we construct the cluster Hamiltonian as an extension to the conventional Hubbard Hamiltonian that governs a conventional Mott insulator. One of the most important insights is the so-called “cluster Hund’s rule”, which helps us identify the factors that need to be considered for a state to qualify as a ground state in the cluster Mott context.

Having built an initial theoretical understanding of a cluster Mott insulator, we apply it to the simple case of a single orbital Hubbard model on clusters of varying sizes and geometry in **Chapter 5**. In addition to providing us with a better understanding of interactions in terms of the orbital language, some non-trivial ground states emerge in some clusters, which have been shown to host interesting physics.

In **Chapter 6**, we extend the idea to a multi-orbital Hubbard model. We combine the analytical and computational concepts introduced thus far in the thesis, to perform an exhaustive study of the ground states of the multi-orbital cluster Hamiltonian across a range of cluster sizes and geometries, and across different fillings on the cluster. In addition, we track how the introduction of hoppings modifies the properties and quantum numbers of ground states in different parameter regimes.

Having used toy models to understand cluster Mott physics so far, the next part of the thesis

---

calls for its applications on real materials. **Chapter 7** hence starts with a brief description of the physical orbitals that any ion in a crystal possesses. This is followed by a detailed discussion on how orbitals of various players in a crystal give rise to fields that potentially influence the ground states of the material. We also discuss another crucial ingredient to any real material – spin-orbit coupling. Having built this background knowledge of important factors at play in crystals puts us in a good position to analyze cluster Mott candidate materials.

In **Chapter 8**, we discuss the work we carried out in collaboration with experimentalists at McMaster University, Canada. It was observed that, the dimer material that they synthesized,  $\text{Ba}_4\text{LiIr}_3\text{O}_{12}$ , showed evidence of magnetism despite its structure pointing towards a non-magnetic ground state. Relying on *ab-initio* studies for approximate parameter regimes for this class of materials, we discovered the presence of non-trivial origins of the ground state degeneracies observed in  $\text{Ba}_4\text{LiIr}_3\text{O}_{12}$ . We were hence able to extract the properties and quantum numbers of the ground state. We end this chapter with a short survey on the occurrence of such non-trivial degeneracies in other classes of materials and the reason for their occurrence.

**Chapter 9** is concerned with materials that host trimer clusters. Many such materials have been synthesized but have not been subject to theoretical treatment yet. We start with a survey of materials synthesized in this category so far, followed by a study of various limits of the Hamiltonian governing them. We then combine this with the insight we gained of cluster Mott materials from the previous chapters, to study different materials that host varying numbers of electrons on trimer clusters. We also analyze their measured effective magnetic moments and make predictions for materials in various parameter regimes, which are yet to be synthesized.

In **Chapter 10**, we summarize our results and discuss the outlook for the area of cluster Mott insulators.



## **Part I**

# Theoretical Foundations



# Localization of electrons in solids

In the business of studying various microscopic particles, numerous models are proposed across different branches of physics. Some models successfully capture certain aspects of observed or expected behavior of said subatomic particles, while others might address other aspects. In this continual process of research spanning multiple decades, new physics emerges from the collective contributions of various such models and theories, that not only deepen our understanding of these particles but also make predictions for behavior yet to be observed.

Every branch of physics is rife with such models. Ever since the first quantum mechanical principles were laid down in the 1900s, many theories and models that attempted to capture various aspects of condensed matter systems have had their eras of successes and failures. However, few have achieved the iconic status that the Hubbard model holds, more than half a century after its conception [41–43]. This thesis focuses on understanding a specific class of materials called cluster Mott insulators. However, any attempt to understand them has to start from revisiting the Hubbard model.

In the subsequent chapters, we will take a more in-depth look at how the Hubbard model serves as a platform to understand cluster Mott insulators better and vice versa. In this chapter, however, we will try to give a more overarching picture of where we stand in terms of understanding real materials and how the Hubbard model serves as a starting point.

The Hubbard model, in its earliest and simplest form, considers two ingredients as being essential in describing how electrons on a lattice interact: the Hubbard interaction term  $U$  and the hopping term  $t$ :

$$H = U \sum_i n_{i\uparrow} n_{i\downarrow} - t \sum_{\langle i,j \rangle, \sigma} c_{i\sigma}^\dagger c_{j\sigma} + h.c. \quad (2.1)$$

Despite this simplicity, the model has been analytically solved, and its ground state is known only in one dimension, using the Bethe ansatz [44, 45]. A variety of analytical and computational studies have made strides in studying its higher dimensional versions, such as perturbative expansions [46–48], mean-field theories and cluster expansions [49–51], slave Boson theory [52–54], fermionic quantum Monte Carlo approaches [55–58], and tensor network approaches [59–61], which mostly all lead to contradicting quantitative and even qualitative results [43]. But these attempts have only enhanced our theoretical understanding of strongly correlated systems, since the Hubbard model has, throughout the years, proven to contain an incredibly rich plethora of phases such as Mott insulating phases, quantum magnetism, possible connections

to high-temperature superconductivity, etc. The prospect of high- $T_c$  superconductivity hosted by the Hubbard model has prompted further theoretical and experimental research [62–66]. In recent years, there has been a push towards the model’s realization. Since the presence of a lattice on which electrons interact is an essential ingredient in the Hubbard model, there have also been attempts to use optical lattices to simulate this atomic lattice [67–69].

Another consequence of the Hubbard model is the concept of localization. This can be seen better when we consider different limits. Let us first consider the non-interacting limit of the Hubbard model:

$$H_{TB} = \sum_{\langle i,j \rangle} c_i^\dagger c_j + h.c. \quad (2.2)$$

This limit is called the tight-binding limit. A simple Fourier transform of this term gives us

$$H = \sum_i \epsilon(k) c_{ik}^\dagger c_{ik}. \quad (2.3)$$

Here,  $\epsilon(k)$  is the single-particle spectrum, and its form depends on the lattice and the types of hopping terms taken into consideration (that is, between nearest neighbors, next nearest neighbors etc). This tight binding approximation for electrons in solids gives us a “band” to fill electrons with, according to the Pauli exclusion principle, as shown in Fig. 2.1(a-b).

In the opposite limit, the hopping term will be zero, leaving us with just the Hubbard  $U$ -term

$$H = U \sum_i n_{i\uparrow} n_{i\downarrow}. \quad (2.4)$$

In this limit, we see that the term is just an on-site density term. Hence, in the absence of hopping, the electrons are localized to a single site. Now, let us say an electron occupies some energy level at  $\epsilon_a$ ; it would take an energy penalty  $U$  to place the next electron, and hence the next energy level would be at  $\epsilon_a + U$ . This leads to a “Hubbard staircase”, and is a standard artifact of the atomic limit of the Hubbard model, as shown in Fig. 2.1(c).

This discrete energy level picture of the atomic limit is modified when hopping is introduced. When both  $U$  and  $t$  are finite, the two energy levels develop a finite width  $W = 2zt$ , where  $z$  is the number of nearest neighbors. This width is a function of the hopping. The two discrete energy levels thus evolve into two bands of states of width  $2zt$ , centered around  $\epsilon_a$  and  $\epsilon_a + U$ , respectively. These bands are called Hubbard sub-bands (Fig. 2.1(d)), with the lower one called the lower Hubbard band (LHB) and the higher one called the upper Hubbard band (UHB). When the Coulomb repulsion  $U \gg W$ , the electrons prefer to be localized instead of moving around in the bands. At half-filling, this gives rise to a Mott insulator. A Mott-metal insulator transition is obtained when we have the opposite scenario: when the  $W > U$ .

Even though the Hubbard model is a very successful description of how electrons behave on a lattice, it is very far from capturing the sheer number of factors and degrees of freedom, and the resulting complexity of the environment in which electrons operate in real materials. Various additional phenomena in real materials might occur because of multiple shells of every element in the material, for example: How the electrons belonging to one element (or a site, in

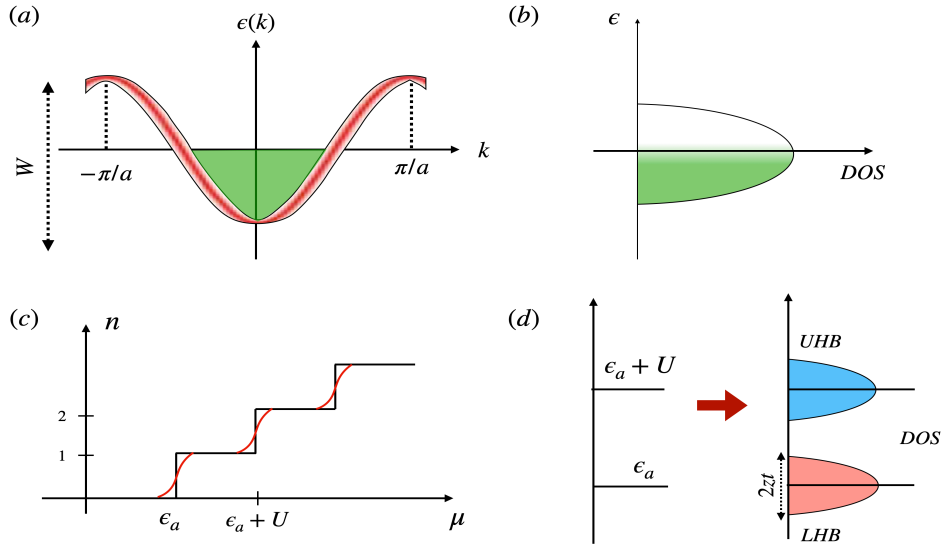


**Figure 2.1 – Various limits of the Hubbard model.** (a-b) The non-interacting limit, shown here for a metal. The filled levels are colored green. (c) The Hubbard staircase in the atomic limit. (d) In the presence of both interactions and hopping, the discrete energy levels become Hubbard sub-bands, with the width of these sub-bands being a function of hopping.

more theoretical terms), respond to the field that electrons from neighboring elements create, and so on. The influence of the environment in a crystal is discussed in detail in Chapter 7. However, it is equally essential to understand electronic movement across various sites, and its consequences in a crystal.

## 2.1 Oxidation states and valency

It is a known fact that an atom usually possesses multiple electrons, but not all of them actively participate in transport or bonding. Only the electrons in the valence shell are usually involved in bonding; depending on what the valence shell is, the factors to be considered while studying an ion and its environment in a crystal are very different.

The innermost shell has principal quantum number  $n = 1$ . It consists of only the  $s$ -orbital, whose azimuthal quantum number  $l = 0$ , and can hold a maximum of 2 electrons. The next shell with  $n = 2$  consists of the  $s$ -orbital with  $l = 0$  and  $p$ -orbital with  $l = 1$ ; since the three  $p$ -orbitals differ from each other in their  $m_z$  quantum number, the  $p$ -orbitals can hold a maximum of six electrons. The third shell with  $n = 3$  consists of  $s, p, d$  orbitals, where the five  $d$ -orbitals can hold 10 electrons in total, and the fourth shell with  $n = 4$  consists of  $s, p, d, f$  orbitals and so on. The shapes of different orbitals are shown in Fig. 2.2. It can be seen that, even in the valence shell, there are various orbitals, all of which might or might not lend themselves to bonding. In this thesis, we almost exclusively deal with metallic ions that have 3 or more shells (called transition metal ion, or TMI); hence, the valence electrons in their  $d$ -orbitals and/or  $f$ -orbitals are the most important electrons since they are not only involved in bonding, but

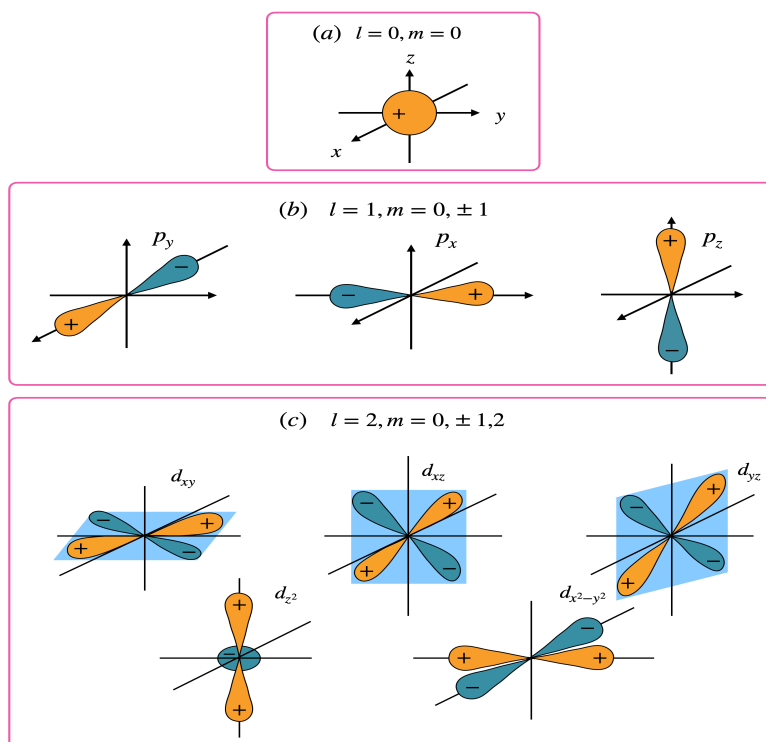


**Figure 2.2** – Different possible orbitals in an atom. (a) An angular momentum quantum number of  $l = 0$  corresponds to the  $s$ -orbital. (b) Three  $p$ -orbitals are obtained when  $l = 1$ , owing to different values of  $m$ . (c) Similarly, five  $d$ -orbitals are obtained when  $l = 2$ .

are also the electrons whose localization we aim to study.

When we speak of bonding, metallic ions usually tend to lose electrons to a more electronegative element to attain the nearest inert configuration. This loss or gain is represented using an oxidation number. These integer charge transfers follow a set of simple rules: firstly, the charge of atoms in their elemental form is taken to be zero; when it approaches another atom that can help reach the nearest fully filled configuration, charges are transferred between the atoms such that the sum of oxidation states for all atoms in a given, stable material is zero, to ensure electroneutrality. A loss of electrons is assigned a positive oxidation number and a gain is indicated by a negative oxidation number. For example, halogen atoms such as chlorine, fluorine, etc. gain an electron to become a halide ion:  $\text{Cl}^-$ ,  $\text{F}^-$ . In the same way, the oxidation number of oxygen is always -2, and so on. Transition metal ions are usually capable of having multiple oxidation numbers because of their partially filled  $d$ -valence shells.

Beyond predicting the bonding outcomes and the stoichiometry of compounds, oxidation states are also helpful in grossly predicting or determining physical properties. Tools such as valence-shell electron-pair repulsion (VSEPR) theory make use of oxidation states to predict structure [70]; crystal field theory helps predict other spectroscopic responses – this is especially important when studying transition metal ion complexes because every oxidation state that a transition metal is capable of assuming usually has distinct spectroscopic and magnetic signatures [71]. For example, transition metal ions whose oxidation states lead to fully filled

orbitals usually have negligible magnetic moment, and this can be predicted without having to measure the susceptibility.

### 2.1.1 Hybridization and coordination bonds

The oxidation state has another essential purpose: it also tells us how various positive and negative ions are oriented in the crystal. When atoms transfer or share electronic charges, the bond formed can be one of the following three main types [72, 73].

Localized valence bonds are formed when each participating atom contributes equally to the bond formation, with the two electrons involved in bonding occupying a localized bonding orbital. This is the conventional covalent bond that can be seen in, for example, a hydrogen or nitrogen molecule, etc. Since these bonds are localized, resonance structures neither exist nor do they need to be assumed. An example of this type of bonding is shown in Fig. 2.3(a).

The second class of bonds are linearly delocalized bonds, where the bonding orbitals that electrons occupy are delocalized either over the entire molecule or part of the molecule. These “resonance” bonds are quite common in organic compounds and metallic chain structures, an example of which is shown in Fig. 2.3(b).

The third class of compounds are those in which the electrons for bonding are lent entirely by one (metallic) ion. However, they are center-delocalized in three dimensions. Electronegative ions, called ligands, that require the electrons lent by the metallic ion, arrange themselves in space around the metallic ion such that they form several completely delocalized central-atom ligand bonds in three dimensions. These bonds are called coordination bonds and such compounds are called coordination compounds. An example of coordination bonding is shown in Fig. 2.3(c). This distinct spatial requirement makes coordination compounds different from typical donor-acceptor compounds. Another important ingredient is high-coordination: ligands around the central metallic ion determine how the environment affects the physical properties of the compound, via crystal field splitting (this is discussed in detail in Chapter 7). The nature of delocalization in space and the crystal environment required to form coordination bonds can only be realized via  $d$  or  $f$  orbitals because they have lobes that are differently oriented in space. This is in contrast to  $s$  and  $p$  orbitals, which, by virtue of being planar, can only provide localized or linearly delocalized orbitals. The  $s$  and  $p$  orbitals, could, at the most, hybridize to increase the coordination number to a maximum of 4 (in the case of  $sp^3$  hybridization); however, these are still localized due to hybridization. Many materials involving a  $d$  or  $f$  metallic element are coordination compounds, such as organometallic compounds, crystals, alloys, and so on. Transition metal elements are capable of forming coordination bonds with a variety of ligands, and this determines the geometry of the crystal.

### 2.1.2 Mixed oxidation states

As mentioned previously, transition metal elements can usually assume different oxidation numbers because they can donate electrons to the ligands from multiple orbitals. For example, manganese can donate electrons either from its  $3d$  orbital or from the  $4s$  orbital; hence, it can

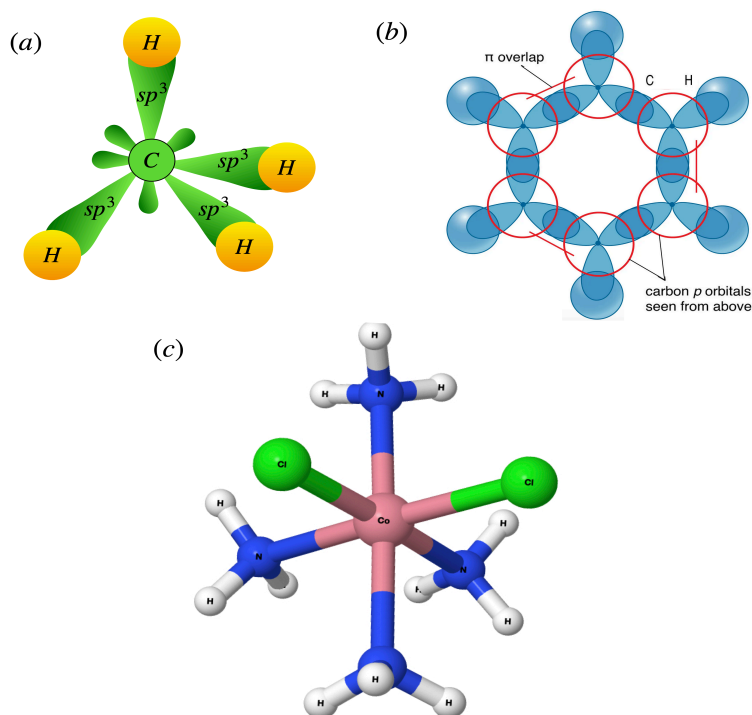


**Figure 2.3 – Examples of different kinds of bonding.** (a) In methane (CH<sub>4</sub>), one *s*-orbital and three *p*-orbitals of carbon hybridize to give four *sp*<sup>3</sup> orbitals, each of which forms a covalent bond with hydrogen and mutually shares a pair of electrons. (b) In benzene (C<sub>6</sub>H<sub>6</sub>), the two of the three *p*-orbitals on each carbon atom overlap, enabling the delocalization of a pair of electrons across the entire molecule. Figure taken from [74]. (c) In [Co(NH<sub>3</sub>)<sub>4</sub>Cl<sub>2</sub>]<sup>+</sup>, the bond between cobalt and chloride ion is composed of electrons that come entirely from cobalt. Molecule produced using [75].

assume oxidation states of +2, +3, +4,+6, or +7. The periodic table with all elements and their possible oxidation numbers can be found in Appendix B.

However, these different oxidation numbers of the same element can sometimes be found in the same material. These materials are called mixed-valence (MV) compounds. As we will see in subsequent chapters, some cluster Mott materials also fall into this category. In mixed-valence compounds, the transition metal ions can all be considered as having the same oxidation state, except for one or two ions, which accommodate the excess electrons, causing their oxidation state to differ from the uniform value. However, in this thesis, we instead choose the second proposed mechanism for mixed valences, in which the electrons are considered to be delocalized over all (or part) of the metallic ions displaying mixed valency.

The presence of mixed valence in a material, in some instances, also means that different ligands might be attached to the transition metal ion. Hence, it is necessary to delineate the relation between ligands and mixed valence metallic ions. The following classification was provided by Robin and Day [73, 76, 77]:

1. Class I: In this class of MV compounds, the metal ions contributing to the mixed valence are in ligand fields of varying symmetries and strengths. This also means the excess electrons are strongly localized to specific ions.

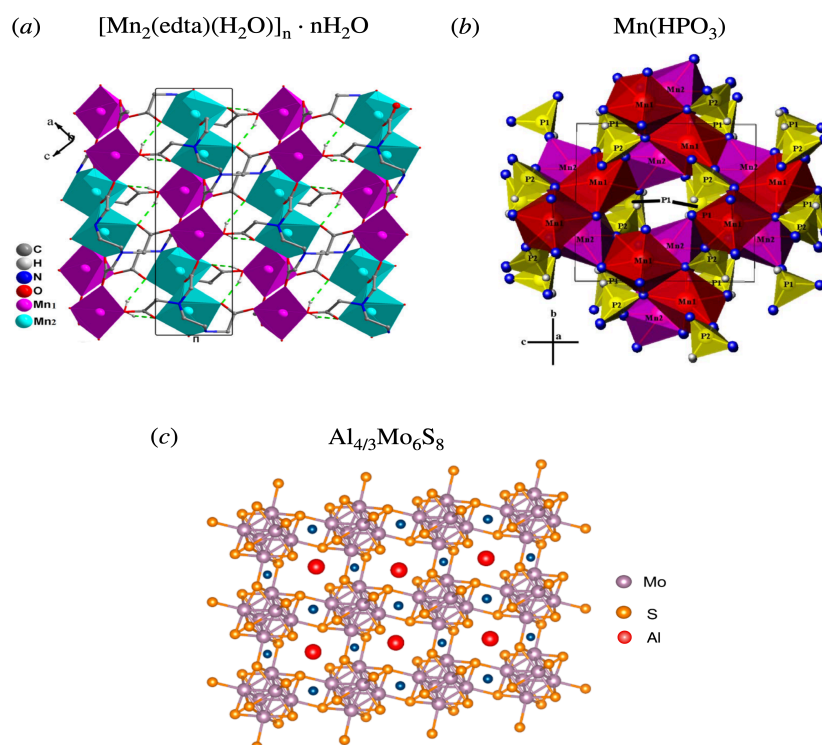


**Figure 2.4 – Examples of mixed valence materials.** (a)  $[\text{Mn}_2(\text{edta})(\text{H}_2\text{O})]_n \cdot n\text{H}_2\text{O}$  is a class I MV compound, where manganese is in two different oxidation states:  $\text{Mn}^{1+}$  and  $\text{Mn}^{2+}$ . These two states have different coordination numbers, with  $\text{Mn}^{1+}$  being hexa-coordinated and  $\text{Mn}^{2+}$  being hepta-coordinated. Adapted from [78], Copyright (2011), with permission from Elsevier. (b)  $\text{Mn}(\text{HPO}_3)$  is a class II MV compound, where both  $\text{Mn}^{1+}$  and  $\text{Mn}^{2+}$  ions have the same coordination number but with each of them surrounded by octahedral ligand fields that differ by a slight distortion. Adapted from [79], Copyright (2005), with permission from Elsevier. (c)  $\text{Al}_{4/3}\text{Mo}_6\text{S}_8$  is a class III compound where  $\text{Mo}_6\text{S}_8$  forms clusters in which all participating molybdenum ions have the same oxidation state. Adapted from [80], Copyright (2018) American Chemical Society.

2. Class II: In this class of MV compounds, the metal ions attach themselves to near-identical ligands, with slight distortions, using which different valencies can still be distinguished. All metal ions in the material, irrespective of the individual oxidation states, are surrounded by ligand fields of near-identical symmetry.
3. Class IIIA: In this category, the metal ions are grouped into clusters in which they are equivalent.
4. Class IIIB: This is the case where there is no mixed valence, and all metallic ions have the same oxidation state throughout the material.

Examples of different mixed valence materials are shown in Fig. 2.4. In reality, there are many factors that make the classification of MV compounds more difficult. Temperature can be one such factor: for example, a phase transition in  $\text{Fe}_3\text{O}_4$  brings in structural changes, because of which the oxidation state of iron changes from  $\text{Fe}^{3+}$  to a charge ordering of +2 and +3, which had been controversial for many years [70]. Similarly, high correlations also make it

challenging to study mixed valences, especially in  $f$ -electron coordination compounds.

## 2.2 Role of relativistic effects in the atom

Relativistic effects play an important role in shaping the physics of coordination compounds. For this, one has to consider the Dirac equation, which is the generalization of the Schrodinger equation in a relativistic setting. It is the underlying equation for all fermionic systems, since it describes the intrinsic origin of the fermionic spin and its relativistic behavior, such as spin-orbit coupling, from first principles. We start with the famous relation between energy and momentum from relativity:

$$E = \sqrt{(mc^2)^2 + \mathbf{p}^2 c^2}, \quad (2.5)$$

where the symbols hold their usual meaning. Using the correspondences  $E \rightarrow i\hbar\partial/\partial t$  and  $p \rightarrow \hbar\nabla/i$ , a preliminary “relativistic” form of the Schrodinger equation could be

$$i\hbar\frac{\partial\psi}{\partial t} = \sqrt{(mc^2)^2 - (\hbar c)^2\nabla^2}\psi. \quad (2.6)$$

Now, if we make use of the expression for the differential operator [81]

$$D = \beta mc^2 + \sum_{j=1}^3 \alpha_j p_j c, \quad (2.7)$$

such that  $\beta, \alpha_j$  satisfy the relations

$$\beta^2 = 1, \quad \beta\alpha_j + \alpha_j\beta = 0, \quad \alpha_i\alpha_j + \alpha_j\alpha_i = 2\delta_{ij}, \quad (i, j = 1, 2, 3) \quad (2.8)$$

and consequently

$$D^2 = (mc^2)^2 - (\hbar c)^2\nabla^2, \quad (2.9)$$

then the Dirac equation for a free particle of mass  $m$  is given by [82, 83]

$$i\hbar\frac{\partial\psi}{\partial t} = (mc^2\beta + c\boldsymbol{\alpha} \cdot \mathbf{p})\psi. \quad (2.10)$$

It can be shown that the Dirac equation for a particle of mass  $m$  and charge  $e$  in the presence of an electromagnetic field can be given by:

$$i\hbar\frac{\partial\psi}{\partial t} = \left[ c\boldsymbol{\alpha} \cdot \left( \mathbf{p} + \frac{e}{c}\mathbf{A} \right) + \beta mc^2 + V(r) \right] \psi, \quad (2.11)$$

where the coupling of the electron to the scalar potential is included via

$$V(r) = -e\Phi(r) = -\frac{e^2}{r}. \quad (2.12)$$

Here,  $\mathbf{A}$  is the external vector potential, and  $\Phi$  is an electromagnetic scalar potential.

Now, if we consider

$$H^{(0)} = \frac{\mathbf{p}^2}{2m} + V \quad (2.13)$$

as the non-relativistic terms, then corrections to this can be derived by using  $A = 0$  and solving for the appropriate Hamiltonian  $H$  that acts on the spinor  $\psi$ . It is seen that the resulting expression for the Hamiltonian  $H$  is given by [82, 84]

$$H = H^{(0)} + H_{\text{rel}} + H_{\text{SOC}} + H_{\text{Darwin}} \quad (2.14)$$

where

$$H_{\text{rel}} = -\frac{\mathbf{p}^4}{8m^3c^2} \quad (2.15)$$

is the relativistic energy correction,

$$H_{\text{Darwin}} = \frac{\hbar^2}{8m^2c^2} \nabla^2 V \quad (2.16)$$

is the Darwin correction, and

$$H_{\text{SOC}} = \frac{1}{2m^2c^2} \frac{1}{r} \frac{dV}{dr} \mathbf{L} \cdot \mathbf{S} \quad (2.17)$$

is the spin-orbit coupling. This term can be rewritten so that

$$H_{\text{SOC}} = \lambda \mathbf{L} \cdot \mathbf{S} \quad (2.18)$$

where the prefactor  $\lambda = \frac{e^2}{2m^2c^2} \frac{1}{r^3}$  determines the strength of spin-orbit coupling.

Spin-orbit coupling (SOC) is hence a relativistic effect that connects the spin angular momentum of the electron with the electrostatic potential of its environment. In a crystal, the potential is dominated by the spherical atomic potential  $E = -\nabla V(r)$ , and hence the atomic nuclei form the largest contributors to spin-orbit coupling in such a case.

SOC holds importance across various areas of research in physics; for example, M. Goeppert-Mayer and H. Jensen showed just how important spin-orbit coupling is in the physics of nuclear structure, where the addition of spin-orbit coupling to the mean field of the nucleons successfully predicted nuclear magic numbers and stability of the nucleus [85, 86]. This work was subsequently awarded the Nobel Prize in Physics in 1963. In recent years, SOC has also gained considerable spotlight in condensed matter physics, an illustration of which we will see in subsequent chapters.

In the context of transition metal complexes or coordination compounds, the most important effect of the spin-orbit coupling is that it causes shifts in the electron's atomic energy levels. This, in competition with crystal fields formed by surrounding ligands and Coulomb repulsions, determines the bandstructure of the material. This is discussed in more detail in Chapter 7.

### 2.2.1 Coupling schemes

It is worth mentioning that the extent to which SOC leads to energy level splitting varies significantly with the atomic mass of the transition metal element. For light transition metal elements (especially  $3d$  transition elements), the splitting due to SOC is a lot smaller than multiplet splitting (that is, energy differences between states in the same angular momentum in a subshell, which arises from electron-electron repulsion). When relativistic SOC is introduced as a perturbation, the multiplet terms  $^{2s+1}L$  split into

$$^{2s+1}L_J, \quad (2.19)$$

where each of these new levels is characterized by the total angular momentum  $J$ . This is called the *term symbol representation*.

As discussed previously,  $L$  can take values of  $0, 1, 2, \dots$  and they are denoted in the term symbol as letters  $S, P, D, F, \dots$  respectively, with the spin-multiplicity  $(2s+1)$  denoted as the left superscript. The total angular momentum is denoted as the right subscript. This perturbative approach to SOC is called  $L - S$  coupling, and is usually used for lighter transition metal elements. In  $L - S$  coupling, spin and angular momentum are considered as being a sum total of all electrons involved. That is,

$$\begin{aligned} L &= \sum_i L_i \\ S &= \sum_i S_i. \end{aligned} \quad (2.20)$$

This scheme is usually applied to  $3d$  transition metal ions, where spin-orbit coupling is usually weak or at best, moderate. Hence, the spin-orbit coupling term can then be written using the  $L - S$  scheme as

$$H = \lambda L \cdot S \quad (2.21)$$

This expression for spin-orbit coupling in the  $L - S$  scheme then combines spin and angular momentum to give us the total angular momentum  $J = L + S$ . The energy contribution of the SOC term is then given by the expectation value

$$\langle L \cdot S \rangle = J(J + 1) - L(L + 1) - S(S + 1). \quad (2.22)$$

The expression for total angular momentum shows that it can take a range of values from  $[|L - S|, |L - S + 1|, \dots, |L + S - 1|, |L + S|]$ . The introduction of SOC leads to states with different  $J$  values also differ in their energies. The  $L - S$  coupling scheme for a two-electron system is shown in Fig. 2.5(a).

However, as we move to heavier transition metal elements, especially  $4d$  and  $4f$  elements, the strength of SOC also increases, and in the strong SOC regime, the  $L - S$  coupling scheme is no longer a valid description. We instead use perturbation theory in the opposite direction: we first calculate the splitting of energy levels under the influence of SOC, and then introduce

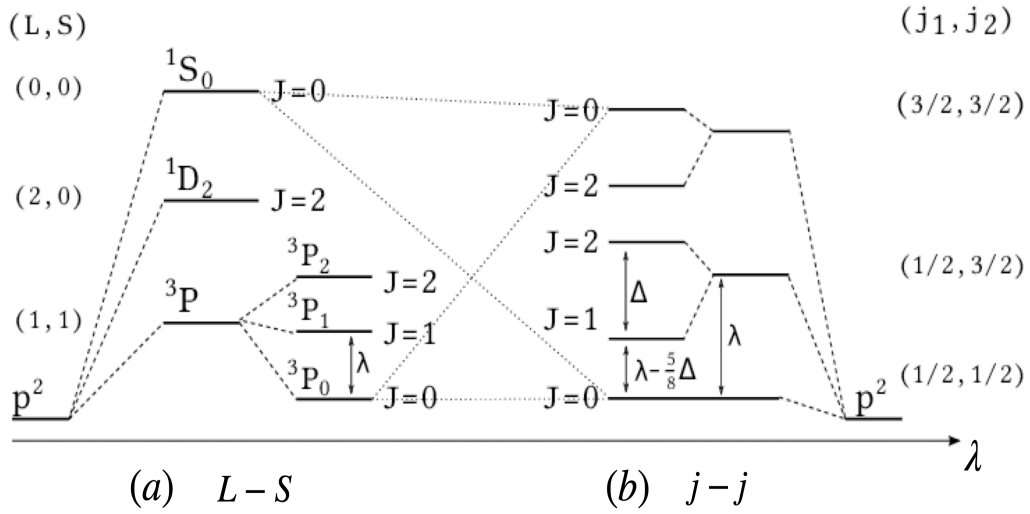


**Figure 2.5 – Types of coupling schemes.** Here, they are illustrated for a  $p^2$  configuration, shown as the SOC coupling strength  $\lambda$  increases. (a)  $L - S$  coupling applies in the lower SOC regime. (b)  $j - j$  coupling applies in the strong SOC regime. Here,  $\Delta$  is the splitting between the  $J = 1$  and  $J = 2$  states. Illustration adapted with permission from [87]. Copyright (2018) by the American Physical Society.

electron-electron repulsion as a perturbation. This approach is called the  $j - j$  coupling scheme – the spin and angular momentum of each electron are first summed up, and the total angular momentum for each electron is given by  $j_i = l_i + s_i$ . The total angular momentum of the atom is then expressed as a sum of those of all the constituent electrons:  $J = \sum_i j_i$ . The  $j - j$  coupling scheme for a two-electron system is shown in Fig. 2.5(b).

In practice, this only works for extremely heavy elements, where spin-orbit coupling is large enough to almost neglect electron-electron repulsion. In most stable atoms, however, SOC is sufficiently strong such that  $L - S$  coupling no longer holds, but is not strong enough to dominate electron-electron repulsions. Hence, neither can be treated as a perturbation, and both have to be considered on equal footing. This is called intermediate coupling. In the intermediate coupling regime, the Hamiltonian has significantly lower symmetry compared to either of the extreme limits. Hence, the energy levels can no longer be characterized by quantum numbers unlike the  $L - S$  or  $j - j$  schemes.

### 2.2.2 Racah parameters

We saw previously that energy multiplets depend closely on how various terms in the Hamiltonian split these energy levels, and various coupling schemes were proposed to characterize some of the resulting energy levels using different quantum numbers. In practice, it is also important to quantify the splitting; for this, the conventional procedure is to start by constructing eigenstates  $|L, M; S, \Sigma\rangle$  of the angular momenta, which spans the multiplet term  $^{2S+1}L$ . This can be done because the electron-electron repulsion is invariant under simultaneous inversion and rotation of all electrons, while also being independent of spin. Given these basis states, the energy corrections caused by electron repulsion can be calculated as matrix elements.

In the special case of partially filled  $d$ -orbitals, a more compact way of expressing the total

repulsion and various contributions to it is in terms of Racah parameters  $A, B, C$ , which are given by [73, 88]

$$\begin{aligned} A &= F^0 - \frac{49}{441}F^4 \\ B &= \frac{1}{49}F^2 - \frac{5}{441}F^4 \\ C &= \frac{35}{441}F^4, \end{aligned} \quad (2.23)$$

where  $F^0, F^2$  and  $F^4$  are Slater-Condon parameters<sup>1</sup>. Parameter  $A$  determines the energy of destabilization due to an average electron interaction, which is usually an offset that can be excluded by choosing a reference appropriately. Parameter  $B$  determines the effect of coordination bond strength between the ligand and metallic ion, and hence becomes important when crystal field is present. The parameter  $C$  is used when the energies of a set of states differ in multiplicity from the ground state. Parameters  $B$  and  $C$  are obtained from empirical spectroscopic data of free atoms and ions, though  $C$  is usually approximated as  $C \approx (1/4)B$ . Because of different charge distributions and spin orientations in different one-electron states, and hence different inter-electron interactions, even states with same electronic configuration can have different energies. Racah parameters are used to calculate the energies of each of these configurations. For example, in Fig. 2.6, the interaction energies for different arrangements of electrons for certain fillings in the  $d$ -orbital are shown. Let us consider  $d^2$ , for example. We can see that the term with the lowest energy is  ${}^3F$ : that is, with  $S = 1$  and  $L = 3$ . This is the term with the highest spin multiplicity  $((2S + 1) = 3)$  and maximal allowed angular momentum among all the terms with 2 electrons, confirming Hund's rules. Hence, Hund's rules can be understood as a natural consequence of comparing various interaction energies, which can be expressed in a compact way using Racah parameters. The use of Racah parameters also makes

<sup>1</sup>Consider two-electron interaction integrals of the type [73]

$$R^{(k)}(abcd) = e^2 \iint R_{n(a)l(a)}^*(r_1)R_{n(b)l(b)}(r_1)K_k(r_1, r_2) \times R_{n(c)l(c)}^*(r_2)R_{n(d)l(d)}(r_2)r_1^2r_2^2dr_1dr_2, \quad (2.24)$$

where  $a$  and  $b$  are one-electron functions of the first electron, while  $c$  and  $d$  are those of the second electron,  $K_k$  is the exchange integral between two electrons,  $n$  and  $l$  are the principal and azimuthal quantum numbers of the respective electrons. We then define

$$\begin{aligned} R^{(k)}(aabb) &= F^{(k)} \\ R^{(k)}(abba) &= G^{(k)}, \end{aligned} \quad (2.25)$$

where  $F^{(k)}$  and  $G^{(k)}$  are Slater-Condon parameters. These parameters are commonly used in the Hartree-Fock method and in the construction of many-body wavefunctions. There are three primary types of integrals referred to as Slater-Condon parameters. The integrals  $F^{(k)}$  describe the average Coulomb repulsion between electrons in different orbitals. When  $k = 0$ , it represents the direct Coulomb integral, which is the average repulsion energy between two electrons in the same orbital. Higher-order parameters, which have  $k > 0$ , describe the angular part of the electron-electron repulsion. Similarly, the Slater-Condon parameter  $G^{(k)}$ , describes the exchange interaction between electrons.

Electronic Configuration	Term	Relative Electron Interaction Energy	
$d^1, d^9$	${}^2D$		
	$d^2, d^8$	${}^3F$	$A - 8B$
		${}^3P$	$A + 7B$
		${}^1G$	$A + 4B + 2C$
		${}^1D$	$A - 3B + 2C$
	${}^1S$	$A + 14B + 7C$	
$d^3, d^7$	${}^4F$	$3A - 15B$	
	${}^4P$	$3A$	
	${}^2H, {}^2P$	$3A - 6B + 3C$	
	${}^2G$	$3A - 11B + 3C$	
	${}^2F$	$3A + 9B + 3C$	
	${}^2D', {}^2D''$	$3A + 5B + 5C \pm (193B^2 + 8BC + 4C^2)^{1/2}$	

**Figure 2.6** – Racah parameters for a few of the possible fillings in  $d$ -orbitals. Energies of fillings  $d^{10-n}$  differ from those of  $d^n$  by an offset. Terms that have the same  $L$  and  $S$  are distinguished by primes, for example in the case of  $d^3$ . Figure adapted from [73].

the understanding of level splittings in various regimes significantly easier and more intuitive to understand, as will be shown in Chapter 7.

## 2.3 Conclusion

In this chapter, we have seen how the Hubbard model realizes localization in solids. In real materials, however, many other factors play into localizing electrons; electrons can be shared, donated, or localized at a site or within a group of sites. This led us to discuss oxidation states and why they are important while studying materials with transition metal ions. Relativistic effects such as spin-orbit coupling, combined with electron localization at and around various centers in a crystal, together determine a variety of properties of the material, ranging from observables such as specific heat, susceptibility, etc, to energy level splittings and phase transitions. In the subsequent chapters, we will see how exactly this interplay determines the above properties and how best to understand them in cluster Mott materials.



Irrespective of the nature of the Hamiltonian, whether classical or quantum, a natural attempt towards understanding the system it describes is to solve the Hamiltonian for its energies and eigenstates. In the case of a quantum many-body problem, we would have to solve the Schrödinger equation

$$H|\psi\rangle = E|\psi\rangle. \quad (3.1)$$

Being equipped with this knowledge, a variety of static or dynamic observables relevant to the system can be computed, using exact diagonalization techniques. As is in the name, exact diagonalization (ED) provides exact solutions to the Schrödinger equation for the given Hamiltonian, up to machine precision. Hence is especially useful for providing highly accurate results for systems with a relatively small number of particles, such as quantum dots, small molecules, or clusters of atoms. Owing to the accuracy, solutions obtained through exact diagonalization also serve as benchmarks for other numerical (usually) approximate methods.

However, owing to the many-body nature of the Hamiltonian, a few complications arise. The no-frills approach of ED also means that the computer can only handle limited system sizes: for a system with  $N$  particles, which each have  $m$  degrees of freedom, the Hilbert space grows as  $m^N$ . The Hilbert space thus grows exponentially with the size of the system, which at a certain point would become impossible to handle for even the most powerful computers. One has to thus take care of drawing any inferences of the thermodynamic limit from exact-diagonalization studies.

One way to handle such large Hilbert spaces is to take advantage of the inherent symmetries of the Hamiltonian. This allows us to break the Hilbert space into smaller sectors, which can then be selectively looked at depending on which particulars of the Hamiltonian we are interested in.

### 3.1 Constructing the Hamiltonian matrix

The most essential ingredient to building a Hamiltonian matrix in the first place is to ascertain what basis we want to express it in. As mentioned before, depending on the symmetries and the particular sectors we want to look at, we can use them as a starting point to build a set of many-body basis states.

The key idea in expressing basis states is to use bit values to denote the degrees of freedom – and this forms the fundamental building block for the list of many-body basis states. Let us consider a linear  $N$ -site spinless fermionic chain as an example. Here, a site on the chain can have one of the following possibilities: it can either contain a fermion, or be empty. A bit value of 0 can be used to denote a state in which the site is unoccupied, and a bit value of 1 can be used to denote a state in which the site is occupied. Note that this is merely a convention, and it can very well also be the other way around.

The labels from 0 to  $2^N - 1$  are used for the states, and the bit values of these integers directly correspond to the arrangement of spins on the chain. Once we have these states, one can construct the Hamiltonian in real space by iterating over all basis states and making a note of how each operator in the Hamiltonian operates on the given sequence of fermions, or, in our language, a sequence of 0's and 1's. Let us consider a simple tight-binding Hamiltonian

$$H = \sum_{\langle i,j \rangle} c_i^\dagger c_j + h.c. \quad (3.2)$$

as an example. A code snippet in Alg. 1 shows how respective entries in its corresponding Hamiltonian matrix are updated. An operator (here,  $c_i^\dagger c_j$  acts upon a state with integer label  $a$ , on a bit level. In this way, one can directly deal with the actual sequence of fermions via the integer labels. This operation leads to a resultant sequence (encoded in bits), and one has to look up the integer label corresponding to the resultant state: let us assume it corresponds to label  $b$ . The matrix entry  $H[a, b]$  is then updated with the prefactor that the operator carries with it in the Hamiltonian.

There are a few observations to be made from Alg. 1. Note that the operator at hand by definition is off-diagonal. It is because of this fact that we would have to look up the integer index corresponding to the resultant state. We can very well also have operators (for example, a density operator of sorts) that is diagonal – in that case, the diagonal entry  $H[a, a]$  would be updated accordingly, without the need to look up a second  $b$  index.

---

**Algorithm 1** ED for tight binding model (off-diagonal)

---

**Require:**  $H$  is Hermitian matrix of size  $N \times N, N > 0$

**Require:**  $t$  is some tight-binding parameter

```

for a = 0 to  $2^{N-1}$  do
  state = binary(a)
  if state[i]  $\neq$  state[j] then
    newstate = bitflip(state, i, j)
    b = Integer(newstate)
     $H[a, b] \leftarrow H[a, b] + 0.5t$ 

```

$\triangleright$  we require that a neighboring site  $j$  of a site  $i$  be unoccupied  
 $\triangleright$  Operator acts upon state:  $c_i^\dagger c_j |state\rangle = |newstate\rangle$   
 $\triangleright$  Filling the relevant entries in the Hamiltonian matrix

---

Now that we have familiarized ourselves with the scheme of labeling and operating upon

many-body states, we can now take a closer look at how symmetry considerations would ease computations.

## 3.2 Block diagonalization of the Hamiltonian matrix

In the previous subsection, we used a “default” basis to express our Hamiltonian in and iterated over all possible states for the case of an  $N$ -site chain with spins on it. However, this is an issue when the Hamiltonian grows exponentially with the number of sites and becomes increasingly unfeasible computationally. Hence, symmetries should be used whenever possible/necessary. This reduces the Hamiltonian to a block diagonal form, each block corresponding to a different quantum number of the conserved quantity. These blocks are disjoint from one another and hence can be diagonalized independently, as shown in Fig. 3.1. Based on the requirement, one might sometimes not need all the blocks either. Thus, the block diagonal form significantly reduces the computational cost of building and diagonalizing the Hamiltonian.

The simplest starting point is to consider particle number conservation. For the tight-binding example at hand, the number operator  $n_f = \sum c_{i\sigma}^\dagger c_{i\sigma}$  commutes with the Hamiltonian. This means the entire Hilbert space can be broken into various mutually exclusive sectors that are each characterized by their unique value of  $n_f$  (in the case of a spinful system,  $S_z$  conservation plays a similar role):

$$H = \bigoplus_{n_f=0}^N H_{n_f}. \quad (3.3)$$

This already makes evaluating the Hamiltonian very convenient because, if we are only interested in studying, say  $n_f < N$  fermions on an  $N$ -site chain, we need only consider basis states that satisfy this condition (which constitute just a fraction of the entire Hilbert space), and use them to construct the Hamiltonian matrix [89]. Extracting these select basis states from the full list is relatively straightforward (for particle number conservation), as shown in Alg. 2.

---

### Algorithm 2 Constructing basis for a particular particle number sector

---

**Require:**  $N \geq 0$

**Ensure:**  $y = x^n$

$y \leftarrow 1$

$X \leftarrow x$

$N \leftarrow n$

**for**  $a = 0$  to  $2^{N-1}$  **do**

    state = binary( $a$ )

**if** sum(state) ==  $n_f$  **then**

        append(basis,  $a$ )

$\triangleright$  we add up all the bit values in the bit array to infer how many sites are occupied  
 $\triangleright$  the integer  $a$  is now part of the list of basis states

---

Another symmetry that can very often be exploited to break the Hamiltonian blocks to even

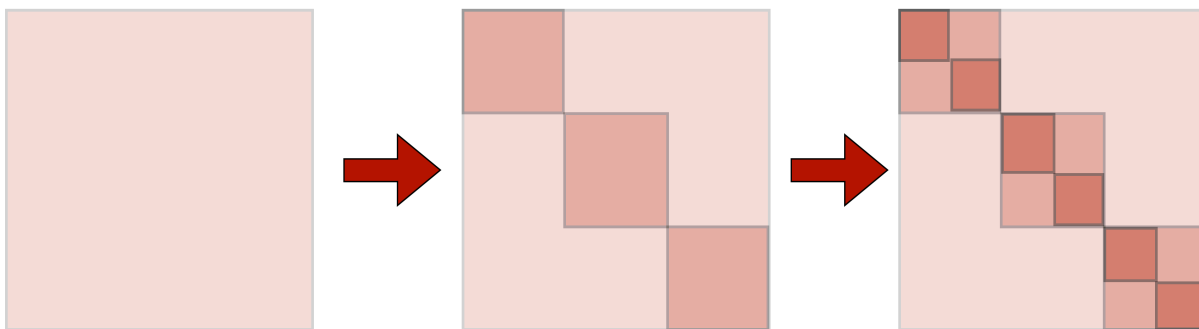


**Figure 3.1 – Schematic representation of block diagonalization.** In the leftmost figure, the Hamiltonian has no structure to it. Once we make use of a symmetry, the Hamiltonian acquires a structure in which it is split into individual blocks, each of a different allowed quantum number (middle figure). More than one symmetry can be used at a time, if the symmetries commute with each other. In such a case the Hamiltonian acquires an even finer block-diagonal structure, such that each of the smallest blocks now pertain to a definite permutation of the allowed quantum numbers of the symmetries used (rightmost figure).

smaller blocks is momentum conservation. The core idea is that in a particular momentum sector, a state can be expressed in terms of a reference state and all its translations. That is,

$$|\Psi(k)\rangle = \frac{1}{\sqrt{N_0}} \sum_{r=0}^{r=N-1} e^{-ikr} T^r |\Psi\rangle. \quad (3.4)$$

With symmetries such as momentum, where there are several states which are essentially equivalent to one another by virtue of the symmetry, the methodology of building a basis is different; we not only check for which states lie in a specific momentum sector but also check if a state can be a suitable representative for all the states that are obtained by performing translations on it [90]. This is shown in Alg. 3. Similarly, other spatial symmetries of the problem can be used to block diagonalize the Hamiltonian in different ways. Multiple symmetries can be used simultaneously, given that they commute with each other. The implementation of any symmetry follows a similar idea, where the corresponding operator is operated upon on a bit-level for a certain state, and the resultant state decides which entry in the Hamiltonian matrix needs to be updated.

While thus setting up the Hamiltonian in a convenient block-diagonal form, it is also essential to revisit some technical subtleties that come along with expressing a chain of fermions in terms of bit arrays and manipulating these bit arrays using various operators. This is required before feeding the Hamiltonian matrix into a diagonalization routine.

### 3.2.1 Computer storage of states

In the previous section, we have seen how different routines can be used to take advantage of symmetries and construct the Hamiltonian matrix. One of the main pillars of ED rests on how basis states are stored and manipulated by various operators.

A state is stored as a string of bits in the computer. Hamiltonians, which are spinless, are the easiest case: here, bit value “0” can be used to indicate an empty site, and a bit value “1”

---

**Algorithm 3** Check if a state lies in a given momentum sector
 

---

**Require:**  $N \geq 0$ **Require:**  $0 \leq k < N$ phase  $\leftarrow -1$ representative  $\leftarrow |\text{oldlabel}\rangle$  $|\text{newlabel}\rangle \leftarrow |\text{oldlabel}\rangle$ **for**  $j = 1$  to  $N$  **do**
 $|\text{newlabel}\rangle = \text{bit-translate}(|\text{oldlabel}\rangle)$      $\triangleright$  translations of spins in a state with a certain integer label are carried out by moving the relevant bits around
**if**  $|\text{newlabel}\rangle < |\text{oldlabel}\rangle$  **then**
 representative =  $|\text{newlabel}\rangle$      $\triangleright$  here, the convention we have chosen is the smallest integer would be the representative
**else if**  $|\text{newlabel}\rangle = |\text{oldlabel}\rangle$  **then**
 phase =  $e^{-2i\pi kj/N}$      $\triangleright$  If a given state is not a representative, phase tells us how many translations it takes to get to the representative
 

---

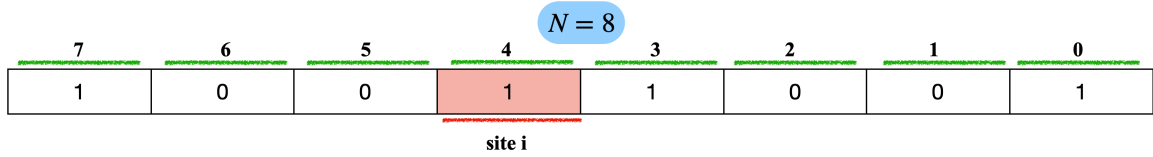
can be used to indicate that a site is occupied by a fermion. Similarly, spin-1/2 models also need only two building units: a bit value of “1” can indicate an up-spin, and a bit value of “0” can indicate a down-spin. This is shown in Fig. 3.2(a). Depending on zero-based or one-based indexing, the bits are either labeled starting from 0, in which case the length of a state goes till  $N - 1$ , or from 1, in which case the string goes till  $N$ . To perform operations on specific sites, a particular site can be singled out by simply using the same convention as used for an array: One can obtain information on the occupation on site  $i$ , by simply using  $a[i]$ .

Let us now marginally increase the complexity: let us say there are now three possible occupations a site can have: a site can either be occupied by an up-spin or a down-spin or be unoccupied. In such a case, we might need more than one bit to denote the occupation information on a site: we now denote “00” as an unoccupied site, “01” to be occupied by an up-spin, “10” to be occupied by a down-spin, and “11” to denote both up-spin and down-spin on a site. The “11” bits would be excluded if we assume a hard-core condition and enforce single-occupation. Hence, the bit string will now be twice as long as the previous case, with each site now allotted two units, starting at 0 (or 1) and ending at  $2(N - 1)$  (or  $2N$ ). This is shown in Fig. 3.2(b).

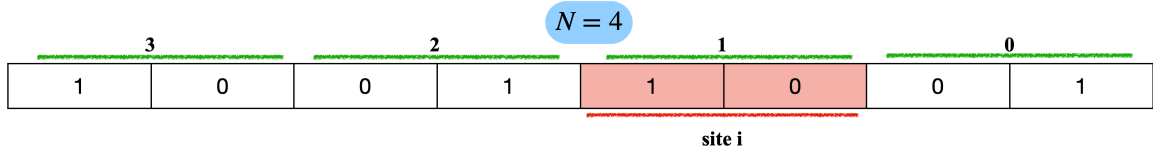
Another factor that might increase the number of bits dedicated to a site is if it has more underlying structures, such as multiple orbitals. If a site has multiple orbitals, each orbital can hold two spins at the maximum. Assuming a site has  $m$  orbitals, we would then need  $2m$  bits per site to capture the occupation information on the site. This also means that to access any position on the string, we would need information on its site index as well as its orbital index. An example is shown in Fig. 3.2(c).

One need not necessarily use a binary base all the time. Another way of denoting occupation information is by using a higher base instead of base 2: for example, if we adopt a base 3, we

(a) **Hamiltonian with spineless fermions** :  $|0\rangle \rightarrow 0, c^\dagger|0\rangle \rightarrow 1$



(b) **Single-orbital Hamiltonian with spinful fermions** :  $|0\rangle \rightarrow 00, c^\dagger_\uparrow|0\rangle \rightarrow 01, c^\dagger_\downarrow|0\rangle \rightarrow 10, c^\dagger_\uparrow c^\dagger_\downarrow|0\rangle \rightarrow 11$



(c) **Multi-orbital Hamiltonian with spinful fermions** :  $|0\rangle \rightarrow 0000, c^\dagger_{m\uparrow}|0\rangle \rightarrow 0001, c^\dagger_{m\downarrow}|0\rangle \rightarrow 0010, c^\dagger_{m\uparrow\downarrow}|0\rangle \rightarrow 0011, c^\dagger_{n\uparrow}|0\rangle \rightarrow 0100, c^\dagger_{n\downarrow}|0\rangle \rightarrow 1000, c^\dagger_{n\uparrow\downarrow}|0\rangle \rightarrow 1100$

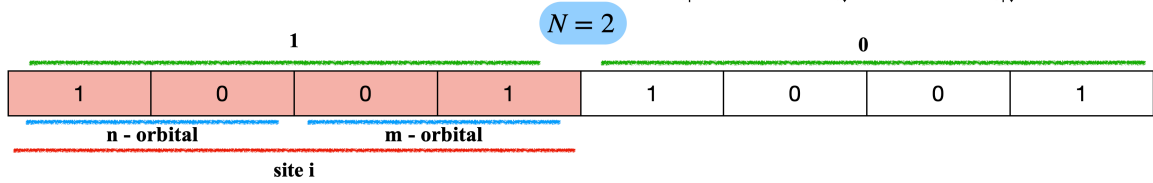


**Figure 3.2** – How basis states can be stored in different ways, depending on the requirement. (a) If we need to represent just two possible states using base 2, then one bit per site is sufficient. (b) If we need to represent four states using base 2, then every site would need two bits. As a result, an  $N$ -site chain would require  $2N$ -bits. (c) Similarly, in a case where every site needs four bits, an  $N$ -site chain would then need  $4N$ -bits.

could denote an unoccupied site by “0”, an up-spin by “1”, and a down-spin by “2” (assuming hard-core condition). This makes handling a large number of sites easier. In this way, increasing the degrees of freedom that are accommodated on a site further decreases the system sizes that ED can ultimately handle.

### 3.3 Jordan-Wigner strings

So far, we have seen how to construct basis states with given symmetry considerations in terms of bit sequences and how operators manipulate these bit sequences to ultimately populate the Hamiltonian matrix accordingly. To that end, we considered an example of a simple tight-binding model, which consisted of creation ( $c^\dagger_j$ ) and annihilation ( $c_j$ ) operators.

One has to straighten out the subtle difference between the physics of the system and what the computer makes of it – operators in any such algorithms are usually assumed by the computer to be bosonic, even while we have a system of fermions at hand. This calls for a way of reconciling the two, which is done by introducing Jordan-Wigner strings. The Jordan-Wigner transformation is a mapping between a Hilbert space of spineless fermions and a Hilbert space of “hard-core” bosons (that is, double occupancy on a site is not allowed). The idea can also be extended to include the case of fermions with spin. If  $c^\dagger_i(c_i)$  are fermionic creation(annihilation) operators and  $b^\dagger_i(b_i)$  are bosonic creation (annihilation) operators, then the Jordan-Wigner transformation connecting the two reads

$$\begin{aligned} c_j &= \mathcal{F}_j b_j \\ c_j^\dagger &= b_j^\dagger \mathcal{F}_j, \end{aligned} \quad (3.5)$$

where

$$\mathcal{F}_j = e^{i\pi \sum_{l < j} n_l} \quad (3.6)$$

holds information on the occupation of all sites preceding site  $j$ . In this way, one can see that the Jordan-Wigner transformation essentially expresses a local operator in terms of non-local operators by attaching a “string” to the bosons, as shown in Fig. 3.3.

In terms of the ED routine, factoring in these non-local Jordan-Wigner strings becomes especially important in two instances. Firstly, they need to be accounted for when we have off-diagonal operators. For example, considering the example of tight binding Hamiltonian again, the tight-binding term when strings are accounted for, becomes [91]

$$c_i^\dagger c_j + c_i^\dagger c_j = a = b_i^\dagger \exp(i\pi(n_{i+1}n_{i+2} \cdots n_{j-1})) b_j + b_j^\dagger \exp(i\pi(n_{j+1}n_{j+2} \cdots n_{i-1})) b_i. \quad (3.7)$$

Here we see that the string that counts is the one between sites  $i$  and  $j$ .

A second instance where these strings are important is when we are faced with periodic boundary conditions: moving a fermion across the boundary also moves the string attached to it around, and this requires book-keeping in the code. This is particularly important for operators at the boundaries: terms such as  $c_1^\dagger c_N + c_N^\dagger c_1$ . The Jordan-Wigner string, going by Eq. (3.7), is  $(-1)^N$ , where  $N$  is the total number of fermions. Hence, this boundary term becomes:

$$c_1^\dagger c_N + c_N^\dagger c_1 = -(-1)^N (b_1^\dagger b_N + b_N^\dagger b_1). \quad (3.8)$$

Since  $(-1)^N$  can take only two values,  $+1$  and  $-1$ , there exist two cases of the above expression. When we are in the odd fermion sector, we get a Hamiltonian similar to what we started with, despite the inclusion of Jordan-Wigner strings. However, in the even fermion sector, an additional negative sign has to be taken into account when fermions hop across the boundary.

Once we have used the above techniques to reduce the complexity of our Hamiltonian matrix and make it physically consistent, the next step is to perform the diagonalization. Since the Hamiltonian matrix will still be quite sizable, it is very likely that the Hamiltonian would still not lend itself very well to a straightforward routine diagonalization protocol. We instead take advantage of the fact that one of the most important pieces of information usually relevant to quantum many-body systems is the ground state energies – the entire spectrum is very often not necessary. Hence, we use specialized diagonalization routines that help us extract to very high accuracy, the first few eigenvalues and eigenstates based on our requirement. One of the most popular of such routines is the Lanczos method.

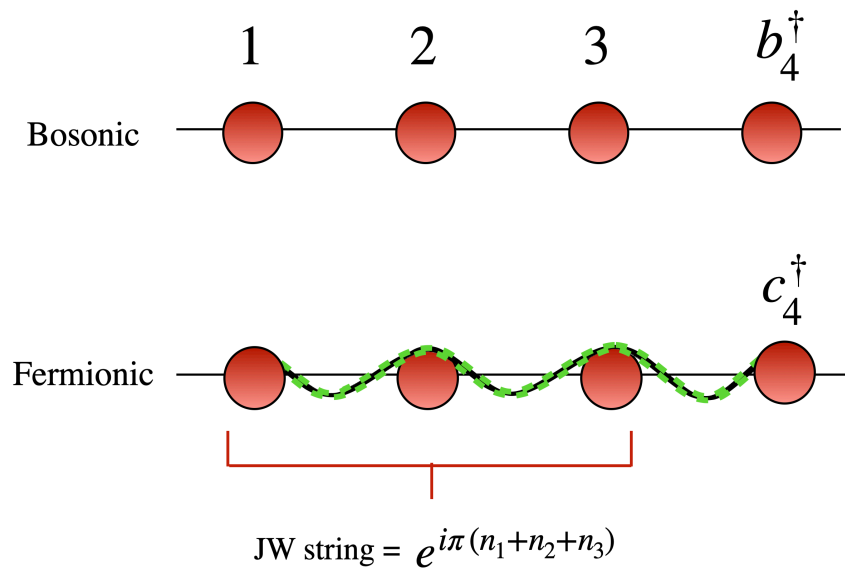


**Figure 3.3 – Jordan-Wigner transformation at play.** A non-local Jordan-Wigner “string” is attached so that the operators now obey fermionic commutation rules and thus describe a system of fermions accurately. Illustration inspired by [92].

### 3.4 Krylov space techniques and the Lanczos method

Once the Hamiltonian is constructed by using various symmetries, the next logical step is to diagonalize the Hamiltonian matrix. A standard matrix diagonalization is computationally not feasible given that the matrices in ED are usually very large. Such large sparse matrix eigenvalue problems appear in most applications of scientific computing. However, iterative methods such as Krylov subspace methods can take advantage of sparseness, making them a useful tool for solving large systems of linear and non-linear equations and, by extension, large eigenvalue problems.

The main idea of a general iterative solver is the following: consider a system of linear equations of the form

$$\mathbf{A}\mathbf{x} = \mathbf{b}, \quad (3.9)$$

where  $\mathbf{A}$  is a non-singular matrix and  $\mathbf{b}$  is a vector. A general procedure to find its solution involves starting from an initial guess  $\mathbf{x}_0$ , and finding a sequence  $\mathbf{x}_n$  which approximates  $\mathbf{x}^*$ , where  $\mathbf{x}^*$  is the solution to Eq. (3.9). Krylov subspace methods for solving such a system of linear equations have the special feature that  $\mathbf{A}$  need only be an operator: that is, for any  $N$ -vector  $\mathbf{y}$ , one must be able to compute the matrix-vector product  $\mathbf{A}\mathbf{y}$ ; so  $\mathbf{A}$  may be given as a function, operator, procedure, or subroutine.

There are several types of Krylov subspace solvers; however, any Krylov space solver starts from some initial approximation  $\mathbf{x}_0$  and the corresponding residual  $\mathbf{r}_0 := \mathbf{b} - \mathbf{A}\mathbf{x}_0$ , and iterates  $\mathbf{x}_n$  such that [93]

$$\mathbf{x}_n - \mathbf{x}_0 \in \mathcal{K}_n(\mathbf{A}, \mathbf{r}_0). \quad (3.10)$$

Here,  $\mathcal{K}_n(\mathbf{A}, \mathbf{r}_0)$  is called the  $n^{\text{th}}$  Krylov subspace, where  $n \leq N$ , generated by the non-singular matrix  $\mathbf{A} \in \mathbb{C}^{N \times N}$ :

$$\mathcal{K}_n := \mathcal{K}_n(\mathbf{A}, \mathbf{r}_0) := \text{span}(\mathbf{r}_0, \mathbf{A}\mathbf{r}_0, \dots, \mathbf{A}^{n-1}\mathbf{r}_0). \quad (3.11)$$

$\mathbf{r}_0$  is the  $0^{\text{th}}$  residual, and a general residual  $\mathbf{r}_n$  satisfies [94]

$$\mathbf{r}_n \in \mathbf{r}_0 + \mathbf{A}\mathcal{K}_n(\mathbf{A}, \mathbf{r}_0) \subseteq \mathcal{K}_{n+1}(\mathbf{A}, \mathbf{r}_0), \quad (3.12)$$

Here, we see that  $\mathcal{K}_1 \subseteq \mathcal{K}_2 \subseteq \mathcal{K}_3 \dots$ , and that the dimension of a Krylov subspace cannot exceed  $N$ . However, it can be smaller than  $N$  when it is bounded by a  $\nu$  such that  $\nu$  satisfies

$$\nu = \min\{n | \mathbf{A}^{-1}\mathbf{r}_0 \in \mathcal{K}_n(\mathbf{A}, \mathbf{r}_0)\}, \quad (3.13)$$

so that

$$\dim \mathcal{K}_n(\mathbf{A}, \mathbf{r}_0) = \min(n, \nu). \quad (3.14)$$

This upper bound now tells us how convergence might be defined. Let  $\mathbf{x}^*$  be the solution of Eq. (3.9), and  $\mathbf{x}_0$ ,  $\mathbf{r}_0$  and  $\nu$  hold their usual meanings. Then,

$$\mathbf{x}^* \in \mathbf{x}_0 + \mathcal{K}_\nu(\mathbf{A}, \mathbf{r}_0). \quad (3.15)$$

Thus, the main idea behind Krylov subspace solvers is to generate sequences of approximate solutions  $\mathbf{x}_n$  in a Krylov subspace  $\mathcal{K}_n$ , so that the corresponding residuals  $\mathbf{r}_n \in \mathcal{K}_{n+1}(\mathbf{A}, \mathbf{r}_0)$  converge to the zero vector. Here, convergence may also mean that after  $n$  steps  $\mathbf{r}_n = \mathbf{0}$ , so that  $\mathbf{x}_n = \mathbf{x}^*$  and the process stops (finite termination). This is true when the residuals are linearly independent. This is the ideal scenario.

In practice, however, this is not so: the vectors  $\mathbf{A}^j\mathbf{r}, j = 1, 2, \dots$  usually become almost linearly dependent in a few steps; hence, methods relying on Krylov subspaces must involve some orthogonalization scheme. One such method is the Arnoldi orthogonalization algorithm. In the context of exact diagonalization of Hamiltonian matrices, which are Hermitian in nature, a variant of the Arnoldi method, called the Lanczos method, is popularly used.

### 3.4.1 The Lanczos routine

In the Lanczos method, an orthogonal basis is constructed using linear combinations of the Krylov space states  $\mathcal{K}_n(\mathbf{H}, \mathbf{v}), n \leq N$ , (where  $\mathbf{v}$  is an arbitrary vector such that  $\mathbf{v} \in \mathbb{C}^N$ ), such that the Hamiltonian matrix  $\mathbf{H} \in \mathbb{C}^{N \times N}$  written in this basis is tridiagonal.

Thus, we obtain an orthonormal basis  $\mathbf{V}_n$ , where  $\mathbf{V}_n$  is composed of ‘‘Lanczos vectors’’-  $\mathbf{V} = [\mathbf{v}_1, \mathbf{v}_2, \dots, \mathbf{v}_n]$ , such that [94]

$$\mathbf{V}_n^T \mathbf{H} \mathbf{V}_n = \mathbf{T}_n. \quad (3.16)$$

---

**Algorithm 4** the Lanczos routine

---

**Require:**  $\mathbf{H}$  is a Hermetian matrix of size  $N \times N$

**Require:**  $v_1 \in \mathbb{C}^N$  be an arbitrary vector with Euclidean norm 1 .

**Ensure:**  $v_1$  is orthogonal to the ground state of  $\mathbf{H}$

$$a_1 := \langle v_1 | \mathbf{H} | v_1 \rangle / \langle v_1 | v_1 \rangle$$

$$|w_1\rangle := \mathbf{H}v_1 - a_1|v_1\rangle$$

**for**  $j = 2, 3, \dots, n$  **do**

$$b_j = \|w_{j-1}\|$$

**if**  $b_j \neq 0$  **then**

$$v_j = w_{j-1}/b_j$$

**else**

Pick arbitrary  $v_j \perp v_1, v_2, \dots, v_{j-1}$  such that  $\|v_j\| = 1$

$$a_j = \langle v_j | \mathbf{H} | v_j \rangle / \langle v_j | v_j \rangle$$

$$w_j = \mathbf{H}v_j - a_jv_j - b_jv_{j-1}$$


---

$\mathbf{T}_n$  is the tridiagonal matrix

$$\mathbf{T}_n = \begin{pmatrix} a_1 & b_2 & & & & 0 \\ b_2 & a_2 & b_3 & & & \\ & b_3 & a_3 & \ddots & & \\ & & \ddots & \ddots & b_{n-1} & \\ & & & b_{n-1} & a_{n-1} & b_n \\ 0 & & & & b_n & a_n \end{pmatrix}. \quad (3.17)$$

The Lanczos routine is shown in Alg. 4. The eigenvalues of  $\mathbf{T}_n$ , (called Ritz values of  $\mathbf{H}$ ) play an important role in the study of the convergence of Krylov subspace methods: as  $n$  increases, the Ritz values increasingly approximate the eigenvalues of  $\mathbf{H}$  [95].

### Convergence of the Lanczos algorithm

Once the Lanczos routine is executed and allowed to run for a few hundred iterations, the lowest eigenvalues of the trigonal matrix  $\mathbf{T}_n$ , provide an excellent approximation to the eigenvalues of the original Hamiltonian. The approximate ground state eigenvector is given by [96]

$$|\tilde{\Psi}_0\rangle = \sum_{n=0}^L \tilde{\psi}_{0,n} |v_n\rangle, \quad (3.18)$$

where  $|\tilde{\psi}_0\rangle$  is the ground state eigenvector of  $\mathbf{T}_n$ .

As mentioned earlier, an ideal convergence would be when the residual  $\mathbf{r}_n = \mathbf{0}$  at the  $n$ th iteration. If not, a cutoff  $\Lambda \leq n$  for the iterative procedure can be explicitly set. However, the larger  $\mathbf{H}$  is, the more unlikely it is that we ever obtain the exact eigenspace. Despite that, we encounter a situation in Lanczos where  $b_n$  almost vanishes – but this also means that numerical noise gets amplified. This makes  $|v_n\rangle$  have finite overlaps with all the other  $|v_m\rangle$ , even though

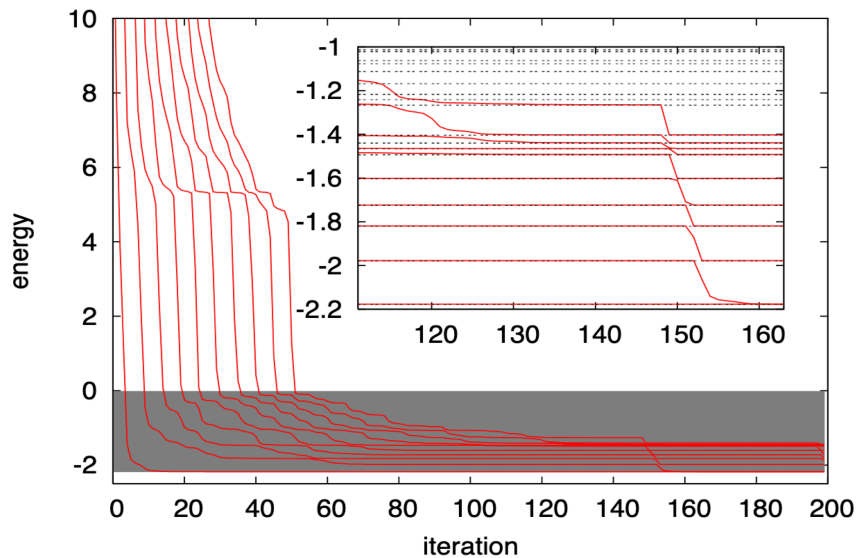


**Figure 3.4 – Convergence and over-convergence in a Lanczos iteration.** In this plot, where the ground state energies of an  $N = 8$  Hubbard chain at half-filling are calculated, we see that after about 85-90 iterations, the energy has converged well. (Inset) If we force the Lanczos routine to continue beyond that, the higher excited states also converge to their exact values (shown in dashed lines) but begin collapsing to the ground state after a point. These manifest themselves as ghost states. Image taken from [96].

they should have been mutually orthogonal in theory. This loss of orthogonality when we are in the vicinity of the exact eigenvalue, manifests itself in the form of multiple copies of eigenvectors, called ghost states, which are a numerical phenomenon and completely unrelated to the actual degeneracies of the actual eigenspace, as shown in Fig. 3.4. This issue of orthogonality loss is amplified when we have dense matrices. Hence, diagonalization subroutines like Lanczos work best with sparse matrices.

### 3.4.2 Conclusion

In this Chapter, we discussed the central computational machinery we would be using for the thesis. Lanczos and Arnoldi routines have now become part of a larger standard toolkit of Krylov subspace methods in scientific computing. However, to use them for strongly correlated systems, the real weight of the problem rests in expressing the Hamiltonian matrix in a way that not only provides the necessary physical information but can also make use of the above-mentioned diagonalization routines as efficiently as possible. We also saw some ways of doing that, especially leveraging symmetries of the Hamiltonian.

There have been many advances in constructing the Hamiltonian matrix, for example, using numerical linked-cluster expansions [97], or different kinds of configuration interaction techniques such as selected configuration interaction [98]. One of the main motivations behind these advances is to make better use of parallelization of the exact diagonalization routine, to achieve higher efficiency.

Another strength of exact diagonalization lies in its ability to provide valuable insight into various static and dynamic observables. such as specific heat, susceptibility, dynamic structure

factor, etc despite only dealing with very small system sizes. For example, exact diagonalization techniques were successfully used to study various lattice models such as Hubbard,  $t - J$  model [99, 100], SYK models [101, 102], etc. Apart from this, they are frequently used as a benchmarking tool. Hence, exact diagonalization remains an indispensable tool while studying strongly correlated systems.

## **Part II**

# Building Blocks for Cluster Mott Insulators



## Localization of electrons on clusters

We have seen previously that strong electronic interactions are an essential ingredient for localization of electrons. We also saw that the Mott insulating phase is one of the most widely-studied examples of how this localization of electrons leads to a rich playground for quantum magnetism. Adding more degrees of freedom, such as multiple orbitals, and electronic charge, makes the question of the character of ground states non-trivial to address. For example, the local moments in spin-orbit entangled Mott insulators, including the  $j_{\text{eff}} = 1/2$  family of compounds, are a combination of both spin and orbital degrees of freedom [103].

Such an interplay of multiple degrees of freedom in determining the ground states is where the concept of a *cluster* Mott insulator comes into picture. In this chapter, we introduce cluster Mott insulators, an extension to the notion of conventional Mott insulators. If a real material hosts well-defined clusters of atoms, then an interplay of intra-cluster hopping, inter-cluster hopping and interactions causes electrons to localize on these clusters rather than single atomic sites. Cluster Mott insulators are likewise governed by the cluster Hubbard model. We will discuss the form of the interactions and hoppings that govern this cluster localization.

In recent years, cluster Mott physics has been increasingly observed in a variety of materials, which are shown to host a wide variety of ground states. In fact, the cluster Mott story begins with experimental studies on several materials that hosted a plethora of clusters. In this chapter, we will take a look at different functional units in different materials that are typically seen to form clusters of varying sizes and geometries and how such clusters come to be – whether they are built into the crystal structure beforehand or whether they emerge spontaneously.

### 4.1 Cluster Mott materials

The main reason why the formation of clusters in lattices is interesting at all in the first place stems from the fact that a wide variety of materials have displayed these clusters in their lattice structure. Candidate cluster Mott insulator (CMI) materials contain clusters that are typically formed by a collection of transition metal (TM) ions surrounded by oxygen ligands. These clusters are distinctly characterized by short TM ion-TM ion distances and are usually embedded on a larger lattice.

In coordination compounds, one has to ascertain which degrees of freedom play a role in determining their properties. In the case of CMI materials, electronic charges are localized to

a cluster, making them charge insulators. An important ingredient is multiple orbitals; this is the main reason why clusters are formed with TM ions – TM ions have five  $d$ -orbitals to offer. Their orientation with one another, as well as the strength of spin-orbit coupling in a material determines which orbitals ultimately participate in cluster Mott physics in the material.

Given the vast zoo of transition metal compounds that might have clusters, it is essential to distinguish these materials based on how clusters come to be, in them. One way of classifying them is based on how clusters come to be in the material and how they respond to phase transitions.

### 4.1.1 Structural clusters

In cluster Mott materials with structural clusters, TM ion clusters pre-exist in the crystal structure itself, and the crystal does not undergo any structural phase transition. These clusters, might be a collection of two ions (dimer), three ions (trimer/triangle), and so on, and will be discussed in detail in Chapter 5. The simplest clusters are those with two ions: a dimer. Dimer clusters have been observed in the  $M_2O_9$  family of compounds, with  $M$  being a  $4d$  or  $5d$ -transition metal ion. These dimer clusters are typically face-sharing octahedra, which form the structural units of 6H perovskite class of compounds<sup>1</sup>  $A_3BM_2O_9$ .

The  $M_2O_9$  family is one of the most extensively studied classes of cluster Mott materials, and has contributed to a large part of the current understanding of cluster Mott physics. The filling in the  $d$ -shell of the  $M$  ion hints at whether one might expect a magnetic or a non-magnetic ground state; using that as the initial starting point, the interplay of various factors ultimately determines the nature of the ground state. For example, the completely occupied  $d$ -shell of the  $Ir^{5+}$  ion in the Iridate  $Ba_3ZnIr_2O_9$  hints at a possible  $J_{\text{eff}} = 0$  insulating ground state especially with strong spin-orbit coupling. However, substantial frustration due to the presence of strong interdimer exchange interactions induce quantum fluctuations, suppressing long-range magnetic order and leading to a spin-orbital liquid ground state. This was confirmed by heat capacity and  $\mu$ SR studies, see Fig. 4.1 [105].

On the other hand, an odd number of electrons leads to a variety of ground states, with both high or low effective spin degrees of freedom. Let us consider mixed valence ruthenate dimers  $Ba_3MRu_2O_9$  as an example. Ruthenates in which  $M = Y, In$  show significant orbital hybridization, resulting in one spin-1/2 moment distributed equally over the two Ruthenium sites [106]. However,  $Ba_3LaRu_2O_9$  has a ground state with an unusual molecular spin-3/2 degrees of freedom, which corresponds to neither the high spin nor low spin limits [107], as shown in Fig. 4.2. Some of these materials also displayed strong deviations from Curie-Weiss behavior, which was shown to be due to field-induced mixing of different multiplets, leading to

---

<sup>1</sup>A conventional oxide perovskite is a material with the formula  $AMO_3$ , where  $A$  is a larger cation and  $M$  is a smaller metallic ion [104]. A hexagonal perovskite has a hexagonal symmetry, in contrast to the cubic symmetry of conventional oxide perovskites. Hexagonal symmetry allows for the existence of face-sharing  $MO_6$  octahedra. This is an important factor that allows for cluster formation in hexagonal perovskites. Structural layers in a unit cell are described by a number, indicating the number of layers, followed by a letter that indicates the type of stacking. Hence, “6H” means the material has 6 layers with a hexagonal stacking. Similarly, “R” indicates rhombohedral stacking, and “C” indicates cubic stacking.

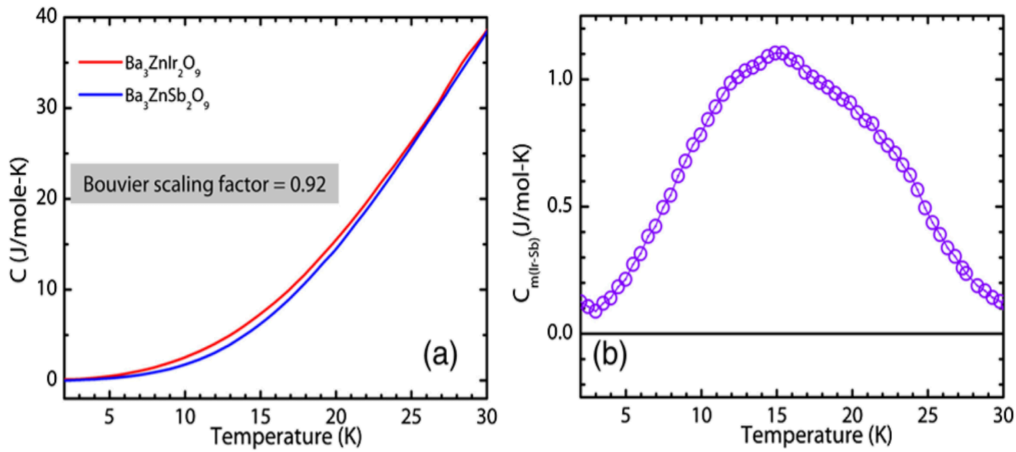


**Figure 4.1** – Specific heat capacity measurements for  $\text{Ba}_3\text{ZnIr}_2\text{O}_9$ . (a) Temperature dependence of specific heat. Note that there is no peak or anomaly, indicating the absence of any structural and/or long-range magnetic phase transition (b) Magnetic heat capacity after subtracting the lattice contribution. There is a broad peak at around 15K. Fitting it to  $C_m = \gamma T + \beta T^2$  indicates a strong T-linear contribution of  $\gamma = 25.9 \text{ mJ/molK}^2$ . Plots adapted with permission from [105], Copyright(2016) by the American Physical Society.

additional contributions such as Van Vleck terms and a nontrivial temperature dependence of the magnetic susceptibility [108, 109].

Similar to their dimer cousins, trimer clusters of the form  $\text{M}_3\text{O}_{12}$  form the structural units of the 12H perovskite class of compounds. In contrast to the dimer case, the M transition metal ion can be either  $3d$ ,  $4d$ , or  $5d$ . It should also be noted that while most materials have either  $t_{2g}$  or  $e_g$  orbitals constituting the ground state, for rare instances such as  $\text{Ba}_4\text{NbMn}_3\text{O}_{12}$ , all five  $d$ -orbitals have to be taken into consideration. Moreover,  $\text{Ba}_4\text{NbMn}_3\text{O}_{12}$  is also an interesting example of a geometrically frustrated Mott insulator where the formation of molecular orbitals is not observed [110, 111], as opposed to other materials in the  $\text{M}_3\text{O}_{12}$  trimer family, which are cluster Mott insulators.

An essential ingredient that is common among all the materials mentioned so far seems to be short metal-metal distances, which lead to the clustering of TM ions within their lattices in the first place. This is facilitated by face-sharing of metal-oxygen octahedra in a wider family of hexagonal oxide perovskites [112]. Apart from dimer and trimer clusters, a variety of materials with longer linear clusters, such as tetramers and heptamers, has been synthesized, as well as materials which contain more than one type of cluster [112, 113], as shown in Fig. 4.3. Different structural cluster units can be achieved with the same TM ions by changing the ratios of TM ions and ligand ions in the material, or in other words, tuning the oxidation states of the TM ions and ligands.

Apart from the hexagonal perovskite family, another interesting family of compounds is those with  $\text{Mo}_3\text{O}_8$  clusters. These compounds typically contain stacked anisotropic kagome layers, on which the  $[\text{Mo}_3\text{O}_{13}]^{15+}$  clusters form a triangular lattice, as shown in Fig. 4.4. There has been considerable debate over the microscopic nature of magnetism in such materials. For example, magnetic susceptibility and heat capacity measurements for  $\text{LiZn}_2\text{Mo}_3\text{O}_8$  [115] indicated that it

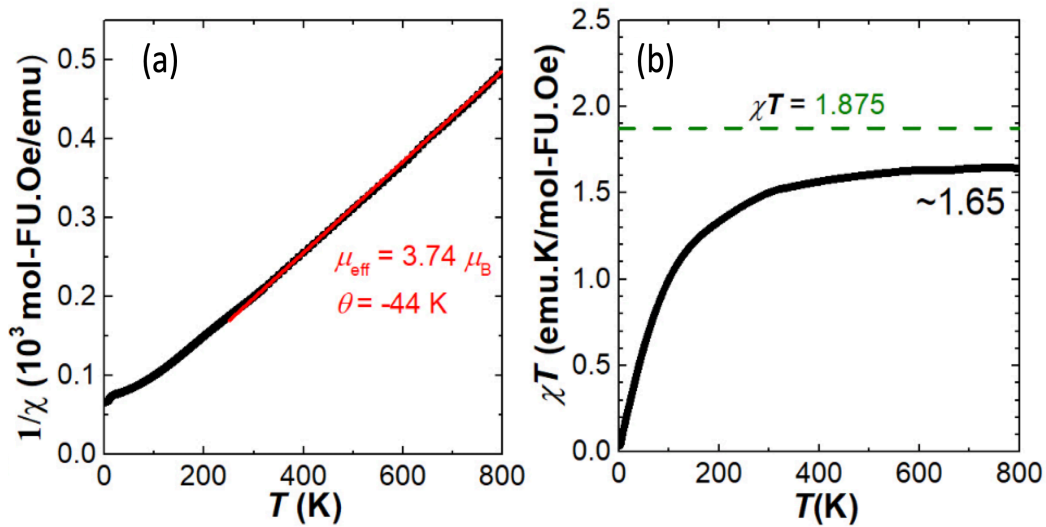


**Figure 4.2 – Susceptibility measurements for  $\text{Ba}_3\text{LaRu}_2\text{O}_9$ .** (a) Inverse susceptibility  $1/\chi$  plotted against temperature. The Curie-Weiss fit is shown in red. (b) Temperature dependence of the product of susceptibility and temperature,  $\chi T$ . The saturation value is close to that of  $S = 3/2$ , which is shown as a green dashed line. Plots adapted with permission from [107]. Copyright (2020) by the American Physical Society.

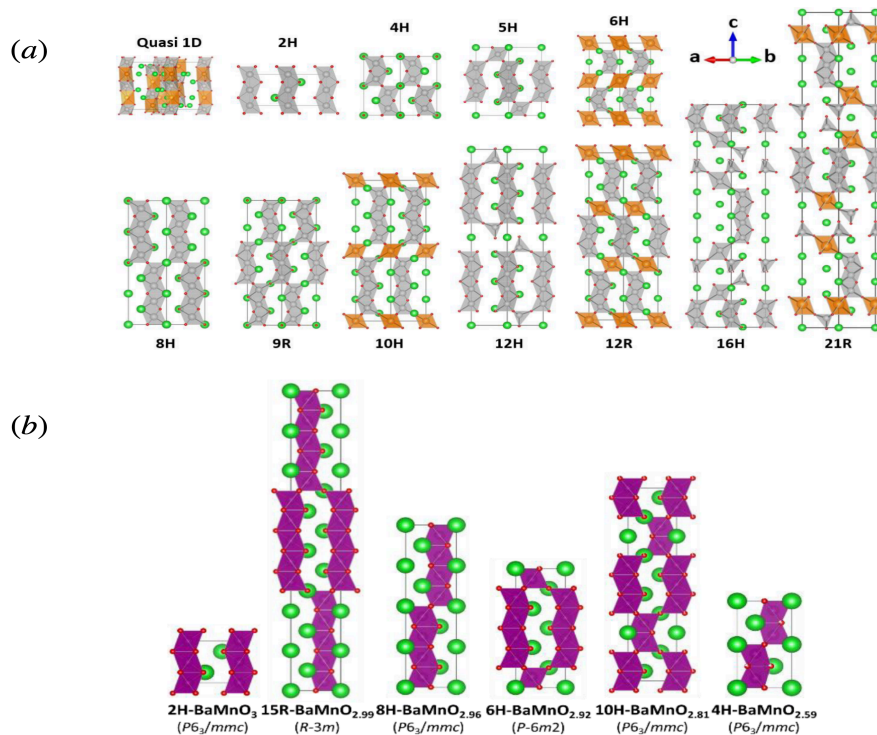


**Figure 4.3 – Zoo of hexagonal perovskites with structural clusters.** (a) Crystals can either have clusters with uniform geometry, or they can also host clusters with diverse geometries. For example, we see in the 16H and 21R materials that dimer/trimer clusters coexist along with tetrahedral clusters in the same material. (b) One can also achieve clusters of varying geometries or sizes in the same compound by tuning the oxidation numbers of the TM ion. Shown here are different types of  $\text{BaMnO}_{3-x}$  structures. Images adapted with permission from [112], Copyright (2021) American Chemical Society.

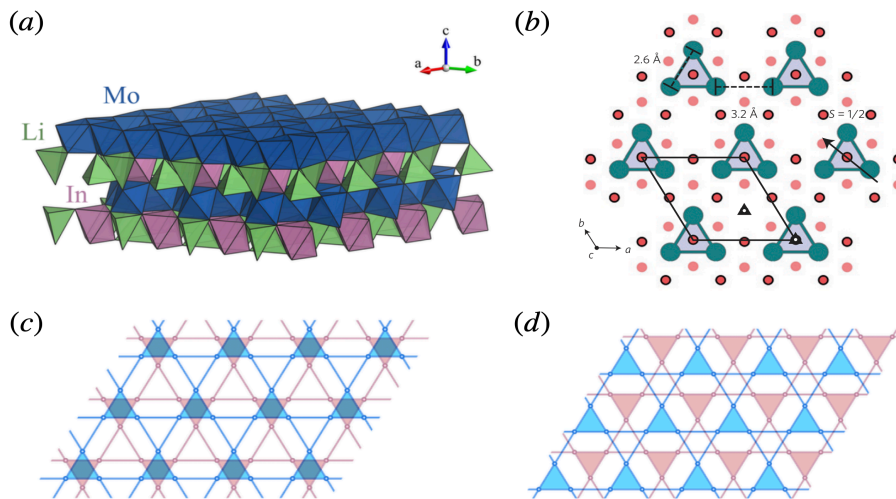


**Figure 4.4** – Illustrative crystal structures of materials in the  $\text{Mo}_3\text{O}_8$  family. (a) Crystal structure of  $\text{Li}_2\text{InMo}_3\text{O}_8$ . Figure taken from [114]. Copyright (2021) by Springer Nature. (b) Top-down view of an  $\text{Mo}_3\text{O}_8$  layer. One can see the triangular clusters formed by the molybdenum ions (in green). Oxygen ions are shown in red. Illustration taken with permission from [115]. Copyright (2012) by Springer Nature. (c-d) Two different ways in which the kagome layers can be stacked along the  $c$ -axis. Here, blue and pink correspond to different layers.  $\text{Li}_2\text{InMo}_3\text{O}_8$  and  $\text{Li}_2\text{ScMo}_3\text{O}_8$  correspond to the dd-stacking, and  $\text{LiZn}_2\text{Mo}_3\text{O}_8$  displays a cdcdd-stacking. Figure taken from [114]. Copyright (2021) by Springer Nature.

exhibits geometric magnetic frustration between  $S = 1/2$  magnetic clusters, with two-thirds of the spins condensing into singlets below approximately  $T = 96\text{K}$ . This absence of static singlets indicated that  $\text{LiZn}_2\text{Mo}_3\text{O}_8$  hosts a resonating valence-bond state. Attempts at a theoretical explanation have ranged from an emergent honeycomb lattice [116], to the material hosting a  $U(1)$  quantum spin liquid state [117]. However, this theory could not explain features of a fellow material in the same family,  $\text{Li}_2\text{InMo}_3\text{O}_8$ , where magnetic moments were well localized on triangular clusters [118, 119]. This motivated a closer look at possible extensions of the Hubbard model on the anisotropic kagome lattice [114, 120].

### 4.1.2 Emergent clusters

Clusters need not always pre-exist in a lattice. In some materials, clusters tend to emerge as a result of phase transitions. A large class of spinel compounds<sup>2</sup> have been observed to exhibit this tendency. An example is the group of  $\text{AB}_2\text{X}_4$  spinels, in which A is a tetrahedral cationic site, and B is an octahedral cationic site. Similar to how the mixed-valence of transition metal ions that participate in cluster formation gave rise to cluster Mott physics in materials with structural clusters, mixed-valence B-site cations also lead to unusual properties. The thiospinel compound  $\text{CuIr}_2\text{S}_4$  is an interesting case, which is known to undergo a metal-insulator transition at 230K accompanied by a loss of localized magnetic moments. Crystallographic studies [121] revealed that  $\text{CuIr}_2\text{S}_4$  undergoes a simultaneous charge ordering of both  $\text{Ir}^{3+}$  and  $\text{Ir}^{4+}$  iridium

<sup>2</sup>Spinel is a class of materials with formula  $\text{AB}_2\text{X}_4$ , where A and B are cations, and X is an anion, usually oxygen. If X is any other chalcogenide such as sulphur, selenium or tellurium, then the material is called a thiospinel.

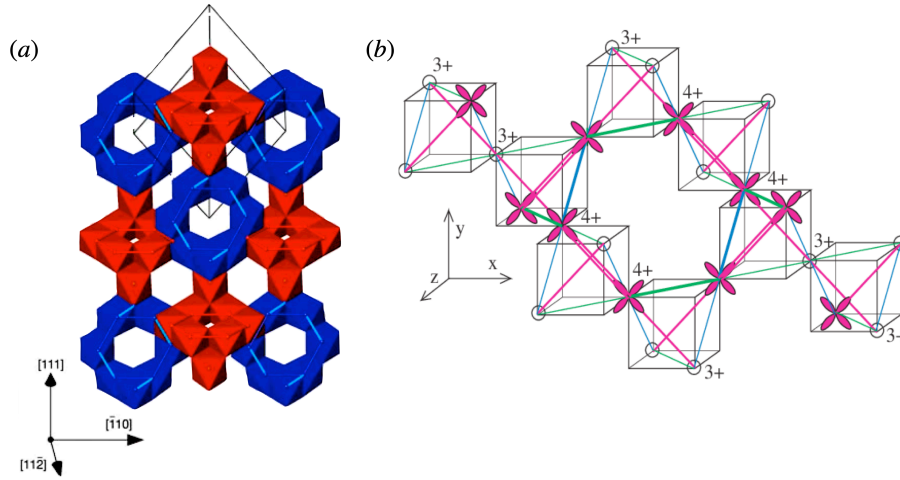


**Figure 4.5 – Structure of  $\text{CuIr}_2\text{S}_4$ .** (a) The low-temperature crystal structure of  $\text{CuIr}_2\text{S}_4$ . Red and blue octahedra correspond to the presence of  $\text{Ir}^{3+}$  and  $\text{Ir}^{4+}$ , respectively, at the centres, and sulphur ligands at the corners. In the case of  $\text{Ir}^{4+}$  octahedra, the dimerized iridium bonds are indicated with light-blue cylinders. Image reproduced from [121], with permission from Springer Nature. (b) Charge and orbital ordering in  $\text{CuIr}_2\text{S}_4$ . The octamer cluster is shown by green and blue thick lines, and short singlet bonds are shown by double lines. Image reprinted with permission from [122]. Copyright (2005) by the American Physical Society.

ions into isomorphic octamers of  $\text{Ir}_8^{3+}\text{S}_{24}$  and  $\text{Ir}_8^{4+}\text{S}_{24}$ . Further,  $\text{Ir}^{4+}$  chains undergo spin-dimerization, as shown in Fig. 4.5. There have been various claims regarding the nature of its ground state, ranging from a proposed spin-singlet state [122] to that of an exotic spin glass-like state below 100 K [123]. Another prominent example of a spinel showing emergent clusters is  $\text{Al}_2\text{V}_2\text{O}_4$ . A number of studies on the cluster-formation process below its 700K charge ordering transition have been carried out, which have proposed  $\text{V}_7^{17+}$  heptamer clusters [124, 125]. Between 700K-1100K, these heptamer clusters are conjectured to break into pairs of spin-singlet  $\text{V}_3^{9+}$  trimers and  $\text{V}_4^{8+}$  tetramers [126].

However, spinels are just one class of compounds where clusters are seen to emerge; other examples include certain silicate pyroxenes<sup>3</sup> such as  $\text{NaTiSi}_2\text{O}_6$ , which consists of characteristic one-dimensional chains of edge-sharing  $\text{TiO}_6$  octahedra. X-ray scattering studies showed a dimerization of Ti-Ti clusters along the chain below  $T_c = 230\text{K}$  [127].

A common feature of materials with emergent clusters is the phenomenon of dimensionality reduction [128]: we saw in  $\text{CuIr}_2\text{S}_4$  that a spinel crystal structure exhibited dimers below the metal-insulator transition temperature, which is a cluster of lower dimensionality. Similarly,  $\text{Al}_2\text{V}_2\text{O}_4$  lowered its dimensionality from hosting heptamer clusters to trimers and tetramers. One of the main reasons is the spatial orientation of orbitals in the crystal – electrons are able to hop from a certain orbital to certain orbitals more easily than others owing to physical proximity. This leads to strong anisotropy of many physical properties, leading to a reduction of dimensionality in materials with emergent clusters.

<sup>3</sup>Pyroxenes are materials with a general formula  $\text{XY}(\text{Si}, \text{Al})_2\text{O}_6$ , where X and Y can represent a range of cations. Common ones are calcium, sodium, aluminum, iron, manganese, etc.

## 4.2 Hamiltonian considerations

In the previous section, we saw that materials with a huge variety of clusters have been synthesized, with a commensurately fascinating variety of ground states. Irrespective of whether clusters are structural or emergent, their presence indicates a pattern of electron localization that is in need of theoretical treatment. As we have seen, materials in the same class of compounds can have vastly different properties. Though there have been many focused theoretical studies attempting to explain certain observations in specific materials, the world of clusters in materials is still in need of an overarching theoretical framework that might attempt to capture most, if not all, of their essential physics. Hence, we try to formulate a blueprint to study these clusters in this section.

As we saw in Chapter 2, the single-orbital Hubbard model is given by

$$H = +U \sum_i n_{i\uparrow} n_{i\downarrow} - t \sum_{\langle i,j \rangle, \sigma} (c_{i\sigma}^\dagger c_{j\sigma} + h.c.), \quad (4.1)$$

where  $c_{i\sigma}^\dagger$  ( $c_{i\sigma}$ ) creates (annihilates) an electron with spin  $\sigma \in \{\uparrow, \downarrow\}$  on site  $i$ , and hopping takes place between all pairs of neighboring sites  $\langle i, j \rangle$ . The Mott insulating phase is obtained at half-filling, i.e., one electron per site, when  $U \gg t$ , that is, in the strong interaction limit of the Hubbard Model. In this limit, the Hamiltonian can be split as

$$H = H_0 + V, \quad (4.2)$$

where  $H_0$  is the on-site Hubbard term, and the hopping term between sites is treated as a perturbation  $V$ . We first need to find the possible ground states of  $H_0$  to be able to perform perturbation theory. Since it is a sum of single-site terms, it suffices to study just a single site. Fig. 4.6 indicates the possible electron fillings  $n_f$  for a single site and the corresponding energies of  $H_0$ . While a singly-occupied site has zero energy, adding an extra electron generates a large energy penalty of  $U$ , making the singly-occupied state the lower energy state. Extending this to the full lattice, the ground states at half-filling consist of all states with precisely one electron per site. Thus, there is a localized effective  $S = 1/2$  degree of freedom at each site. Note that the localized electrons in the case of the Mott insulator carry a purely spin character. Once the ground states of  $H_0$  are determined, one can derive an effective Heisenberg model perturbatively in the hopping  $V$ , and this effective Hamiltonian correctly captures the magnetic physics of the Mott insulating phase.

Now, we would like to extend the above idea to a “cluster Hubbard” Hamiltonian. A cluster, for the purposes of writing down the Hamiltonian, is just a collection of sites in a lattice, arranged in a certain geometry. The language now changes from classifying terms in Eq. (4.1) in terms of “on-site” and “inter-site” terms, to the language of clusters, where we now have terms classified as being “on-cluster” and “inter-cluster” :

$$H = \sum_C H_C + \sum_{\langle C, C' \rangle} H_{CC'}, \quad (4.3)$$

Configuration	$n_f$	$S$	GSD	Energy
	1	1/2	2	0
	2	0	1	U

**Figure 4.6 – Spectrum of the Hubbard model for a single site.** A singly occupied, that is, half-filled site, is of lower energy (i.e, zero) than a doubly occupied one, which comes with a huge cost of  $U$  in the strongly interacting limit. Note that the trivial case of  $n_f = 0$  also has zero energy.

where  $H_C$  is the collection of “on-cluster” terms, which we will henceforth refer to as the intra-cluster Hamiltonian, containing electronic interactions and hopping between sites within cluster  $C$ . Similarly,  $H_{CC'}$  is the collection of “inter-cluster” terms. The inter-cluster Hamiltonian contains interactions and hopping between sites belonging to neighboring clusters  $C$  and  $C'$ .

Similar to how localization of electrons on every site was essential to realizing a Mott insulating ground state, in the cluster case, it is essential that electrons are localized on every cluster. This can be achieved if all intra-cluster terms are large enough compared to inter-cluster terms so as to prevent electrons from leaving the cluster. Hence, we split the Hamiltonian in Eq. (4.3) into an unperturbed Hamiltonian  $H_0 = \sum_C H_C$ , which is nothing but the intra-cluster Hamiltonian summed over all clusters, and then treat the inter-cluster terms as perturbations,  $V = \sum_{CC'} H_{CC'}$ . The way forward again proceeds with the same two steps as in the more familiar single site single orbital case discussed above. First, we need to find the possible ground states of  $H_0$ . Since this is a simple sum over clusters, it suffices to study just a single cluster. The ground states determine the potential localized degrees of freedom available. Once the ground states of  $H_0$  are determined, an effective Hamiltonian can be derived perturbatively in  $V$ , which links clusters together.

In this work, we study the ground states of the intra-cluster cluster Hamiltonian  $H_0$ , determining the different potential localized degrees of freedom. As we will see in subsequent sections, the combination of cluster filling, cluster geometry, and the interplay between various parameters in the Hamiltonian gives rise to an incredibly rich variety of ground states of distinct character.

#### 4.2.1 Intra-cluster hopping and molecular orbitals

The intra-cluster Hamiltonian  $H_C$  can be split into two parts: the non-interacting part and the interaction part. In this study, the non-interacting part contains only hopping terms. The potential impact of other non-interacting terms relevant to many materials, such as crystal-field splitting or spin-orbit coupling, will be discussed in Chapter 7. For the single orbital case, we consider the simplest intra-cluster hopping Hamiltonian as

$$H_{\text{non-int}} = -t \sum_{\langle i,j \rangle, \sigma} (c_{i\sigma}^\dagger c_{j\sigma} + h.c.). \quad (4.4)$$

For many real materials, however, there is an additional degree of freedom involved along with the existing spin and charge degrees of freedom – that is, multiple orbitals. The non-interacting

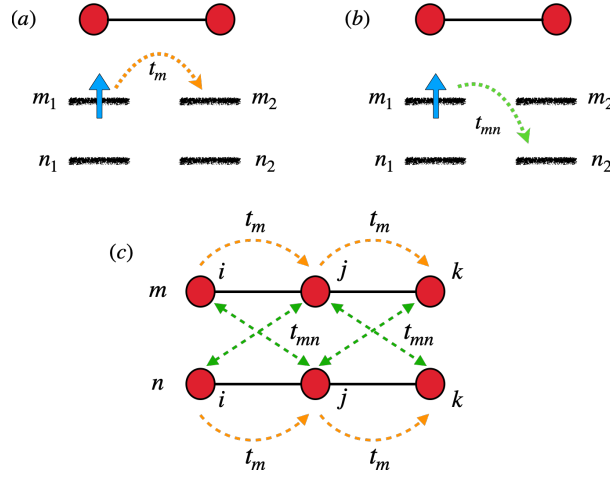


**Figure 4.7 – Hopping mechanisms in  $H_{\text{non-int}}$ .** (a)  $t_m$  hops an electron from one orbital on site  $i$  to the same kind of orbital on site  $j$ . (b)  $t_{mn}$  hops an electron from one orbital on site  $i$  to a different kind of orbital on site  $j$ . (c) Another way of understanding the two kinds of hopping is that  $t_m$  (shown in orange) hops spins in the same “orbital plane”, whereas  $t_{mn}$  hops spins across different orbital planes (shown in green).

Hamiltonian for such materials is typically constructed using knowledge of the orbitals involved (including surrounding ligands), the point group symmetry of the cluster, and the relevant Slater-Koster parameters. Here, as we are aiming for a simpler, more overarching perspective, we consider a simplified form of intra-cluster hopping as

$$H_{\text{non-int}} = -t_m \sum_{\langle i,j \rangle} \sum_{m,\sigma} (c_{im\sigma}^\dagger c_{jm\sigma} + h.c.) - t_{mn} \sum_{\langle i,j \rangle} \sum_{m \neq n, \sigma} (c_{im\sigma}^\dagger c_{jn\sigma} + h.c.),$$

where  $t_m$  corresponds to diagonal, intra-orbital hopping,  $t_{mn}$  to off-diagonal, inter-orbital hopping and the operator  $c_{im\sigma}^\dagger$  ( $c_{im\sigma}$ ) creates (annihilates) an electron with spin  $\sigma$  in atomic orbital  $m$  on site  $i$ . This form of hopping is illustrated in Fig. 4.7.

We refer to the energy levels of the non-interacting Hamiltonian as molecular orbitals. The symmetries of the molecular orbital levels have two contributions. The first contribution comes from the spatial symmetry of the cluster. As we will be agnostic regarding the spatial characteristics of the orbitals, open chains, including the dimer, trimer, and tetramer clusters, are assumed to have only inversion symmetry and hence designated as belonging to an “ $i$ ” point group, with  $[+]$  and  $[-]$  indicating even or odd under inversion respectively. The point groups of the other clusters are indicated in Fig. 5.2.

The second contribution comes from the internal symmetry among the orbitals. In the absence of the off-diagonal hopping  $t_{mn}$ , the hopping Hamiltonian has an enlarged  $SU(2)$  and  $SO(3)$  orbital symmetry for the case of two and three orbitals respectively. However, finite  $t_{mn}$  breaks these symmetries, with the two-orbital case reduced to a  $C_2$  orbital point group (corresponding to swapping of the two orbitals), and the three-orbital case reduced to a  $C_{3v}$  orbital point group (corresponding to cyclic permutations of the orbitals and swapping of any two). We will use a shorthand  $[G_C, G_O]$  notation<sup>4</sup>, with  $G_C$  referring to the spatial point

<sup>4</sup>Not to be confused with a commutator.

group of the cluster and  $G_O$  referring to the orbital symmetry group. Finally, the Hamiltonian is time-reversal symmetric, meaning that all single-particle levels possess a two-fold Kramers degeneracy.

Note that since we are, for all practical purposes, studying a toy model to capture the core physics of cluster Mott insulating ground states, we obscure all details of the environment of these clusters, including crystal fields and spin-orbit coupling. This also means some of the symmetry groups of these clusters in a real material might be different from what is considered here.

### 4.2.2 Intra-cluster interactions

In the case of multiple orbitals, it can be shown that the most general interaction term is a screened Coulomb interaction  $V_c$ , with matrix elements [129, 130]

$$A_{ijkl}^{mnpq} = \int d\mathbf{r}d\mathbf{r}' \phi_{im\sigma_1}^*(\mathbf{r}) \phi_{jn\sigma_2}^*(\mathbf{r}') V_c(\mathbf{r}, \mathbf{r}') \phi_{kp\sigma_3}(\mathbf{r}') \phi_{lq\sigma_4}(\mathbf{r}), \quad (4.5)$$

where  $\phi(\mathbf{r})$  is some localized Wannier basis,  $i, j, k, l$  are site indices,  $m, n, p, q$  are orbital indices, and  $\sigma_1, \sigma_2, \sigma_3, \sigma_4$  are spin indices. We will consider only local on-site terms and hence drop site indices in the remainder of this section.

The on-site interaction between electrons in a single orbital, that is, the Hubbard interaction  $U$ , is obtained when we set  $m = n = p = q$ , and  $\sigma_1 \neq \sigma_2$ :

$$U = \int d\mathbf{r}d\mathbf{r}' \phi_{m\sigma_1}^*(\mathbf{r}) \phi_{m\sigma_2}^*(\mathbf{r}') V_c(\mathbf{r}, \mathbf{r}') \phi_{m\sigma_1}(\mathbf{r}) \phi_{m\sigma_2}(\mathbf{r}'). \quad (4.6)$$

A similar interaction would be an on-site term between electrons in different orbitals. If we set  $m = q, n = p$  we get

$$U' = \int d\mathbf{r}d\mathbf{r}' \phi_{m\sigma_1}^*(\mathbf{r}) \phi_{n\sigma_2}^*(\mathbf{r}') V_c(\mathbf{r}, \mathbf{r}') \phi_{m\sigma_1}(\mathbf{r}) \phi_{n\sigma_2}(\mathbf{r}'), \quad (4.7)$$

where a change of variable  $p \rightarrow n$  is used. Similarly, we get two more interaction terms that are non-diagonal in orbital space, which are the  $J$ -interactions

$$\begin{aligned} J_1 &= \int d\mathbf{r}d\mathbf{r}' \phi_{m\sigma_1}^*(\mathbf{r}) \phi_{n\sigma_2}^*(\mathbf{r}') V_c(\mathbf{r}, \mathbf{r}') \phi_{m\sigma_1}(\mathbf{r}') \phi_{n\sigma_2}(\mathbf{r}), \\ J_2 &= \int d\mathbf{r}d\mathbf{r}' \phi_{m\sigma_1}^*(\mathbf{r}) \phi_{m\sigma_2}^*(\mathbf{r}') V_c(\mathbf{r}, \mathbf{r}') \phi_{n\sigma_1}(\mathbf{r}') \phi_{n\sigma_2}(\mathbf{r}) \quad (\sigma_1 \neq \sigma_2). \end{aligned} \quad (4.8)$$

If we choose  $\phi_m(\mathbf{r})$  to be real, we get  $J_1 = J_2 = J$  [131]. In the second quantized form, the interactions (4.6), (4.7) and (4.8) combine to give the Hubbard-Kanamori Hamiltonian [129, 132]

$$\begin{aligned}
H_{HK} = & U \sum_m n_{m\uparrow} n_{m\downarrow} + U' \sum_{m \neq n} n_{m\uparrow} n_{n\downarrow} \\
& + (U' - J) \sum_{m \neq n, \sigma} n_{m\sigma} n_{n\sigma} - J \sum_{m \neq n} c_{m\uparrow}^\dagger c_{n\downarrow}^\dagger c_{m\downarrow} c_{n\uparrow} \\
& + J \sum_{m \neq n} c_{m\uparrow}^\dagger c_{m\downarrow}^\dagger c_{n\downarrow} c_{n\uparrow},
\end{aligned} \tag{4.9}$$

where the operator  $c_{m\sigma}^\dagger (c_{m\sigma})$  creates (annihilates) an electron with spin  $\sigma$  in atomic orbital  $m$ .

In the above equation, the first three terms are density-density interactions:  $U$  governs the repulsion between opposite spins in the same orbital,  $U'$  between opposite spins in different orbitals and  $U' - J$  being between parallel spins on different orbitals. The  $J$ -terms are Hund's terms, governing inter-orbital exchange and pair-hopping terms. The mechanisms for all terms in Eq. (4.9) are illustrated in Fig. 4.8.

It is important to note that the parameters in Eq. (4.9) are not independent of one another, and relations among them are dictated by symmetry considerations. It was shown in various works using different approaches that in order for the Hamiltonian in Eq. (4.9) to be invariant under rotations in spin, charge, and orbitals, one needs to impose [133, 134]

$$U' = U - 2J, \tag{4.10}$$

along with the existing  $J_1 = J_2$  criterion. Though  $U'$  and  $J$  take different values in terms of Racah Parameters [135] for different number of orbitals,  $U$  is independent of the choice of orbitals. As a result, Eq. (4.10) holds for any number of orbitals, irrespective of the angular momentum. For example, in the three orbital case, this relation holds if we consider a partially quenched orbital angular momentum from  $l = 2$  for the entire  $d$ -shell, down to  $l = 1$ . However, in the most general case, Eq. (4.10) does not hold; there would exist terms in addition to  $U, U'$  and  $J$  which might not vanish by symmetry. In that case, the Hubbard-Kanamori Hamiltonian would only be approximate.

For the intra-cluster interaction Hamiltonian, we consider the standard multi-orbital Hubbard-Kanamori Hamiltonian on each site, with the resulting total Hamiltonian given by

$$\begin{aligned}
H_{\text{int}} = & \sum_i \left( U \sum_m n_{im\uparrow} n_{im\downarrow} + U' \sum_{m \neq n} n_{im\uparrow} n_{in\downarrow} + (U' - J) \sum_{m \neq n, \sigma} n_{im\sigma} n_{in\sigma} \right. \\
& \left. - J \sum_{m \neq n} c_{im\uparrow}^\dagger c_{in\downarrow}^\dagger c_{im\downarrow} c_{in\uparrow} + J \sum_{m \neq n} c_{im\uparrow}^\dagger c_{im\downarrow}^\dagger c_{in\downarrow} c_{in\uparrow} \right).
\end{aligned} \tag{4.11}$$

We will henceforth use Eq. (4.11) in the cluster context, with the additional criterion given by Eq. (4.10). In the case of a single orbital, only the first term survives.

### 4.2.3 Cluster Hund's rules

It is possible to rewrite the Hubbard-Kanamori Hamiltonian in a more compact form [136]. We define orbital operators for the two and three orbital cases as

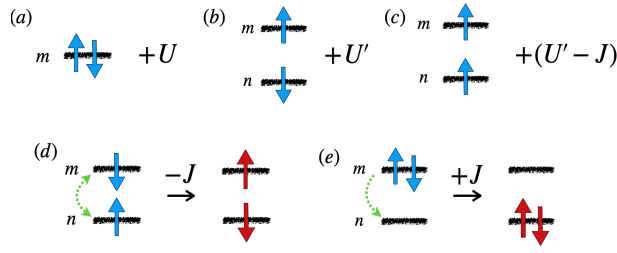


**Figure 4.8** – Nature of interactions governed by various terms of the **Hubbard-Kanamori Hamiltonian**. (a) The on-site  $U$  term, (b) density term for opposite spins in orbitals  $m$  and  $n$ , (c) density term for parallel spins in orbitals  $m$  and  $n$ , (d) two opposite spins on orbitals  $m$  and  $n$  are flipped at the same time, (e) a pair of spins, initially on orbital  $m$ , hop at the same time to orbital  $n$ .

$$\text{Two-orbitals: } T_i^\alpha = \frac{1}{2} \sum_{\sigma} \sum_{mm'} c_{im\sigma}^\dagger \tau_{mm'}^\alpha c_{im'\sigma}, \quad (4.12)$$

$$\text{Three-orbitals: } L_i^m = \sum_{\sigma} \sum_{m'm''} \epsilon_{mm'm''} c_{im'\sigma}^\dagger c_{im''\sigma},$$

where  $\tau^\alpha$  are the Pauli matrices. The spin operator similarly defined as

$$S_i^\alpha = \frac{1}{2} \sum_m \sum_{\sigma\sigma'} c_{im\sigma}^\dagger \tau_{\sigma\sigma'}^\alpha c_{im\sigma'}. \quad (4.13)$$

Using these expressions, we can write the full interaction Hamiltonian as

$$H_{\text{int}} = \frac{(U - 3J)}{2} \sum_i N_i^2 - 2J \sum_i (\vec{S}_i^2 + Q_i^2) + \alpha n_f, \quad (4.14)$$

where  $Q_i$  is an orbital operator that depends on the number of orbitals,  $Q_i = T_i^y$  and  $Q_i = \vec{L}_i/2$  in the two and three-orbital cases, respectively.  $\alpha n_f$  is akin to a chemical potential:  $n_f$  is the number of electrons on the cluster, and

$$\begin{aligned} \text{Two-orbitals: } \alpha &= (7J - U)/2, \\ \text{Three-orbitals: } \alpha &= (8J - U)/2. \end{aligned} \quad (4.15)$$

Let us try to understand how Eq. (4.14) determines which states should constitute the ground states in different parameter regimes. We consider an example of a dimer cluster with three orbitals per site and eight electrons on the cluster. Let us focus on the first term (see Fig. 4.9(a) for an illustrative example). When  $U \gg J$ , then the  $\sum_i N_i^2$  term, which is the sum of the number of electrons on each site of the cluster, has to be minimized so as to lower the energy. This is possible when the electrons are distributed as uniformly as possible, across the cluster sites. In the opposite regime, when  $J \gg U$ , the opposite holds true: a distribution of electrons where they are arranged as unevenly as possible across the cluster sites is energetically favored. The first term thus determines how many electrons every site of the cluster should hold. The term  $U - 3J$  is sometimes referred to as an effective interaction. Typically, only the  $U > 3J$

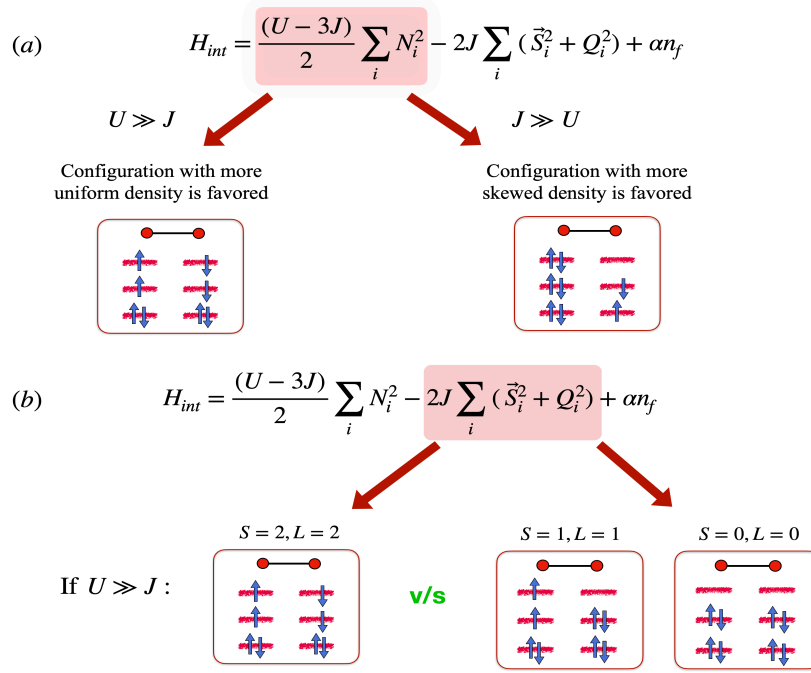


**Figure 4.9 – Example of cluster Hund’s rules at play.** Here, we consider an example of a dimer cluster with 3 orbitals per site, and 8 electrons on the cluster. (a) How the first term chooses the ground state. (b) How the second term chooses the ground state. To show this, we have assumed we are in the  $U \gg J$  regime. The second term is the conventional Hund’s rule.

regime is physically relevant to cluster materials. However, there are cases, such as rare-earth nickelates [132, 137], where certain mechanisms have been proposed that realize the  $U < 3J$  regime. In Chapter 6, we will explore the full  $U, J$  parameter space along with hoppings in order to gain a more complete picture of the underlying physics at play.

Now, let us assume the first term is fixed, and focus on the second term, akin to the case of a single-site Mott insulator. This term governs the configuration of electrons on the orbital level on each site and hence determines the quantum numbers of the spin and orbital operators. Due to the negative sign before the second term, states with maximal  $\vec{S}_i^2$  and maximal  $Q_i^2$  are favored. This is what we observe in Fig. 4.9(b). This is nothing but a reflection of Hund’s first two selection rules. This fact is also evident, for example, in Fig. 6.14, where the quantum numbers and energies for a single site with three orbitals are given. For, say  $n_f = 2$ , the state with the lowest energy is the one with maximal spin  $\vec{S}_i^2$  and maximal angular momentum  $\vec{L}_i^2$ .

In a CMI, the individual  $N_i$  are not fixed. Only the total electron number  $n_f = \sum_i N_i$  on the cluster is fixed. In this case, the  $N_i^2$  term in Eq. 4.14 typically dominates the energy (the eigenvalues of  $N_i^2$  are typically much larger than that of  $\vec{S}_i^2$  and  $Q_i^2$ ). As a result, one gets an additional “cluster Hund’s rule” which must first be satisfied. In the physically relevant regime of  $U > 3J$ , one must first minimize  $\sum_i N_i^2$ , and then, as usual, maximize  $\sum_i \vec{S}_i^2$ , and finally  $\sum_i Q_i^2$ . On the other hand, when  $U < 3J$ , competition between the different terms may arise, potentially resulting in a more complex selection process. Minimal  $\sum_i N_i^2$  favors a uniform spread of electrons across the cluster. Conversely, maximal  $\sum_i N_i^2$  favors a more

skewed distribution of electrons. We will discuss these points in more detail in the examples that follow, in Chapter 6.

A natural question arises – is there any regime where the normal Hund’s rules fail and a cluster Hund’s rule has to be compulsorily considered? It turns out that the conventional Hund’s rules, by default, hold in the region where  $U \gg J$ . This is also the regime where  $\sum_i N_i^2$  is minimal, and hence, both the first and second terms in Eq. (4.14) contribute in determining the ground state. As a result, the conventional Hund’s rules, which are the second term, are also involved. In the  $J \gg U$  region,  $\sum_i N_i^2$  is maximal, and hence in this regime, conventional Hund’s rules are not sufficient because  $\sum_i N_i^2$  is the major factor determining the ground state.

### 4.3 Conclusion

In this chapter, the concept of cluster Mott insulators was introduced and we discussed how these clusters are realized in materials. Irrespective of whether clusters are structural or emergent, their presence indicates a pattern of electron localization that is in need of theoretical treatment. Materials in the same class of compounds are seen to have vastly different properties. Hence, the world of clusters in materials is in need of an overarching theoretical framework that might capture most, if not all, of their essential physics. In an attempt to do the same, we constructed a cluster Hamiltonian and studied its nature. We discovered in our work that one of the core concepts governing interactions is the “cluster Hund’s rule”, which selects the ground states of the intra-cluster Hamiltonian in different parameter regimes.

There have been studies on classes of candidate cluster Mott materials, such as transition metal compounds with  $\text{Mo}_3\text{O}_8$  clusters, where a single-orbital Hubbard model on the cluster was assumed, and it was shown that performing second-order perturbation theory resulted in a Heisenberg-like Hamiltonian, with the effective coupling having a complex dependence on different interaction terms and crystal fields [114]. The generalization of these results and their extension to multiorbital models, though beyond the scope of this project, remains an exciting potential direction within the area of cluster Mott insulators.

# Single orbital Hubbard model

In the previous chapter, we introduced the concept of clusters and the Hubbard-Kanamori Hamiltonian. The single orbital Hubbard model is a special case of the more generalized Hubbard-Kanamori Hamiltonian of Eq. (4.11), where the inter-orbital terms  $U'$  and  $J$  vanish by virtue of there being just one orbital per site. Nevertheless, this provides insight into using the language of the molecular orbital basis. In addition, the single orbital Hubbard model on various clusters has been demonstrated as being a starting point for introducing inter-cluster terms. This, in turn, opens up a zoo of multiple insulating phases arising from an interplay of inter-cluster and intra-cluster hoppings, and lattice geometries. Some examples include insulating phases on decorated lattices whose low-energy effective theories include the spin-1/2 Heisenberg model on the kagome lattice and the spin-1/2 and spin-1 Heisenberg models on the honeycomb lattice [138, 139].

## 5.1 Molecular orbital levels

In the case of a single orbital, there is no question of inter- or intra-orbital hopping. Hence, we have just one type of hopping, as in Eq. (4.4). The molecular orbitals for different clusters are shown in Fig. 5.2. Since each site has just a single orbital, an  $N$ -site cluster has  $N$  two-fold degenerate levels. For clusters with a well-defined  $C_N$ -fold rotational symmetry, such as the dimer, triangular, and square clusters, molecular orbital basis operators for an  $N$ -site cluster can be easily defined as

$$b_{l\sigma}^\dagger = \frac{1}{\sqrt{N}} \sum_i c_{i\sigma}^\dagger e^{i(2\pi l/N)x_i}, \quad (5.1)$$

where  $l \in [1, N]$  denotes the quantum number corresponding to rotations of the cluster along the  $N$ -fold axis of symmetry, and hence, in this case, denotes the different molecular orbitals, and  $x_i \in [1, N]$  is a site-index [138]. In this basis, the hopping Hamiltonian can be trivially diagonalized and becomes

$$H_{\text{non-int}} = -2t \sum_{l\sigma} \cos(2\pi l/N) b_{l\sigma}^\dagger b_{l\sigma}. \quad (5.2)$$

One has to be mindful of the fact that the assumption of space groups of clusters in Fig. 5.2 is a gross simplification solely done for the purpose of capturing the core physics using such a toy model. In real materials, however, the environment of the cluster sites considered plays an

essential role in determining the geometry of the cluster. We briefly saw this in Chapter 2, but we will discuss it in more detail in Chapter 7.

### 5.1.1 Interaction Hamiltonian

As with the hopping,  $U'$  and  $J$  terms in the Hubbard-Kanamori Hamiltonian vanish, owing to the presence of a single orbital, thus leaving us with only the Hubbard interaction. For clusters with a well-defined  $C_N$ -fold rotational symmetry, the molecular orbital operators can be expressed as in Eq. (5.1). The interaction terms in the Hamiltonian can hence be written in this operator basis. The density-density term associated with  $U$  in the molecular orbital basis is given as

$$n_{i\uparrow}n_{i\downarrow} = \frac{1}{N} \sum_{lpq} b_{l\uparrow}^\dagger b_{p\downarrow} b_{q\downarrow}^\dagger b_{(l+q-p)\downarrow}, \quad (5.3)$$

where  $l, p, q$  label different molecular orbitals. Now, we can define a molecular orbital spin operator as

$$S_{\text{mo},l}^\alpha = \frac{1}{2} \sum_{\sigma\sigma'} b_{l\sigma}^\dagger \tau_{\sigma\sigma'}^\alpha b_{l\sigma'} \quad (5.4)$$

Along with  $N_{\text{tot}} = \sum_{l\sigma} n_{l\sigma}$ , this finally gives us an expression for the single-orbital interaction Hamiltonian in the molecular orbital basis as [138]

$$\begin{aligned} H_{\text{int}} = & -\frac{U}{N} \vec{S}_{\text{mo}}^2 + \frac{U}{4N} N_{\text{tot}}^2 + \frac{U}{2N} N_{\text{tot}} - \frac{U}{N} \sum_l n_{l\uparrow} n_{l\downarrow} \\ & + \frac{U}{N} \sum_{l \neq p} b_{l\downarrow}^\dagger b_{l\uparrow}^\dagger b_{p\uparrow} b_{(2l-p)\downarrow} \\ & + \frac{U}{N} \sum_{l \neq p \neq q} b_{q\downarrow}^\dagger b_{l\uparrow}^\dagger b_{p\uparrow} b_{(l+q-p)\downarrow} \end{aligned} \quad (5.5)$$

Even though this is an expression for the single orbital case, parallels can be drawn between Eq. (5.5) and the cluster Hund's rules that emerged from rewriting the Hubbard-Kanamori Hamiltonian in Eq. (4.14). Firstly, we see that the  $N_{\text{tot}}^2$  term is positive and the  $\vec{S}_{\text{mo}}^2$  term is negative, giving rise to similar selection rules as Eq. (4.14). In addition, of the two four-operator terms, the first is a ‘‘pair-clumping’’ term if  $2l \neq p$ . This mechanism is shown in Fig. 5.1(a), where the  $(2l - p)^{\text{th}}$  orbital is indicated by  $q$ . If  $2l = p$ , then this term becomes a pair-hopping term, as shown in Fig. 5.1(b). Similarly, the second of these terms, if  $l + q \neq p$ , makes two electrons of opposite spin and in different orbitals hop simultaneously to two different empty orbitals, respectively. This is shown in Fig. 5.1(c). If  $l + q = p$ , this becomes a ‘‘pair-spreading’’ term, which is the mechanism opposite of pair-clumping. This is shown in Fig. 5.1(d).

For the single-orbital case, operating in the molecular orbital basis can hence give us an intuition for ground state selection, similar to cluster Hund's rules. However, in the multi-orbital case, we not only have different types of hopping but many interaction terms, as is encapsulated in the Hubbard-Kanamori Hamiltonian. Hence, expressing all these terms in the molecular orbital basis for a multi-orbital case is not particularly favored.

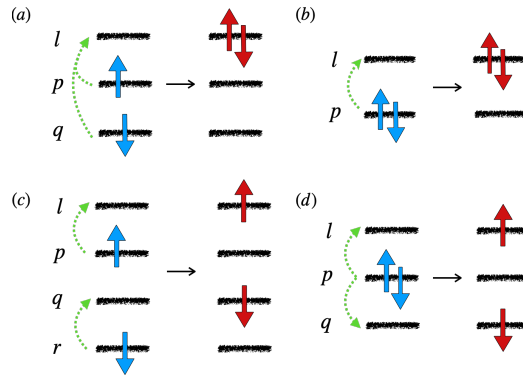


**Figure 5.1** – Various hopping mechanisms in  $H_{\text{int}}$  for a single orbital per site. (a) pair-clumping, (b) pair-clumping becomes pair-hopping when  $p = 2mn - n$ . (c) Two spins hop simultaneously from two orbitals to two other orbitals. (d) This becomes pair-spreading when  $q = m + p - n$ .

### 5.1.2 Results

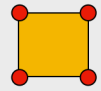
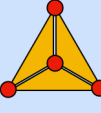
The results for the single-orbital case are shown in Fig. 5.2, where the ground state degeneracy (GSD) is listed for each combination of the choice of cluster and electron filling  $n_f$ . For each combination, the GSD is the same for all finite values of  $U$  (the non-interacting GSDs are shown in square brackets when they differ from the interacting case).

#### Linear clusters

One of the first observations is that for linear chains such as dimer and trimer, every orbital level is two-fold degenerate due to Kramer’s degeneracy. The ground state for the case of all even fillings is unique; this makes sense since the respective orbital is completely filled. The trimer chain differs in structure (and consequently, its molecular orbitals) in the sense that the trimer chain has crystallographically two kinds of sites: the sites on the edge and the site in the middle, in contrast to the dimer where the two sites are equivalent to one another. In addition, it is also plausible that clusters are formed in materials, such that the clusters are constituted of elements with different individual oxidation states [112]. We will see examples of such clusters in Chapter 9.

#### Rotationally symmetric clusters

The  $C_{3v}$  symmetry of the triangle cluster is reflected in its non-interacting bandstructure, which has an  $A_1$  level as the ground state and a two-fold  $E$  level as its excited state. Filling up the  $A_1$  level is very similar to what we saw in the case of dimer and trimer chains, where a fully filled level gives rise to a unique ground state when  $n_f = 2$ . However, this is not the case when  $n_f = 4$ . This corresponds to placing two spins on the  $E$  levels. In the non-interacting case, it has a six-fold degeneracy, which is constituted of three singlet states (with  $S_{\text{tot}} = 0$ ) and a triplet state (with  $S_{\text{tot}} = 1$ ). When interaction is added, it chooses the triplet state as the ground state, in accordance to Hund’s rules. The ground state degeneracy when  $n_f = 3$  is the same as when  $n_f = 5$ , because while the former amounts to placing one spin on the  $E$  levels

Cluster	Shape	Symmetry	Molecular Orbitals	Effective Degrees of Freedom (GSD)						
				$n_f$	Odd			Even		
Dimer		$i$	$\begin{matrix} [-] & 2t \\ [A_1] & -2t \end{matrix}$	$n_f$	Odd			Even		
				GSD	2			1		
Trimer		$i$	$\begin{matrix} [+] & \sqrt{2}t \\ [-] & 0 \\ [A_1] & -\sqrt{2}t \end{matrix}$	$n_f$	Odd			Even		
				GSD	2			1		
Triangle		$C_{3v}$	$\begin{matrix} [E] & t \\ [A_1] & -2t \end{matrix}$	$n_f$	1	2	3	4	5	
				GSD	2	1	4	3 [6]	4	
Square		$C_{4v}$	$\begin{matrix} [B_1] & 2t \\ [E] & 0 \\ [A_1] & -2t \end{matrix}$	$n_f$	1,7	2,6	3,5	4		
				GSD	2	1	4	1 [6]		
Tetrahedron		$T_d$	$\begin{matrix} [T_1] & 2t \\ [A_1] & -6t \end{matrix}$	$n_f$	1	2	3,7	4	5	6
				GSD	2	1	6	2 [15]	4 [20]	11 [15]

**Figure 5.2** – Effective degrees of freedom for a single orbital per site Hubbard model. This figure shows the non-interacting molecular orbital levels and the GSDs for the full Hamiltonian for all electron fillings for two, three and four site clusters. The numbers in square brackets in the GSD row indicate the GSD in the absence of interaction  $U$ . When square brackets are not indicated, it means the GSD is identical for the non-interacting and interacting limits.

(with completely filled  $A$  levels), the latter can be observed by placing a hole in the  $E$  levels.

In the case of a square cluster, as with the triangle, the molecular orbitals reflect the  $C_{4v}$  symmetry of the cluster. The ground state degeneracies of  $n_f = x$  electrons, say, are the same as that of the  $n_f = 8 - x$  sector (since the cluster can accommodate a maximum of eight electrons). The  $n_f = 4$  sector has a six-fold degeneracy in the non-interacting limit, but when interactions are added, a unique  $S_{tot} = 0$  ground state is chosen. This has interesting implications, as we will see in the next subsection.

The tetrahedral cluster is the only cluster among those considered, which has a triply degenerate energy level. Because of this, we see that  $n_f = 2$  is the only even filling in which the ground state is unique, irrespective of the presence or absence of interactions. The ground state degeneracies are also, in general, higher, especially at higher fillings, due to presence of the triply degenerate level. In the  $n_f = 5$  sector, we observe a mechanism similar to what we saw in case of the  $n_f = 4$  sector in the triangle cluster: in the absence of interactions, there is a high degeneracy, but when a small interaction is added, the degeneracy reduces to being four-fold. This corresponds to all three levels of the  $[T_1]$  state being singly occupied by an electron, resulting in an  $S_{tot} = 3/2$  ground state.

### Mott atomic limits

The half-filled sector in the square lattice (that is, four electrons) is of particular significance because it hosts a non-trivial ground state when a small interaction is introduced. If we assume the square cluster to have a  $C_4$  symmetry, then the ground state transforms in the  $B$  representation of the point group; if we assume a  $C_{4v}$  symmetry, then the ground state at half-filling transforms in the  $B_1$  irreducible representation.

Non-trivial ground states at even-fillings have recently garnered interest in the context of topological quantum chemistry. In a recent work, Soldini et al. [140] reasoned that the machinery of topological quantum chemistry (TQC) is limited to non-interacting systems and, as a result, can only successfully employ single-particle formulations. Hence, they developed an interacting TQC formalism to incorporate interacting states. To that end, they made use of a class of reference states that are used to extend the principle of “atomic limits” in TQC to “ $n$ -Mott atomic limits”. These Mott atomic limits are constructed using  $n$ -entangled electrons that sit at certain Wyckoff positions on the cluster. The simplest example of such an  $n$ -Mott atomic limit is a single-orbital per site Hubbard model on the square cluster, at half-filling.

The three requirements for such a ground state are: the cluster should have an even filling, the ground state should be unique in the presence of interactions, and it should transform in a non-trivial irreducible representation. As mentioned previously, we exhaustively tracked ground state degeneracies at all fillings, both in the presence and in the absence of interactions for a range of clusters (see Fig. 5.2). It turns out that the case of a square cluster at half-filling is the only instance of a non-trivial ground state. Other examples of Mott atomic limits, which have not been dealt with in this chapter, are the single-orbital per site Hubbard model on a diamond cluster at half-filling, a checkerboard cluster at half-filling, as well as the star of David cluster with 12 electrons on the cluster [140]. In all these cases, the ground state transforms non-trivially, in the  $B$  representation.

Though non-trivial ground states were not observed in any single-orbital clusters in our work so far (except for the square case), these clusters are nevertheless capable of hosting non-trivial ground states. Hence, we highlight singly degenerate, non-trivial ground states for various point groups that are dealt with in this chapter, in Appendix A.

## 5.2 Conclusion

In this chapter, we focused on the single-orbital Hubbard model as a starting point to understand the physics of cluster Mott insulators. The molecular orbital basis provided us with a way of rewriting the Hubbard interaction, such that it looked similar to the cluster Hund’s rules. Even though a large number of cluster materials are transition metal coordination compounds, which have multiple orbitals per site, the single-orbital picture still holds significance and has been, for example, used to derive effective Hamiltonians governing  $\text{Mo}_3\text{O}_8$  cluster materials [114]. We also saw that they can serve as playgrounds to explore ways in which interacting states can be incorporated into the topological quantum chemistry framework. In the next chapter, we use the insight and understanding we gained from this chapter, to study phase

diagrams of cluster Mott insulators.

# Multiorbital Hubbard model

We extend the ideas introduced in the previous chapter, to the case of multiple orbitals per site. An added factor to consider is that the bandstructures of the multi-orbital case are governed by a combination of the cluster's spatial symmetry as well as the symmetry of the orbitals. In this chapter, we only consider the cases of two and three orbitals per site. This would include the case of most real materials since the transition metal ions involved in cluster formation very often have either two ( $e_g$ ) or three ( $t_{2g}$ ) orbitals that constitute the ground state.

*This chapter is largely based on publication [P1], to which the author of this dissertation has contributed the major part, namely all numerical simulations, all figures, and all the text (excluding the introduction and discussion sections of the publication). The technical description of the results in this chapter is, therefore, partly adopted from the publication.*

## 6.1 Two orbitals per site

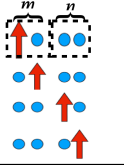
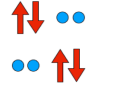
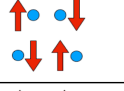
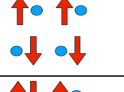
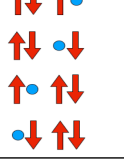
The two-orbital per site Hubbard model is the governing model for all transition metal coordination compounds that have  $e_g$  ground states, for example, manganites, niobium halides, and some quasi-1D materials [141–147]. There have also been various theoretical studies done to understand the two-orbital Hubbard model, such as dynamical mean field theory [148], t-DMRG methods to understand spin-orbit separation [149], or using novel methods such as traveling cluster approximation to incorporate thermal effects [150], among others [151–153]. In this section, we will study the governing interacting and non-interacting terms in the two-orbital case and their interplay in clusters of different geometries and at different electron fillings.

### 6.1.1 Molecular orbital levels

In the two-orbital case, the non-interacting Hamiltonian  $H_{\text{non-int}}$  of Eq. (4.5) is given by:

$$H_{\text{non-int}} = - \sum_{\langle i,j \rangle, \sigma} \mathbf{c}_{i\sigma}^\dagger \begin{pmatrix} t_m & t_{mn} \\ t_{mn} & t_m \end{pmatrix} \mathbf{c}_{j\sigma} \quad (6.1)$$

where  $\mathbf{c}_{i\sigma}^\dagger = (c_{im\sigma}^\dagger, c_{in\sigma}^\dagger)$ . As we saw in section 4.2, the off-diagonal hopping  $t_{mn}$  breaks  $SU(2)$  orbital symmetry, with the orbital character of the bands labeled only by the irreducible representations of  $C_2$ ,  $A$  or  $B$  (symmetric or anti-symmetric under exchange of the two orbitals).

Configuration	$n_f$	$S$	$T_y^2$ [ $T_x^2 + T_z^2$ ]	GSD	Energy	Type of State
	1	1/2	1/4 [1/2]	4	0	
	2	0	0 [2]	1	$U + J$	Symmetric
			1 [1]	1	$U - J$	Anti-symmetric
	2	0	1 [1]	1	$U - J$	Anti-symmetric (singlet)
		1	0 [0]	1	$U - 3J$	Symmetric (triplet)
	2	1	0 [0]	2	$U - 3J$	Symmetric (triplet)
	3	1/2	1/4 [1/2]	4	$3U - 5J$	

**Figure 6.1 – A single site with two orbitals:** Summary of the two-orbital per site interaction Hamiltonian given in Eq. (6.2) for a single site. The number indicated in square brackets are the quantum number for  $T_x^2 + T_z^2$ .

As these are both singly degenerate, there is no possibility of a non-trivial localized degree of freedom protected solely by orbital symmetry in this two-orbital case.

### 6.1.2 Interaction Hamiltonian

We saw in Section 4.2.2 that the interaction Hamiltonian for the two-orbital case is given by

$$H_{\text{int}} = \frac{(U - 3J)}{2} \sum_i N_i^2 - 2J \sum_i [\bar{S}_i^2 + (T_i^y)^2] + \frac{(7J - U)}{2} n_f. \quad (6.2)$$

A prominent feature to note here is that only  $(T_i^y)^2$  appears in the Hamiltonian, thus orbital isospin  $\bar{T}_i^2$  is not conserved. The spectrum of the Hamiltonian for a single site is given in Fig. 6.1. Here, we see that the ground state degeneracy and quantum numbers are the same for the  $n_f = 1$  and  $n_f = 3$  case, and that the  $S = 1$  triplet forms the ground state when  $n_f = 2$ .

### 6.1.3 Some select phase diagrams

We carried out an exhaustive study across all fillings on the clusters discussed in this section. Here, we present results from some select fillings, in which there was a particularly diverse variety of phases.

#### Dimer, $n_f = 3$

Fig. 6.2(a) shows the non-interacting molecular orbital levels of a dimer cluster with two orbitals per site. The presence of both inter- and intra-orbital hopping gives rise to two regimes:

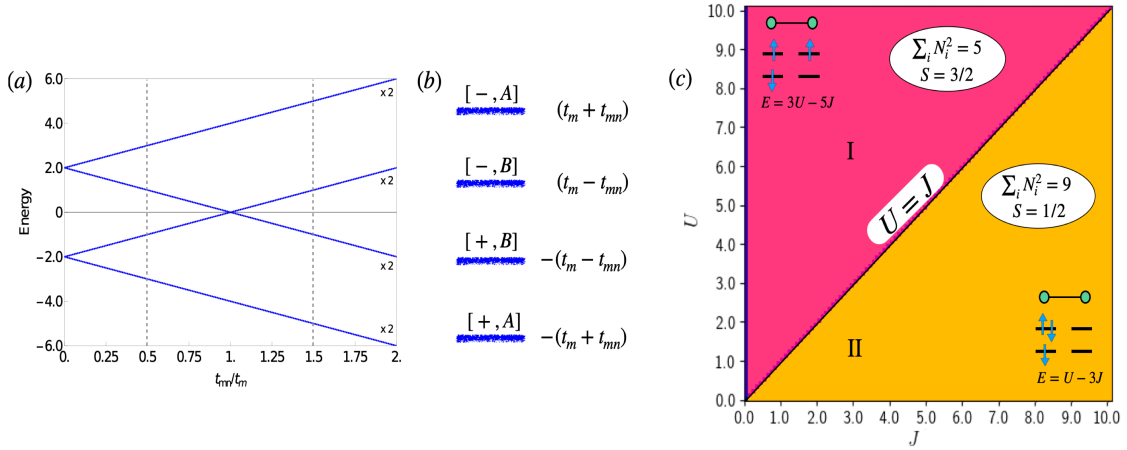


**Figure 6.2** – Different limits for a dimer cluster with two orbitals per site. (a) Non-interacting molecular orbital levels. (b) Single-particle levels with energies and labels indicated: In the label  $[G_C, G_O]$ ,  $G_C$  and  $G_O$  indicate the irreducible representations of the cluster’s spatial and orbital symmetries respectively. (c)  $U - J$  phase diagram of  $H_{\text{int}}$  only for  $n_f = 3$ , i.e. in the absence of hopping.

$t_{mn}/t_m < 1$  and  $t_{mn}/t_m > 1$ . The dimer cluster has a spatial  $i$  point group symmetry, and its orbitals have a  $C_2$  symmetry, which, as mentioned earlier, we denote as  $[i, C_2]$ . We consider here the  $n_f = 3$  sector. In the non-interacting limit, filling the single-particle levels with 3 electrons gives rise to a two-fold GSD with an effective  $S = 1/2$  degree of freedom.

Let us now consider the pure interaction limit. In accordance with cluster selection rules, there are two possible ways electrons can be distributed among two sites: two electrons on one site and one on the other site, that is, a  $(2 + 1)$  configuration, or, three electrons on one site and none on the other site, that is, a  $(3 + 0)$  configuration. From Eq. (6.2), we see that a  $(2 + 1)$  configuration is favored in the large- $U$  limit since this minimizes the  $\sum_i N_i^2$  term with a value  $2^2 + 1^2 = 5$ , and the  $(3 + 0)$  configuration is favored in the large- $J$  limit with a value  $3^2 + 0^2 = 9$ . This is shown in the pure-interaction phase diagram in Fig. 6.2(c). Consider the configuration of  $(2 + 1)$  electrons when  $U > J$ . From Fig. 6.1, we see that the energetically favored combination is the presence of an  $S = 1$  triplet on one site and an  $S = 1/2$  on the second site. The result of this is an effective  $S = 3/2$  degree of freedom in region I in Fig. 6.2(c). The  $(3 + 0)$  configuration constitutes the ground state when  $U < J$ , with an  $S = 1/2$  on one site and an  $S = 0$  on the other, resulting in a two-fold ground state degeneracy in region II in Fig. 6.2(c).

Fig. 6.3 shows phase diagrams for  $n_f = 3$  in the presence of both interactions and hopping, with phase boundaries indicated. The choices of hoppings  $t_{mn} = 0.5$  and  $t_{mn} = 1.5$  are based on the two hopping regimes marked in Fig. 6.2(a). We see remnants of the pure interaction limit even when hopping is switched on: the two configurations of electrons being favored in different parameter regimes is seen in Fig. 6.3(c,e), but the areas encompassed by  $\sum_i N_i^2$  values derived from the pure interaction limit have changed due to an interplay of interactions and hopping. This plot is used as a reference to label different regions in the GSD plots in Fig. 6.3: for example, the purple region in Fig. 6.3(a) gets the label ‘I’ because  $\sum_i N_i^2 \approx 5$  corresponding to that region in Fig. 6.3(b); this is the same value as that of region I in the pure interaction

plot of Fig. 6.2(c). Similarly, the orange lower-triangular area in Fig. 6.3(a) gets the label ‘II’ because  $\sum_i N_i^2 \approx 9$  in Fig. 6.3(b) for that area, and this is the same value as that of region II in Fig. 6.2(c). This labeling convention shall be used in GSD plots for all clusters discussed in the rest of the examples. In addition, the  $U = J$  phase boundary remains as is, and the effective spin-degrees of freedom in regions I and II in Fig. 6.2(a) also follow from the respective regions in Fig. 6.2(c).

When we have non-zero interactions and non-zero hopping, we obtain phase diagrams as shown in Fig. 6.3. In general, we see that the region I shrinks with the introduction of hopping, and the two-fold GSD occupies a larger area. In addition, the  $U = J$  line shifts away from the origin when hopping increases (Fig. 6.3(d)). The non-interacting limit (that is, the origin in the plot:  $U = 0, J = 0$ ) favors a more delocalized distribution of electrons, hence smoothly connecting to the region where a  $(2 + 1)$  configuration forms the ground state. It also favors a lower total spin since the lowest energy levels get filled sequentially, as opposed to a higher effective spin degree of freedom favored in the pure interaction limit (due to Hund’s rules). As a result, there is a competition between favoring a higher effective spin and a lower effective spin when  $U > J$ . As hopping is further increased, there is a tendency of the system to approach the behavior of the non-interacting limit, hence shrinking the region with higher effective spin.

### Trimer, $n_f = 5$

Fig. 6.4(a) shows the non-interacting molecular orbital levels of a trimer cluster with two orbitals per site. We see two regimes:  $t_{mn}/t_m < 1$  and  $t_{mn}/t_m > 1$ . The trimer cluster has a  $[i, C_2]$  symmetry. A distinct feature of the trimer molecular orbital levels are the zero-energy  $[-, A]$  and  $[-, B]$  levels. These levels are protected by inversion symmetry of the trimer cluster. Though dimer and trimer cases are quite similar, the main difference is the presence of these zero energy levels in the trimer, which can be attributed to there being two kinds of sites on the trimer: a site with one neighbor (edge site), and a site with two neighbors (middle site). We have chosen to show the  $n_f = 5$  sector as an example for the trimer case. In the non-interacting limit, filling the single-particle levels with five electrons gives rise to a four-fold ground state degeneracy, with an effective  $S = 1/2$  degree of freedom.

In the pure interaction limit, there are many possible ways in which five electrons can be distributed across three sites of the trimer. Among these configurations, we see from Eq. (6.2) that a  $(2 + 2 + 1)$  configuration is favored in the large- $U$  limit (since this minimizes the  $\sum_i N_i^2$  term) and the  $(4 + 1 + 0)$  configuration is favored in the large- $J$  limit. This is shown in the pure-interaction plot of Fig. 6.4(c).

Fig. 6.5 shows the phase diagrams for  $n_f = 5$  in the presence of both interactions and hopping ( $t_{mn} = 0.5$  and  $t_{mn} = 1.5$ ), with phase boundaries indicated. In Fig. 6.5(a), there are a variety of phases. Firstly, we note remnants from the pure interaction limit: in addition to the  $U = J$  phase boundary, the electronic configurations being favored in different parameter regimes can be seen in Fig. 6.5(b), although the areas corresponding to regions I and II from the pure interaction limit have now shrunk due to an interplay of interactions and hopping. Secondly, as hopping is introduced, we see a new region with  $S = 3/2$  opening up around

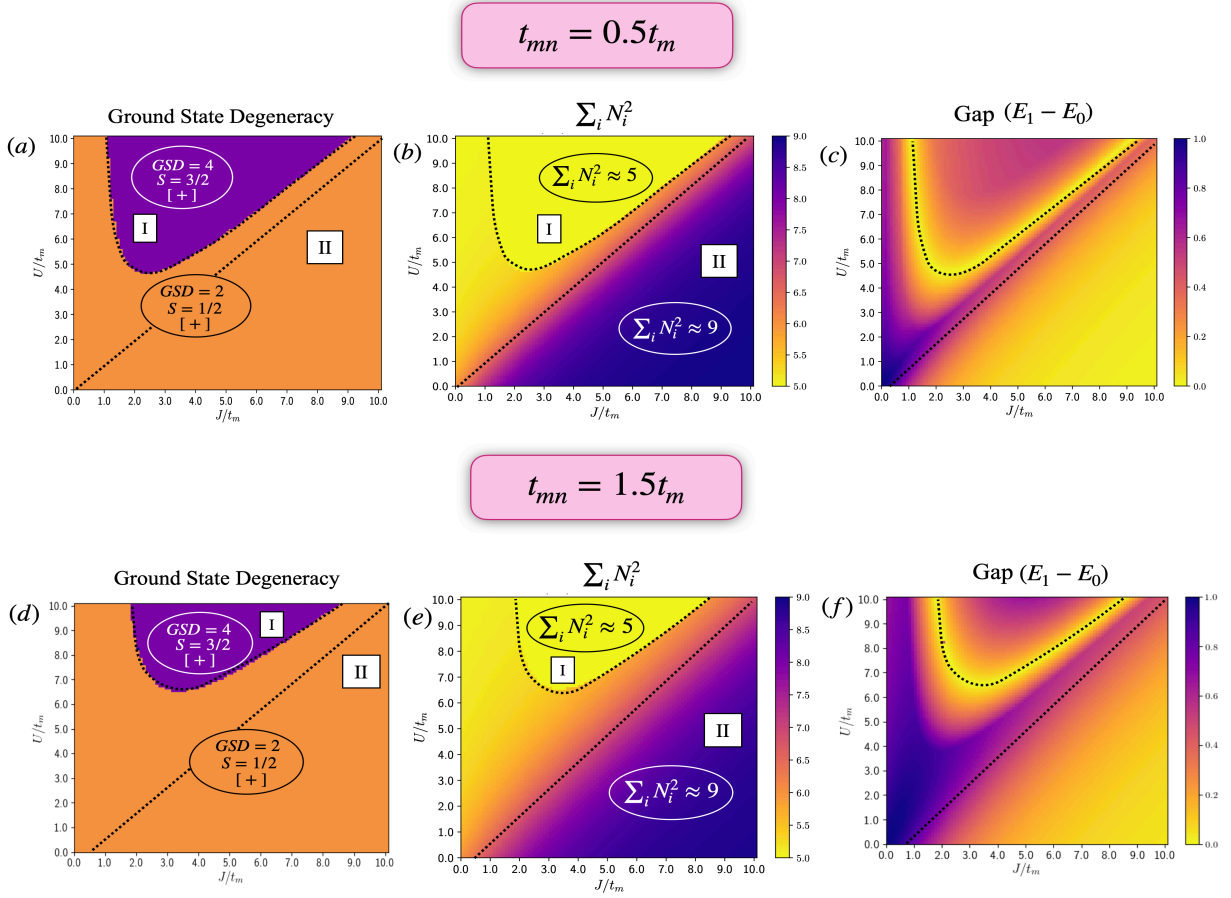


**Figure 6.3** –  $U - J$  phase diagrams for a dimer cluster with two orbitals per site and  $n_f = 3$ . The first row shows the (a) ground state degeneracies (b)  $\sum_i N_i^2$  and (c) gap plots for  $(t_m, t_{mn}) = (1.0, 0.5)$ . The second row shows the (d) ground state degeneracies (e)  $\sum_i N_i^2$  and (f) gap plots for  $(t_m, t_{mn}) = (1.0, 1.5)$ . The GSD plots indicate the GSD, effective spin degree of freedom, and, in square brackets, the inversion quantum number. The dotted boundaries shown in all plots are obtained from the peaks in the second derivative of the ground state energy with respect to  $U$  and  $J$ .

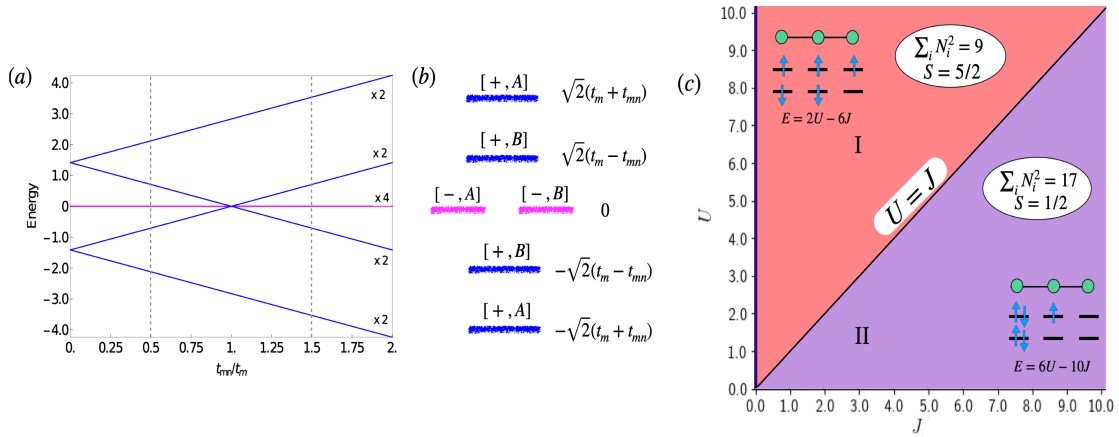


**Figure 6.4** – Various limits for a trimer cluster with two orbitals per site. (a) Non-interacting molecular orbital levels. (b) Single-particle levels with energies indicated, ordered assuming  $t_{mn} < t_m$ . (c)  $U - J$  phase diagram of  $H_{\text{int}}$  only for  $n_f = 5$ , i.e. in the absence of hopping.

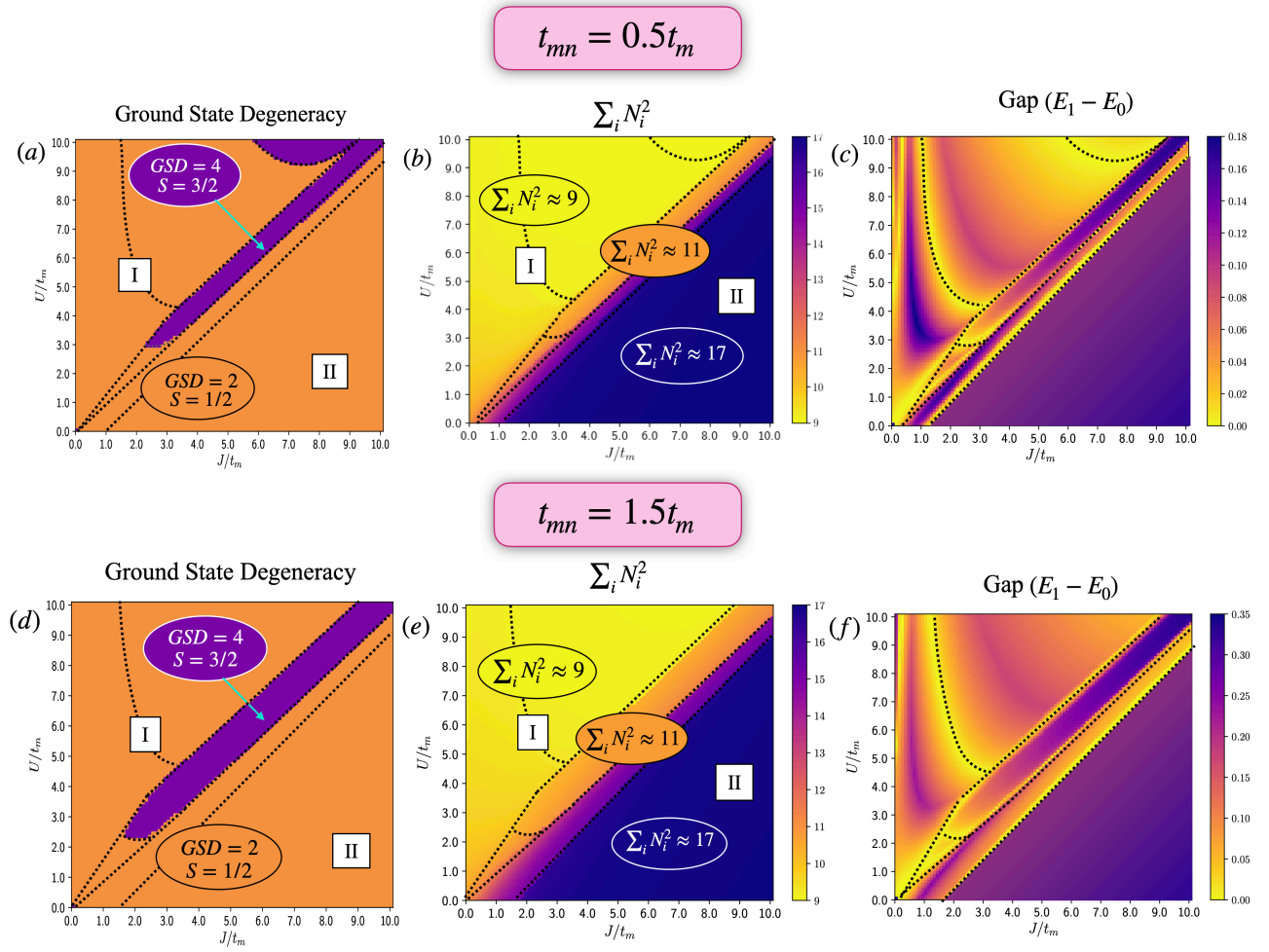


**Figure 6.5** –  $U - J$  phase diagrams for a trimer cluster with two orbitals per site and  $n_f = 5$ . The first row shows the (a) ground state degeneracies (b)  $\sum_i N_i^2$  and (c) gap plots for  $(t_m, t_{mn}) = (1.0, 0.5)$ . The second row shows the (d) ground state degeneracies (e)  $\sum_i N_i^2$  and (f) gap plots for  $(t_m, t_{mn}) = (1.0, 1.5)$ .

the  $U = J$  line, corresponding to the  $(3 + 1 + 1)$  configuration (orange region in Fig. 6.5(e)). Note an interesting pattern: in the presence of both interactions and hopping, we generally expect ground state degeneracies to decrease; but the pockets with higher degeneracies and spin seemed to be favored at higher interactions. This is because of the interplay between hopping and interactions. As hopping is increased, the pockets with high GSD, which are remnants of the interaction regime, find higher and higher values of interaction parameters so as to overpower hopping.

### Triangle, $n_f = 7$

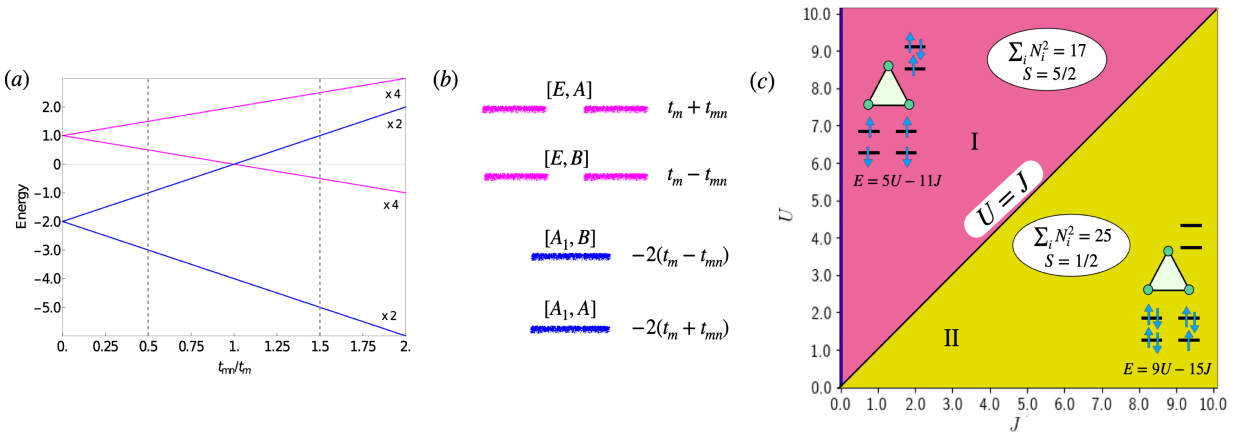
Fig. 6.6(a) shows the non-interacting molecular orbital levels of a triangle cluster with two orbitals per site. The triangular cluster has a  $[C_{3v}, C_2]$  symmetry. A distinct feature of the triangle molecular orbital levels is the two-fold degenerate  $[E, A]$  and  $[E, B]$  levels. These levels are protected by the  $C_3$  symmetry of the triangular cluster. We consider the  $n_f = 7$  sector here as an example. In the non-interacting limit, filling the single-particle levels with 7 electrons

gives rise to a four-fold ground state degeneracy when  $t_{mn}/t_m < 1$  and a two-fold ground state degeneracy when  $t_{mn}/t_m > 1$ .

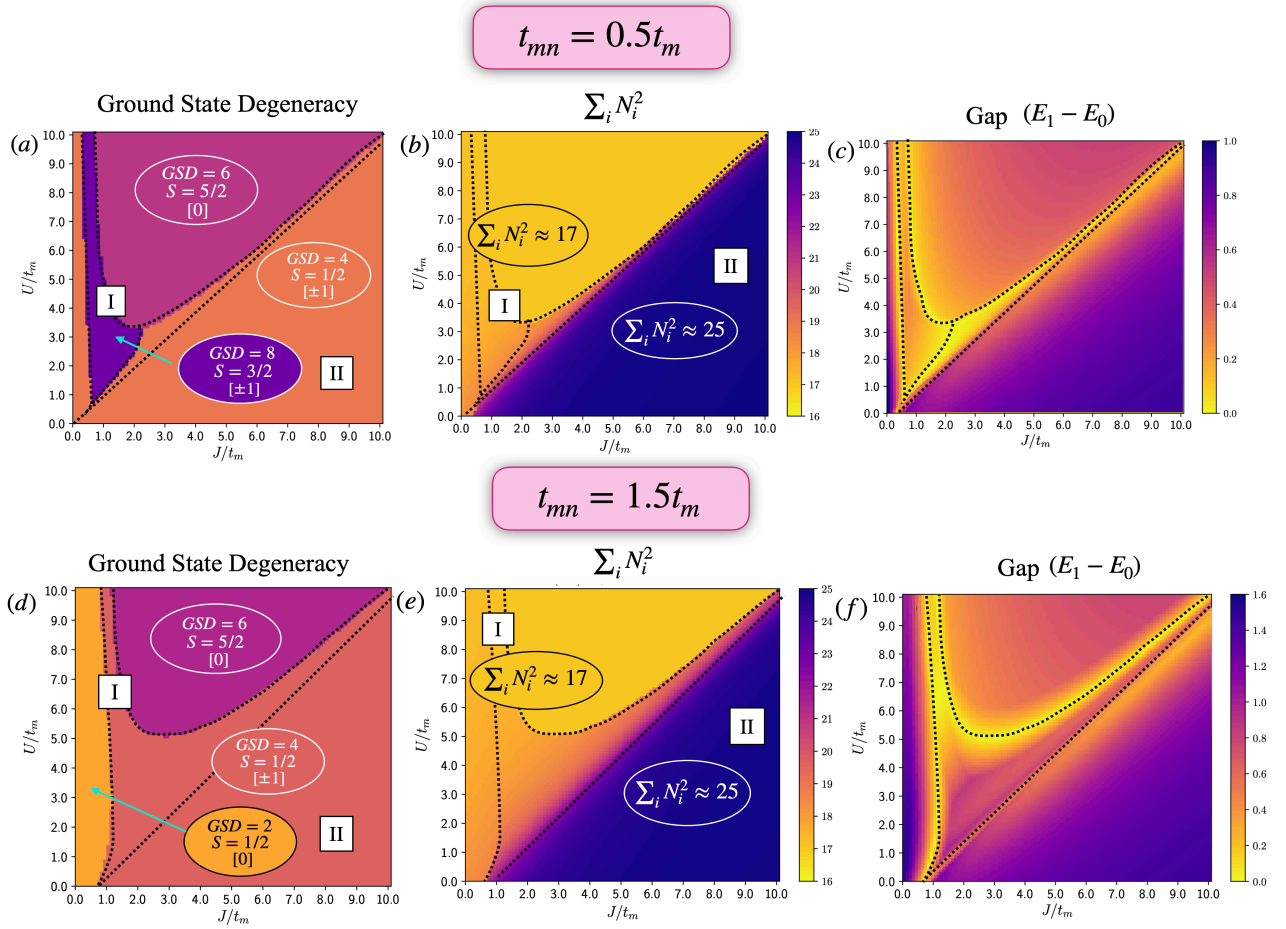
In the pure interaction limit, we see the electrons arrange themselves among the sites of the cluster in two ways. A  $(3 + 2 + 2)$  configuration is favored in the large- $U$  limit (since this minimizes the  $\sum_i N_i^2$  term) and a  $(4 + 3 + 0)$  configuration is favored in the large- $J$  limit, as shown in the pure-interaction plot of Fig. 6.6(c). Consider first the region I. From Fig. 6.1, we see that the energetically favored combination is the presence of an  $S = 1$  triplet on the two sites with two electrons, and an  $S = 1/2$  on the third site (in accordance with Hund's rules). The result of this is an overall effective  $S = 5/2$  degree of freedom. Similarly, in region II, an  $S = 1/2$  on one site and an  $S = 0$  on the other two results in an overall  $S = 1/2$  degree of freedom.

Fig. 6.7 shows the phase diagrams for  $n_f = 7$  with both interactions and hopping. In Fig. 6.7(a), we see a variety of phases in region I and II. Different configurations of electrons being favored in different parameter regimes is seen in the  $\sum_i N_i^2$  plot in Fig. 6.7(b), although the areas encompassed by values close to those of the pure interaction limit have changed due to an interplay of interactions and hopping. Another remnant of the pure interaction limit is the  $U = J$  phase boundary; in addition, the effective spin degrees of freedom in region I (pink area) and region II also follow from their respective pure interaction counterparts in Fig. 6.6(c). Note that while the degeneracy is purely due to the spin degree of freedom in the pink area of region I, the GSD in other areas and regions arise due to a combination of spin and spatial symmetries.

As we increase hopping to  $t_{mn}/t_m > 1$ , we see that region I shrinks, and region II expands (Fig. 6.7(d)). In addition, the  $U = J$  line shifts away from the origin, and the non-interacting limit (that is, the origin in the plot:  $U = 0, J = 0$ ) smoothly connects to the new area with an  $S = 1/2$  degree of freedom, in tune with the preferred ground state in the non-interacting limit. We hence observe a tendency of the system trying to approach this limit, in the lower left area of Fig. 6.7(d).



**Figure 6.6** – Various limits for a triangular cluster with two orbitals per site. (a) Non-interacting molecular orbital levels. (b) Single-particle levels with energies indicated, ordered assuming  $t_{mn} < t_m$ . (c)  $U - J$  phase diagram of  $H_{\text{int}}$  only for  $n_f = 7$ , i.e. in the absence of hopping.



**Figure 6.7** –  $U - J$  phase diagrams for a triangular cluster with two orbitals per site and  $n_f = 7$ . The first row shows the (a) ground state degeneracies (b)  $\sum_i N_i^2$  and (c) gap plots for  $(t_m, t_{mn}) = (1.0, 0.5)$ . The second row shows the (d) ground state degeneracies (e)  $\sum_i N_i^2$  and (f) gap plots for  $(t_m, t_{mn}) = (1.0, 1.5)$ . The quantum number indicated in square brackets corresponds to rotation about the cluster's  $C_3$  axis.

### Tetramer, $n_f = 7$

Fig. 6.8(a) shows the non-interacting molecular orbital levels of a tetramer cluster with two orbitals per site. The presence of both inter- and intra-orbital hopping gives rise to three regimes:  $t_{mn} < 1/\sqrt{5}$ ,  $1/\sqrt{5} < t_{mn} < 1$ , and  $t_{mn}/t_m > 1$ . Of these, only the second and third regimes are highlighted (for reasons discussed below). The tetramer cluster has a  $[i, C_2]$  symmetry. We show here  $n_f = 7$  as an example. In the non-interacting limit, filling the single-particle levels with 7 electrons gives rise to a doubly degenerate ground state with an effective  $S = 1/2$  degree of freedom.

In the absence of hopping, among all the different ways that 7 electrons can be distributed among four sites, the  $(2 + 2 + 2 + 1)$  configuration is favored in the large- $U$  limit, and the  $(4 + 3 + 0 + 0)$  configuration is favored in the large- $J$  limit, as shown in the pure-interaction plot of Fig. 6.8(c).

We now switch on  $U$  and  $J$  and study how these ground states evolve. In the first regime of  $t_{mn} < 1/\sqrt{5}$ , there is a uniform two-fold degeneracy arising from an effective  $S = 1/2$

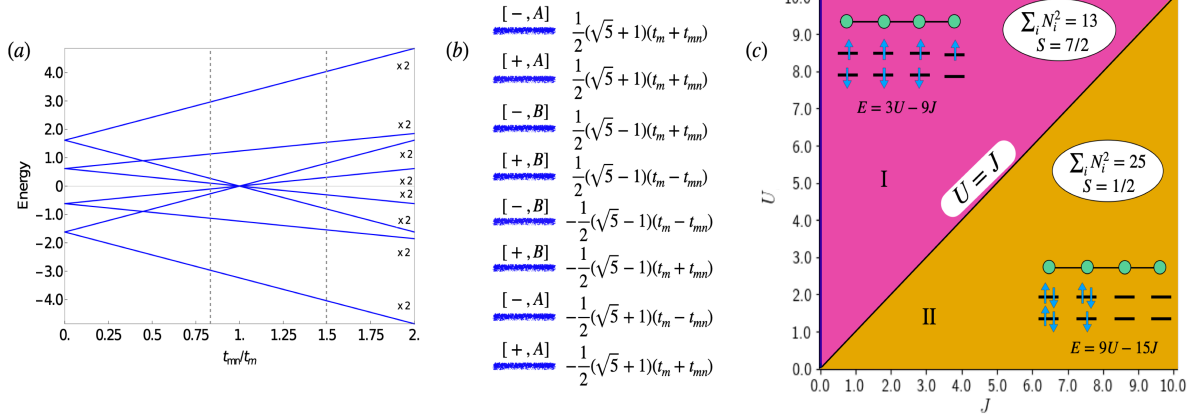


**Figure 6.8** – Different limits for a tetramer cluster with two orbitals per site. (a) Non-interacting molecular orbital levels. (b) Single-particle levels with energies indicated, ordered assuming  $t_{mn} < t_m$ . (c)  $U - J$  phase diagram of  $H_{\text{int}}$  only for  $n_f = 7$ , i.e. in the absence of hopping.

everywhere. Hence, plots for this regime are not shown. Fig. 6.9 shows the phase diagrams for  $n_f = 7$ , with phase boundaries indicated. The choices of hoppings  $t_{mn} = 0.8$  and  $t_{mn} = 1.5$  are based on the two hopping regimes of Fig. 6.8(a).

In Fig. 6.9(a), there are a variety of phases in regions I and II, either with a two-fold or a four-fold GSD. The two regions of different electronic configurations are confirmed by Fig. 6.9(b), although the areas encompassed by a “pure”  $(2 + 2 + 2 + 1)$  configuration (region I) and a “pure”  $(4 + 3 + 0 + 0)$  configuration (region II) have changed.

When  $t_{mn}$  is increased, we see that region I shrinks, and that the area of two-fold degeneracy (region II) expands. In addition, the  $U = J$  line shifts away from the origin (Fig. 6.9(d)), with the non-interacting limit now smoothly connected to the  $GSD = 2$  region.

### Tetrahedron, $n_f = 6$

Fig. 6.10(a) shows the non-interacting molecular orbital levels of a tetrahedral cluster with two orbitals per site. Note that the tetrahedral cluster is the only three-dimensional cluster considered, whereas all the other clusters are either linear chains or planar. The tetrahedral cluster has a  $[T_d, C_2]$  symmetry. A distinct feature of these molecular orbital levels is the  $[T, A]$  and  $[T, B]$  levels, with a three-fold degeneracy each. We show here  $n_f = 6$  as an example. In the non-interacting limit, filling the single-particle levels with 6 electrons gives rise to a fifteen-fold ground state degeneracy, with individual states that can have either  $S = 0$  or  $S = 1$  effective degrees of freedom.

In the opposite limit of pure interactions, in accordance with applying cluster Hund’s rules to distribute six electrons on a tetrahedron, the  $(2+2+1+1)$  configuration is favored in the large- $U$  limit, and the  $(4+2+0+0)$  configuration is favored in the large- $J$  limit. The  $(2+2+2+0)$  configuration is favored in the intermediate regime. This is shown in the pure-interaction plot of Fig. 6.10(c).

Fig. 6.11 shows the phase diagrams for  $n_f = 6$  in the intermediate regime of both interactions

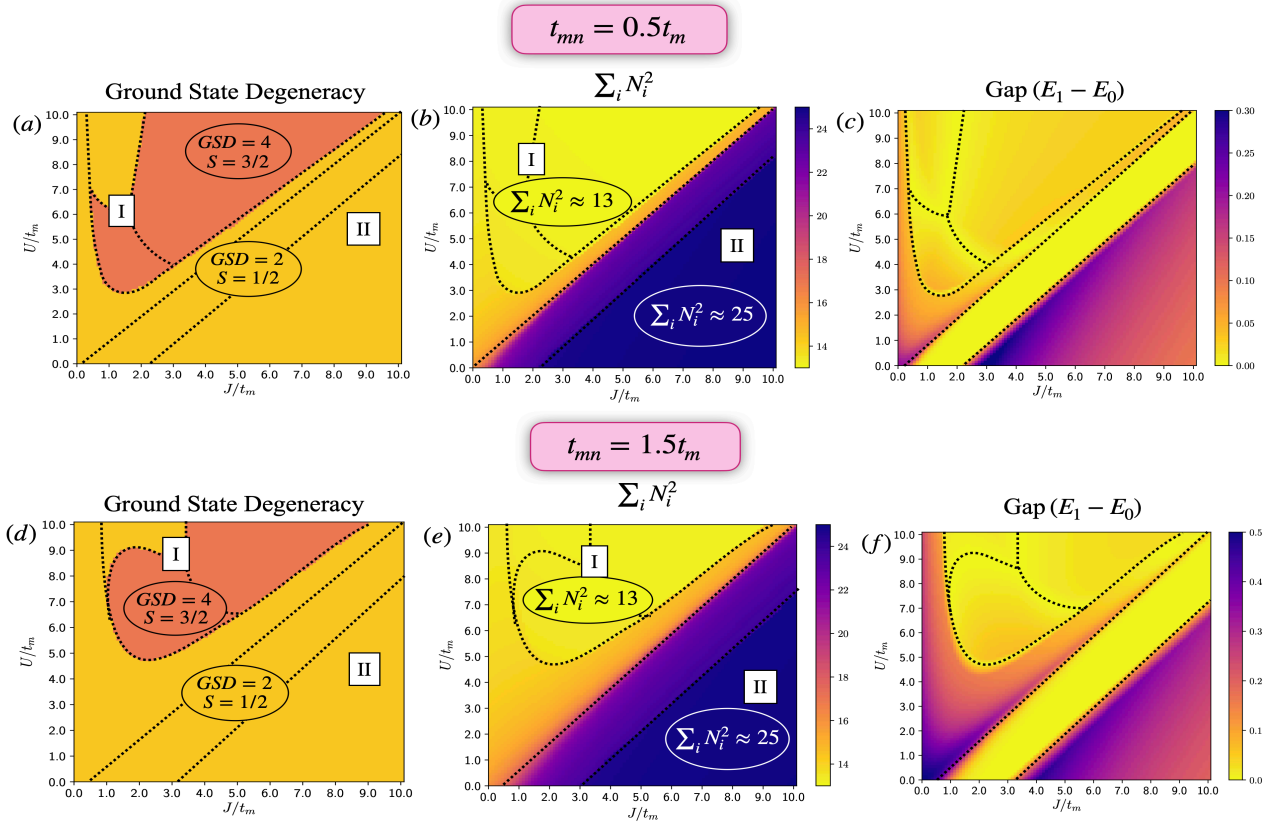


**Figure 6.9** –  $U - J$  phase diagrams for a tetramer cluster with two orbitals per site and  $n_f = 7$ . The first row shows the (a) ground state degeneracies (b)  $\sum_i N_i^2$  and (c) gap plots for  $(t_m, t_{mn}) = (1.0, 0.5)$ . The second row shows the (d) ground state degeneracies (e)  $\sum_i N_i^2$  and (f) gap plots for  $(t_m, t_{mn}) = (1.0, 1.5)$ .

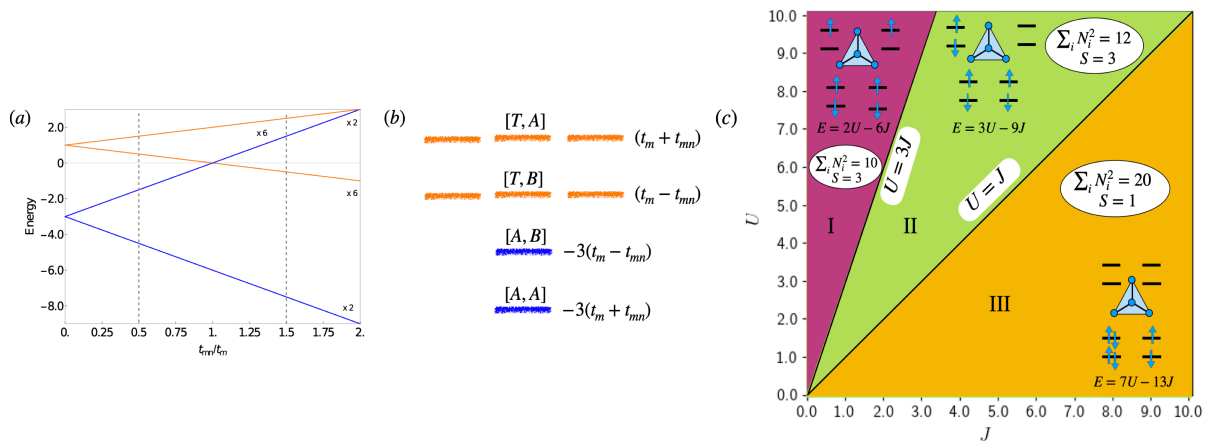


**Figure 6.10** – Various limits for a tetrahedral cluster with two orbitals per site. (a) Non-interacting molecular orbital levels. (b) Single-particle levels with energies indicated, ordered assuming  $t_{mn} < t_m$ . (c)  $U - J$  phase diagram of  $H_{\text{int}}$  only for  $n_f = 6$ , i.e. in the absence of hopping.

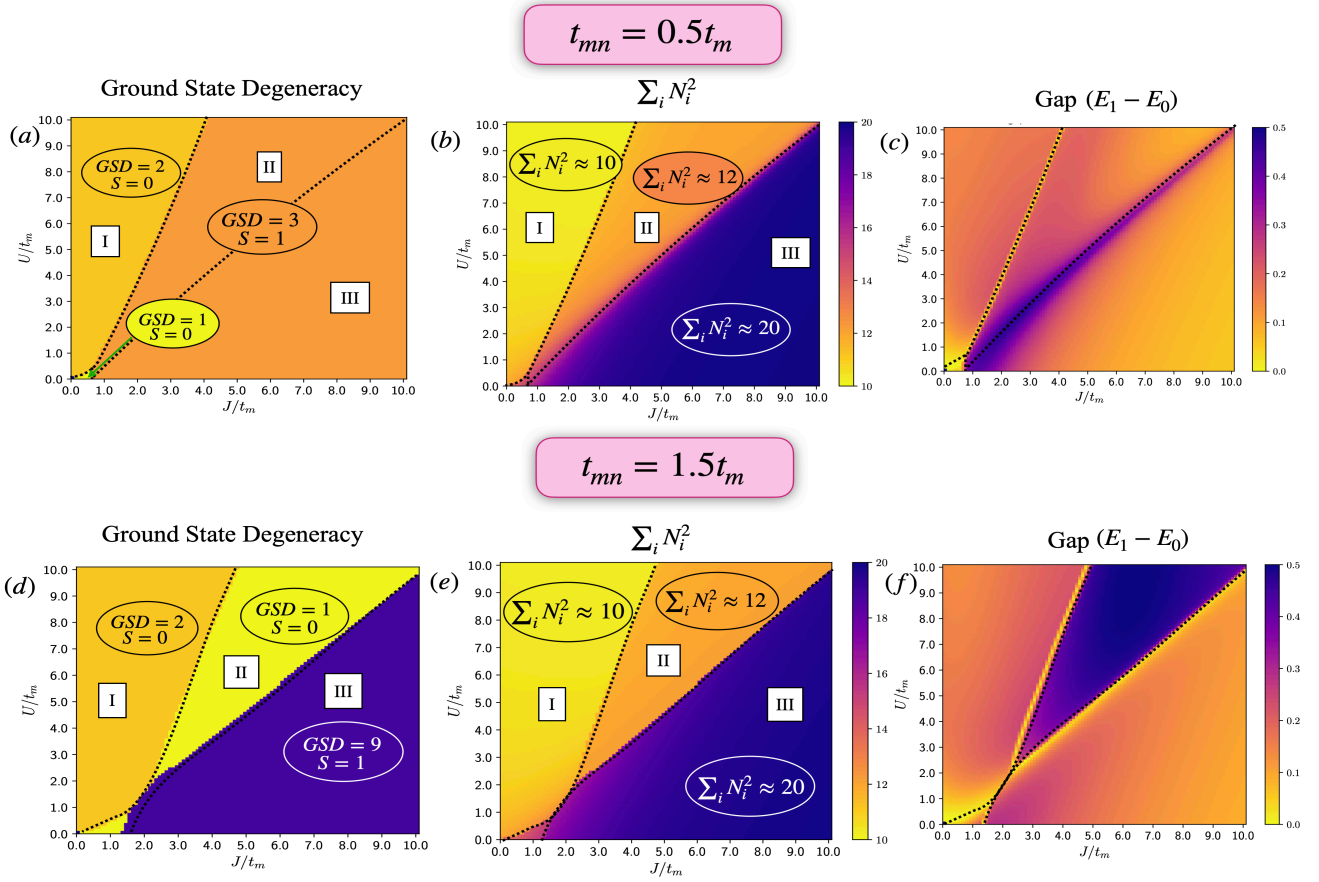


**Figure 6.11** –  $U - J$  phase diagrams for a tetrahedral cluster with two orbitals per site and  $n_f = 6$ . The first row shows the (a) ground state degeneracies (b)  $\sum_i N_i^2$  and (c) gap plots for  $(t_m, t_{mn}) = (1.0, 0.5)$ . The second row shows the (d) ground state degeneracies (e)  $\sum_i N_i^2$  and (f) gap plots for  $(t_m, t_{mn}) = (1.0, 1.5)$ .

and hopping. Note that while the degeneracy is purely due to spin degrees of freedom in region II and region III in Fig. 6.11(a), the ground state in region I is a spin singlet and its two-fold GSD is instead due to spatial symmetry of the cluster.

As we increase hopping, region II expands and now has a unique ground state (Fig. 6.11(d)). In addition to the cluster's  $T_d$  symmetry protecting the two-fold GSD in region I, we also see a spatial contribution to the GSD in region III, which when combined with the  $S = 1$  spin contribution, results in an overall nine-fold degeneracy. This is an example where a unique, non-trivial ground state is found in region II, transforming in the  $A_2$  irreducible representation. We also observe that although the non-interacting point is not smoothly connected to any neighboring regions, adding a small  $U$  or a small  $J$  to this point gives an  $S = 0$  ground state, and ground states with higher effective spin degrees of freedom can only be realized at larger  $J$ .

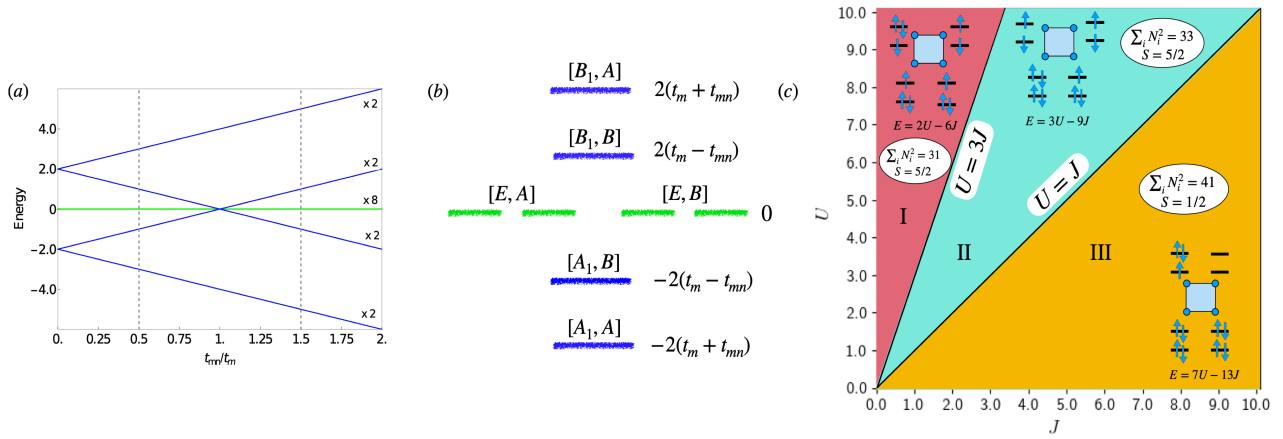


**Figure 6.12** – Various limits for a square cluster with two orbitals per site. (a) Non-interacting molecular orbital levels for a square cluster with two orbitals per site. (b) Single-particle levels with energies indicated, ordered assuming  $t_{mn} < t_m$ . (c)  $U - J$  phase diagram of  $H_{\text{int}}$  only for  $n_f = 11$ , i.e. in the absence of hopping.

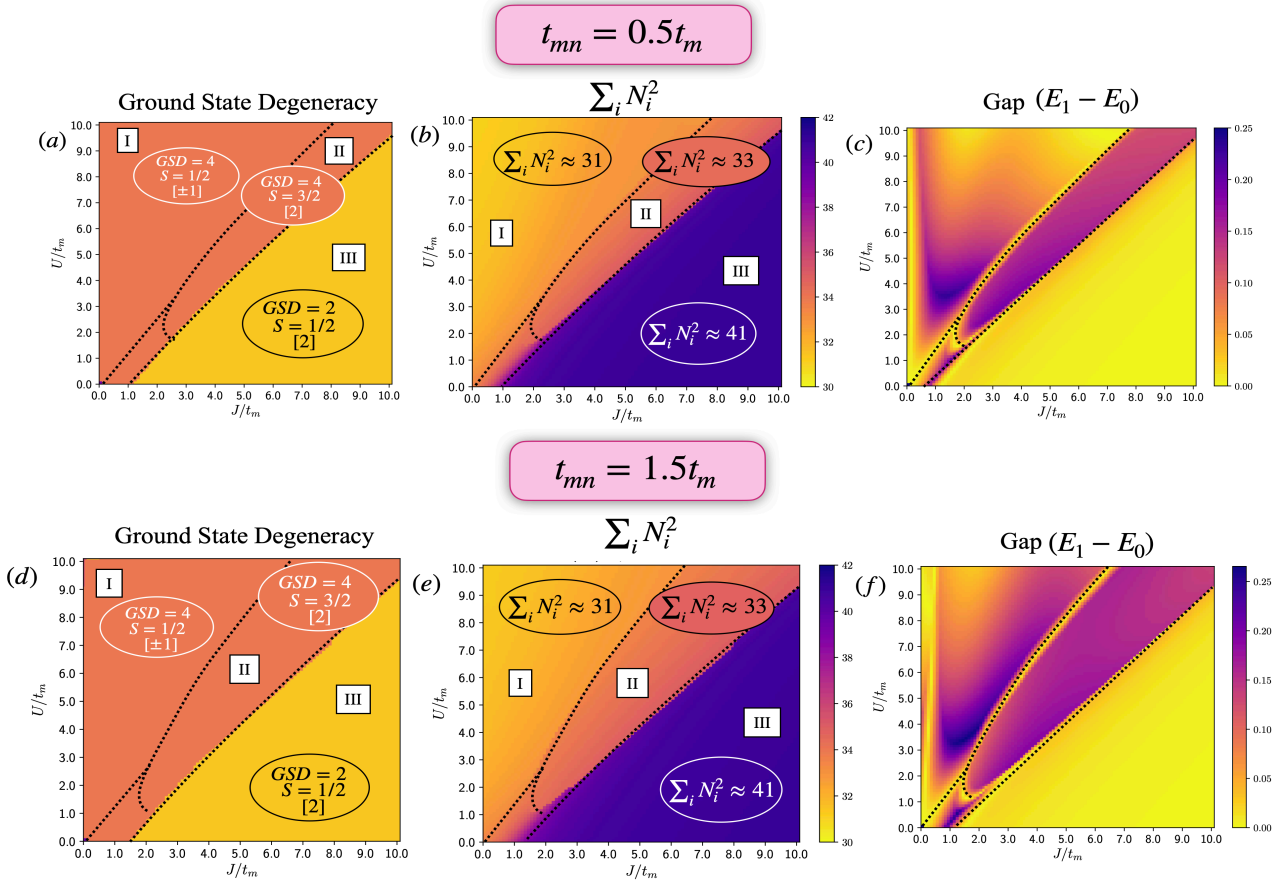
### Square, $n_f = 11$

Fig. 6.12(a) shows the non-interacting molecular orbital levels of a square cluster with two orbitals per site. The square cluster has a  $[C_{4v}, C_2]$  symmetry. A distinct feature of the square molecular orbital levels is the zero-energy  $[E, A]$  and  $[E, B]$  levels. These levels can be split by breaking the cluster  $C_{4v}$  down to  $C_{2v}$ . We have chosen to show  $n_f = 11$  here as an example. In the non-interacting limit, filling the single-particle levels with 11 electrons gives rise to an eight-fold ground state degeneracy with an effective  $S = 1/2$  degree of freedom.

In the pure interaction limit, a  $(3 + 3 + 3 + 2)$  configuration is favored in the large- $U$  limit and a  $(4 + 4 + 3 + 0)$  configuration is favored in the large- $J$  limit. The intermediate region has a  $(4 + 3 + 2 + 2)$  configuration as its ground state, as shown in the pure-interaction plot of Fig. 6.12(c).

Fig. 6.13 shows the phase diagrams for  $n_f = 11$ , with both interactions and hoppings switched on. As with the other cases, we see remnants from the pure interaction limit even though hoppings are now introduced: that is, regimes where different electronic configurations constitute the ground state, as seen in Fig. 6.13(b), although the areas encompassed have shifted. Note that while the degeneracy is purely due to the spin degree of freedom in region II and region III in Fig. 6.13(a), the GSD in region I arises due to a combination of spin symmetry and the  $C_4$  rotational symmetry of the cluster.

As we increase hopping, there are a few observations to make: regions I and III gradually shrink, whereas there is a very slight increase in the area of region II. The non-interacting point is distinct from the surrounding regions; however, adding a small  $U$  or  $J$  leads to a four-fold ground state degeneracy, with different effective spin degrees of freedom.



**Figure 6.13** – The  $U - J$  phase diagrams for a square cluster with two orbitals per site and  $n_f = 11$ . The first row shows the (a) ground state degeneracies (b)  $\sum_i N_i^2$  and (c) gap plots for  $(t_m, t_{mn}) = (1.0, 0.5)$ . The second row shows the (d) ground state degeneracies (e)  $\sum_i N_i^2$  and (f) gap plots for  $(t_m, t_{mn}) = (1.0, 1.5)$ . The quantum number indicated in square brackets corresponds to rotation about the cluster's  $C_4$  axis.

## 6.2 Three orbitals per site

The three-orbital per site Hubbard model is the governing model for all transition metal coordination compounds that have  $t_{2g}$  levels as their ground state. This includes a majority of cluster materials that we saw in Chapter 4. Of particular interest are hexagonal perovskites with dimer and trimer clusters since a zoo of them have been synthesized and have been subject to extensive experimental and theoretical studies over the years. Those with trimer clusters will be dealt with in entirety in Chapter 9. In this section, we will study the governing interacting and non-interacting terms in the three-orbital case and their interplay in clusters of different geometries and at different electron fillings.

### 6.2.1 Molecular orbital levels

In the three-orbital case, the non-interacting Hamiltonian  $H_{\text{non-int}}$  is given by:

$$H_{\text{non-int}} = - \sum_{\langle i,j \rangle, \sigma} \mathbf{c}_{i\sigma}^\dagger \begin{pmatrix} t_m & t_{mn} & t_{mn} \\ t_{mn} & t_m & t_{mn} \\ t_{mn} & t_{mn} & t_m \end{pmatrix} \mathbf{c}_{j\sigma} \quad (6.3)$$

where  $\mathbf{c}_{i\sigma}^\dagger = (c_{im\sigma}^\dagger, c_{in\sigma}^\dagger, c_{ip\sigma}^\dagger)$ . As already mentioned, the inter-orbital hopping  $t_{mn}$  breaks the continuous  $SO(3)$  orbital symmetry down to a discrete  $C_{3v}$  symmetry. In addition to its singly-degenerate irreducible representations,  $A_1$  and  $A_2$ ,  $C_{3v}$  also contains a two-fold degenerate irreducible representation,  $E$ . In stark contrast to the two-orbital case, this thus allows for the possibility of a non-Kramers doublet protected purely by orbital symmetry.

### 6.2.2 Interaction Hamiltonian

From Section 4.2.2 we saw that the Hubbard-Kanamori Hamiltonian for a cluster with three orbitals per site is given by

$$H_{\text{int}} = \frac{(U - 3J)}{2} \sum_i N_i^2 - 2J \sum_i [\vec{S}_i^2 + (\vec{L}_i/2)^2] + \frac{(8J - U)}{2} n_f \quad (6.4)$$

The spectrum of this Hamiltonian for a single site is shown in Fig. 6.14 [132]. Note here that the angular momentum at each site,  $\vec{L}_i^2$ , is conserved, in contrast with the two-orbital case.

### 6.2.3 Some select phase diagrams

We carried out an exhaustive study across all fillings on dimer and trimer clusters. Here, we present results from some select fillings, in which there was a remarkably diverse variety of phases. As mentioned in section 4.1, dimer and trimer clusters are of particular interest from a material perspective, since a wide range of hexagonal perovskite materials are shown to host them.

$n_f$	$S$	$L$	$GSD$	Energy
0[6]	0	0	1	0[15U - 30J]
1[5]	1/2	1	6	0[10U - 20J]
2[4]	1	1	9	$U - 3J$ [6U - 13J]
2[4]	0	2	5	$U - J$ [6U - 11J]
2[4]	0	0	1	$U + 2J$ [6U - 8J]
3	3/2	0	4	$3U - 9J$
3	1/2	2	10	$3U - 6J$
3	1/2	1	6	$3U - 4J$

**Figure 6.14 – A single site with three orbitals:** Summary of the three-orbital per site interaction Hamiltonian given in Eq. (6.4), for a single site. The energies given in square brackets correspond to the  $n_f$  given in square brackets.

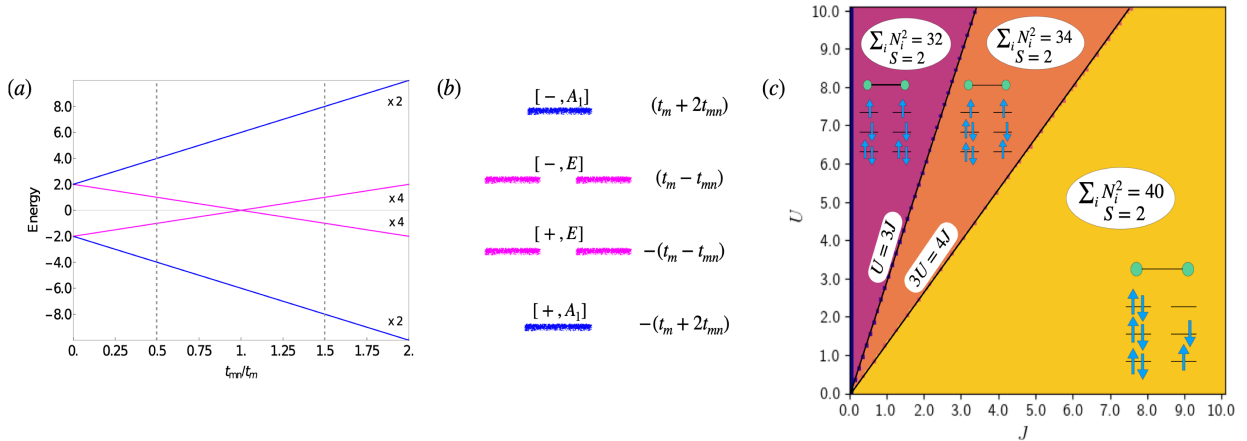


**Figure 6.15 – Various limits for a dimer cluster with three orbitals per site.** (a) Non-interacting molecular orbital levels for a dimer cluster with three orbitals per site. (b) Single-particle levels with energies indicated, ordered assuming  $t_{mn} < t_m$ . (c)  $U - J$  phase diagram of  $H_{\text{int}}$  only for  $n_f = 8$ , i.e. in the absence of hopping.

**Dimer,  $n_f = 8$** 

Fig. 6.15(a) shows the non-interacting molecular orbital levels of a dimer cluster with three orbitals per site. As always, there is the  $t_{mn}/t_m < 1$  and  $t_{mn}/t_m > 1$  regimes. The dimer cluster has a  $[i, C_{3v}]$  symmetry. A distinct feature of these molecular orbital levels is the  $[\pm, E]$  levels. These levels are protected by the orbital  $C_3$  symmetry (Fig. 4.7(c)). We show here  $n_f = 8$  as an example. In the non-interacting limit, filling the single-particle levels with 8 electrons gives rise to a six-fold ground state degeneracy, with individual states that can either have an  $S = 0$  or  $S = 1$  effective degree of freedom.

In the pure interaction limit, for  $n_f = 8$ , there are only three possible ways the electrons can be distributed among the two sites of the cluster. Of these, it can be shown that the  $(4+4)$  configuration is favored in region I, the  $(6+2)$  configuration in region II, and the  $(5+3)$  configuration in region III (see Fig. 6.15(c)).

Fig. 6.16 shows the phase diagrams for  $n_f = 8$ , with both interactions and hoppings. Note that while the degeneracy is purely due to the spin degree of freedom in region III in Fig. 6.16(a), the GSD in regions I and II have different origins: the two-fold GSD in region I is protected entirely by the  $C_{3v}$  symmetry of the orbitals, whereas the GSD in region II arises due to a combination of both spin and orbital symmetry.

As the hopping increases, regions I and II shrink, region III expands, and the  $U = J$  line shifts away from the origin (see Fig. 6.16(d)). The non-interacting limit smoothly connects to the region with  $GSD = 3$ . As with the previous cases, we observe that, as hopping is increased, the system tends to approach the behavior of the non-interacting limit.

**Trimer,  $n_f = 7$** 

Fig. 6.17(a) shows the non-interacting molecular orbital levels of a trimer cluster with three orbitals per site, with again the distinct  $t_{mn}/t_m < 1$  and  $t_{mn}/t_m > 1$  regimes. The trimer cluster has a  $[i, C_{3v}]$  symmetry. A distinct feature of the molecular orbital levels is the two-fold degenerate  $[+, E]$  levels and the zero-energy  $[-, A]$ ,  $[-, E]$  levels. The  $[+, E]$  bands are protected by the orbital  $C_3$  symmetry. The zero-energy  $[-, A]$  and  $[-, E]$  levels are protected by inversion symmetry. We have chosen to show  $n_f = 7$  as an example. In the non-interacting limit, filling the single-particle levels with 7 electrons gives rise to a six-fold degenerate ground state with an  $S = 1/2$  degree of freedom.

In the pure interaction limit, for  $n_f = 7$ , the configurations shown in the pure-interaction plot of Fig. 6.17(c) are favored in the respective parameter regimes. Switching on  $U$  and  $J$ , Fig. 6.18 shows the phase diagrams for  $n_f = 7$ , with phase boundaries indicated. In Fig. 6.18(a), we see that many new regions have emerged. Moreover, the configurations being favored are confirmed by Fig. 6.18(b), with the  $(3+2+2)$  (region I),  $(3+3+1)$  (region II), and  $(6+1+0)$  (region III) configurations visible in the values of  $\sum_i N_i^2$ . Note that the GSD in region I and part of region III arises due to a combination of spin and orbital symmetries of the cluster. In contrast, GSD elsewhere arises purely due to spin.

As we increase hopping, we see that the region with  $S = 3/2$  has drastically shrunk, and a larger area of the plot is occupied by different regions having an  $S = 1/2$  degree of freedom. In

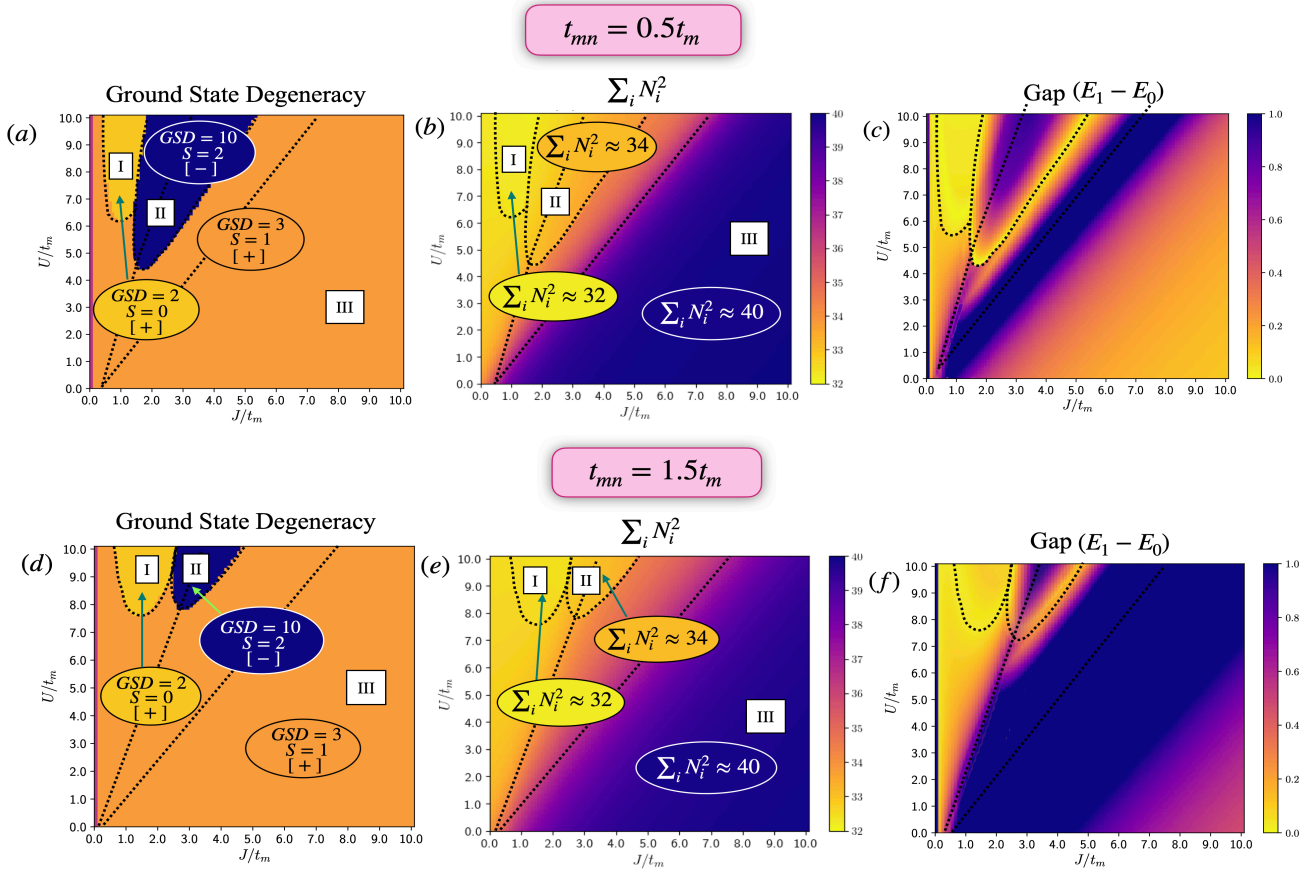


**Figure 6.16** –  $U - J$  phase diagrams for a dimer cluster with three orbitals per site and  $n_f = 8$ . The first row shows the (a) ground state degeneracies (b)  $\sum_i N_i^2$  and (c) gap plots for  $(t_m, t_{mn}) = (1.0, 0.5)$ . The second row shows the (d) ground state degeneracies (e)  $\sum_i N_i^2$  and (f) gap plots for  $(t_m, t_{mn}) = (1.0, 1.5)$ . Indicated in square brackets in (a) and (d) is the inversion quantum number.

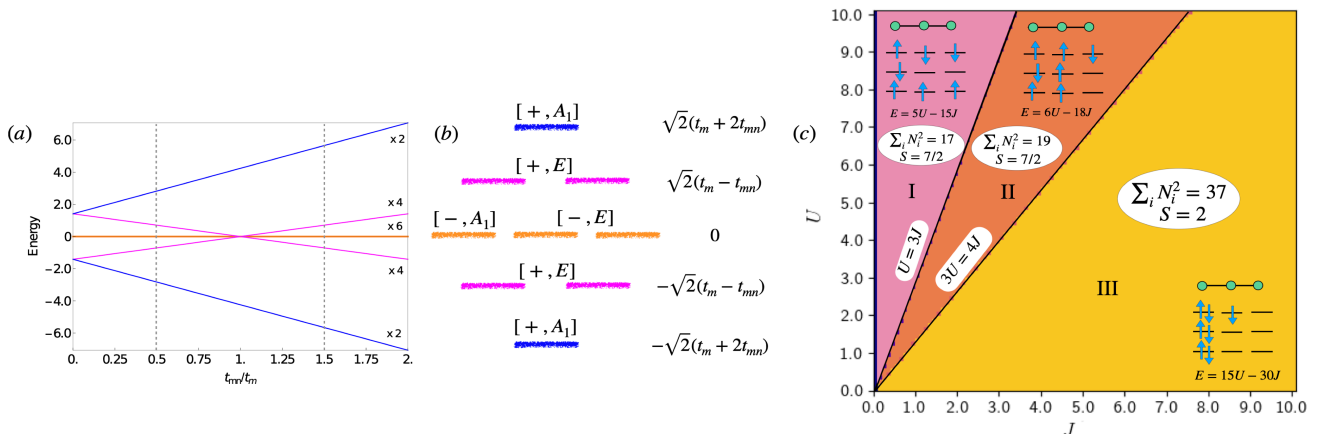


**Figure 6.17** – Different limits for a three orbitals per site trimer cluster. (a) Non-interacting molecular orbital levels for a trimer cluster with three orbitals per site. (b) Single-particle levels with energies indicated, ordered assuming  $t_{mn} < t_m$ . (c)  $U - J$  phase diagram of  $H_{\text{int}}$  only for  $n_f = 7$ , i.e. in the absence of hopping.

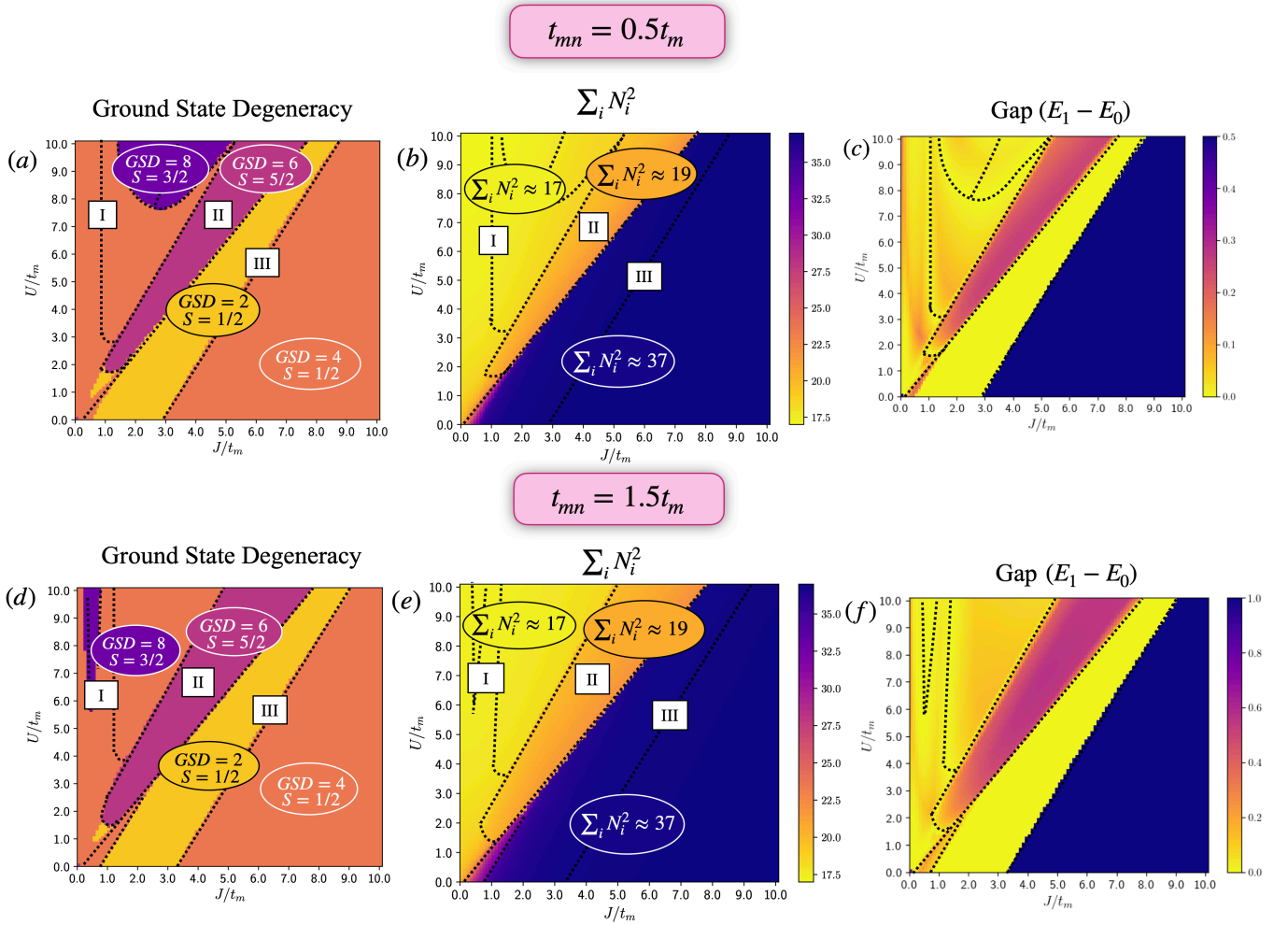


**Figure 6.18** –  $U - J$  phase diagrams for a trimer cluster with three orbitals per site and  $n_f = 7$ . The first row shows the (a) ground state degeneracies (b)  $\sum_i N_i^2$  and (c) gap plots for  $(t_m, t_{mn}) = (1.0, 0.5)$ . The second row shows the (d) ground state degeneracies (e)  $\sum_i N_i^2$  and (f) gap plots for  $(t_m, t_{mn}) = (1.0, 1.5)$ .

addition, the  $U = J$  line has very slightly shifted away from the origin.

## 6.3 Conclusion

In this chapter, we combined analytical insights on the ground state selection rules in different parameter regimes that we saw in Chapter 4, with the computational machinery of exact diagonalization that we encountered in Chapter 3. This helped us perform an exhaustive study of clusters of all geometries that have been observed in real materials so far across all possible fillings. We observed how cluster Hund's rules were obeyed in various clusters: in some cases, we had a binary pure-interaction phase diagram, but increasing the number of sites in the cluster and/or the number of orbitals per site paved the way for more diverse phases. There was an overall decrease in the ground state degeneracies across the board owing to broken symmetries that accompanied the introduction of hopping. Nevertheless, each of these regions behaved differently with the introduction of hopping: while some regions smoothly connected to the non-interacting limit, regions with higher spins were pushed to higher values of interaction parameters, illustrating the interplay between the two.

Tracking the way regions of varying character behave with the tuning of various parameters gives us some foundation to build our understanding of real cluster materials. It is still one step removed from giving us direct insight into candidate cluster Mott materials since material-specific factors like spin-orbit coupling and crystal field splitting have not yet been accounted for. In the next section, this is what we will address; we will survey and study various candidate cluster Mott materials, especially dimer and trimer cluster materials, and try to understand their physics.



## **Part III**

# Candidate Cluster Mott Insulator Materials



# The transition metal ion

In the previous chapters, we introduced the cluster Hubbard Hamiltonian to study the effects an added orbital degree of freedom would have on cluster Mott insulating ground states for various fillings and cluster geometries. In reality, however, these orbitals are not entirely equivalent to one another: they have different orientations in space, and depending on which orbitals are close to those of neighboring ions, this can have a profound effect on the geometry of the crystal, and ultimately, the ground states of the material we are studying. There are many ways in which various orbitals in any atom can be distinguished. The most prominent ones are the principal quantum number,  $n$ , and the azimuthal quantum number (or the orbital angular momentum quantum number),  $l$ . To briefly recapitulate these concepts, the principal quantum number  $n$  is used to indicate the shell of the atom. The value of  $n$  ranges from 1 to the shell containing the outermost electrons of that atom. The azimuthal quantum number  $l$  is used to indicate the sub-shell within a certain shell and groups various orbitals within a shell that have the same orbital angular momentum, which is related to  $l$  as

$$L^2|l, m_l\rangle = \hbar^2 l(l+1)|l, m_l\rangle. \quad (7.1)$$

Orbitals with  $l = 0$  are called  $s$ -orbitals, orbitals with  $l = 1$  are called  $p$ -orbitals, those with  $l = 2$  are called  $d$ -orbitals, orbitals with  $l = 3$  are called  $f$ -orbitals, and so on. The value of  $l$  for a given  $n$  ranges from 0 to  $(n-1)$ , so that the number of orbitals per shell is fixed. Orbitals with a certain  $l$  are all degenerate in energy.

Now, we must establish how many orbitals with a certain azimuthal quantum number exist in a given shell. The magnetic quantum number is used for that purpose – it labels all the specific orbitals that have a given  $l$ , which all differ from one another by the projection of the orbital angular momentum along a specified axis, usually the  $z$ -axis:

$$L_z|l, m_l\rangle = m_l \hbar |l, m_l\rangle. \quad (7.2)$$

The value of  $m_l$  ranges from  $-l$  to  $+l$ ; hence, there is one orbital with  $l = 0$ , three orbitals with  $l = 1$ , five orbitals with  $l = 2$  and so on.

Transition metal compounds have a  $d$ -valence shell or an  $f$ -valence shell; In this thesis, we will mostly be dealing with transition metal ions which have  $d$ -valence shells. Hence, it is essential to take a closer look at the geometries and behavior of these orbitals when the transition metal ion is part of a crystal. The five  $d$ -orbitals are as shown in Fig. 7.1. They are:  $d_{xy}, d_{yz}, d_{xz}, d_{x^2-y^2}$

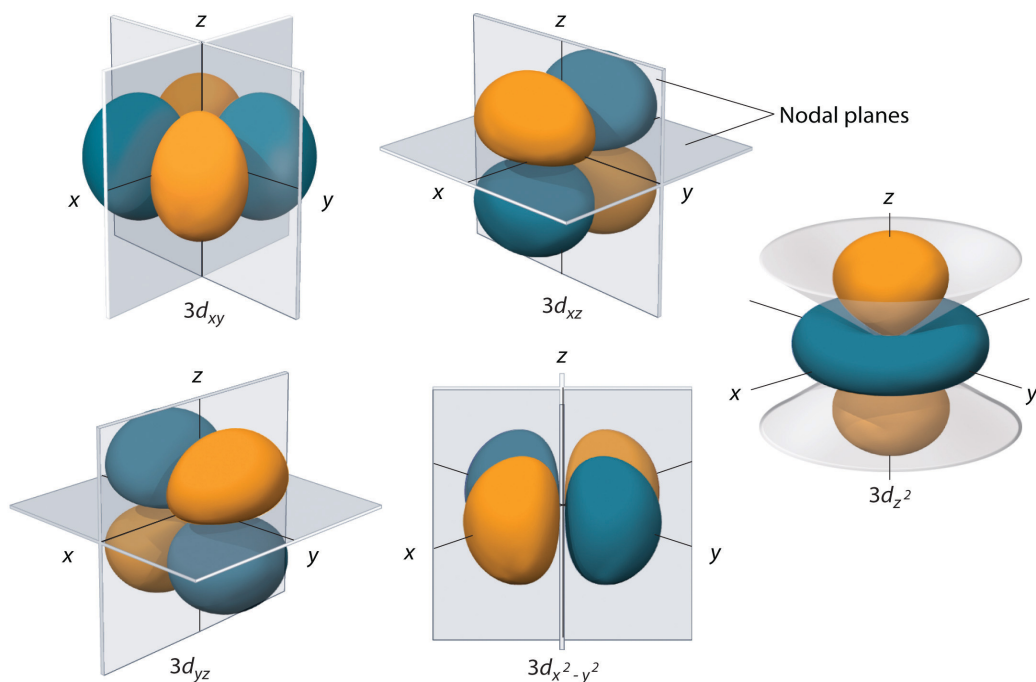


**Figure 7.1 – The five  $d$ -orbitals.**  $d_{xy}$ ,  $d_{yz}$ ,  $d_{zx}$  orbitals are similar in structure to the three  $p$ -orbitals. Figure taken from [154].

and  $d_{z^2}$ . Irrespective of whether it is  $d$ -orbitals or any other orbitals, they all possess spherical symmetry by virtue of being atomic orbitals in an isolated transition metal ion.

## 7.1 Crystal field splitting

The environment of a transition metal ion need not always be spherically symmetric. When the transition metal ion is placed in an environment of anions (or ligands), the five  $d$ -orbitals are destabilized. In addition, the arrangement of anions now determines the local point group symmetry of the crystal. By virtue of their shape and orientation, the five  $d$ -orbitals interact differently with ligands, and hence, along with the breaking of spherical symmetry, the five-fold degeneracy is also broken. The splitting that thus occurs due to the electrostatic field generated by ligands is called crystal field splitting. Depending on the type of ligands surrounding the transition metal ion, the splitting might be of various kinds, some of which we will come across in this chapter. Hence, the total consequence of the presence of ligands around a transition metal ion is a sum of two effects: destabilization and splitting [71, 73].

### 7.1.1 Octahedral crystal fields

The most common ligand in the context of cluster Mott materials is the oxygen ligand. Eight oxygen ligands often arrange themselves around the transition metal ion, giving rise to an octahedral geometry, as shown in Fig. 7.2(a). The oxygen ligand ions are shown in purple, and

the central transition metal ion is the black dot in the center. This arrangement of ligands lowers the spherical symmetry of the ion and gives rise to an  $O_h$  geometry.

Due to this arrangement of oxygen ligands around the TM ion, there is repulsion between the electrons in the  $p$ -orbitals of the oxygen ions and the  $d$ -orbitals of the TM ion. This rearranges the electron density in the five  $d$ -orbitals of the TM ion's valence shell, as shown in Fig. 7.3. The lobes of the  $3d_{z^2}$  and  $3d_{x^2-y^2}$  orbitals are oriented directly towards the  $p$ -orbital lobes of the oxygen ion; because of this, these orbitals experience maximum Coulomb repulsion. On the other hand, one can see that the lobes of  $d_{xy}$ ,  $d_{xz}$  and  $d_{yz}$  are oriented such that each of their lobes lies between two lobes of the ligand orbitals. As a result, the Coulomb repulsion that they experience is weaker. Because of this difference in response, the latter three orbitals are lower in energy, and the remaining two are higher in energy. In other words, the  $l = 2$   $d$ -orbitals split as [73]

$$D \rightarrow T_{2g} + E_g, \quad (7.3)$$

according to the Mulliken notation<sup>1</sup>. Here, the letter of the irreducible representation indicates its dimensionality, and its subscript indicates how it changes under spatial inversion. Hence, “ $E_g$ ” indicated a doubly degenerate state which is even with respect to spatial inversion, and “ $T_{2g}$ ” indicates a triply degenerate state which is also even under spatial inversion. However, these are only two of the ten irreducible representations of  $O_h$ , as shown in the  $O_h$  character tables of Fig. 7.2(b). Note the distinction in nomenclature of these irreducible representations: single-electron states are denoted by lowercase letters, whereas many-electron states of the same symmetry are denoted by the corresponding uppercase letters.

In the Hamiltonian, crystal field is an on-site term, since it only has to do with the response of one TM ion to ligands in its vicinity. In this way, the full spherical symmetry is broken down to a local  $O_h$  point group symmetry due to the surrounding ligands.

### Trigonal distortions

In some cases, however, even the  $t_{2g}$  orbitals might not be fully degenerate. The crystal could physically be distorted along different directions, depending on which the degeneracy between  $t_{2g}$  orbitals is lifted in different ways. Distorted octahedral complexes are usually described by an axis along which a compression, elongation, or other changes may occur. Possibilities are a tetrahedral distortion (along a  $C_4$  axis), a trigonal distortion (along a  $C_3$ ), or a diagonal distortion (along a  $C_2$ ). These axes are indicated in Fig. 7.2(a).

One of the most common is a trigonal distortion along the local [111] direction. When this happens, the  $t_{2g}$  levels split into a singlet,  $a_{1g}$ , and a doublet,  $e_g$  (nomenclature is, again, based on the character table of  $O_h$ , refer to Fig. 7.2(b)). These wavefunctions for  $a_{1g}$  and  $e_g^\pi$  levels in terms of the original  $t_{2g}$  orbital wavefunctions are [155]:

<sup>1</sup>Details on the Mulliken notation can be found in Appendix A.

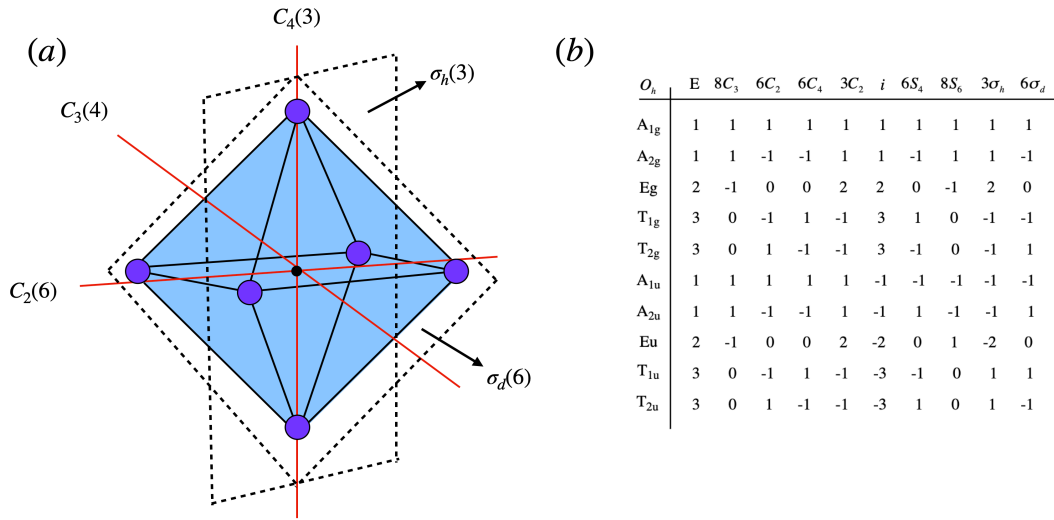


**Figure 7.2 – The octahedral crystal point group.** (a) The octahedral field created by the six oxygen ligands (shown in purple). Various symmetry planes are also shown. The number of axes of rotation/planes of symmetry is indicated in parenthesis. (b) Character tables for the  $O_h$  point group.

$$\begin{aligned}
 |a_{1g}\rangle &= \frac{1}{\sqrt{3}}(|xy\rangle + |xz\rangle + |yz\rangle), \\
 |e_g^\pi\rangle &= \pm \frac{1}{\sqrt{3}}(|xy\rangle + e^{\pm 2\pi i/3}|xz\rangle + e^{\mp 2\pi i/3}|yz\rangle).
 \end{aligned}
 \tag{7.4}$$

The crystal field Hamiltonian can now be restricted to a trigonal term:

$$H_{CF} = - \sum_i c_{i\sigma}^\dagger \begin{pmatrix} 0 & \Delta & \Delta \\ \Delta & 0 & \Delta \\ \Delta & \Delta & 0 \end{pmatrix} c_{i\sigma},
 \tag{7.5}$$

with

$$c_{i\sigma}^\dagger = (c_{xy}^\dagger, c_{yz}^\dagger, c_{xz}^\dagger)_{i\sigma}.
 \tag{7.6}$$

One can understand the nature of the new  $a_{1g}$  and  $e_g^\pi$  orbitals by looking at their interaction with the surrounding oxygen ligands. The  $|a_{1g}\rangle$  orbital has two lobes, and is aligned along [111], the axis of trigonal distortion, which is also the local  $z$ -axis. However, Eq. (7.4) shows that the two  $e_g^\pi$  orbitals are complex in nature: their shape is that of a torus with the axis being [111], the axis of distortion. When there is a trigonal contraction, three oxygen ions lying along the axis of distortion move away from each other, reducing the Coulomb repulsion between them and the  $a_{1g}$  orbital, which lies along [111]. As a result, the  $a_{1g}$  orbital would have a lower energy than the  $e_g^\pi$  doublet, as shown in Fig. 7.4(c).

On the other hand, in the case of a trigonal elongation, three oxygen ions are pulled closer to one another, increasing the Coulomb repulsion between them and the  $a_{1g}$  orbital, which lies along the [111] direction. Hence, a trigonal elongation results in the  $e_g^\pi$  doublet forming the ground state.

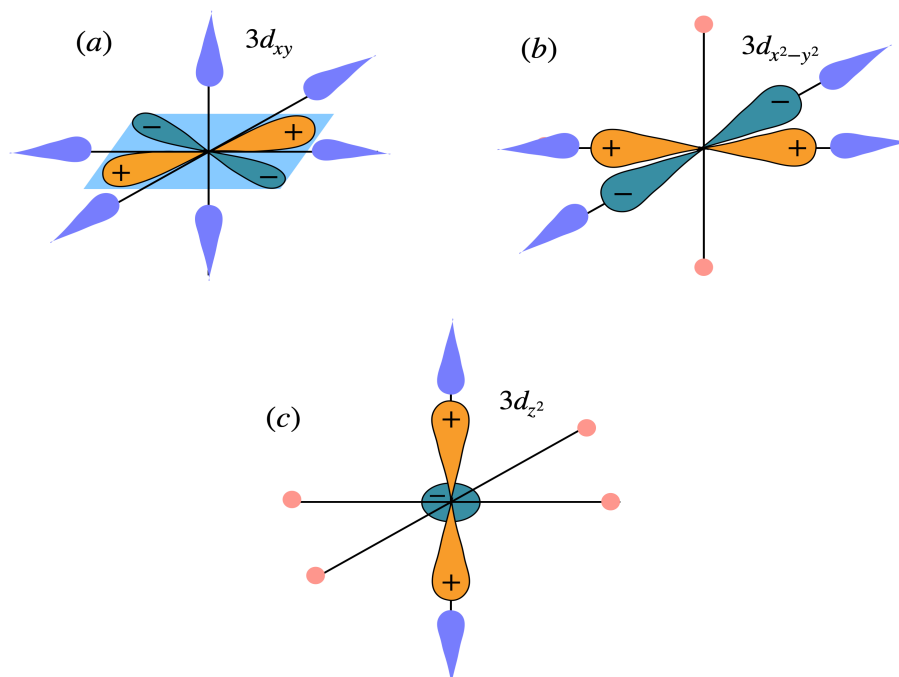


**Figure 7.3** – How the  $p$ -orbital lobes of the oxygen ligand align close to various  $d$ -orbital lobes of the transition metal ion. Proximity of ligand orbital lobes redistributes charges in the transition metal orbitals, shown here are orange lobes for positively charged and green lobes for negatively charged orbitals.

### Other crystal distortions

Though trigonal distortions are the ones we will predominantly use in the future chapters, there could very well be crystal distortions along other directions.

Consider, for example, the deformation of the octahedron along its  $C_4$  axis,  $[001]$ , also called tetrahedral distortions. In case of a tetrahedral elongation, the distance between the oxygen ions lying along the axis of distortion (that is, the global  $C_4$  axis) and the TM ion increases, decreasing the Coulomb repulsion between the ligands and the orbitals whose lobes are oriented entirely or partially along the  $C_4$  axis. As a result, the energy of  $|xz\rangle$  and  $|yz\rangle$  orbitals decreases, whereas the energy of  $|xy\rangle$  orbital increases. There is also a split in the  $e_g$  levels due to this reason, and hence the  $|z^2\rangle$  orbital would have a lower energy than the  $|x^2 - y^2\rangle$  orbital (Fig. 7.4(b)). Conversely, when there is a tetragonal compression, the order of energy level splittings is reversed. Similarly, the crystal can also undergo a diagonal distortion, deforming along the  $C_2$  axis.

#### 7.1.2 Tetrahedral crystal fields

Tetrahedral crystal fields arise when a central metal ion is surrounded by ligands arranged in a tetrahedral geometry. This arrangement is characterized by four ligands positioned at the corners of a tetrahedron around the central metal ion.

The action of tetrahedral crystal fields on  $d$ -orbital splitting is distinct from that of octahedral crystal fields: in fact, it is the opposite of the action of octahedral fields. In the tetrahedral

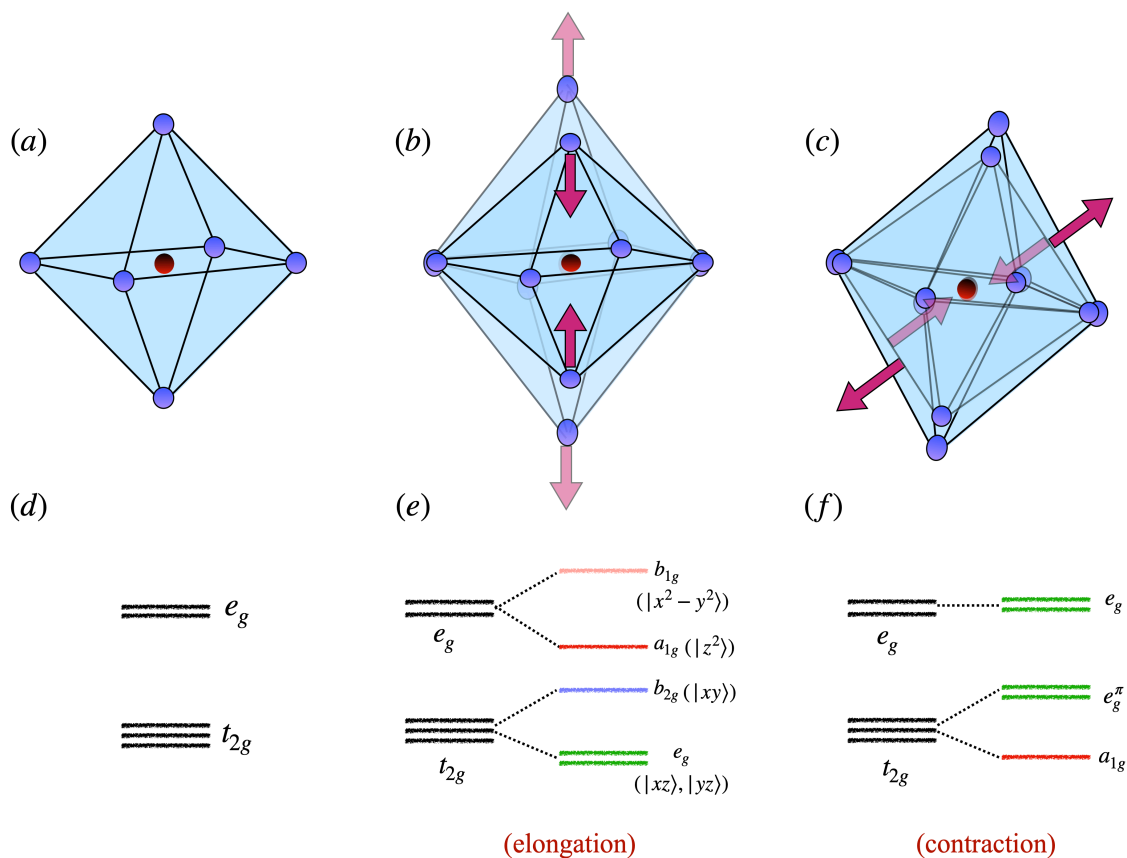


**Figure 7.4** – Effect of distortions in the octahedral ligand fields, on energy levels. (a,d) This is the structure of the energy levels in the presence of an octahedral crystal field, which splits a five-fold degenerate ground state into triply degenerate  $t_{2g}$  and doubly degenerate  $e_g$  levels. (b,e) Tetrahedral distortion along the  $C_4$  axis. Elongation splits the  $t_{2g}$  levels in the manner shown, and compression switches the order of levels. (c,f) Trigonal distortion along the  $C_3$  axis. Trigonal contraction splits the levels as shown, and elongation leads to the same splitting but with the ordering reversed.

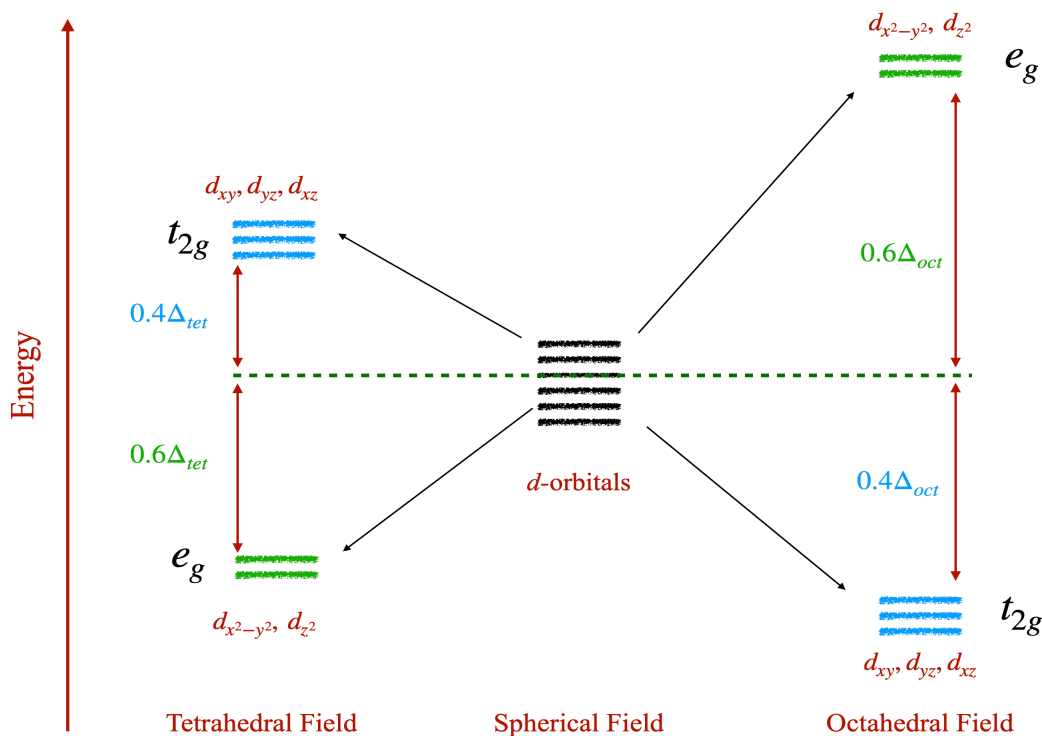


**Figure 7.5 – Splitting of energy levels in a tetrahedral vs octahedral field.** The crystal field in the octahedral case  $\Delta_{oct}$  is larger than the tetrahedral case  $\Delta_{tet}$  because of higher number of ligand ions leading to mutual repulsion.

case, the  $t_{2g}$  orbitals are oriented in such a way that their lobes are closer to the four ligands than the  $e_g$  orbitals. Hence,  $t_{2g}$  orbitals experience a much stronger Coulomb repulsion than  $e_g$  orbitals, increasing their energy. In the Mulliken notation, this is expressed as [73]

$$D \rightarrow E + T_2. \quad (7.7)$$

A comparison of energy splittings in the tetrahedral and octahedral cases is shown in Fig. 7.5. We also observe that the tetrahedral crystal field is generally smaller than the octahedral crystal field; this is due to differences in the geometry and symmetry of the ligand arrangement around the central metal ion. In the octahedral case, the ligands directly face the central metal ion, in contrast to the tetrahedral case. As a result, the  $d$ -orbitals experience stronger Coulomb repulsion from ligands in an octahedral field. In addition, there are more ligand ions in the octahedral case (six), compared to four ligands in the tetrahedral case, further enhancing the energy difference in splitting in the two cases.

Though octahedral and tetrahedral fields are two of the most common crystal fields, the electronegativity of ligand ions and the number of ligand ions can also lead to different ligand fields in the crystal. For example, in a cubic crystal field, the five-fold degenerate state splits into a lower  $e_g$  pair and  $t_{2g}$  set of states. On the other hand, in a square planar crystal field, the splittings are very different: the five-fold degenerate state splits into a lower  $e_g$ , followed by singly degenerate  $a_{1g}$ ,  $b_{2g}$ , and  $b_{1g}$  states.

### 7.1.3 Effect of ligand fields in multi-electron systems

Real materials often have cases where there might be more than one valence electron in the  $d$ -shell of the transition metal ion. In such a case, the  $d$ -electrons are influenced by repulsion not only from the neighboring  $p$ -electrons of the ligands but also by repulsion amongst themselves. This complicates the determination of energy levels and their splitting. Bethe [156] classified electronic splittings observed in transition metal compounds as being a result of the interplay between three main factors:

1. Weak ligand fields – when the ligand is weaker than both interelectron and spin-orbital interactions.
2. Intermediate ligand fields – when ligand fields are weaker than interactions, but stronger than spin-orbit coupling
3. Strong ligand fields – when ligand fields are stronger than both interactions and spin-orbit coupling.

In this section, we will take a look at how the strength of ligand fields influences electronic splittings.

#### Weak ligand fields

This is the limit where the central transition metal ion experiences weak ligand fields. This might either be entirely due to the nature of the ligand itself, or it can be due to screening from the ligand field by the outer  $s, p$  and  $d$  electrons. The screening effect is more prevalent in transition metal ions with an  $f$ -valence shell, and as a result, experiences weak ligand fields by default.

If the ligand fields are weak, then the influence of the ligands can be treated as a perturbation. As a result, the  $L - S$  coupling scheme for multi-electron systems still holds, and Hund's rules are used to determine the ground states. Since Hund's rules pick the states with the highest spin-multiplicity as the ground state, the complexes with weak ligand fields are also called high-spin complexes.

The energy splittings can be calculated for multi-electron  $d$ -shell systems using perturbation theory [73, 157], with the important assumption that the crystal (or ligand) fields are sufficiently small compared to  $d$ -electron repulsions. The splittings, for a  $d^2$ -system (with 2 electrons), are shown in Fig. 7.6(a). For complexes with crystal distortions that lower the  $O_h$  symmetry, degenerate levels are subject to further splitting, the effects of which have been discussed previously.

The qualitative picture of energy-level splittings for electronic configurations with more than 2 electrons can be similarly derived using perturbation theory. We also take advantage of the complementary rule<sup>2</sup> for a higher number of electrons, taking care of the fact that using the

---

<sup>2</sup>According to this principle, the configuration with  $n$  equivalent electrons has the same types of terms as the configuration  $N-n$ , where  $N$  is the number of electrons in the closed shell under consideration. The rule is

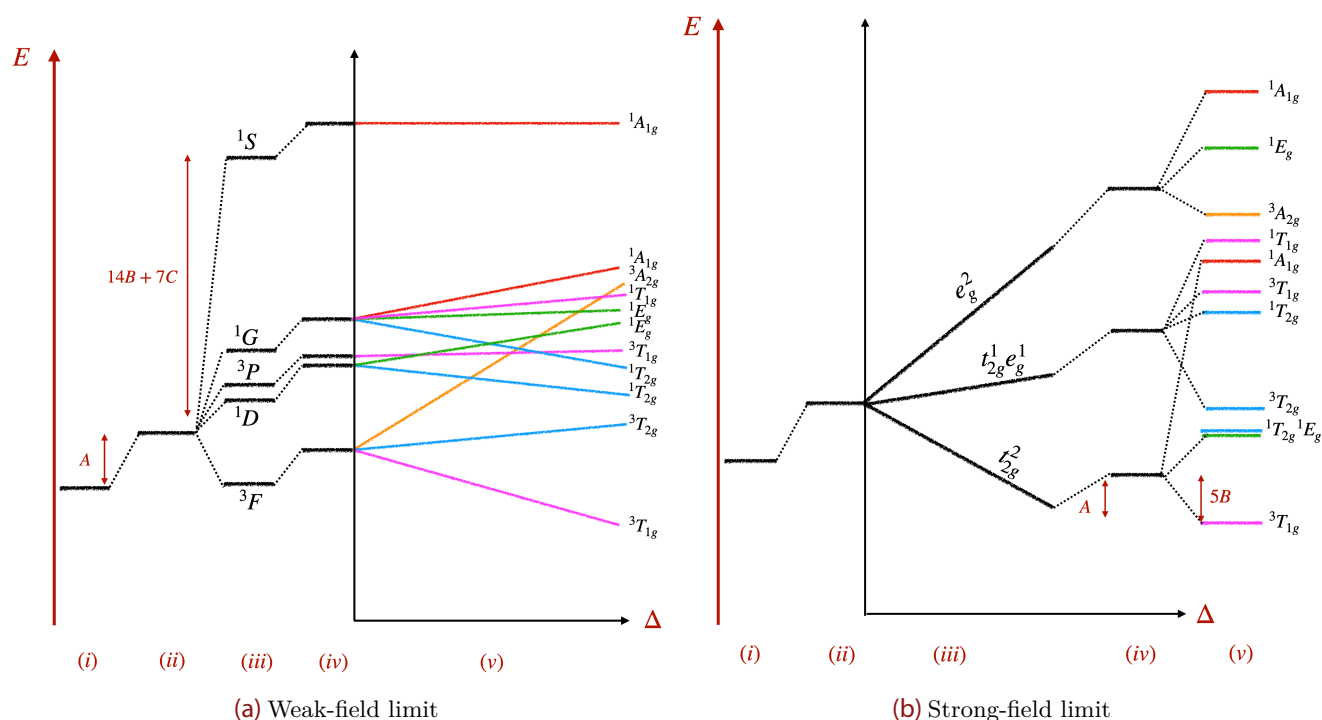


**Figure 7.6 – Splitting of energy levels in the presence of a weak octahedral crystal field vs strong crystal field, for two electrons in the  $d$ -orbitals.** In (a) the weak field limit, (i) indicates the  $d$ -orbital energy level. (ii) When electrons are added, it causes mutual electron repulsion. (iii) The possible electronic arrangements– atomic terms (see Fig. 2.6). (iv) Ligand field destabilization. (v) Crystal field splitting as a function of  $\Delta$ . In (b) the strong field limit, (i) indicates the  $d$ -orbital energy level. (ii) Ligand field destabilization. (iii) Crystal field splitting as a function of  $\Delta$ . (iv) Inter-electron repulsion. (v) Electron interaction splitting.  $A, B, C$  are Racah parameters. Figures inspired by [73].

hole picture also means reversing the signs of various terms involved – repulsive ligand fields become attractive in the hole picture and vice versa.

### Strong ligand fields

In the other limit is the case of a strong ligand field, which surpasses both interaction terms and spin-orbit coupling in terms of strength. In such a case, the  $d$ -electrons choose their orientation entirely based on the ligand field. Hence, one has to take into account the distinction between the  $t_{2g}$  and the  $e_g$  states. If  $t_{2g}$  states are lower in energy,  $d$ -electrons prefer to completely occupy all available  $t_{2g}$  orbitals first (which can accommodate six electrons in total), and then proceed to occupy the  $e_g$  orbitals starting from the seventh electron.

To illustrate the effect of strong ligand fields, consider again a  $d^2$ -system (Fig. 7.6). Two electrons can be accommodated among the five  $d$ -orbitals in the following ways: they can both be placed on  $t_{2g}$  orbitals ( $t_{2g}^2$ ), or they can each be placed on a  $t_{2g}$  and an  $e_g$  ( $t_{2g}^1 e_g^1$ ) or they can both be placed on  $e_g$  orbitals ( $e_g^2$ ). Based on the reasons above, the order of these three

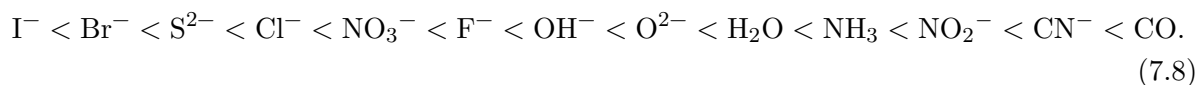
also valid for half-filled shells for which all the orbital states are occupied. This means that for  $d^4$  one can use the configurations of  $d^5 - d^4 = d^1$  ( $d^5$  is a half-filled shell), for  $d^6$ , one can use that of  $d^{10} - d^6 \rightarrow d^4 \rightarrow d^1$ , and so on. Hence all the terms of  $d^n$  configurations can be reduced to those of  $d^1$  and  $d^2$  [73, 88].

configurations energetically would be  $t_{2g}^2 < t_{2g}^1 e_g^1 < e_g^2$ . The energy spacing can be expressed using Racah parameters [157, 158].

Since strong ligand fields cause sequential filling of  $t_{2g}$  and  $e_g$  orbitals, the spin multiplicity of the ground state is always lower in the strong-field limit than in the weak-field limit. Therefore, the complexes with strong ligand fields are called low-spin complexes, in contrast to high-spin complexes in the weak-field limit.

### Spectrochemical series

We have seen in this section, so far, that the strength of the ligand field plays a crucial role in ultimately determining how energy-level splitting occurs and what spin multiplicity the ground state might potentially have. There is also a regularity in the trend of crystal field strength of various ligands, with semi-empirical rules governing them. For instance, the ligand field strongly increases with the oxidation state of the transition metal ion: the ligand field for  $TM^{2+} < TM^{3+} < TM^{4+}$  and so on. Second, for a given oxidation state, ligand field strength increases as we go down a column in the periodic table: that is,  $\Delta$  for a TMI in  $3d < 4d < 5d$  and so on. This gives rise to the spectrochemical series [155]



One should note here that the spectrochemical series does not take into account the hybridization of  $p$ -orbitals of the ligand and the  $d$ -orbitals of the TMI. Different ligands can be arranged in a similar series when other criteria are taken into consideration; for example, they can also be arranged based on their absorption spectra, etc. In cluster Mott materials, the ligand field is almost always that of a chalcogenide or a halide. For example, if we are in the perovskite family of materials (of the form  $M_2O_9$  or  $M_3O_{12}$ ), then we usually see an oxygen ligand field. In  $AB_2X_4$  spinels [36], the transition metal ions are surrounded by chalcogen ligand fields, usually selenium or tellurium. In  $Nb_3X_8$  cluster materials [142], the ligand fields are those of either chlorine, bromine, or iodine. Referring back to the spectrochemical series, one can see that cluster materials therefore have ligand fields whose strength lies in the intermediate range.

## 7.2 Spin-orbit coupling

As we saw in Chapter 2, spin-orbit coupling is another very important factor that plays a role in determining the energy-level splitting in transition metal compounds. It couples the intrinsic spin angular momentum of the electron and its orbital angular momentum as it moves in an electromagnetic field, which is expressed as

$$\begin{aligned}
H_{SOC} &= \lambda \sum_i \mathbf{L}_i \cdot \mathbf{S}_i \\
&= \lambda \sum_i L_{ix} \otimes S_{ix} + L_{iy} \otimes S_{iy} + L_{iz} \otimes S_{iz} \\
&= \lambda \frac{i}{2} \sum_i \epsilon_{\alpha\beta\gamma} c_{i\alpha}^\dagger \tau_{\sigma\sigma'}^\alpha c_{i\beta\sigma'},
\end{aligned} \tag{7.9}$$

where the sum goes over all transition metal ions. The above equation holds if both the spin and angular momentum are written in the same coordinates.

The role of spin-orbit coupling becomes important in the case of partially filled  $d$ -shells of transition metal ions. The interplay of spin-orbit coupling and crystal fields decides how the energy levels are split into various multiplets. The Hubbard-Kanamori Hamiltonian is rotationally invariant, with both  $\mathbf{L}$  and  $\mathbf{S}$  being conserved and hence good quantum numbers. The crystal field term, however, is not rotationally invariant, and mixes different  $\mathbf{L}$  terms. Lastly, the SOC term mixes states of different crystal-field levels ( $t_{2g}$  and  $e_g$  in our case), and terms of different  $\mathbf{L}$  levels as well.

As we saw in the previous section,  $3d$ ,  $4d$ , and  $5d$  systems, including cluster Mott materials, fall under the strong and intermediate ligand field range of Bethe's classification, where spin-orbit coupling is typically the weakest force governing energy splittings. As a result, the effects of intermixing of  $t_{2g}$  and  $e_g$  levels caused by spin-orbit coupling can be neglected. A consequence of this is that SOC for  $t_{2g}$  levels can be treated separately.

### 7.2.1 T-P equivalence

This calls for a revisit to the definition of angular momentum for  $d$ -electron systems. The matrix elements of orbital angular momentum  $\mathbf{L}$  for a single site in the  $d$ -orbital basis,  $\{d_{xy}, d_{yz}, d_{xz}, d_{z^2}, d_{x^2-y^2}\}$  are [159]:

$$L_x = \begin{pmatrix} 0 & 0 & 0 & -\sqrt{3}i & -i \\ 0 & 0 & i & 0 & 0 \\ 0 & -i & 0 & 0 & 0 \\ \sqrt{3}i & 0 & 0 & 0 & 0 \\ i & 0 & 0 & 0 & 0 \end{pmatrix}, L_y = \begin{pmatrix} 0 & 0 & -i & 0 & 0 \\ 0 & 0 & 0 & \sqrt{3}i & -i \\ i & 0 & 0 & 0 & 0 \\ 0 & -\sqrt{3}i & 0 & 0 & 0 \\ 0 & i & 0 & 0 & 0 \end{pmatrix}, L_z = \begin{pmatrix} 0 & i & 0 & 0 & 0 \\ -i & 0 & 0 & 0 & 0 \\ 0 & 0 & 0 & 0 & 2i \\ 0 & 0 & 0 & 0 & 0 \\ 0 & 0 & -2i & 0 & 0 \end{pmatrix}. \tag{7.10}$$

We compare these to the the angular momentum components for  $p$ -orbitals written in the  $\{p_x, p_y, p_z\}$  basis:

$$L_{px} = \begin{pmatrix} 0 & 0 & 0 \\ 0 & 0 & -i \\ 0 & i & 0 \end{pmatrix}, L_{py} = \begin{pmatrix} 0 & 0 & i \\ 0 & 0 & 0 \\ -i & 0 & 0 \end{pmatrix}, L_{pz} = \begin{pmatrix} 0 & -i & 0 \\ i & 0 & 0 \\ 0 & 0 & 0 \end{pmatrix}. \tag{7.11}$$

By comparing the matrix elements of the angular momentum pertaining to  $t_{2g}$  states with those of  $p$ -orbitals, we arrive at a mapping between the two:



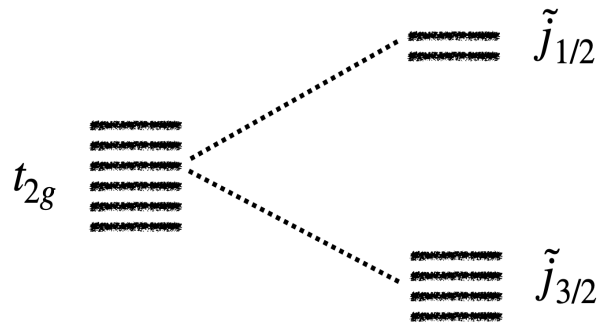


Figure 7.7 – Splitting of energy levels in the presence of spin-orbit coupling.

### 7.2.2 Energy splitting due to SOC

T-P equivalence is important in the case of  $d$ -orbital systems because the quenched orbital angular momentum is used to define the total angular momentum, which is the only good quantum number in the presence of SOC. SOC breaks total spin conservation and angular momentum conservation. Hence, with SOC present,  $\mathbf{L}$  and  $\mathbf{S}$  are no longer good quantum numbers. However, it conserves total angular momentum,  $\mathbf{J}$ , given by

$$\mathbf{J} = \mathbf{L} + \mathbf{S}. \quad (7.17)$$

Here, we have used  $\mathbf{L} = \mathbf{L}_{eff}$ , where  $\mathbf{L}_{eff} = \mathbf{L}_p = -\mathbf{L}_{t_{2g}}$ , owing to T-P equivalence. Hence, the definition of  $\mathbf{J}$  is also modified accordingly:  $\mathbf{J} = \mathbf{S} + \mathbf{L}_{t_{2g}} = \mathbf{S} - \mathbf{L}_{eff}$ . Henceforth, we shall use the shorthand  $\tilde{L}$  to refer to the quenched orbital angular momentum and  $\tilde{J}$  to refer to the total angular momentum which takes angular momentum quenching into account.

We have studied how crystal fields cause energy splitting in the previous sections. In a similar fashion, spin-orbit coupling is also another important factor that causes splitting. In the presence of SOC, the  $t_{2g}$  levels split into  $\tilde{j}_{1/2}$  and  $\tilde{j}_{3/2}$  levels, corresponding to  $s - \tilde{l}$  and  $s + \tilde{l}$  with  $s = 1/2$  and  $\tilde{l} = 1$ . Here, the  $\tilde{j}_{3/2}$  states form the ground states, as shown in Fig. 7.7.

This splitting is valid in the single-particle case; similarly, in the two-electron sector, we have  $s = 1$  and  $\tilde{l} = 1$ , and we get  $\tilde{J} = 2, 1, 0$ , with  $\tilde{J} = 2$  being the ground state. Hence, we see that the state with maximal  $\tilde{J}$  forms the ground state. However, when the  $t_{2g}$  sub-shell is more than half-filled, the scenario is reversed – the state with minimal  $\tilde{J}$  forms the ground state. This is because of the extra negative sign that factors into the angular momentum as a consequence of T-P equivalence.

### 7.2.3 Effect of SOC on magnetic moments

Since transition metal coordination compounds ultimately involve an intricate interplay of various factors (as discussed) which influence the electrons in the crystal, magnetic susceptibility measurements are a very common, yet important diagnostic tool to assess the magnetic nature of such materials. This is done by applying an external magnetic field and measuring how the material behaves. The magnetic susceptibility  $\chi$  is related to the applied field as:

$$\mu_0 \mathbf{M} = \chi \mathbf{B}. \quad (7.18)$$

This relates the material's magnetization,  $\mathbf{M}$  and the strength of the applied field,  $\mathbf{B}$ .

The magnetization  $\mathbf{M}$  of a material is determined by the magnetic moments  $\mu$ . For a free electron, the magnetic moment associated with its spin is given by [73, 160]

$$\mu_s = \frac{e\hbar}{mc} \mathbf{S}, \quad (7.19)$$

whereas the magnetic moment associated with its orbital motion is given by

$$\mu_L = \frac{e\hbar}{mc} \mathbf{L}. \quad (7.20)$$

In the presence of a small spin-orbit coupling, or in the  $L-S$  coupling scheme limit, the effective magnetic moment has both a spin and an angular momentum contribution:

$$\mu_{\text{eff}} = \mu_B (g_S \sqrt{S(S+1)} + g_L \sqrt{L(L+1)}), \quad (7.21)$$

where we have set  $\mu_B = e\hbar/mc$ ; this quantity is called the Bohr magneton.  $g_S = 2, g_L = 1$  are the Landé  $g$  factors due to pure spin and pure orbital angular momentum, respectively. When a transition metal ion is placed in a ligand field, the contribution of the orbital part becomes zero. This is because of the way ligand fields split degenerate energy levels. The magnetization due to orbital contributions arises due to the free orientation of the orbital magnetic moment along the direction of the external field. In the absence of crystal fields, this free orientation is possible because there is no fixed direction for the orbital moment. When ligand fields are introduced, degenerate energy levels are split, and the orbital moment of the ground state gets restricted in orientation. As a result, though the orbital angular momentum might be non-zero, it has difficulty manifesting fully in the magnetic behavior of the electrons, since the orbital magnetic moment cannot freely follow the direction of the external field. Hence, in the presence of ligands, the effective magnetic moment is as if the orbital contribution vanished [73]:

$$\mu_{\text{eff}} \approx \mu_B g_S \sqrt{S(S+1)}. \quad (7.22)$$

In the limit of strong SOC or when the  $j-j$  scheme is used, then, as discussed previously, the total angular momentum is considered. In such a case, we can also associate a magnetic moment  $\mu_J$  to the total angular momentum  $\mathbf{J}$ , by taking the projection of  $\mu$  on  $\mathbf{J}$  and keeping in mind  $\langle \mathbf{J}^2 \rangle = J(J+1)$ :

$$\mu_J = \mu_B g \sqrt{J(J+1)}, \quad (7.23)$$

where the Landé  $g$  factor is given by

$$g = g_L \frac{J(J+1) - S(S+1) + L(L+1)}{2J(J+1)} + g_S \frac{J(J+1) + S(S+1) - L(L+1)}{2J(J+1)}. \quad (7.24)$$

### 7.2.4 Contributions to the susceptibility

As mentioned before, the susceptibility is a measure of how susceptible a material is to the presence of an external magnetic field. Due to the presence of varied types of local moments, they also contribute differently to the total response of the material to an external field. In 1927-28, Van Vleck derived a formula which encapsulated all these contributions to the total susceptibility per unit volume, in the zero field limit [161–164]. Neglecting nuclear contributions and contributions due to inter-electron repulsion, the total susceptibility is given by [165]

$$\chi = \chi_\beta + \chi_{Vv} + \chi_{La}. \quad (7.25)$$

Here,  $\chi_{La}$  is called the Larmor term, which is purely diamagnetic in nature. This is generated by the quadratic part of the Zeeman Hamiltonian:

$$H_{\text{quad}} = \frac{e^2}{2mc^2} \sum_i \left( \frac{\mathbf{B} \times \mathbf{r}_i}{2} \right)^2, \quad (7.26)$$

where  $\mathbf{B} = B\mathbf{e}_k$  is the external constant magnetic field and  $\mathbf{r}_i$  stands for the position vector of the  $i$ -th electron. On the other hand, the Van Vleck susceptibility  $\chi_{Vv}$  is purely paramagnetic in nature, and is generated by the linear part of the Zeeman Hamiltonian

$$H_{\text{lin}} = \mu_B(g_L\mathbf{L} + g_S\mathbf{S}) \cdot \mathbf{B}. \quad (7.27)$$

The  $\chi_{La} + \chi_{Vv}$  part of the total susceptibility is independent of temperature. It can be shown that the first order correction to the energy of the  $j^{\text{th}}$ -state due to Van Vleck and Larmor contributions is given by [165]

$$E_j^{(1)} = \mu_B \langle j | g_L\mathbf{L} + g_S\mathbf{S} | j \rangle, \quad (7.28)$$

and the second order corrections are given by

$$E_j^{(2)} = -N \frac{e^2}{6mc^2} \sum_i \langle j | (\mathbf{r}_i \times \mathbf{e}_k)^2 | j \rangle + 2\mu_B^2 \sum_{l \neq j} \frac{|\langle j | (\mathbf{L} + g_0\mathbf{S}) \cdot \mathbf{e}_k | l \rangle|^2}{E_j - E_l}. \quad (7.29)$$

Since the above terms are temperature-independent contributions, we make use of the first order corrections to the ground state ( $j = 0$ ) energy as given by Eq. (7.28), to calculate zero temperature effective moments in our exact diagonalization routine [109].

The temperature-dependent part,  $\chi_\beta$ , is given by

$$\chi_\beta = \frac{N_A}{3kT} \mu_{\text{eff}}(T)^2. \quad (7.30)$$

In typical cases where ligand fields eliminate any low-lying excited multiplets, or when the spin-orbit coupling is small, the  $\mu_{\text{eff}}$  in Eq. (7.30) takes the form of Eq. (7.22); in this scenario, Eq. (7.30) reduces to a pure Curie-Weiss law [166].

### 7.3 Conclusion

In this chapter, we saw that the properties of transition metal coordination compounds, including cluster Mott materials, are determined by an intricate interplay of various factors, some of the most important for our purpose being ligand fields and spin-orbit coupling. These factors affect the various degrees of freedom that are available, such as spins, lattice, orbitals, etc. Understanding the influence of these factors on energy level splittings helps us diagnose the origin of the observed ground state degeneracies, and also helps us in understanding observed properties, such as how a given material responds to an external magnetic field, etc. These ingredients are an extremely essential addition to our existing theoretical framework for cluster materials, and which will, as we will see in the next chapters, help us apply our framework directly to real cluster Mott candidate materials that have recently been synthesized and await a theoretical treatment.

# Non-Kramers doublets in

## $\text{Ba}_4\text{LiIr}_3\text{O}_{12}$

In this chapter, we discuss the results of our collaboration with Qiang Chen at McMaster, Canada. We introduce the material  $\text{Ba}_4\text{LiIr}_3\text{O}_{12}$ , synthesized by Chen, a cluster Mott material which was initially expected to be non-magnetic, but showed magnetic signatures in its observables. We were able to demonstrate that  $\text{Ba}_4\text{LiIr}_3\text{O}_{12}$  hosts “non-Kramers doublets” and with this, the material became the first cluster Mott candidate to host such non-trivial degeneracies. We also further discuss how other materials, such as other potential cluster Mott materials and pyrochlores, might host these non-Kramers doublets.

### 8.1 The dimer compound $\text{Ba}_4\text{LiIr}_3\text{O}_{12}$

The motivation behind the synthesis of the material  $\text{Ba}_4\text{LiIr}_3\text{O}_{12}$  by Qiang Chen et. al was two-fold: Firstly, prior studies on  $\text{M}_2\text{O}_9$  cluster compounds, and secondly, their interest in studying rich physics of iridate materials in general. When one operates in a regime where the strengths of interactions, crystal fields, and spin-orbit coupling are comparable, various interesting physics is observed. For instance, it was conjectured that the double perovskite  $\text{Sr}_2\text{YIrO}_6$  might exhibit long-range magnetic order. A mechanism where electron hopping between neighboring sites led to an exchange interaction that could compete with the onsite spin-orbital singlet was responsible for the observed local moments. Such anomalous moments have also been observed in a variety of materials, such as  $A_2\text{YIrO}_6$  ( $A = \text{Sr}$  and  $\text{Ba}$ ) and  $\text{R}_2\text{Os}_2\text{O}_7$  [167–170]. It was shown in various works that extrinsic factors such as impurities and lattice defects play a significant role in the magnetism of such materials. For example, it was shown that the observed susceptibilities of  $\text{Sr}_2\text{YIrO}_6$  were due to paramagnetic impurities without long-range magnetic ordering. In addition to paramagnetic impurities [171], lattice defects were also observed to be contributing factors for  $\text{Ba}_2\text{YIrO}_6$  [172].

However, the above materials contain transition metal configurations that are pentavalent. For both  $4d$  and  $5d$  transition metal ions, with four electrons in the valence shell, the ground state is expected to be non-magnetic irrespective of the strength of correlations, as shown in Fig. 8.1(c). In the strong interactions (or  $L - S$  coupling) limit, Hund’s rules are at play, which maximize both spin and angular momentum, leading to a total  $S = 1$  and total  $L = 1$ ,

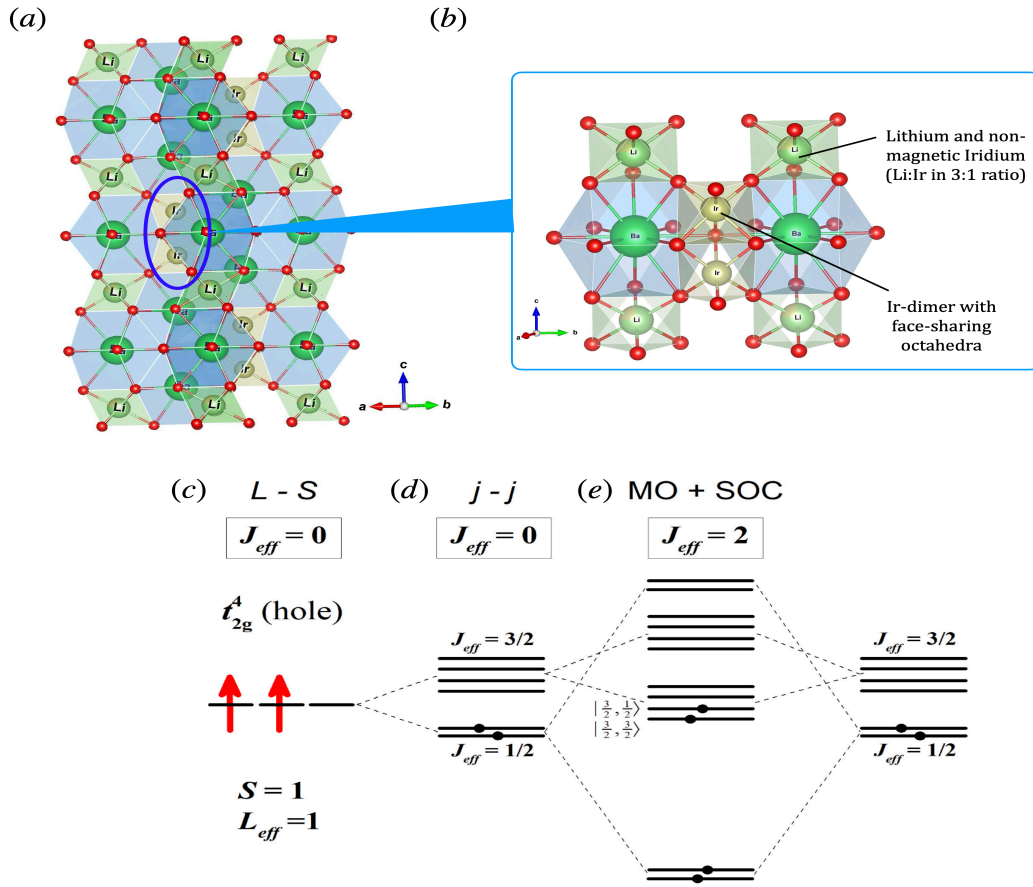


**Figure 8.1** –  $\text{Ba}_4\text{LiIr}_3\text{O}_{12}$ . (a) Crystal structure of  $\text{Ba}_4\text{LiIr}_3\text{O}_{12}$ . (b) Zooming in to reveal the iridium dimer, we see the iridium ions surrounded by oxygen ligands in an octahedral crystal field. The third iridium and lithium share the same position, as shown. (c-d) For 8 electrons on the dimer, both  $L-S$  and  $j-j$  coupling limits point towards a non-magnetic  $J_{\text{eff}} = 0$  ground state. (e) Mechanism proposed by Chen to realize a  $J_{\text{eff}} = 2$  ground state. Illustration taken from [173].

with SOC treated as a weak perturbation. With the introduction of strong spin-orbit coupling, this ultimately leads to a non-magnetic state with a local  $J = 0$  on every site. In the weak interactions (or  $j-j$  coupling) limit, the  $t_{2g}$  shell is split into  $j = 3/2$  and  $j = 1/2$  levels, in which the  $j = 3/2$  levels are fully filled. This again leads to a non-magnetic ground state, as shown in Fig. 8.1(d).

The material at hand,  $\text{Ba}_4\text{LiIr}_3\text{O}_{12}$ , is distinct from the iridates mentioned so far because of the conspicuous presence of iridium dimer clusters, which automatically facilitates strong intra-dimer hopping. Qiang Chen et. al [173] synthesized this material and gathered a wide range of experimental observations by combining X-ray diffraction, magnetic susceptibility, heat capacity, muon spin relaxation, resonant inelastic X-ray scattering (RIXS), and X-ray absorption (XAS) studies.

The material  $\text{Ba}_4\text{LiIr}_3\text{O}_{12}$  (Fig. 8.1(a)) is a curious one. It is a perovskite compound belonging to the  $P6_3/mmc$  space group. It consists of three iridium ions; X-Ray absorption spectroscopy measurements were carried out to ascertain the valency of iridium in the mate-

rial; this would, in turn, tell us how many electrons are present, in total, among the three iridium atoms, and which of them participate in cluster formation. These studies showed that the iridium ions are pentavalent in nature; combined with structural information of the  $\text{Ba}_4\text{LiIr}_3\text{O}_{12}$  crystal, this tells us there are 8 electrons on the  $\text{Ir}_2\text{O}_9$  iridium dimer, whereas the third iridium does not participate in cluster formation.

The iridium dimer clusters have a  $D_{3h}$  point group symmetry. They are composed of two face-sharing  $\text{IrO}_6$  octahedra, in which each octahedron consists of a central iridium ion surrounded by six oxygen ligands. This shortens the distance between the two iridium ions, which facilitates direct Ir-Ir orbital hopping, in turn giving rise to strong intra-dimer interactions. On the other hand, the isolated octahedra that form a quasi-2D triangular lattice are occupied by a mixture of lithium and iridium atoms in a 3:1 ratio. Of all the iridium present in this material, a significant portion of it participates in cluster formation, with the ratio of iridium on dimer sites to those on the triangular lattice sites being 8:1. Hence, each formula unit of  $\text{Ba}_4\text{LiIr}_3\text{O}_{12}$  consists of  $4/3$  units of iridium atoms as dimers and  $1/3$  units of the rest of the iridium (Fig. 8.1(b)).

### 8.1.1 Experimental observations

Fig. 8.2(a) shows the magnetic susceptibility  $\chi$  (as M/H) for  $\text{Ba}_4\text{LiIr}_3\text{O}_{12}$  plotted against a temperature range of 2K – 350K. A linear fit to  $1/\chi$  gives the Weiss-temperature  $\Theta = -523$  K and effective moment  $\mu_{\text{eff}} = 4.17\mu_B$ , as is shown in the figure. This signature is uncharacteristic of a material expected to have a non-magnetic singlet ground state, since it has fully occupied shells in the ground state.

Specific heat and muon-spin relaxation measurements were also carried out to investigate the non-zero magnetic moment further, and probe whether this magnetic moment indicated an onset of any long-range magnetic order in the material. The temperature dependence of the specific heat in Fig. 8.2(b) shows a transition at  $\approx 78$  K, in agreement with long-range magnetic order in this material. They also inferred the magnetic entropy, and it was seen to saturate at a value of 16.2 J/mol-FU.K.

To explain how different iridium ions in the material might have contributed to the observed magnetic moment, Chen et. al proposed that [173]

$$\mu_{\text{eff}} = \sqrt{\frac{4}{3}\mu_1^2 + \frac{1}{3}\mu_2^2}, \quad (8.1)$$

where  $\mu_1$  and  $\mu_2$  are the moments of  $\text{Ir}_1$ , iridium ions that participate in cluster formation, and  $\text{Ir}_2$ , iridium ions that do not participate in cluster formation, respectively. Since the second iridium ion is assumed to be non-magnetic, they set  $\mu_2 = 0$ . Hence, making use of the standard relation

$$\mu_1 = g_J \sqrt{J(J+1)} \quad (8.2)$$

and

$$g_J = 1 + \frac{J(J+1) + S(S+1) - L(L+1)}{2J(J+1)}, \quad (8.3)$$

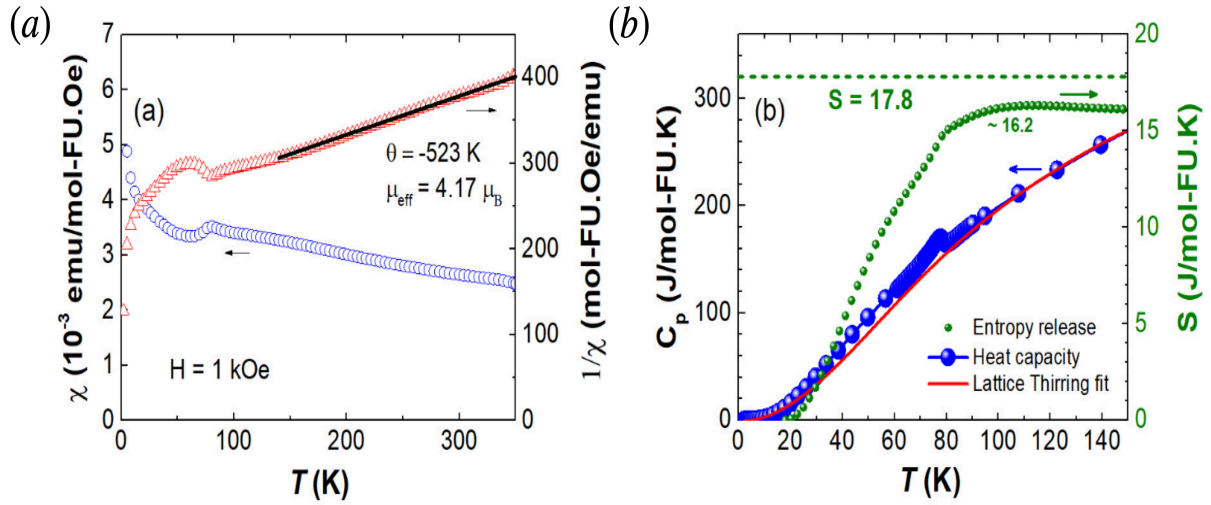


**Figure 8.2 – Observables for  $\text{Ba}_4\text{LiIr}_3\text{O}_{12}$ .** (a) Susceptibility measurements as a function of temperature. A Curie-Weiss fit gives a  $\mu_{\text{eff}} = 4.17\mu_B$ . (b) Specific heat measurements as a function of temperature. The red curve presents a fit of the lattice contribution to the specific heat. The entropy release per formula unit of  $\text{Ba}_4\text{LiIr}_3\text{O}_{12}$  saturates at a value of 16.2 J/mol-FU.K. The entropy release value of 17.8 J/mol-FU.K for a conjectured  $J_{\text{eff}} = 2$  phase is also shown. Images adapted from [173].

they arrived at  $\mu_1 = 3.67\mu_B$ , and  $\mu_{\text{eff}} = 4.24\mu_B/f.u.$ , which is close to the experimental value of  $\mu_{\text{eff}} = 4.17\mu_B$ . This calculated value can be arrived at when  $J_{\text{eff}} = 2$ . The mechanism as to how a  $J_{\text{eff}} = 2$  could be achieved was also proposed, as shown in Fig. 8.1(e). Hence, they conjectured that an  $S = 1, L = 1$  state on the iridium dimer, resulting in  $J_{\text{eff}} = 2$  for the iridium dimer and a  $J_{\text{eff}} = 0$  for the third, non-magnetic iridium, could explain the observed effective magnetic moment. The magnetic entropy for the iridium dimer would be  $S = 4/3R\ln 5 = 17.8$  J/mol-FU.K, which is close to the experimental value of 16.2 J/mol-FU.K, also shown in the specific heat plots.

## 8.2 Kramers vs non-Kramers degeneracies

The material  $\text{Ba}_4\text{LiIr}_3\text{O}_{12}$ , as we saw in the previous section, hosts iridium dimers that consist of eight electrons per dimer. With fully filled levels, one would expect the material to be non-magnetic. However, measurements of various observables proved otherwise. Hence, we briefly review where this might originate from.

In Chapter 6, we saw that ground state degeneracies are protected by various factors. There might be cluster symmetries such as inversion symmetry for dimer clusters, or a  $C_{3v}$  rotational symmetry for triangular clusters, and so on. Similarly, there might also be orbital symmetries by virtue of being in a multi-orbital setting. We also saw in Chapter 7 that when SOC is added to a non-interacting bandstructure, the spin and orbital degrees of freedom intertwine with each other, and as a result, real space and spin space are tied together. Crystal fields were also an additional factor, in the presence of which the available symmetries that protect ground states are broken further.

This prompts the question: Are there any degeneracies that are not broken in the end? The answer lies in Kramers theorem. According to Kramers theorem, the degeneracy cannot be entirely lifted when the system possesses time-reversal symmetry and a half-integer total spin. As a result, any energy levels or ground states of any material are at least two-fold degenerate when there is an odd number of electrons. This degeneracy is robust to crystal fields and spin-orbit coupling, and can only be lifted in the presence of an external magnetic field. Hence, in any material, a two-fold degenerate ground state in the absence of an external field immediately implies a Kramers degeneracy. For an even number of electrons, since this amounts to an integer total spin, the ground state is unique.

However, when a material consists of a degenerate ground state in the presence of an even number of electrons, it cannot be attributed to a Kramers origin. Hence, such degeneracies are aptly called “non-Kramers” degeneracies. Unlike Kramers doublets, non-Kramers doublets are an artifact of the crystal’s symmetry, and hence can be broken by a strong crystal distortion in addition to the presence of crystal fields.

### 8.2.1 Interpreting degeneracies in the presence of SOC

Consider the character table of a point-group  $G$  of any crystal. The left-most column indicates all irreducible representations of  $G$ , and the top row indicates all the symmetry operations (a detailed introduction to character tables can be found in Appendix A). The numbers that fill the table, that is, characters, essentially indicate how a particular irreducible representation behaves under a given symmetry operation. Of particular interest is the identity operation,  $E$ . The characters under this operation directly indicate the degeneracy of a particular irreducible representation. Hence, an  $E_g$  state is two-fold degenerate,  $A_g$  is singly degenerate,  $T_{2g}$  is triply degenerate, and so on. More importantly, the identity operation also indicates a  $2\pi$  rotation, which leaves the states unchanged.

In the presence of SOC, the stationary states of the system are classified by the quantum number  $J = L + S$ , the total angular momentum of the total momentum, since this is the conserved quantity, in contrast to spin and orbital angular momentum of the system.  $J$  can take a range of values,  $J = L + S, L + S - 1, \dots, |L - S|$ . In the case of an odd number of electrons,  $S$  is a half-integer, and hence  $J$  is also commensurately a half-integer. In accordance with Dirac’s relativistic description, it follows that half-integer angular momentum values are described not by simple functions, but by four-component bispinors, which are reduced to two-component spinors in quasirelativistic settings. Under symmetry operations, the two-component spinors, unlike simple functions, transform in a special way by realizing the so-called two-valued representations. As a result, for symmetry descriptions of molecular and solid-state electronic systems with half-integral angular momentum states, two-valued representations are needed in addition to conventional symmetry groups. Bethe [174] circumvented these difficulties by using groups  ${}^2G$  of twice the order of the ordinary crystallographic groups  $G$ .

Let us now take a closer look at how this can be done. Taking into account the way a spinor transforms under direct or inverse rotations, corresponding to the identity  $E$  of the single group there will be in the double group two operations  $E$  and  $\bar{E}$ . The operator  $\bar{E}$  changes only the sign

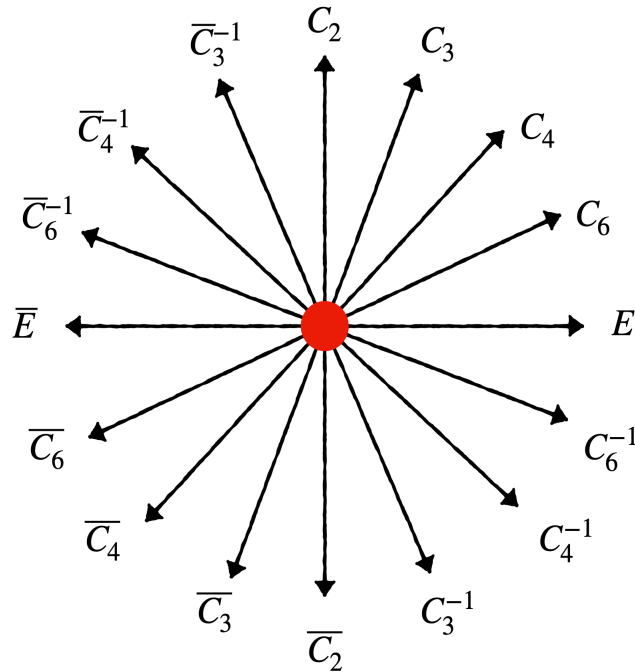


**Figure 8.3** – Schematic representation of double group operators. Illustration inspired by [178].

of the spinor. Similarly, each operation  $Q$  gives rise to the two operations:  $Q$  and  $\bar{Q} = \bar{E}Q$  [175, 176]. By applying the operation  $E$ , that is, a rotation through  $2\pi$ , we do not return to identity but obtain a change in the sign of the spinor. An additional rotation of  $2\pi$ , thus a total rotation of  $4\pi$  brings us back to the identity  $E$ . In particular,  $C_n^n = \bar{E}$ ,  $C_n^{2n} = E$ ,  $\sigma^2 = \bar{E}$ ,  $\sigma^4 = E$ , and so on [73]. As a result, considering the standard symmetry operators and the groups that can be constructed from them, we are led to the concept of double groups. Each crystallographic point group has a double group associated with it; hence, we have 32 double groups.

One can obtain the double group of  $G$  by using  $G$  as a starting point [177]. The relation between a pure rotation and its double group counterpart (or “barred” counterpart) can be visualized as shown in Fig. 8.3. It is set up in such a way that a  $2\pi$  rotation of the diagram implies a physical rotation of  $4\pi$ . This also means that a rotation of say  $R$ , supplemented with a  $\pi$  rotation in the diagram, results in its barred counterpart. Note that these operations still preserve the relationship  $RR^{-1} = I$  and  $\bar{R}\bar{R}^{-1} = I$  [178].

Hence, the core difference between an ordinary point group and a double group is the identity element  $E$ , which now means different things: Either a  $2\pi$  rotation in the case of integer angular momentum and a  $4\pi$  rotation for half-integer angular momentum. In such cases, irreducible representations of the double group corresponding to a crystal’s point group are used to label non-interacting energy levels of the crystal.

An example of a double group that is very common in transition metal crystals is the  $D_{3h}$  double group (Fig. 8.4(a)). The subscripts in  $E_{1/2}$ ,  $E_{3/2}$ , and  $E_{5/2}$  irreducible representations indicate the total angular momentum – the half-integer value implies the presence of an unpaired electron. Hence, these three irreducible representations are used in the case of odd electron fillings on a cluster, in the context of a cluster Mott insulator, for example, to label the non-

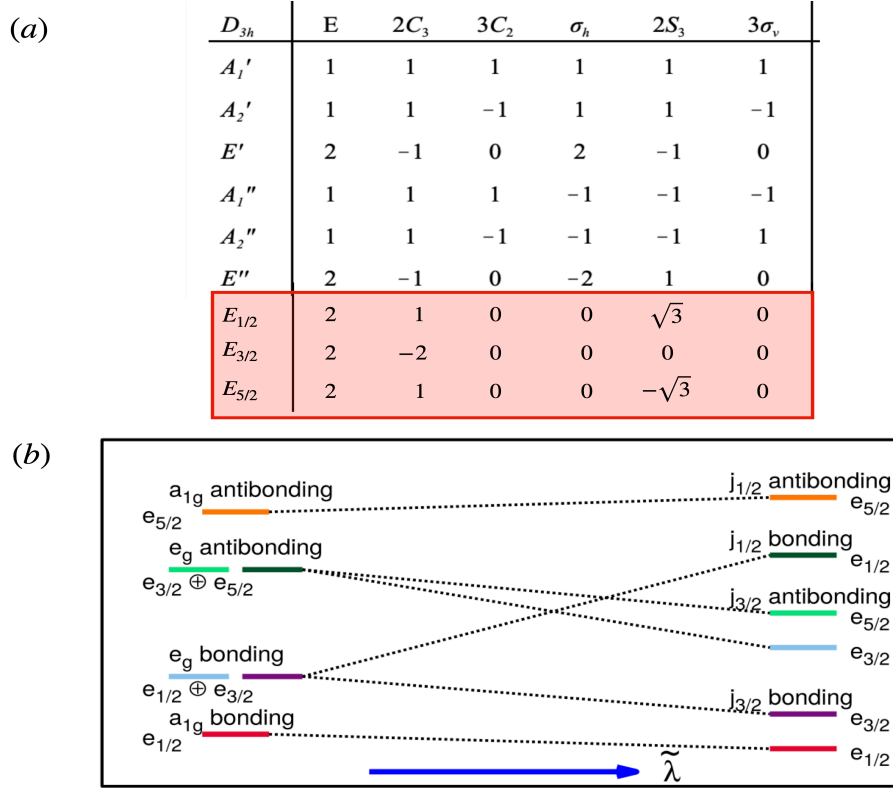


**Figure 8.4** – (a) The  $D_{3h}$  double group. The part highlighted in red consists of irreducible representations with a half-integer total angular momentum, indicated in their respective subscripts. (b) Double group irreducible representations are used to label energy levels in the non-interacting bandstructure of  $\text{M}_2\text{O}_9$  dimers. Illustration taken with permission from [108]. Copyright (2020) by the American Physical Society.

interacting levels with [108], as shown in Fig. 8.4(b). When there are no unpaired electrons – that is, in the case of an even number of electrons on the cluster, the doubly degenerate  $E'$  and  $E''$  irreducible representations indicate non-Kramers doublets.

### 8.3 Non-Kramers degeneracies in $\text{Ba}_4\text{LiIr}_3\text{O}_{12}$

Though Chen et. al proposed a mechanism to realize a state with non-zero total angular momentum, these were conjectures. The origin of magnetic signatures in  $\text{Ba}_4\text{LiIr}_3\text{O}_{12}$  was still not known. The collaboration between their group at McMasters and us came about to verify the source of magnetism in this cluster material, which was expected to have a non-magnetic ground state owing to its containing 8 electrons on the cluster. Using exact diagonalization and tracking the evolution of ground states over a wide parameter range, we concluded that the source of magnetism in  $\text{Ba}_4\text{LiIr}_3\text{O}_{12}$  is the presence of non-Kramers doublets.

In our analysis, we took into account the proposed range for Coulomb interaction  $U$ , Hund's coupling  $J_h$  and spin-orbit coupling  $\lambda$  as derived from various *ab-initio* studies for iridium cluster materials [179–181]. Using these *ab-initio* parameters as a reference, we conducted an intensive search for a doubly-degenerate ground state over a mesh of around  $6 \times 10^7$  parameter values, which, along with the quantities mentioned above, also took crystal fields and hoppings

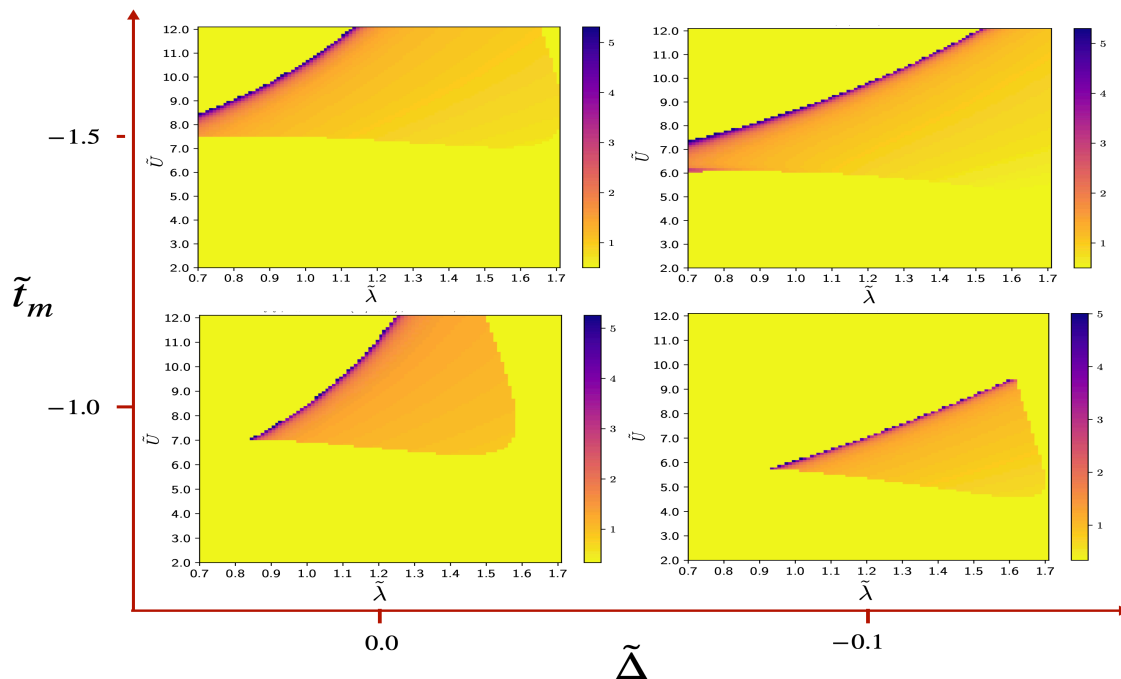


**Figure 8.5** –  $\tilde{U} - \tilde{\lambda}$  phase diagrams which show the values of  $\mu_{\text{eff}}$ . These are shown as a function of intra-orbital hopping  $\tilde{t}_m$  and crystal field splitting  $\tilde{\Delta}$ . Here, we have set  $\tilde{J}_h = 0.25\tilde{U}$ . In the parameter range relevant to iridium cluster materials, the regions hosting non-Kramers doublets are substantial for negative values of intra-orbital hoppings and crystal fields.

into consideration.

We find that there does exist an area of the parameter space that hosts non-Kramer’s doublets. These doublets belong to the  $E'$  irreducible representation of the  $D_{3h}$  point group. To track how the non-Kramers area varies, we considered some cuts in the parameter space, of which we have shown some of them here. Fig. 8.5 shows non-Kramers areas in terms of  $\mu_{\text{eff}}$  values, on  $\tilde{U} - \tilde{\lambda}$  phase diagrams, and how the area varies with hopping and crystal fields (here, all parameters have been scaled with respect to the inter-orbital hopping,  $t_{mn}$ . This is shown by a tilde over all parameters.) Note that, for these cuts, we used the parameter-space sweep to zero in on which values of spin-orbit coupling, crystal fields, and Hund’s couplings to consider, at which a substantial non-Kramers area could be shown. We observed from the extensive parameter sweep that the areas of non-Kramers doublets occupy substantial parameter space when hoppings are of opposite sign and for non-positive crystal fields; hence, these are the areas of choice to choose our fixed quantities from.

There are a few key observations to make here. Firstly, we see that a large region has  $\mu_{\text{eff}} \approx 0$ ; these are non-magnetic regions where the ground state is unique. The regions where the magnetic moment is non-zero are those that host non-Kramers doublets. Secondly, we see that in the doubly degenerate region, the magnetic moment takes a range of values. The expected window of around  $\mu_{\text{eff}} \approx 3.4 - 4.0$  forms a small part of the region; this area lies especially close to the phase boundary between the  $GSD = 1$  and the  $GSD = 2$  regions. At this phase boundary, the effective moment peaks and then saturates to a lower value before

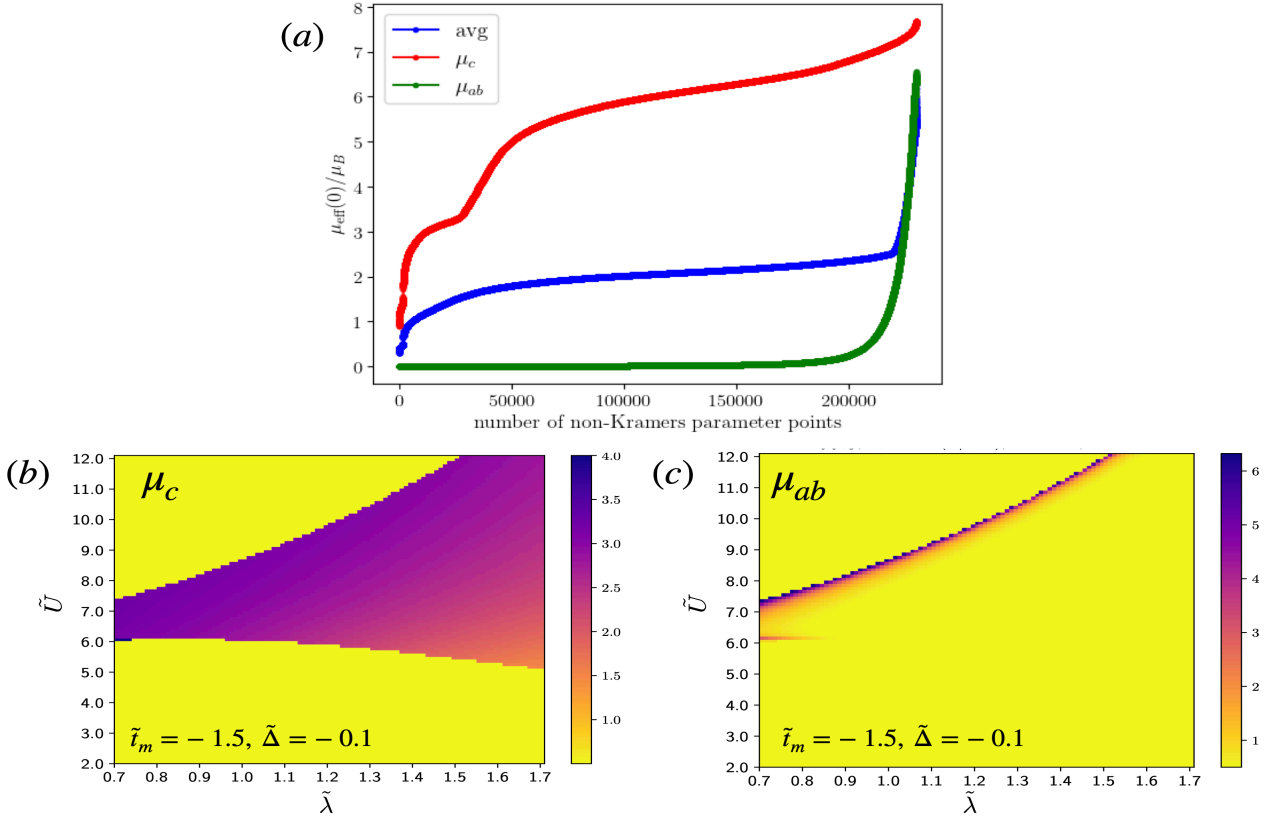


**Figure 8.6 – Composition of the obtained magnetic moments.** (a) Of the  $\approx 2 \times 10^7$  parameter points that host non-Kramers doublets, we see that very few of them have a  $\mu_{\text{eff}}$  close to the experimental value of  $\mu_{\text{eff}} \approx 3.4 - 4.0$ . We also see that for those that do lie in the range, the  $\mu_{ab}$  value shoots up, while its contribution is almost zero for the rest of the non-Kramers doublets. (b-c) This is further corroborated by tracking how  $\mu_c$  and  $\mu_{ab}$  change, in the respective phase diagrams. The material might hence lie on the very narrow strip in (c) where  $\mu_{ab}$  is substantial.

further decreasing to the lower right of the doubly degenerate region. Thus, the region we are looking for might precariously lie on the phase boundary between a magnetic and a non-magnetic region.

Next, we take a look at the composition of the magnetic moment. Fig. 8.6(a) shows contributions of  $\mu_c$  and  $\mu_{ab}$ , the components along and perpendicular to the crystallographic  $c$ -axis, respectively, to the effective moment. We observe that for a large number of non-Kramers parameter points, the contribution from  $\mu_{ab}$  is negligible, and all the observed magnetic moment comes from the part along the crystallographic  $c$ -axis. We use the phase diagrams Fig. 8.6(b-c) to find out where in the parameter space the region of negligible  $\mu_{ab}$  might lie. We observe that  $\mu_{ab}$  is negligible in the large non-Kramers region away from the phase boundary. However, near the phase boundary, it is the significant increase of the  $\mu_{ab}$  component that increases the overall effective moment. This also corroborates our observations in Fig. 8.5.

The second observation is that the doubly degenerate area has a spin  $S \approx 2$ , and an angular momentum  $L \approx 1$ , as seen in the phase diagrams for  $\langle S^2 \rangle$  and  $\langle L^2 \rangle$  in Fig. 8.7(a-b). Using these values and Eq. (8.2), we conclude that the ground state of  $J_{\text{eff}} \approx 1$  would be a more

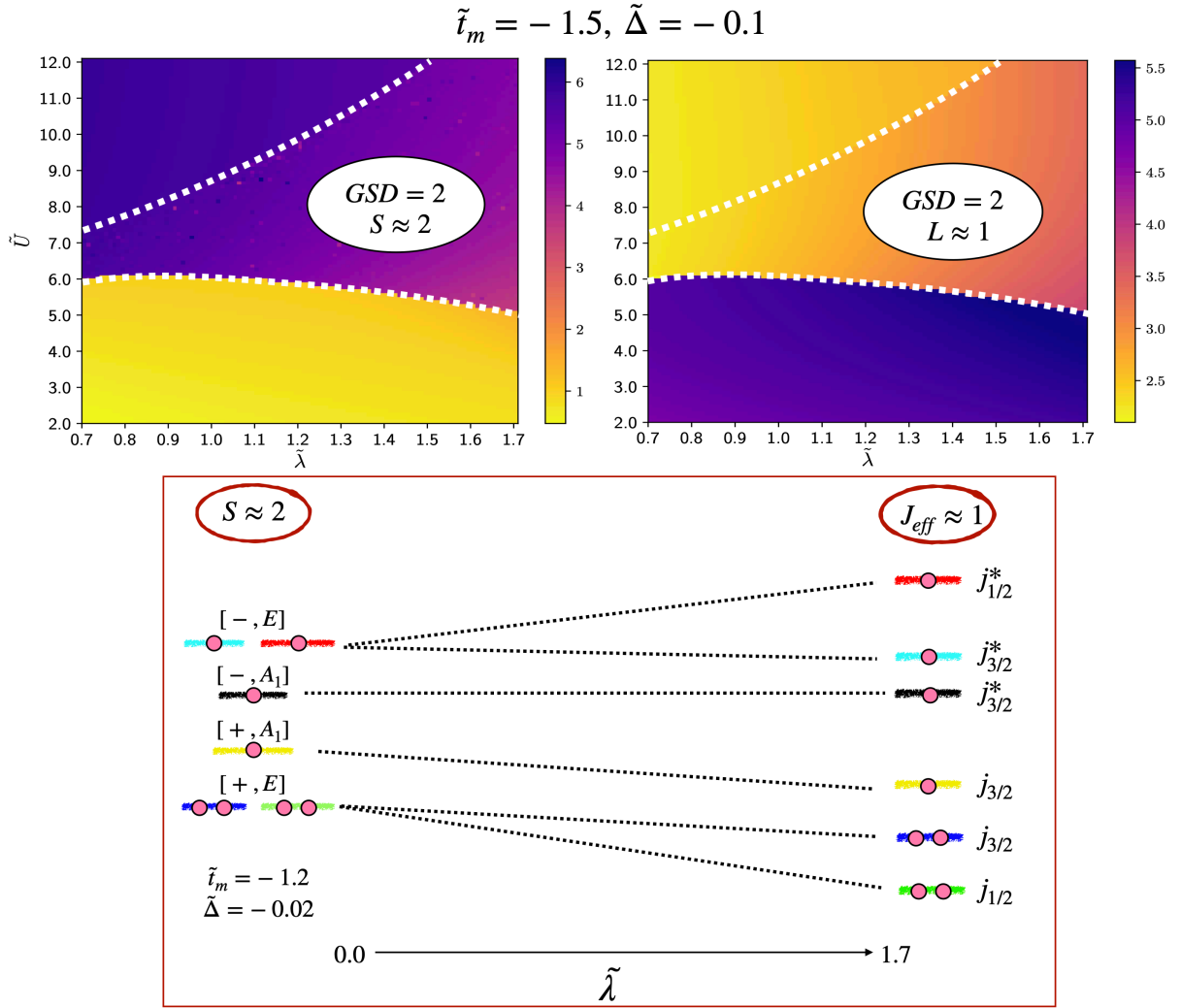


**Figure 8.7** – Quantum numbers for the non-Kramers region. (a-b) Tracking spin and angular momentum for the non-Kramers regions. We see that  $S \approx 2, L \approx 1$ . (c) Mechanism to realize a  $J_{\text{eff}} \approx 1$  ground state, starting from an  $S \approx 2$  state in the zero SOC limit.

suitable candidate for the ground state. Using these values for  $S, L, J$  and using Eq. (8.2) and Eq. (8.3), we get  $\mu_1 = 3.535$  and, in turn,  $\mu_{\text{eff}} = 4.0824$ . This is in very close agreement with the experimental value of  $\mu_{\text{eff}} = 4.17\mu_B$ .

We also proposed a mechanism for how a  $J_{\text{eff}} = 1$  might have been achieved, as shown in Fig. 8.7(c). On the left of this figure, we present a single-particle, non-interacting bandstructure with the given values of crystal fields and hoppings, in the absence of spin-orbit coupling. This would be a good description for energy levels in the low SOC region of the phase diagram. In the absence of SOC, a high-spin  $S = 2$  pocket exists in the intermediate Hund’s coupling region, as we saw in Fig. 6.16(a). With the introduction of spin-orbit coupling, this region hosts non-Kramers doublets, with  $J \approx 1$  being nominally achieved by placing a hole each on the  $j_{1/2}$  bonding level, two  $j_{3/2}$  antibonding levels, and the highest  $j_{1/2}$  bonding level. Here, we have made use of the  $j_{1/2} - j_{3/2}$  eigenstates to denote the energy levels in the presence of spin-orbit

coupling.

Using the value of  $J_{\text{eff}} \approx 1$  for the ground state, the magnetic entropy would be  $S = (4/3)R \ln 3 = 12.1784 \text{ J/mol-FU.K}$ , which is smaller than the experimental value of  $16.2 \text{ J/mol-FU.K}$ . This might indicate that the third iridium ion, assumed to be completely non-magnetic due so far, might not be so after all.

## 8.4 Non-Kramers degeneracies in other materials

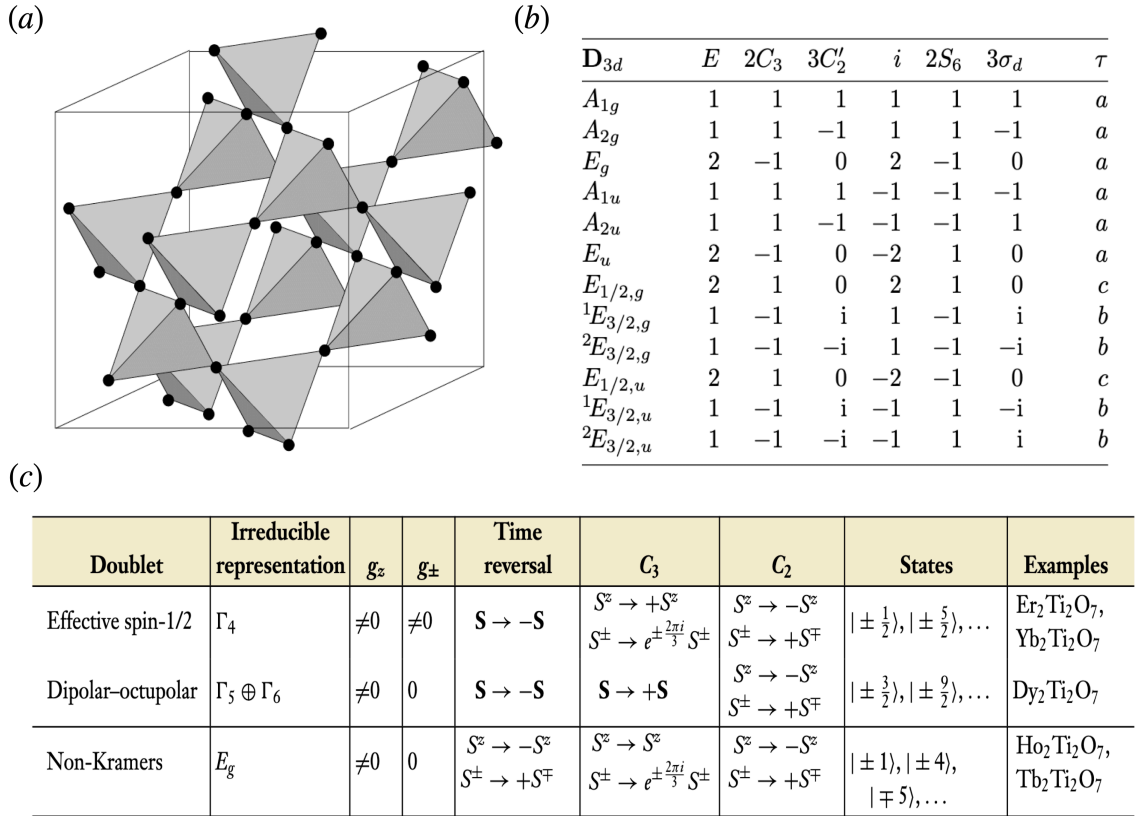


**Figure 8.8 – non-Kramers doublets in pyrochlores.** (a) Structure of a pyrochlore material. Image taken from [182]. (b) Character table of  $D_{3d}$  point group. Table taken from [183]. (c) Types of crystal field doublets in rare-earth pyrochlores. Note the difference in notation of doublets between this figure and the  $D_{3d}$  character tables. Figure adapted with permission from [182], Copyright (2010) Annual Reviews, Inc.

Through our collaborative work, we have thus demonstrated that non-Kramers degeneracies serve as sources of observed magnetism in  $\text{Ba}_4\text{LiIr}_3\text{O}_{12}$ . With this,  $\text{Ba}_4\text{LiIr}_3\text{O}_{12}$  has become the first cluster Mott material to host non-Kramers doublets. However, while the occurrence of non-Kramers doublets is novel and new in the context of cluster Mott materials, they have been previously observed and investigated in other classes of materials. The dimer material  $\text{Ba}_4\text{LiIr}_3\text{O}_{12}$  has a  $D_{3h}$  symmetry; another class of materials with a similar point group, which also hosts non-Kramers doublets, are pyrochlore rare-earth materials.

Frustrated and highly anisotropic rare-earth pyrochlores hence lend themselves to closer scrutiny in this section. The pyrochlore crystal structure consists of atoms that are arranged

to form a lattice of tetrahedra joined at each corner (Fig. 8.8(a)). In this case, the hierarchy of competing interactions is very clear-cut, with Coulomb interactions dominating over spin-orbit coupling, which, in turn, dominates over crystal fields. As per the rules and mechanisms discussed in Chapter 7, this means that spin-orbit coupling splits the energy manifold into levels with different total angular momenta. The crystal field splits the levels further, till we are left with a two-fold degenerate ground state. In case of an integer- $J$ , the only way a doublet ground state can be realized in the presence of crystal fields and SOC is if it is non-Kramers in nature [182].

This becomes clear when we take a closer look at the pyrochlore lattice. The pyrochlore case corresponds to the  $D_{3d}$  site symmetry. In the non-interacting limit, we are mostly left with doublets in the bandstructure. Each of these doublets can be classified in terms of the irreducible representations of  $D_{3d}$  and its double group. Using Fig. 8.8(b), we can deduce that three distinct types of these doublets are possible:  $E_g$ ,  $E_{1/2,*}$  and  $\bigoplus_r E_{3/2,*}$  (where  $* \in \{u, g\}, r \in \{1, 2\}$ ), with the first being non-Kramers and the rest being Kramer's doublets. These doublets are shown in Fig. 8.8(c). Note that the third doublet is built using two one-dimensional irreducible representations.

In the same vein, another group of materials that are similar in structure to the dimer material  $\text{Ba}_4\text{LiIr}_3\text{O}_{12}$  are materials of the type  $\text{Ba}_2\text{MOsO}_6$ . These materials are double perovskites, and hence lie in the larger perovskite class of materials. They were shown to be  $d$ -orbital based single-atom Mott insulators, which host antiferromagnetically coupled  $5d^2$   $\text{Os}^{6+}$  ions decorating a face-centered cubic (fcc) lattice. Given a perfectly cubic lattice, the ground state of these materials is a non-Kramers  $E_g$  doublet, which hosts quadrupole and octapole moments [184–188].

## 8.5 Conclusion

In conclusion, we studied the character and origin of the observed non-zero magnetic moment in  $\text{Ba}_4\text{LiIr}_3\text{O}_{12}$ . Through a vast parameter sweep, it was seen that there is a finite area of non-Kramers doublets, but only a small portion of the parameter space we considered hosted doublets whose effective magnetic moment was close to the experimental value. Moreover, this region lay very close to a phase boundary and was marked by an enhanced moment perpendicular to the crystallographic  $c$ -axis. Experimental measurement of  $\mu_{ab}$  would hence serve as a good diagnostic tool to confirm whether the material indeed lies close to such a phase boundary. If  $\mu_{ab}$  is not as large as our studies expect, this would also indicate that the material might lie outside the parameter space we have considered. Since all experimental measurements so far have been done using a powder sample, measuring  $\mu_{ab}$  might not be straightforward. As an outlook, the availability of single crystals of the material will pave the way to a better agreement between observations and theory. We also suspect that there might be additional contributions to the magnetic entropy from the third iridium ion. Experiments that can concretely estimate the role of this iridium ion in the material would also bring about a better understanding of the ground states of  $\text{Ba}_4\text{LiIr}_3\text{O}_{12}$ .

We briefly surveyed pyrochlores rare-earths, an adjacent class of materials that can also host non-Kramers doublets. Similar to how these doublets were responsible for a large magnetic moment in  $\text{Ba}_4\text{LiIr}_3\text{O}_{12}$ , they are responsible for the quadrupolar moments observed in pyrochlores. Non-Kramers doublets were also shown to respond differently to structural disorder in certain pyrochlores. Such non-Kramers degeneracies have been a long-standing subject of early theoretical and experimental studies [189–193], but they have also found renewed interest ever since having been recently observed in a variety of materials, such as cage compounds [194–198], triangular lattice antiferromagnets [199, 200], and pyrochlores [182, 201], among others [202, 203]. The discovery of non-Kramers doublets in  $\text{Ba}_4\text{LiIr}_3\text{O}_{12}$  opens the doors to exploring their fingerprints in many more such cluster materials in the future.



# Properties of materials with $M_3O_{12}$ trimer clusters

In the previous chapters, we have made progress on understanding cluster Mott insulators using a bottom-up approach. Firstly, we set out to understand what cluster Mott insulators are from a material and theoretical perspective in Chapter 4, and secondly, we studied how the interplay between various terms in the governing Hamiltonian results in the observed phase diagrams for various fillings, and thus established some essential building blocks for the same in Chapter 6. In Chapter 7, we also introduced ingredients such as crystal field splitting and spin-orbit coupling, that are essential for the observed physics of cluster Mott candidate materials.

In this chapter, we study cluster Mott materials with trimer clusters, most of which have been synthesized, but not much theoretical work exists on them as of now. We shall combine the framework we have built so far with material-specific factors, to gain some insight into their ground states.

*This chapter is based on publication [U1], which is currently a work in progress at the time of writing. The parts for which the author of this thesis is responsible are presented below.*

## 9.1 Survey of materials

Trimer cluster materials synthesized so far are generally 12H hexagonal perovskites of the form  $A_4BM_3O_{12}$ . Here, M is the transition metal ion, which can range from being  $3d$  to  $5d$ . While the A cation in materials so far has been barium, B can be any rare-earth ion. The trimers are made of three face-sharing  $M_3O_{12}$  octahedra. While the stacking sequence of different layers in the material determines magnetic interaction paths, the size of the B cation contributes to the extent of distortion of the crystal.

The earliest trimer cluster materials were synthesized by Shimoda et al. [204], which had ruthenium trimers in combination with a range of lanthanides. For lighter lanthanides (B = La – Gd) the crystals have a monoclinically distorted cell, whereas for heavier lanthanides, the materials have a hexagonal unit cell, as shown in Fig. 9.1. It was found that for B = Ce, Pr and Tb, the B cation is tetravalent, and the ruthenium ion was also tetravalent in nature; while no magnetic anomaly was observed in  $Ba_4CeRu_3O_{12}$  down to 0.5K (due to the nonmagnetic ground state ( $J = 0$ ) of the  $Ru_3O_{12}$  trimer), it was seen that trimer materials with Pr and Tb (that is,  $Ba_4PrRu_3O_{12}$  and  $Ba_4TbRu_3O_{12}$ ) displayed antiferromagnetic ordering.

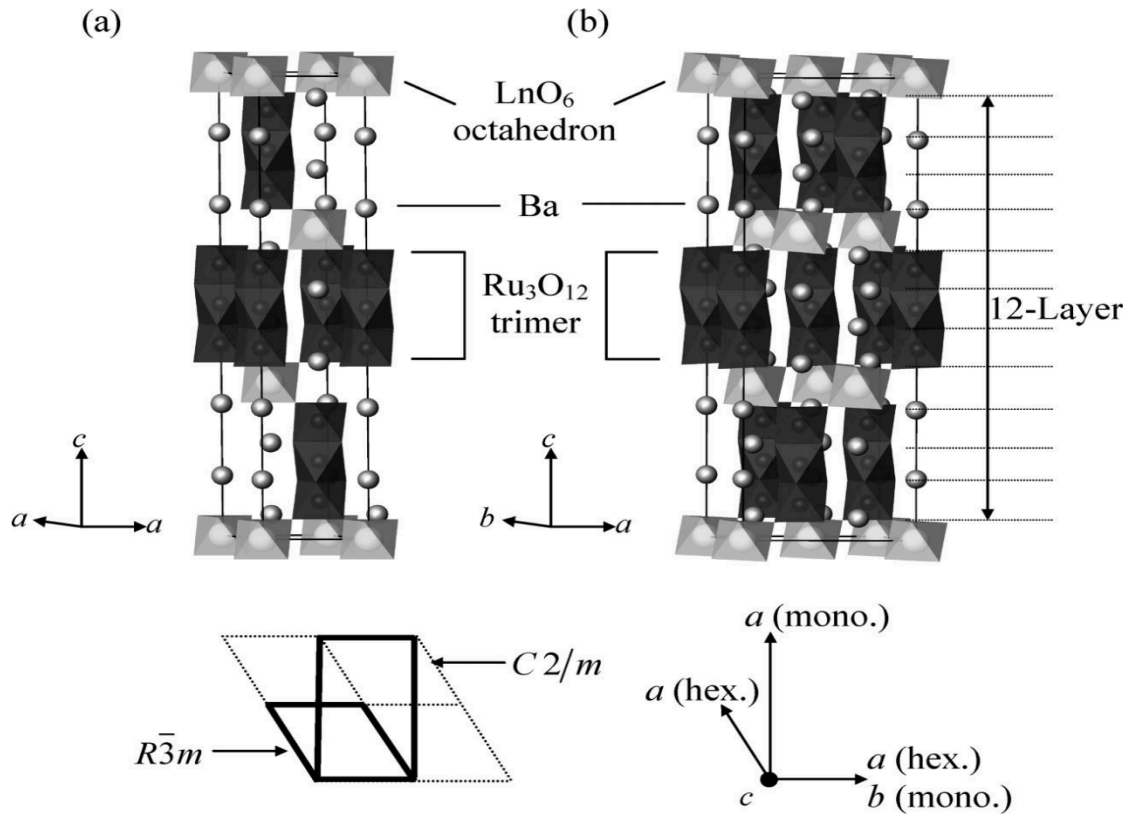


**Figure 9.1** – Crystal structure of different ruthenium trimer materials. (a) Materials with heavier lanthanide ions have a hexagonal unit cell, whereas (b) materials with lighter lanthanide ions have a monoclinic unit cell. Images adapted with permission from [204]. Copyright(2008) American Chemical Society.

However, the valency of the transition metal ion and the  $B$  cation can also take other values, resulting in different observed physical and ground-state properties. For example, Shimoda et al. also later synthesized the  $\text{Ba}_4\text{EuM}_3\text{O}_{12}$  group of materials with  $M=\text{Ir}, \text{Ru}$ , where the  $B=\text{Eu}$  cation was found to be trivalent in nature [205]. This commensurately also changed the oxidation states of the transition metal ions as well: it was seen that the  $M$  ion is in a mixed-valence state between +4 and +5, and that its average oxidation state is +4.33. Though these two compounds have a virtually identical crystal structure, they display different magnetic properties. In the case of  $\text{Ba}_4\text{EuIr}_3\text{O}_{12}$ , experimental measurements of magnetic susceptibilities pointed towards the possibility of the presence of tiny amounts of paramagnetic impurities, because the Curie constant  $C$  was found to be significantly smaller than the theoretical value (0.375 emu/mol) for a localized system of spins with  $S = 1/2$  [205]. This led to the conjecture that the ground state of the  $\text{Ir}_3\text{O}_{12}$  trimer might be nonmagnetic. On the other hand, with a non-zero magnetic moment of  $\mu_{\text{eff}} = 1.18\mu_B$ , the magnetic interactions between ruthenium trimers in  $\text{Ba}_4\text{EuRu}_3\text{O}_{12}$  showed indications of being antiferromagnetic in nature.

A significant progress on the experimental front was made when Cava et al. synthesized the  $\text{Ba}_4\text{NbM}_3\text{O}_{12}$  class of materials [111, 206], and by doing so, showed that the  $B$  cation need not have to be a lanthanide for the material to host transition metal trimer clusters in such perovskite materials [110, 207–210]. These materials have a rhombohedral structure, in

contrast to the family of materials  $\text{Ba}_4\text{LnM}_3\text{O}_{12}$  with a tetravalent lanthanide cation, synthesized by Shimoda et al. However, the individual  $\text{NbO}_6$  octahedra and  $\text{M}_3\text{O}_{12}$  trimers in these  $\text{Ba}_4\text{NbM}_3\text{O}_{12}$  phases alternate along the  $c$ -axis to generate the 12-layer stacking sequence similar to the lanthanide case.

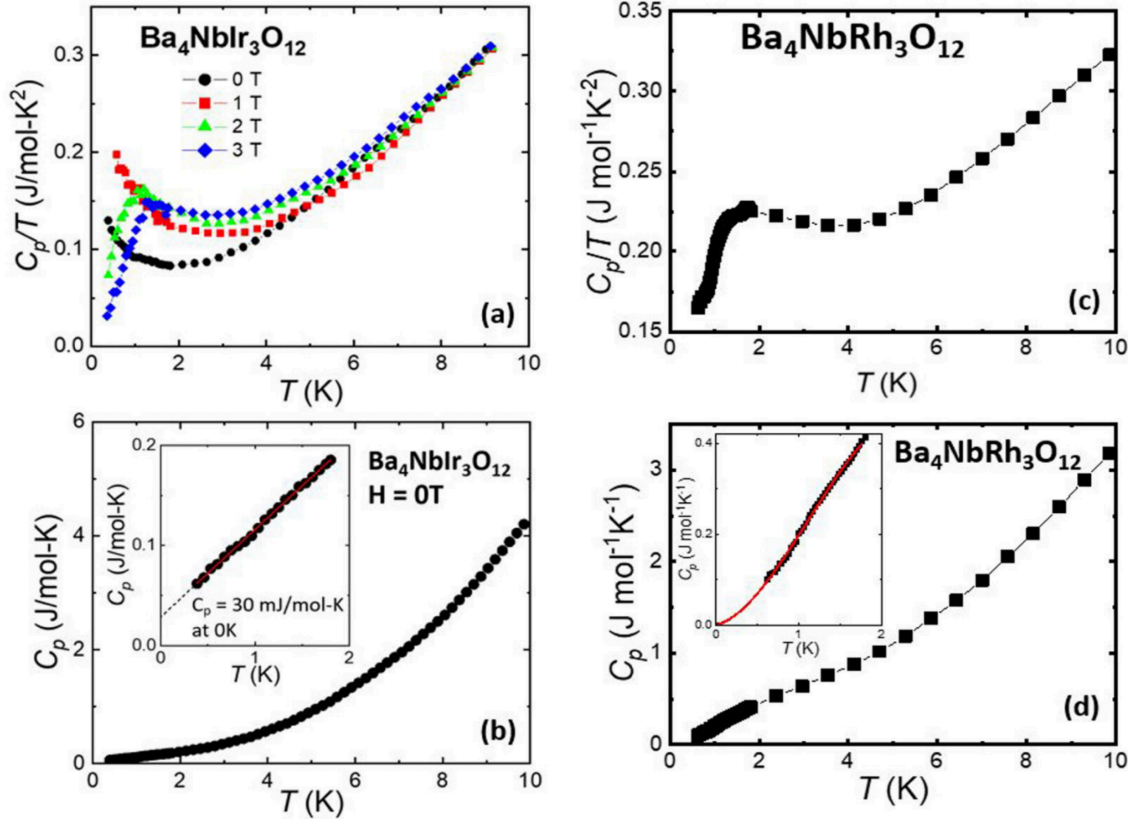


**Figure 9.2** – Comparison of low-temperature molar heat capacities divided by temperature. It is shown here for (a)  $\text{Ba}_4\text{NbIr}_3\text{O}_{12}$ . The upturn, marked in red, at a field of 1 T suggests that it might be a candidate spin liquid. This is in contrast to that of (c)  $\text{Ba}_4\text{NbRh}_3\text{O}_{12}$ . Molar heat capacities have been plotted against temperature for the two materials in (b) and (d). Images adapted with permission from [211]. Copyright (2019) by the American Physical Society.

Synthesis of trimer materials with a niobium cation opened up yet another possible valency for both the B cation and the transition metal ions, with the niobium cation in these materials being pentavalent ( $\text{Nb}^{5+}$ ) and non-magnetic in nature. The average valence of the transition metal ion (Rh/Ir) is +3.67 without the presence of any fractional valence in these materials, which is also a feature distinct from the lanthanide case. However, materials in which the transition metal ion had the same oxidation state behaved differently. For example, specific heat studies of the materials  $\text{Ba}_4\text{NbIr}_3\text{O}_{12}$  and  $\text{Ba}_4\text{NbRh}_3\text{O}_{12}$  showed widely different outcomes, as is evident in Fig. 9.2. The specific heat curve for the rhodium case shows at least some signatures of magnetic ordering down to 1.5K. In contrast, the upturn of specific heat in the case of iridium is suppressed by the applied field, a signature of lack of magnetic ordering which has been displayed by spin liquid candidate materials in the past [119, 212, 213]. Hence, the iridium trimer material was proposed as a promising spin liquid candidate [211].

Another recent spin liquid candidate is the rhodium trimer material  $Ba_4NbRh_3O_{12}$ . Susceptibility measurements show it has an effective moment of  $\mu_{\text{eff}} = 0.73-0.8\mu_B/\text{Rh}$ , and even though there are considerable antiferromagnetic interactions between these local rhodium moments, specific heat measurements show an absence of magnetic ordering down to 50 mK. Moreover, temperature dependent magnetic specific heat measurements also indicate the presence of a spinon Fermi surface [209].

However, spin liquid ground states are not the only ground states that these trimer materials are conjectured to host. A recent experimental study on the trimer material  $Ba_4Nb_{1-x}Ru_{3+x}O_{12}$ , where  $|x| < 0.2$ , was carried out for various concentrations of the B cation and the transition metal ion by Cao et al. [214]. Combining insights from specific heat, susceptibility, resistivity and conductivity measurements, they conjectured the discovery of an unusual spinon Fermi surface made of charge-neutral spinons, that underpins both a heavy-fermion strange metal and a quantum spin liquid.

Drastically different behavior is observed when  $4d$  or  $5d$  transition metal ions are replaced by manganese, a  $3d$  transition metal ion. Compared to the entire family of trimer materials, which, like most transition metal compounds, have considerable spin-orbit coupling, the manganese trimer material  $Ba_4NbMn_3O_{12}$  has negligible spin-orbit coupling. Studies showed the material might consist of ferromagnetic manganese trimer layers, stacked antiferromagnetically. It was shown that the intra-cluster interactions are not strong enough to localize the electrons on these trimers, and that it might be better described as a conventional Mott insulator where electrons are localized on individual manganese ions [110, 111].

In general, trimer materials lend themselves to hosting a wide variety of ground states, similar to their cousin, the  $M_2O_9$  dimer family. Extensive experimental and theoretical work has been done regarding these dimers, and one of the defining features of  $M_2O_9$  dimers is that there is a higher likelihood of the net magnetic moment of these dimers being zero. For example, in the case of  $S = 1/2$  on each site,  $S_{\text{dimer}} = S_1 + S_2 = 0$ . Unlike the dimer case, the net magnetic moment of individual  $M_3O_{12}$  trimers in this case cannot vanish, that is  $S_{\text{trimer}} = S_1 + S_2 + S_3 \neq 0$ , and hence we might expect to see an even wider range of physical properties in  $M_3O_{12}$  trimer materials [215].

The sheer number of trimer materials that have been synthesized and await a more systematic analysis is the primary motivation behind this work. Here, we first look into the structure of the single particle, non-interacting part of the Hamiltonian governing these materials. We use insights from it to explore the phase diagrams for some of these materials.

## 9.2 Structure and Hamiltonian particulars

Fig. 9.3 shows the structure of a trimer functional unit. The trimer unit is formed of three transition metal ions, which are surrounded by oxygen ligands. The oxygen ions give rise to an octahedral ligand field, as a result of which the trimer cluster consists of three face-sharing octahedra stacked on top of each other, with the transition metal ions in the center of each of these octahedra. This gives rise to a  $D_{3h}$  point group symmetry for the trimer, though the

individual atoms themselves have a  $D_{3d}$  symmetry. The two outer metal ions, shown in orange, are equivalent. The middle ion, shown in blue, transforms trivially under inversion, in contrast to the outer ions. The local coordinates for the outer ions are defined in the basis of the global coordinates as:

$$R_o = \begin{pmatrix} -1/\sqrt{6} & -1/\sqrt{2} & -1/\sqrt{3} \\ -1/\sqrt{6} & 1/\sqrt{2} & -1/\sqrt{3} \\ \sqrt{2/3} & 0 & -1/\sqrt{3} \end{pmatrix}, \quad (9.1)$$

whereas the local coordinates for the middle ion is defined as

$$R_m = \begin{pmatrix} 1/\sqrt{6} & 1/\sqrt{2} & -1/\sqrt{3} \\ 1/\sqrt{6} & -1/\sqrt{2} & -1/\sqrt{3} \\ -\sqrt{2/3} & 0 & -1/\sqrt{3} \end{pmatrix}. \quad (9.2)$$

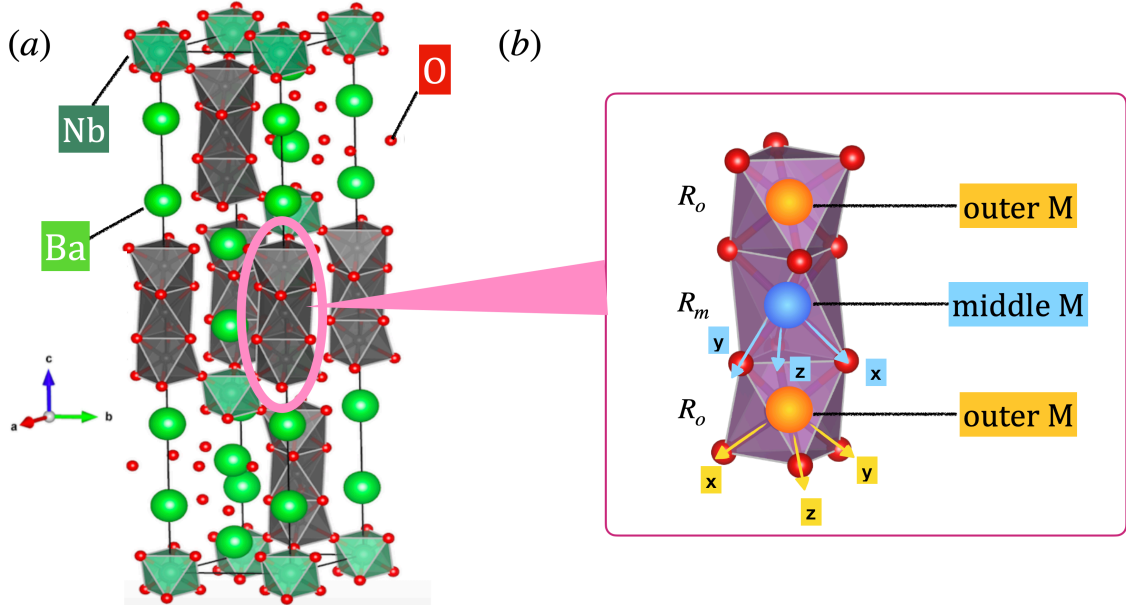


**Figure 9.3 – Structure of  $Ba_4NbM_3O_{12}$  materials.** (a) Crystal structure of  $Ba_4NbM_3O_{12}$ . The trimer units are shown in grey. The red balls denote oxygen ligands, whereas the  $B$  cation is shown in dark green. The  $A$  cation, usually Barium, is shown as light green balls. Image adapted with permission from [181]. Copyright (2020) by the American Physical Society. (b) Trimer unit zoomed in. It consists of three  $M$  ions, with the outer ions shown in orange and the middle ion shown in blue. Local coordinates for each ion is also shown.

### 9.2.1 Interactions and hopping

The governing Hamiltonian consists of four essential parts:

$$H = H_{\text{int}} + H_{\text{hop}} + H_{CF} + H_{SOC}, \quad (9.3)$$

where  $H_{\text{int}}$  is the Hubbard-Kanamori interaction Hamiltonian

$$\begin{aligned}
 H_{\text{int}} = \sum_i \left( U \sum_m n_{im\uparrow} n_{im\downarrow} + U' \sum_{m \neq n} n_{im\uparrow} n_{in\downarrow} + (U' - J) \sum_{m \neq n, \sigma} n_{im\sigma} n_{in\sigma} \right. \\
 \left. - J \sum_{m \neq n} c_{im\uparrow}^\dagger c_{in\downarrow}^\dagger c_{im\downarrow} c_{in\uparrow} + J \sum_{m \neq n} c_{im\uparrow}^\dagger c_{im\downarrow}^\dagger c_{in\downarrow} c_{in\uparrow} \right). \quad (9.4)
 \end{aligned}$$

Here,  $i$  labels the sites,  $m, n \in \{xy, yz, zx\}$  label the physical  $t_{2g}$  orbitals. The terms hold their usual meanings as discussed in Chapters 4 and Chapter 6. With regards to the hopping, the hopping Hamiltonian  $H_{\text{hop}}$  is given by

$$H_{\text{hop}} = H_{xyz}^{\text{hop}} = -t_m \sum_{im\sigma} c_{im\sigma}^\dagger c_{jm\sigma} - t_{mn} \sum_{i\sigma, m \neq n} c_{im\sigma}^\dagger c_{jn\sigma}, \quad (9.5)$$

where

$$\mathbf{c}_{i\sigma}^\dagger = (c_{xy}^\dagger, c_{yz}^\dagger, c_{zx}^\dagger)_{i\sigma}. \quad (9.6)$$

To make the mechanism of  $t_m$  and  $t_{mn}$  more explicit, let us write it out in matrix form. Eq. (9.5) would hence read as

$$H_{xyz}^{\text{hop}} = \sum_{i\sigma} -c_{i\sigma}^\dagger \begin{pmatrix} t_m & 0 & 0 \\ 0 & t_m & 0 \\ 0 & 0 & t_m \end{pmatrix} \mathbf{c}_{j\sigma} - c_{i\sigma}^\dagger \begin{pmatrix} 0 & t_{mn} & t_{mn} \\ t_{mn} & 0 & t_{mn} \\ t_{mn} & t_{mn} & 0 \end{pmatrix} \mathbf{c}_{j\sigma}. \quad (9.7)$$

As we saw in Chapter 7, local trigonal distortions split the  $t_{2g}$  levels into  $a_{1g}$  and  $e_g$  levels. Consequently, single particle energy levels in literature, especially in *ab-initio* studies, are generally labeled in terms of these irreducible representations of the resulting local crystal symmetry, which is  $D_{3h}$  in our case, and the hoppings are also expressed in this basis. Hence, it is necessary to draw a correspondence between the two.

The hopping Hamiltonian in the  $\{a_{1g}, e_{g1}, e_{g2}\}$  basis is:

$$H_{a_{1g}-e_g}^{\text{hop}} = \tilde{\mathbf{c}}_{i\sigma}^\dagger \begin{pmatrix} t_\sigma & 0 & 0 \\ 0 & t_\pi & 0 \\ 0 & 0 & t_\pi \end{pmatrix} \tilde{\mathbf{c}}_{j\sigma}, \quad (9.8)$$

where

$$\tilde{\mathbf{c}}_{i\sigma}^\dagger = (c_{a_{1g}}^\dagger, c_{e_{g1}}^\dagger, c_{e_{g2}}^\dagger)_{i\sigma}. \quad (9.9)$$

Here,  $t_\sigma$  is the hopping between  $a_{1g}$  orbitals of site  $i$  and  $j$ , and  $t_\pi$  is the hopping between the two  $e_g$  orbitals of site  $i$  and  $j$ . In contrast to the hoppings in the  $t_{2g}$  basis, which consisted of a diagonal component (intra-orbital hopping) and an off-diagonal component (inter-orbital hopping), we see that hoppings in the  $a_{1g} - e_g$  basis are entirely diagonal: there is no mixing of  $a_{1g}$  and  $e_g$  orbitals. We obtain  $(t_m, t_{mn})$  in terms of  $(t_\sigma, t_\pi)$  when we do a basis transformation to go from  $\{a_{1g}, e_{g1}, e_{g2}\}$  basis to  $\{xy, yz, zx\}$ . We thus get

$$H_{xyz}^{hop} = \frac{1}{3} \mathbf{c}_{i\sigma}^\dagger \begin{pmatrix} (2t_\pi + t_\sigma) & (t_\sigma - t_\pi) & (t_\sigma - t_\pi) \\ (t_\sigma - t_\pi) & (2t_\pi + t_\sigma) & (t_\sigma - t_\pi) \\ (t_\sigma - t_\pi) & (t_\sigma - t_\pi) & (2t_\pi + t_\sigma) \end{pmatrix} \mathbf{c}_{j\sigma}. \quad (9.10)$$

Comparing Eq. (9.5) and Eq. (9.10), we get

$$t_m = -\frac{(2t_\pi + t_\sigma)}{3}, t_{mn} = \frac{(t_\pi - t_\sigma)}{3}. \quad (9.11)$$

The hopping Hamiltonian in the  $\{a_{1g}, e_{g1}, e_{g2}\}$  basis in terms of  $t_m$  and  $t_{mn}$  will now look like:

$$H_{a_{1g}-e_g}^{hop} = \tilde{\mathbf{c}}_{i\sigma}^\dagger \begin{pmatrix} (2t_{mn} + t_m) & 0 & 0 \\ 0 & t_m - t_{mn} & 0 \\ 0 & 0 & t_m - t_{mn} \end{pmatrix} \tilde{\mathbf{c}}_{j\sigma}. \quad (9.12)$$

From here we can see that

$$t_\sigma = (2t_{mn} + t_m), t_\pi = (t_m - t_{mn}). \quad (9.13)$$

## 9.2.2 Crystal fields and spin-orbit coupling

We have seen previously that the trimer consists of an octahedral crystal field. Trimer materials usually possess a trigonal distortion. Hence, the crystal field term is restricted to the trigonal form:

$$H_{CF} = - \sum_{i\sigma} \mathbf{c}_{i\sigma}^\dagger \begin{pmatrix} 0 & \Delta & \Delta \\ \Delta & 0 & \Delta \\ \Delta & \Delta & 0 \end{pmatrix} \mathbf{c}_{i\sigma}. \quad (9.14)$$

Note that the crystal fields remain unaltered irrespective of the basis in which they are expressed.

As mentioned in section 7.2, in order to express spin-orbit coupling in terms of local orbital definitions, it is necessary to transform the spin operator  $\mathbf{S}_i$  written in global coordinates on each site, to local coordinates,  $\mathbf{S}'_i$ . We recall from Eq. (7.16), that the spin-orbit coupling then takes the form

$$\begin{aligned} H_{SOC} &= \sum_i \mathbf{L}_i \cdot \mathbf{S}'_i \\ &= \frac{i}{2} \sum_i \epsilon_{\alpha\beta\gamma} R_{i\alpha\nu} c_{i\nu\sigma}^\dagger \tau_{\sigma\sigma'}^\nu c_{i\beta\sigma'}, \end{aligned} \quad (9.15)$$

where the rotation matrices for the three sites are given by Eq. (9.1) and Eq. (9.2).

### 9.2.3 Parameter selection

Motivated by the synthesis and experimental observations of  $M_3O_{12}$  trimers with niobium, Khomskii et al. carried out *ab-initio* calculations of the electronic structures of iridium, rhodium and manganese trimer materials [181]. Our selection of the parameter space in this work is based on the values given by these *ab-initio* studies. The parameter choice we work with is given below:

Test Material	$\tilde{U}$ range	$\tilde{J}_h$	$\tilde{\lambda}$ range	$\tilde{\Delta}_m$	$\tilde{\Delta}_o$	$\tilde{t}_m$
Mn-like	0.0 - 30.0	0-10.0	0.0	-0.15	-0.1	0.125
Rh-like	0.0 -15.0	$0.2U$	0.0 -1.5	0.7	0.0	-0.2

**Table 9.1** – Final choice of sample parameters used in the chapter, for different trimer materials.

Note that this is all in the  $\{xy, yz, xz\}$  basis. These quantities have all been scaled by the inter-orbital hopping  $t_{mn}$ , and this is indicated by the hats on top of all parameters.

There are a few observations to make here. There exist two broad “categories” of materials: In rhodium-like materials (which encompass materials with rhodium, ruthenium or iridium trimers), the spin-orbit coupling is substantial. Hence, it plays an important role in determining ground state properties in these materials. This is in contrast to the manganese case, where, by virtue of being a  $3d$  transition metal, spin-orbit coupling plays a negligible role. Hence, the properties of manganese materials are determined largely by interactions rather than spin-orbit coupling. The second distinction is in the crystal fields: in the rhodium case, only the middle site in the trimer experiences crystal fields, whereas the outer sites are unaffected; this is in contrast to the manganese case, where all three trimer sites experience similar magnitudes of crystal fields. This, as we will see in the subsequent sections, will impact how the non-interacting energy levels in both cases split.

## 9.3 Single-particle sector and molecular orbitals

While analyzing the single-particle non-interacting limit of the Hamiltonian, we take into account the fact that every atom constituting the trimer possesses a  $D_{3d}$  symmetry. Hence, the non-interacting energy levels are labeled according to the irreducible representations of the  $D_{3d}$  point group. The character table for  $D_{3d}$  can be found in Appendix A.

### 9.3.1 Zero SOC

In the absence of SOC, the local trigonal crystal field splits the  $t_{2g}$  orbitals present on each site into a singly degenerate  $a_{1g}$  and doubly degenerate  $e_g$  levels (see Fig. 9.4). As seen in the last section, the hoppings in the  $\{xy, yz, xz\}$  basis consist of a diagonal part (intra-orbital  $t_m$ ) and an off-diagonal part (inter-orbital  $t_{mn}$ ). However, hoppings are diagonal in the  $\{a_{1g} - e_g\}$  basis (as shown in Eq. (9.8)). Because of this purely diagonal hopping, the  $a_{1g}$  and  $e_g$  levels on the three sites of the trimer give rise to bonding, anti-bonding, and non-bonding molecular orbitals on the cluster, as shown in Fig. 9.4(b). Note that the atomic  $t_{2g}$  orbitals are written

in the  $\{a_{1g} - e_g\}$  basis to understand the resultant molecular orbitals better, though there are no crystal field terms explicitly introduced to split the  $t_{2g}$  atomic orbitals into  $a_{1g}$  and  $e_g$ .

The non-bonding molecular orbitals are special in that only the outer sites (denoted by “o”) are involved in their formation, whereas all three sites participate in the formation of bonding and anti-bonding orbitals. The main feature which distinguishes the trimer from a dimer cluster is that the dimer sites are identical to each other (with respect to the physics). However, the addition of an extra site now gives rise to two kinds of sites on the trimer: the middle site, and the outer site. It is the combination of contributions from these two types of sites that results in bonding, anti-bonding, and non-bonding molecular orbitals. Because of the nature of the two types of sites on the trimer, they respond differently to the application of crystal fields, which can be seen in Table 9.1.

Another interesting feature to note is that the  $a_{1g}$  orbitals on each of the sites result in one bonding, one anti-bonding and one non-bonding  $A_{1g}$  molecular orbital, and similarly, the  $e_g$  orbitals on each of the sites result in one pair of bonding, one pair of anti-bonding and one pair of non-bonding  $E_g$  molecular orbitals. This is, again, because the hoppings are diagonal in the  $\{a_{1g} - e_g\}$  basis. To distinguish them from their atomic counterparts, the molecular orbitals are denoted in uppercase. This convention is similar to that mentioned in section 7.1.

Note the similarities and differences between Fig. 9.4(a) and Fig. 9.4(b): while the former is written in the  $\{xy, yz, xz\}$  basis, the latter is written in the  $\{a_{1g} - e_g\}$  basis. The splitting in the energy levels in the former is due to the presence of a non-zero  $t_{mn}$ , without which we would have three energy levels, each of which are three-fold degenerate. The splitting in energy levels in the latter is due to the fact that the inter-site  $t_\sigma$  hopping between  $a_{1g}$  orbitals is different from the inter-site  $t_\pi$  hopping between  $e_g$  orbitals. The split in the energy levels is hence proportional to the difference between the two, that is  $t_\sigma - t_\pi$ . However, we can see from Eq. (9.13) that this difference is nothing but  $t_{mn}$ .

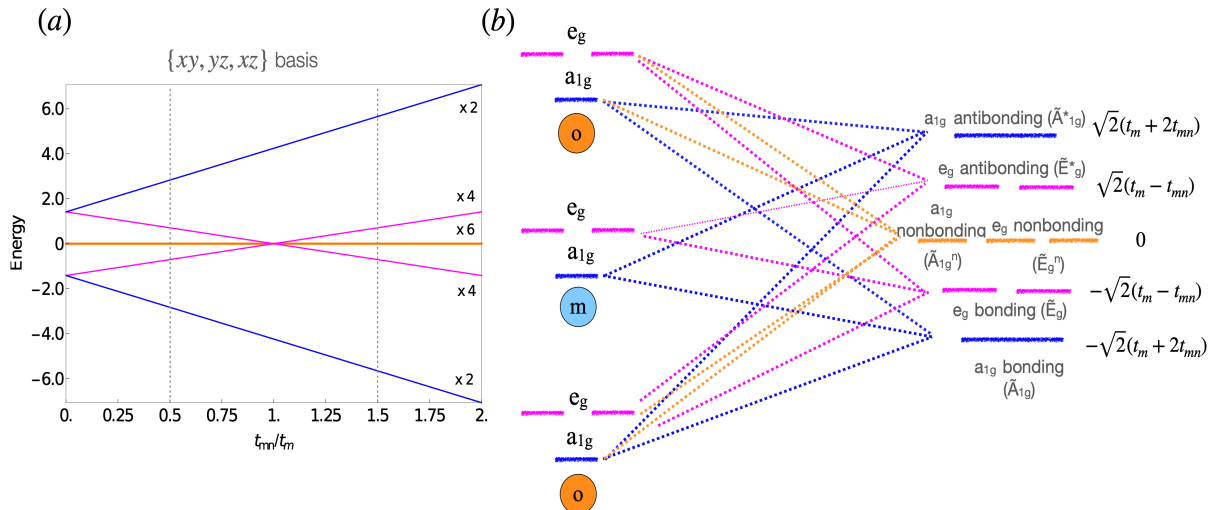


**Figure 9.4 – Non-interacting limit for the trimer cluster in the absence of SOC.** (a) Non-interacting bandstructure. (b) The trigonal crystal field splits the three degenerate levels on each of the sites, and they combine to give rise to bonding, anti-bonding and non-bonding levels of the trimer cluster.

### 9.3.2 Non-zero SOC

On the other limit, let us look at the non-interacting energy levels of the trimer in the presence of SOC but in the absence of hopping. SOC splits the levels into six  $j_{3/2}$  energy levels and three  $j_{1/2}$  energy levels.

When spin-orbit coupling is added, the energy levels rearrange themselves as  $\lambda$  is increased. Fig. 9.5 shows the evolution of energy levels as a function of  $\tilde{\lambda} = \lambda/t_{mn}$ . In the previous section, we saw that a majority of  $M_3O_{12}$  trimer materials can be either categorized as being “Rh-like”, or “Mn-like”. Hence, these energy levels are shown for a choice of physically relevant non-interacting parameters taken from Table 9.1.

There are a few observations to make in Fig. 9.5. Since the crystal fields are of opposite signs for the two classes of materials, this also affects the ground state – in the Rh-like case, the doubly degenerate  $e_g$  levels form the ground state, whereas in the Mn-like case, the  $a_{1g}$  level forms the ground state. Energy level crossings in both cases are also indicated, and we will see that they will become relevant when we consider phase diagrams of real materials in the next section. Though there are level crossings beyond a certain value of SOC, say  $\tilde{\lambda} = 4.0$ , the energy levels are more or less parallel to each other.

#### The Rh-like case

Since the Rh-like case is where spin-orbit coupling is essential, we will take a closer look at its non-interacting levels. In the presence of SOC, it is more convenient to describe the single particle levels in terms of the doublet  $j_{1/2}$  (with  $S = 1/2, L_{\text{eff}} = 1, J_{\text{eff}} = 1/2$ ) and quadruplet  $j_{3/2}$  ( $S = 1/2, L_{\text{eff}} = 1, J_{\text{eff}} = 3/2$ ) levels. This is shown in Fig. 9.6. Intra-dimer hopping leads to the mixing of these  $j$ -levels and also the formation of bonding/anti-bonding/non-bonding combinations. As a result, there are two levels each, of bonding, anti-bonding and non-bonding levels with a  $j_{3/2}$  character, and one level each, of bonding, anti-bonding and non-bonding levels with a  $j_{1/2}$  character. The character of these states is dynamic, and evolves with the SOC strength. However, at large values of SOC, each level settles at a certain character entirely. These are the levels shown on the right hand side in Fig. 9.6.

Note that the character and ordering of these levels are an outcome of certain fixed values of hoppings and crystal fields, as mentioned in Table 9.1. This is subject to change, based on the values of these parameters considered. The character of a certain level is also subject to change based on the filling and the strength of SOC. For example, consider the solid blue line, which pertains to either having the eleventh or the twelfth electron on the solid line. The change in the character of this level can be tracked based on where there are level crossings. From the figure, we see that its character changes from being  $j_{1/2}^n$  before the first crossing, to the first  $j_{3/2}^*$  level between two level crossings, and ultimately settling at the second  $j_{3/2}^*$  level.

## 9.4 Phase diagrams and effective moments for select fillings

Having studied the non-interacting limit in detail, we now switch on interactions. In this section, we study the interplay of interactions and spin-orbit coupling for select fillings on the

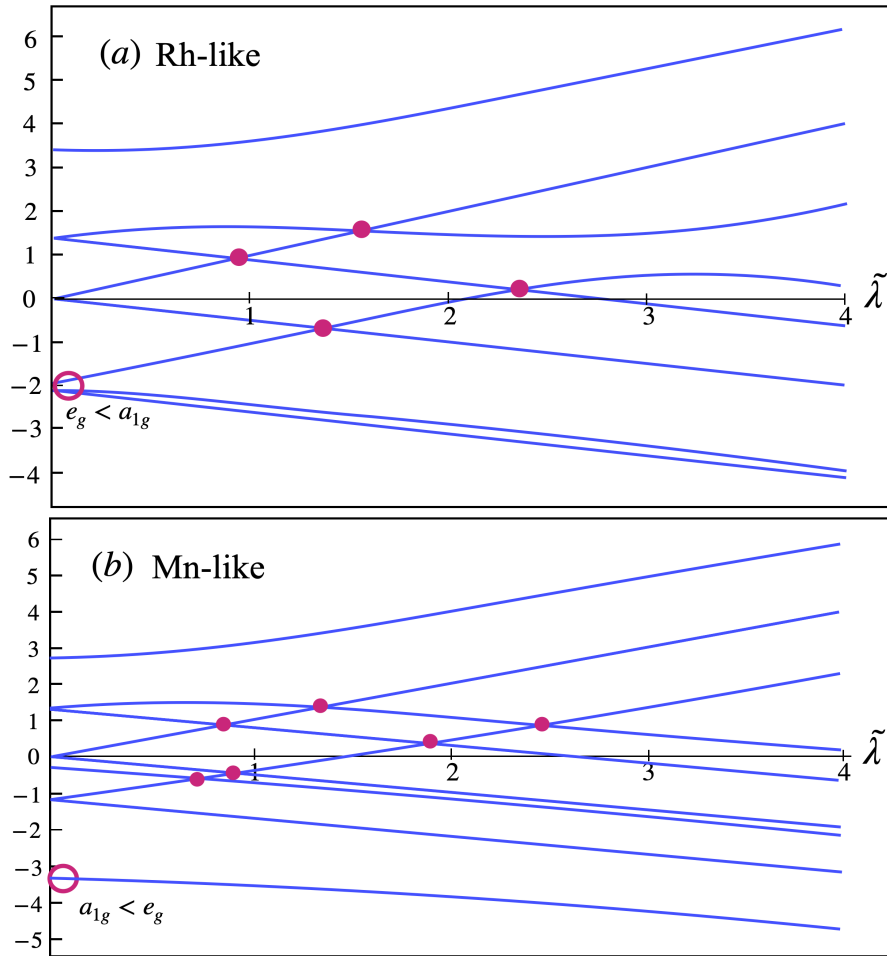


**Figure 9.5** – Non-interacting bandstructure for the trimer cluster, in the presence of SOC. (a) For Rh-like materials, and (b) for Mn-like materials. Level crossings are marked by pink circles. Values pertaining to the two categories of materials are as given in Table 9.1.

trimer, which all pertain to those of trimer materials that have been synthesized so far.

#### 9.4.1 $n_f = 11$ electrons

Fig. 9.7 shows the phase diagrams for the case of 11 electrons on the trimer cluster. We see that there are three principal regions in the phase diagram. In the region of low spin-orbit coupling (region I), an  $S \approx 1/2$  ground state is present, smoothly connected to the non-interacting limit. In the non-interacting limit, we see from Fig. 9.4(b) that the presence of an unpaired electron on  $a_{1g}$  non-bonding or on either of the  $e_g$  non-bonding levels leads to an  $S = 1/2$  ground state, which remains robust with the introduction of interaction. Since this partially occupied single particle level has a predominantly  $j_{1/2}^n$  character, we also refer to this state as having a total  $J_{\text{eff}} = 1/2$ .

In the non-interacting bandstructure in Fig. 9.6, when filled with 11 electrons, we see that the corresponding partially filled level undergoes an energy level crossing at  $\tilde{\lambda} = 0.9$ . Beyond

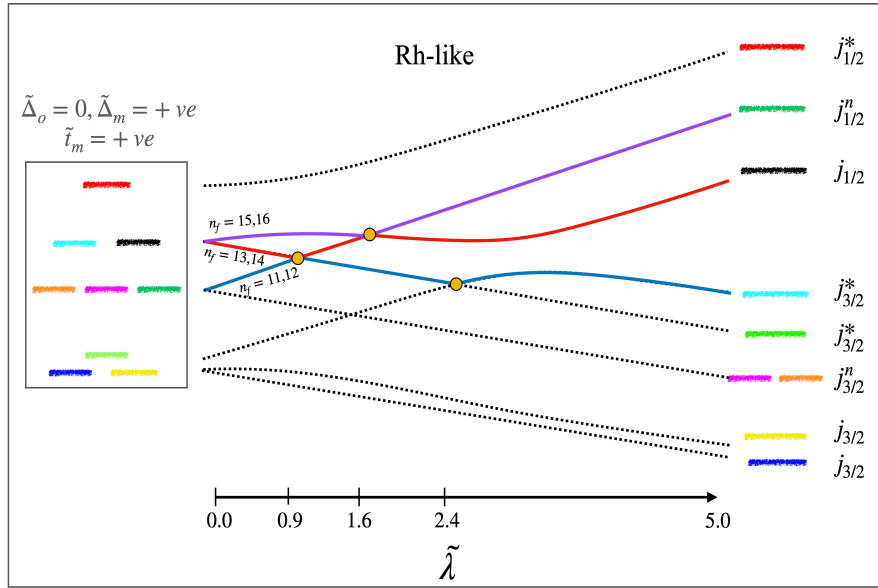


**Figure 9.6** – Evolution of non-interacting levels for Rh-like materials, in presence of SOC. Single particle levels pertaining to a filling of 11 or 12 electrons are highlighted in blue. Similarly, those pertaining to a filling of 13 or 14 electrons are highlighted in red, and the level pertaining to 15 or 16 electrons is highlighted in purple. Energy level crossings are shown as yellow circles, and the corresponding value of  $\tilde{\lambda}$  at specific crossings are also shown. (Right) Single particle levels can be expressed in the  $j_{1/2} - j_{3/2}$  basis when SOC is substantial. A level with no superscript denotes bonding; a level with superscript “\*” denotes anti-bonding; a level with superscript  $n$  denotes non-bonding.

this point, we see that the character of the partially occupied single particle level also changes due to reordering of the levels; hence, its character changes from being  $j_{1/2}^n$  previously to now being  $j_{3/2}^*$ . This is also observed in the full phase diagram of Fig. 9.7(a), where there is a phase transition at this point.

There is another region, region III, in the upper right corner of the phase diagram. The phase boundary seems to indicate that this region might also connect smoothly to a non-interacting limit at some large spin-orbit coupling. We again look to the non-interacting band structure for any other level crossings. Indeed, we observe another crossing at  $\tilde{\lambda} = 2.4$ . Though this value of  $\tilde{\lambda}$  lies beyond the limits of the full phase diagrams and also beyond the range of any of the materials we have so far considered, we conjecture that region III in the phase diagram might indeed smoothly connect to the non-interacting limit at this point.

### Magnetic moments

In Fig. 9.7(b), we show the phase diagram pertaining to the zero temperature limit of the effective magnetic moment per trimer,  $\mu_{\text{eff}}(0)/\mu_B$ , as a function of interactions and spin-orbit coupling. In region I, we see that the effective moment has a spin-only value of  $\sqrt{3}$ , which agrees with the  $j_{1/2}^n$  character of the unoccupied non-interacting level. In region II, this is completely quenched in the non-interacting limit. This is because the level now has a  $j_{3/2}^*$  character; the projection of the magnetic moment onto the  $j_{3/2}$  subspace is zero. This quenching is also

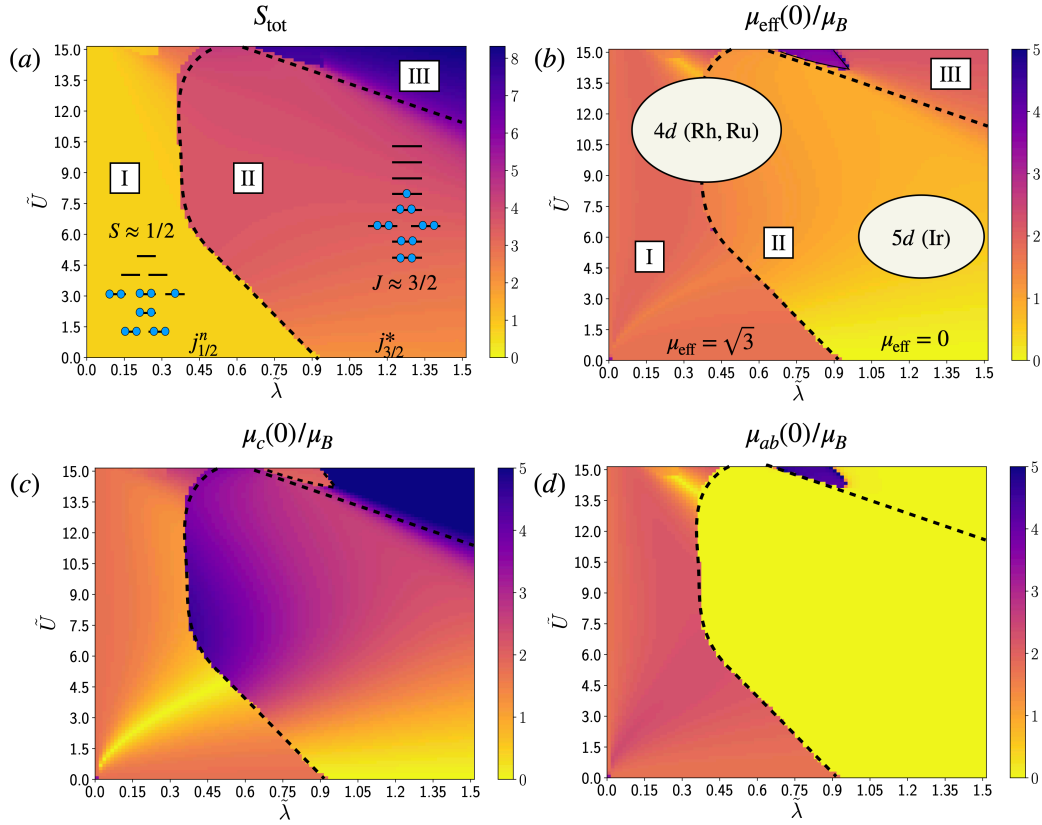


**Figure 9.7** – Phase diagrams for an Rh-like trimer material with 11 electrons on the cluster. Plots are shown here as a function of  $\tilde{U}$  and  $\tilde{\lambda}$ . Parameter ranges and values for the phase diagrams used are given in Table 9.1.

observed in both the longitudinal and transverse components of the magnetic moment, shown in Fig. 9.7(c) and Fig. 9.7(d). When interactions are added, the transverse component is still quenched, but this is lifted in the longitudinal component. These contributions also show up in the total effective moment, which becomes non-zero in region II, the farther we move away from the non-interacting limit. Some distinct features are the bright lines in the  $\mu_c/\mu_B$  and  $\mu_{ab}/\mu_B$  phase diagrams. These lines do not correspond to any phase transition. Hence, they are still an open question, subject to further investigation.

The regions corresponding to real materials are also shown in Fig. 9.7(b). A low spin-orbit coupling of  $\tilde{\lambda} = 0.4 - 0.6$  corresponds to ruthenium trimer materials in which the ruthenium ions have a mixed valence of +4.33, and host 11 electrons per trimer. Most of the ruthenium materials in this regime have  $B$  cations that are also magnetic. Hence, it is essential to take into account their contributions while calculating the magnetic moment of the material. Fig. 9.8 shows the calculated and measured zero-temperature effective moments of ruthenium trimers for a range of trivalent cations, by Hinatsu [215]. The measured free-ion magnetic moments of the  $B$  cations are also shown in the figure. In addition, they assumed an  $S = 1/2$  ground state for ruthenium trimers, and the effective moments calculated under this assumption agreed closely with the measured effective moments in most materials. Our phase diagrams confirm that there indeed exists a large region in the phase diagram with  $S \approx 1/2$ .

Ln	Electron configuration	11 electrons/trimer		14 electrons/trimer	
		Ba <sub>4</sub> LnRu <sub>3</sub> O <sub>12</sub>		Ba <sub>4</sub> LnIr <sub>3</sub> O <sub>12</sub> (or Rh)	
		$\mu_{\text{eff}} (\mu_B)$	$\mu_{\text{cal}} (\mu_B)$	$\mu_{\text{eff}} (\mu_B)$	$\mu_{\text{cal}} (\mu_B)$
La <sup>3+</sup>	4f <sup>0</sup>	2.86	1.73 <sup>*1</sup>	Dia	Dia
Nd <sup>3+</sup>	4f <sup>3</sup>	4.70	4.01 <sup>*1</sup>	3.60	3.62 <sup>*6</sup>
Sm <sup>3+</sup>	4f <sup>5</sup>	2.88	2.29 <sup>*3</sup>	—	—
Eu <sup>3+</sup>	4f <sup>6</sup>	1.18	1.73 <sup>*3</sup>	—	—
Gd <sup>3+</sup>	4f <sup>7</sup>	8.24	8.13 <sup>*1</sup>	7.98	7.94 <sup>*6</sup>
Dy <sup>3+</sup>	4f <sup>9</sup>	11.20	10.77 <sup>*1</sup>	10.71	10.63 <sup>*6</sup>
Ho <sup>3+</sup>	4f <sup>10</sup>	10.79	10.74 <sup>*1</sup>	10.36	10.60 <sup>*6</sup>
Er <sup>3+</sup>	4f <sup>11</sup>	9.72	9.74 <sup>*1</sup>	9.21	9.59 <sup>*6</sup>
Tm <sup>3+</sup>	4f <sup>12</sup>	7.75	7.77 <sup>*1</sup>	7.31	7.57 <sup>*6</sup>
Yb <sup>3+</sup>	4f <sup>13</sup>	4.70	4.86 <sup>*1</sup>	3.86	4.54 <sup>*6</sup>
Lu <sup>3+</sup>	4f <sup>14</sup>	2.86	1.73 <sup>*1</sup>	Dia	Dia

Note: <sup>\*1</sup>: calculated moments for Ln<sup>3+</sup> and  $S = 1/2$ ,

<sup>\*3</sup>: these values are calculated using the susceptibilities of Ln<sup>3+</sup> ions at room temperature,

<sup>\*6</sup>: free ion values for Ln<sup>3+</sup>.

**Figure 9.8** – Effective magnetic moments of Ba<sub>4</sub>LnM<sub>3</sub>O<sub>12</sub>. These measurements were carried out by Hinatsu et al. for a range of lanthanide cations (Ln) [215]. When  $M = \text{Ru}$ , the materials host 11 electron per trimer. When  $M = \text{Ir}$ , the materials host 14 electrons per trimer. Table of values adapted from [215].

In Fig. 9.9, a vertical cut of the magnetic moment phase diagrams pertaining to real materials is shown. Note that the different regions in these plots follow a color scheme that connects the regions to those in Fig. 9.7(a). Hence, region I would be a light yellow, region II is pink, and so on. In Fig. 9.9(a), which is within the range for ruthenium trimer materials, we see that the magnetic moment is completely isotropic and has a pure spin value, in the absence of interactions. The addition of a small interaction already introduces anisotropy in the magnetic moments, such that  $\mu_{ab} > \mu_c$ . There is a phase transition at  $\tilde{U} \approx 5.0$ , where we cross from region I to region II. Increasing interactions beyond this phase boundary not only flips the anisotropy ( $\mu_c > \mu_{ab}$ ), but also completely quenches  $\mu_{ab}$ . We expect that ruthenium trimers would fall into the former category.

In Fig. 9.9(b), which shows magnetic moments within the range of iridium trimers, we see that  $\mu_{ab}$  is uniformly completely quenched. Iridium trimer materials, which host 11 electrons per trimer, have not yet been synthesized. Our analysis hence provides a reference for any trimer material with a  $4d$  transition metal ion, which might potentially be synthesized in the future.

#### 9.4.2 $n_f = 13$ electrons

Fig. 9.10 shows the phase diagrams for 13 electrons per trimer. There are three principal regions, separated by well-defined phase boundaries. In region I, the unpaired electron occupies the doubly degenerate  $e_g$  anti-bonding levels (see Fig. 9.4(b)), thus resulting in an  $S \approx 1/2$  ground state. This region is smoothly connected to the non-interacting limit. Since the partially occupied energy level has a predominantly  $j_{3/2}^*$  character in this limit, we consider this region

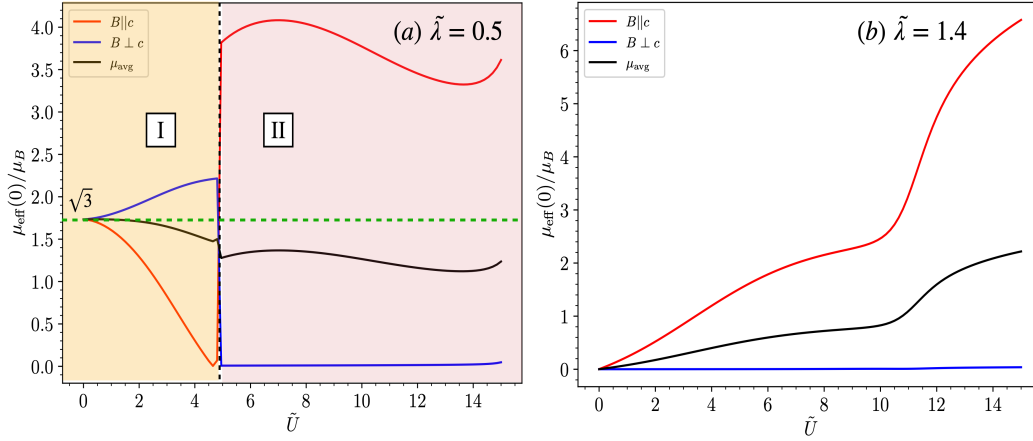


**Figure 9.9** – Cuts from the phase diagrams for the case of 11 electrons on the trimer. They show the evolution of zero-temperature magnetic moments with increasing  $\tilde{U}$ , for physically relevant values of  $\tilde{\lambda}$ . (a) low SOC (b) high SOC.

as having a total  $J_{\text{eff}} = 3/2$  ground state.

As with the previous case, a phase transition is observed at  $\tilde{\lambda} = 0.9$ . Region II is also smoothly connected to the non-interacting limit, at which the ground state now has a  $j_{1/2}^n$  character owing to the reordering of energy levels (Fig. 9.6). The third region does not smoothly connect to the non-interacting limit; however, the phase boundaries seem to suggest it might do so, at a larger spin-orbit coupling. Referring back to Fig. 9.6, one can observe an energy level crossing at  $\tilde{\lambda} \approx 1.6$ . Beyond this value, there is again a reordering of energy levels, and the partially occupied level now has a  $j_{1/2}$  character. We expect region III to hence smoothly connect to the non-interacting limit, and we can characterize the ground state in region III as  $j_{1/2}$ .

### Magnetic moments

In Fig. 9.10(b), we show the zero temperature limit of the effective magnetic moment per trimer as a function of interactions and spin-orbit coupling. Region I is entirely non-magnetic, since the ground state has a  $j_{3/2}^*$  character. This non-magnetic phase is also robust to the addition of interactions. Region II displays a pure spin-1/2 value of  $\sqrt{3}$ , and this is because the ground state now has a  $j_{1/2}^n$  character. However, region III, despite also having a  $j_{1/2}$  character, shows a departure from the pure spin-1/2 value. This can be attributed to stronger spin-orbit coupling, and presence of low-lying excited multiplets – these result in additional contributions to the magnetic moment. As with the previous case, the magnetic moments in this case, especially  $\mu_c/\mu_B$ , have some bright lines in the phase diagram that do not correspond to any phase transition. Their origin is hence yet to be investigated.

In the phase diagrams, parameter regimes corresponding to real materials are indicated. The low spin-orbit coupling regime corresponds to ruthenium trimer materials, which have a mixed valence of +3.67 per ruthenium ion, and 13 electrons on the ruthenium trimer in total. The only trimer material which has been synthesized so far with 13 electrons on the trimer is  $\text{Ba}_4\text{Nb}(5+)\text{Ru}_3(+3.67)\text{O}_{12}$  [206], where niobium is pentavalent and non-magnetic in nature.

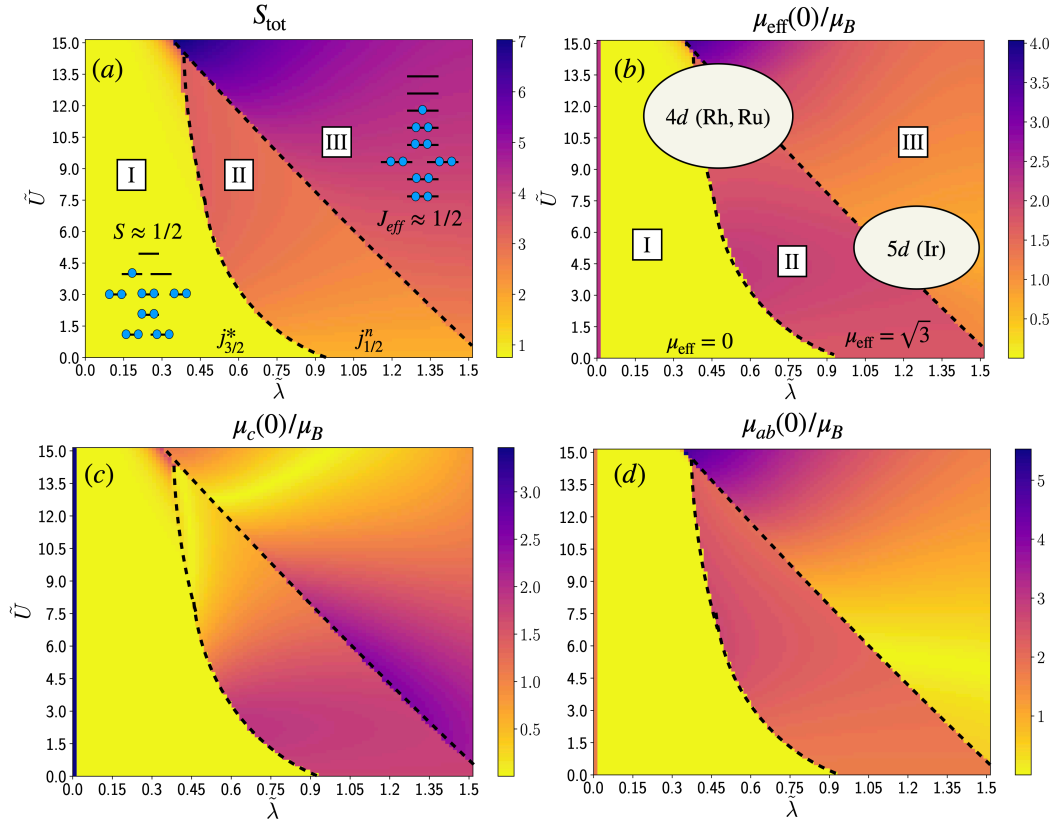


**Figure 9.10** – Phase diagrams for an Rh-like trimer material with 13 electrons on the cluster. Plots are shown here as a function of  $\tilde{U}$  and  $\tilde{\lambda}$ . Parameter ranges and values for the phase diagrams used are given in Table 9.1.

Hence, the niobium cation does not contribute to the magnetic moment. Cava et al. carried out susceptibility measurements, and the zero temperature magnetic moment for the material was measured to be  $\mu_{\text{eff}} = 2.59\mu_B/\text{f.u}$  [206]. In the phase diagram, we see that there is a region which corresponds to the observed magnetic moment.

In Fig. 9.11(a), we show a vertical cut of the magnetic moment at low spin-orbit coupling. The color scheme is similar to the previous case: the color scheme connects the regions to those in Fig. 9.10(a). Hence, region I would be a light yellow, region II is orange, and region III is purple. We see that region I hosts a non-magnetic state, where  $\tilde{U} < 0.5$ . Upon increasing  $\tilde{U}$ , we encounter region II, where an anisotropy is observed, with  $\mu_c$  being suppressed much more strongly than  $\mu_{ab}$ . In Fig. 9.11(b), we show magnetic moments as a function of interactions for high spin-orbit coupling. This corresponds to the parameter regime for 5d transition metal trimers, such as those of iridium, though trimer materials in the strong SOC regime with 13 electrons on the trimer have not yet been synthesized. In Fig. 9.11(b), the magnetic moment is isotropic in the absence of interactions, and its value is that of a pure spin-1/2. Addition of a small interaction not only induces a phase transition, but also introduces a large anisotropy such that  $\mu_{ab} > \mu_c$ . The trend is uniform post the phase-transition, where  $\mu_{ab}$  decreases and  $\mu_c$  uniformly increases.

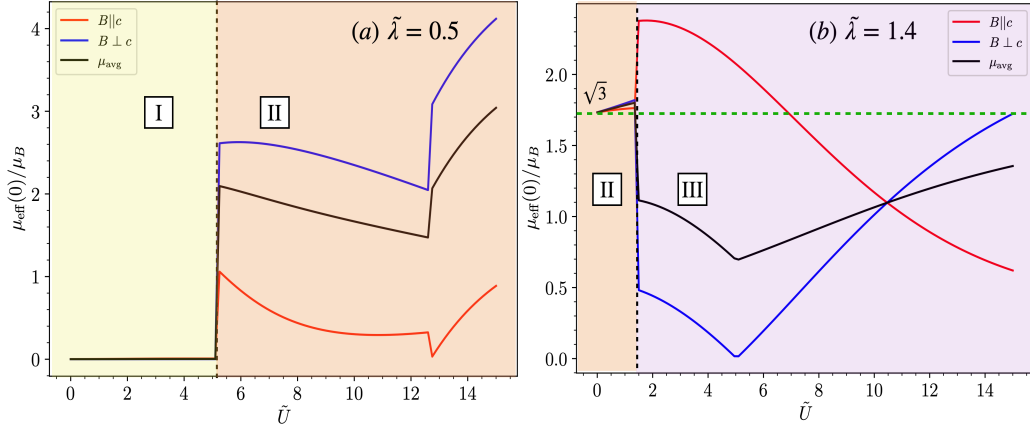


**Figure 9.11** – Cuts from the phase diagrams for the case of 13 electrons on the trimer. They show the evolution of zero-temperature magnetic moments with increasing  $\tilde{U}$ , for physically relevant values of  $\tilde{\lambda}$ . (a) low SOC (b) high SOC.

### 9.4.3 $n_f = 14$ electrons

Fig. 9.12 shows the phase diagrams for the case of 14 electrons on the trimer. There are four principal regions. In region I, in the non-interacting limit, all the energy levels are fully occupied, resulting in a low-spin regime of  $S = 0$  ground state. However, as interactions are increased, the electrons now occupy the  $e_g$  anti-bonding levels such that a high-spin  $S = 1$  forms the ground state. The spin-orbit coupling term completely quenches both spin and orbital angular momentum, whereas addition of a small  $\tilde{U}$  lifts this quenching. At finite  $\tilde{\lambda}$  and  $\tilde{U}$ , these cases are smoothly connected, such that there is no sharp phase transition for a small spin-orbit coupling, on increasing  $\tilde{U}$ . This is indicated by a red circle in Fig. 9.12(a). We also observe that  $S_{\text{tot}}$  also evolves continuously from the low spin to the high spin limit, since it is no longer a good quantum number for finite SOC. Going by the single-particle levels in Fig. 9.6, region II might smoothly connect to the non-interacting limit, whereas regions III and IV are interaction-driven phases.

Region IV is especially interesting, since it is realized only in the presence of strong interactions. It is also the only region in the phase diagram which non-zero effective moment; in fact,  $\mu_{\text{eff}} \approx 3.48$  in region IV. While the origin of this relatively high magnetic moment is an open question, its value corresponds to an  $S \approx 2, L \approx 1$  state.

Iridium and rhodium trimer materials have been synthesized, which contain 14 electrons on the trimer cluster [216]. The trimer can host 14 electrons, provided iridium/rhodium ions have a mixed valence of +4.33 in the material. This oxidation state can be realized in materials of the form  $\text{Ba}_4\text{B}(\text{Ir}, \text{Rh})_3(+4.33)\text{O}_{12}$ , where the B cation is trivalent, usually a lanthanide, as shown in Fig. 9.8. In these materials, the measured magnetic moment of the material was observed to be entirely due to the B cation, implying that the trimer cluster is non-magnetic [216]. This is also vindicated in our phase diagrams, where a large area has a zero effective magnetic moment.

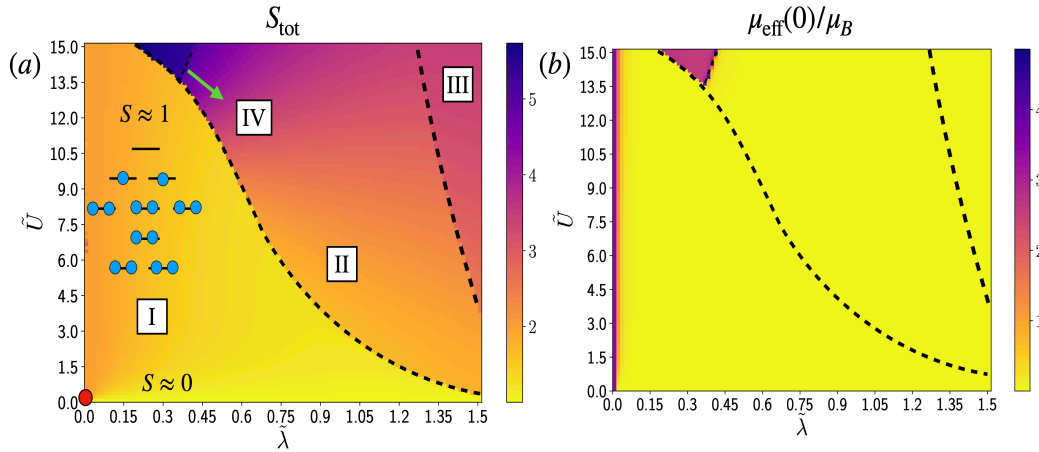


**Figure 9.12** – Phase diagrams for an Rh-like trimer material with 14 electrons on the cluster, as a function of  $\tilde{U}$  and  $\tilde{\lambda}$ . Parameter ranges and values for the phase diagrams used are given in Table 9.1.

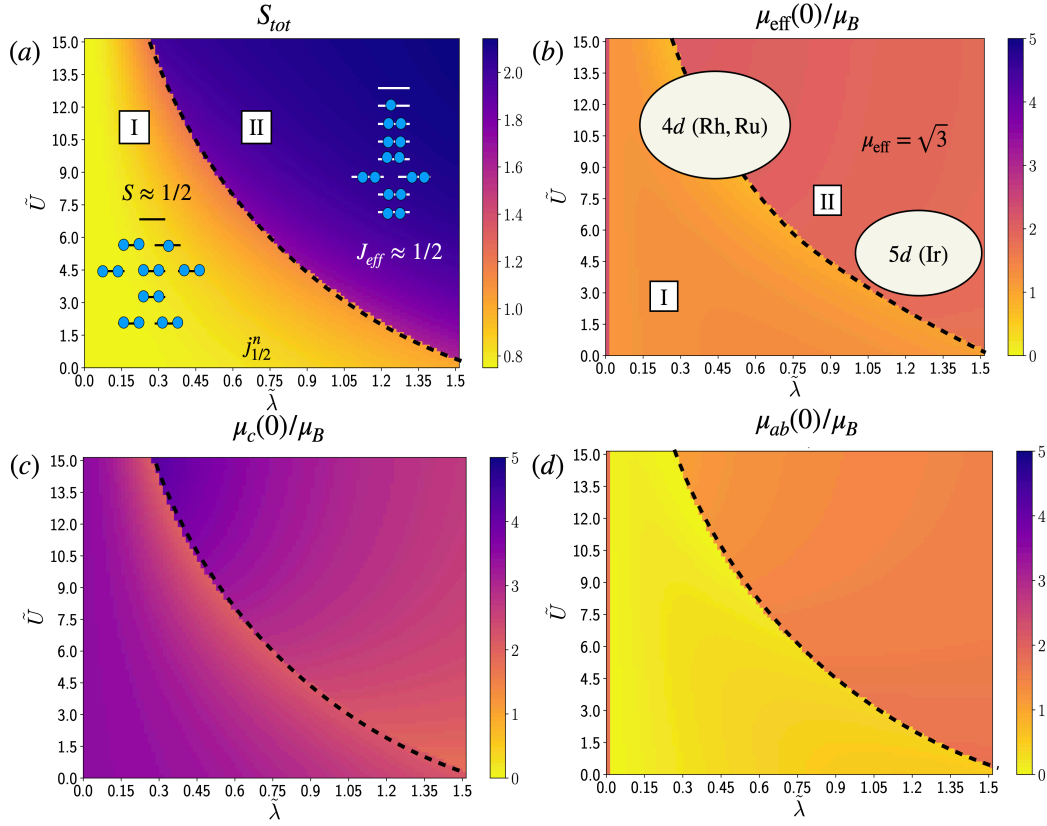
#### 9.4.4 $n_f = 15$ electrons

Fig. 9.13 shows the phase diagrams for the case of 15 electrons on the trimer. In region I, the unpaired electrons nominally occupy the  $e_g$  anti-bonding levels, resulting in a  $S \approx 1/2$  ground state. In the non-interacting limit of region I, the unpaired electron occupies a level which possesses a  $j_{1/2}^*$  character. Region II does not smoothly connect to the non-interacting limit in the phase diagram per se, but we see in Fig. 9.6 that there is an energy level crossing at  $\tilde{\lambda} \approx 1.6$ . Thus, we expect that region II meets the non-interacting axis not very far from the range shown in the phase diagram. Moreover, reordering of single-particle energy levels also results in the partially occupied level now having a  $j_{1/2}$  character.

#### Magnetic moments

Fig. 9.13(b) shows the zero temperature limit of the magnetic moment plotted as a function of interactions and spin-orbit coupling. In region I, the magnetic moment is slightly less than the pure-spin value of  $\sqrt{3}$ , which can be attributed to additional Van Vleck-like contributions. In region II, the pure spin value of  $\sqrt{3}$  is attained in the non-interacting limit, which also remains robust to the introduction of interactions.

The parameter regions pertaining to real materials that have 15 electrons per trimer are also indicated in the phase diagram. Rhodium trimers, which are tetravalent, fall into the low spin-orbit coupling regime. In the rhodium trimer class of materials of the form  $Ba_4BRh_3O_{12}$ , the rhodium ions have a 4+ oxidation state when the B cation is also tetravalent in nature. Hinatsu et al. [216] computed the magnetic moments of various materials in this category assuming a pure spin value of  $\mu_{\text{eff}} = \sqrt{3}$  for the rhodium trimer, and they matched closely with the observed magnetic moments, as shown in Fig. 9.14. In particular, in the cerium material  $Ba_4CeRh_3O_{12}$ , the contribution of the  $Ce^{4+}$  ion towards the magnetic moment of the material is zero. In this case, the observed magnetic moment exactly matches the calculated value. In our phase diagram, we see that there are indeed regions with low spin-orbit coupling, where these materials might lie. Though trimer materials with other 4d transition metal ions like



**Figure 9.13** – Phase diagrams for an Rh-like trimer material with 15 electrons on the cluster. Here, the plots are shown as a function of  $\tilde{U}$  and  $\tilde{\lambda}$ . Parameter ranges and values for the phase diagrams used are given in Table 9.1.

Ba <sub>4</sub> Ln(Ir, Rh) <sub>3</sub> O <sub>12</sub> , 15 electrons/trimer				
$Ln^{4+}$	electronic configuration	$J$	$\mu_{\text{eff}}^a/\mu_B$	$\mu_{\text{cal}}^b/\mu_B$
Ce <sup>4+</sup>	4f <sup>0</sup>	0	1.61	1.73
Pr <sup>4+</sup>	4f <sup>1</sup>	5/2	2.94	3.07
Tb <sup>4+</sup>	4f <sup>7</sup>	7/2	8.02	8.13

a  $\mu_{Ln}$ : free ion values for  $Ln^{3+}$ .

b  $\mu_{\text{cal}}$ : calculated moments for  $Ln^{4+}$  and  $S = 1/2$  (see text).

**Figure 9.14** – Effective magnetic moments of Ba<sub>4</sub>LnM<sub>3</sub>O<sub>12</sub>. These measurements were carried out by Shimoda et al. for a range of lanthanide cations (Ln) [216]. When  $M = \text{Ir}$  or  $\text{Rh}$ , the materials host 15 electrons per trimer. Table of values adapted from [216].

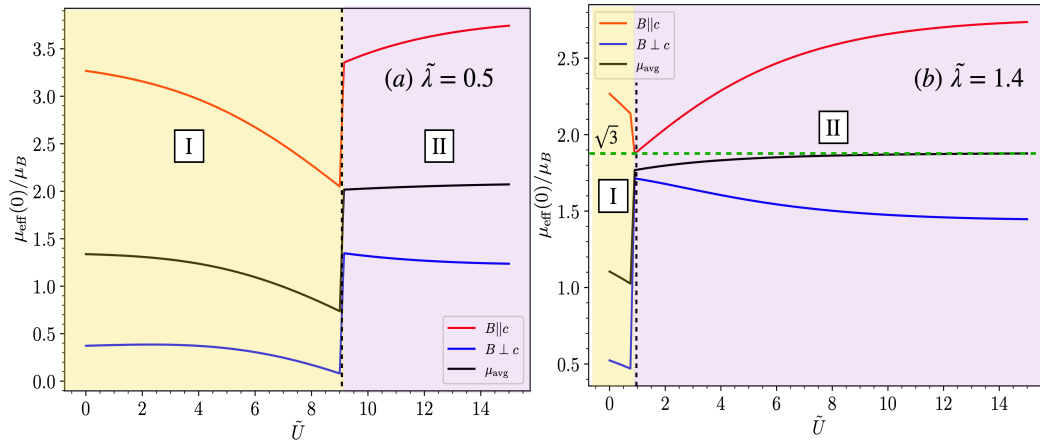


**Figure 9.15** – Cuts from the phase diagrams for the case of 11 electrons on the trimer.. They show the evolution of zero-temperature magnetic moments with increasing  $\tilde{U}$ , for physically relevant values of  $\tilde{\lambda}$ . (a) low SOC (b) high SOC.

ruthenium, containing 15 electrons on the trimer, have not yet been synthesized, we expect them to also lie in the same parameter regime as marked.

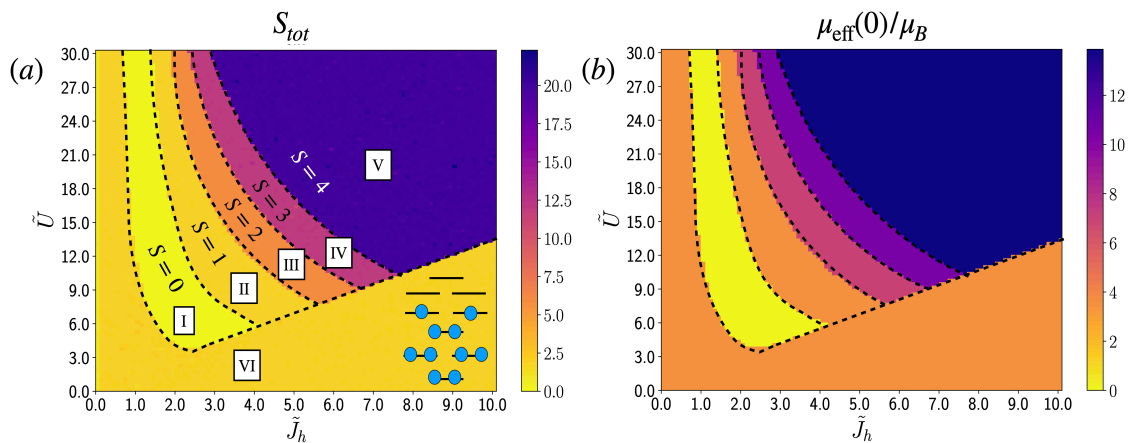
Iridium trimers with a tetravalent iridium ion belong to the high spin-orbit coupling region. These materials are also of the form  $Ba_4BIr_3O_{12}$ , where the B cation is tetravalent. The same can be said of iridium trimer materials as with rhodium – an assumption of  $\mu_{\text{eff}} = \sqrt{3}$  yielded results in close agreement with experimental values. We see that region II in our phase diagram is a vast area which encapsulates not only  $4d$  trimers in the low spin-orbit coupling region, but also  $5d$  trimers like those of iridium in the high spin-orbit coupling region.

Fig. 9.15 shows zero-temperature magnetic moments for these two spin-orbit coupling limits relevant to the respective materials. In Fig. 9.15(a), there is a sharp jump when going from region I to region II, owing to a phase transition. However, the anisotropy caused by the presence of interactions remains uniform throughout, with  $\mu_c > \mu_{ab}$ . In Fig. 9.15(b), there is an anisotropy even in the absence of interactions. The phase transition takes place with the addition of a small interaction, and  $\mu_{ab}$ , which was strongly suppressed, becomes non-zero.

#### 9.4.5 Manganese, $n_f = 10$ electrons

Fig. 9.16 shows the phase diagrams for the manganese case with 10 electrons per trimer. The phase diagrams shown here are distinctly different from the previous cases in that there is no spin-orbit coupling shown here. This is because the physics of  $3d$  transition metal cluster materials, such as those with manganese, is driven more by interactions rather than the negligible spin-orbit coupling [181].

In Fig. 9.16(a), we observe a rich phase diagram: there are six distinct regions. Of them, we can see that region I has  $S = 0$ , and we commensurately see that region being non-magnetic in Fig. 9.16(b). The non-interacting levels are also shown within the phase diagram: we see that filling them with 10 electrons would amount to placing two electrons on a pair of degenerate energy levels, thus giving rise to a triplet ground state. As a result, region VI, where  $S = 1$ , is



**Figure 9.16** – Phase diagrams for a manganese trimer material with 10 electrons on the cluster.

Plots are shown here as a function of  $\tilde{U}$  and  $\tilde{J}_h$ . Parameter ranges and values for the phase diagrams used are given in Table 9.1. Note the absence of SOC, since manganese is a  $3d$  transition metal.

smoothly connected to the non-interacting limit of  $\tilde{U} = 0, \tilde{J}_h = 0$ .

There has been only one manganese trimer material synthesized so far,  $\text{Ba}_4\text{NbMn}_3\text{O}_{12}$ , by Cava et al. [111]. The experimentally measured magnetic moment for this material was  $4.82 \mu_B/\text{f.u.}$  This value is close to 4.89, which is the spin-only value of effective magnetic moment when an  $S = 2$  ground state is assumed. Hence, we look into region III in our phase diagram, where  $S = 2$ . The magnetic moment in region III was found to be around 6.93, which is very far from the experimentally measured value of the magnetic moment. Moreover, we found no region in the entire phase diagram where the magnetic moment lie in a window between 4.0 and 6.0. This points to one of the two possibilities. We might either have considered a parameter window which is out of range for the material at hand, or it could be possible that a minuscule spin-orbit coupling is indeed essential in understanding the physics of the material.

## 9.5 Conclusion

This chapter was a culmination of the story we have built of cluster Mott insulators. Equipped with understanding of the methodology of studying cluster Mott insulators so far, we applied it to the context of real  $\text{M}_3\text{O}_{12}$  trimer materials that have been synthesized. Using *ab-initio* parameter range proposals, we began our analysis with studying the non-interacting bandstructure for different categories of trimer materials that have been synthesized so far. This gave us insight of the character of various single particle energy levels, which we leveraged to study the origin of magnetic moments in the non-interacting limit. We subsequently considered different fillings on the trimer, all corresponding to cases of real trimer materials. With the help of our phase diagrams, we were able to propose parameter ranges in which various materials might lie. We have summarized our main results in Fig. 9.17. Through a systematic treatment, we were able to verify the observed magnetic moments for a wide variety of materials, across different fillings. In addition, we also obtained the composition of magnetic moments in different directions. This is an outlook that can be verified experimentally only when single crystals of

these materials can be grown in the future. We also proposed what the ground state and its magnetic moments should be, for classes of materials that are yet to be synthesized.

Filling	Materials synthesized	Existing experiment vs numerics	Outlook: We made estimates and predictions for
11	$Ba_4Ln(3+)Ru_3O_{12}$ ( $4d$ )	✓	$\mu_{ab}, \mu_c, GS$ character of $5d$ materials
13	$Ba_4NbRu_3O_{12}$ ( $4d$ )	✓	$\mu_{ab}, \mu_c, GS$ character of $5d$ materials
14	$Ba_4Ln(3+)(Rh/Ir)_3O_{12}$ ( $4d, 5d$ )	✓	Purely interaction-driven magnetic moments
15	$Ba_4Ln(4+)(Rh/Ir)_3O_{12}$ ( $4d, 5d$ )	✓	$\mu_{ab}, \mu_c, GS$ character of $4d$ materials with very low SOC
10	$Ba_4NbMn_3O_{12}$ ( $3d$ )	✗	

**Figure 9.17** – Summary of trimer materials that have been considered in the chapter. We were able to explain experimental observations in most cases, except the  $3d$  trimer material with manganese. This might mean we either have to take into account a finite but minuscule SOC for the material, or that the material lies outside the proposed parameter range.

However, this is just part of the story for trimer cluster Mott insulators. With conjectures growing of new and exotic ground states for new trimer materials that are continually being synthesized, theoreticians and experimentalists have their hands full with exciting prospects ahead for understanding trimer cluster materials in their entirety.

## General concluding remarks

In this thesis, the story of cluster Mott insulators comes full circle. We started by briefly discussing the concept of localization in solids, both from a theoretical standpoint and from the perspective of a material. We built the foundation required for the thesis further by introducing exact diagonalization, and explaining the central role that very large-scale sparse matrix eigenvalue problems play when dealing with strongly correlated systems. It is hence vital to learn how best to extract useful information from such matrices. We then introduced the concept of clusters and their presence in coordination compounds. An important principle that the thesis established was the cluster Hund's rule, which provided us with intuition on how the ground states of an interacting cluster Hamiltonian are chosen. Using this, we were able to track how ground states evolved in different parameter regimes, with the addition of hoppings.

However, we have touched only the tip of the iceberg; what we did was to obtain a microscopic view of clusters in strongly correlated materials. In these materials, we saw that some of the main ingredients for realizing clusters are the presence of Hubbard and Hund's interactions, combined with short metal-metal distances. These are not the only materials that can host clusters; the concept of clusters is ubiquitous. Hence, if we want to look for clusters outside of the coordination compound context, we must ensure that the above requirements are met in some form. For example, van der Waals interactions play a significant role in condensing clusters of Rydberg atoms. These clusters can have a variety of geometries, ranging from planar to octahedral and tetragonal, which aggregate further into stacks or clouds [217]. Such Rydberg matter has found wide applications, including optics and energy production [218, 219]. Similarly, colloidal clusters and complex plasmas are used as platforms to study the dynamics of charged clusters and their interactions. Complex plasmas are realized by localizing strongly interacting particles in potential traps, which can be manipulated to create one, two, or three-dimensional Coulomb clusters [220]. Coulomb clusters are also the precursors to Wigner crystals, which are shown to host a vast range of interesting physics and applications [221–224].

In the latter half of the thesis, we applied our theoretical framework to real transition-metal coordination compounds that are cluster Mott candidates. We reviewed some of the most important ingredients to consider, crystal fields and spin-orbit coupling, and how they affect the ground state degeneracies of a crystal. We began the application of our understanding to materials by studying  $\text{Ba}_4\text{LiIr}_3\text{O}_{12}$ , a material synthesized by our collaborators at McMaster,

Canada. This project gave us insight into the presence and role of non-trivial ground state degeneracies in cluster Mott materials. Though non-Kramers doublets have been detected in various materials,  $\text{Ba}_4\text{LiIr}_3\text{O}_{12}$  is the first cluster Mott material whose physics is driven by these doublets. This provides us with new avenues in exploring the consequences of non-trivial degeneracies in a variety of cluster materials, for example, in those with weaker spin-orbit coupling than in iridates.

The final chapter of the thesis was concerned with carrying out a systematic study of trimer materials. We considered a vast range of materials where the trimer clusters hosted different numbers of electrons. This cluster filling was determined by the oxidation numbers of the transition metal and the other cations involved in the material. We also considered a range of spin-orbit coupling strengths. For example, materials with  $3d$  transition metals, such as manganese, have negligible spin-orbit coupling, and materials with  $4d$  transition metals, such as ruthenium and rhodium, have low-to-intermediate spin-orbit coupling. Trimer materials with iridium have the highest spin-orbit coupling. We carried out a study of the ground states and magnetic moments for all these cases. While our numerics matched experimental observations for materials that had already been synthesized, we were also able to discover interesting phases such as purely interaction-driven magnetic moments, and parameter regimes where magnetic moments had non-Curie contributions. In addition, since our study covered a vast expanse of parameter space, we could also read off what the character and magnetic moments would be for materials in spin-orbit coupling regimes that have not been synthesized yet. Thus, our study of trimer materials provided a dictionary of sorts for trimer cluster materials.

The central idea of a cluster Mott insulator arises from the presence of distinct clusters in a material, and their formation may be driven by any combination of various players such as SOC, crystal fields, Coulomb interactions etc., as long as electrons are localized within the clusters. We hence saw in Chapter 9 that cluster Mott insulating phases may also be realized in materials with low or intermediate spin-orbit coupling. It is worth mentioning another class of materials where spin-orbit coupling plays a significant role: spin-orbit entangled Mott insulators. These materials have a very strong spin-orbit coupling, the primary factor stabilizing the Mott state [225]. Non-trivial interactions between the spin-orbit entangled  $J = 1/2$  pseudo-spins led to the proposal that the Kitaev model could potentially be realized on edge-sharing honeycomb lattices made of these pseudo-spins [226]. In a similar vein, we made use of the character of single-particle levels in describing ground states of cluster materials with high SOC, in Chapter 9. In fact, one can also consider cluster Mott insulators as consisting of two kinds of “sites”: Atomic sites and orbital sites, with hoppings, interactions, and crystal fields described in a special way. For instance, crystal fields act only on orbital sites and not atomic sites, and so on. From this perspective, the distinction between a cluster Mott insulator and a spin-orbit entangled Mott insulator is blurred. Hence, an interesting prospect for the future would be to pursue this distinction between the two, both from a theoretical and an experimental perspective.

The work we carried out so far, as described in the thesis, is a crucial advancement in understanding the local cluster physics of cluster Mott insulators. The next logical step in

---

the story of cluster Mott insulators is to consider the many-body picture, by factoring in the inter-cluster Hamiltonian. An effective spin model for a single orbital per site scenario has already been derived for  $\text{Mo}_3\text{O}_8$  cluster materials [114]. However, given the sheer number of parameters to consider, arriving at effective Hamiltonians that apply to most, if not all, multi-orbital cluster materials, will be a challenge. Nevertheless, this is a critical piece of the puzzle and will undoubtedly pave the way for novel ground states and a more exhaustive exploration using many-body numerical methods.

Another perspective worth pursuing would be to vary filling for a fixed parameter set and track the ground states – that is, introduce doping. Adding or removing an electron from a cluster would be more dramatic than doing the same for a single site, because in the case of a cluster, this would mean completely altering the effective degree of freedom associated with the cluster. Research along similar lines has recently been pursued [227–229], where doping was introduced to a ladder of dimers at half-filling. However, the prospect of introducing doping specifically in cluster Mott materials remains an open trajectory of future research.

In conclusion, this thesis has provided a first step towards exploring the local physics of clusters in the world of cluster Mott materials. Cluster Mott insulators provide a great arena to explore the consequences of the interplay of various factors on the localization of electrons on clusters. While new cluster materials with fascinating properties continue to be synthesized, the existing classes of cluster Mott candidates await theoretical exploration from various perspectives, some of which have been outlined above. From the rich variety of physics that cluster Mott materials display to the sheer range of exciting directions that the area might potentially take, cluster Mott insulators stand true to what Anderson famously said: *More is different*.



## Appendices



# Group theory essentials and character tables

In dealing with materials in condensed matter physics or any other branch of physics, we invariably come across a crystal of some kind. We have seen many examples of this in the main body of the thesis. Every crystal possesses some symmetries, which also manifest themselves as symmetries of the ground states of a Hamiltonian on a crystal lattice. Hence, there is a need to classify and express these crystal symmetries in a quantitative, yet compact way. This is the main reason we use character tables corresponding to the point group of the crystal in question.

Before we get to reading and interpreting character tables, it would be useful to briefly recapitulate some main background knowledge to keep in mind.

## A.1 Groups and crystal point groups

A prerequisite to understand the “point group” of a crystal is to understand what a group is. A group is a non-empty set  $G$ , along with an operation “ $\cdot$ ”, such that its elements  $a, b, c, \dots \in G$  satisfy the following axioms:

- **Closure:** for any  $a, b \in G$ ,  $a \cdot b \in G$ .
- **Associativity:** for any  $a, b, c \in G$ ,  $(a \cdot b) \cdot c = a \cdot (b \cdot c)$ .
- **Existence of an identity element:** There exists an element  $e \in G$  such that for any  $a \in G$ , we have  $e \cdot a = a \cdot e = a$ .
- **Existence of an inverse:** For every  $a \in G$ , there exists an element  $a' \in G$  such that  $a \cdot a' = a' \cdot a = e$ .
- **Commutativity** (Only for Abelian groups) : For  $a, b \in G$ , we have  $a \cdot b = b \cdot a$ .

An important aspect of a group is applying an operation between its elements. Hence, it is convenient to tabulate the products between elements in the form of a multiplication table or Cayley table. Note that here, by “multiplication”, we mean being operated upon by

$(\mathbb{Z}_4, +_4)$	0	1	2	3
0	0	1	2	3
1	1	2	3	0
2	2	3	0	1
3	3	0	1	2

**Table A.1** – Cayley table for  $(\mathbb{Z}_4, +_4)$ .

the operation “.”. As a simple example, consider the group  $(\mathbb{Z}_4, +_4)$ , where the operation is addition modulo 4. The Cayley table for this group would be expressed as:

The Cayley table is read in the following way:  $2 +_4 1 = 3$ ,  $3 +_4 2 = 1$ ,  $2 +_4 2 = 0$ , and so on. From here, it is easy to read out which elements are the inverses of other elements, and how the different elements are being operated upon.

### A.1.1 Point groups

We now extend this idea to the case of a crystal: here, every element can be considered a symmetry operation. A symmetry operation on a crystal is any operation that leaves the crystal unchanged. Some standard symmetry operations are as follows:

- **Identity:** this operation does nothing to the crystal. This is similar to the identity element that we came across earlier. As a symmetry operation, it is denoted as  $E$ .
- **(Proper)  $n$ -fold rotation axis:** This is an axis of rotation such that, one rotation about this axis rotates the crystal by  $2\pi/n$ . Hence, rotating a crystal about this axis  $n$  times leaves the crystal unchanged. Such a rotation operation is denoted by  $C_n$ .
- **Mirror plane:** This is a plane of reflection about which the crystal is divided into two, and can be mirrored. The way in which this plane is defined is based on how one divides the crystal: horizontal mirror planes are perpendicular to the principal axis, vertical planes are parallel to the principal axis, and so on. The corresponding reflection operations are denoted by  $\sigma_h, \sigma_v$  etc.
- **Centre of inversion:** a point about which the crystal can be inverted. The corresponding operation is denoted as  $i$ .
- **Improper rotation axis:** This is a combination of a  $n$ -fold rotation axis and a mirror plane that is perpendicular to it. The corresponding operation,  $S_n$ , hence executes both rotation and reflection.

Once these elements, or operations, are hence defined for a crystal, a point group is a group of symmetry operations under the multiplication operation. As an example, let us write out the Cayley table for a point group  $C_{2v}$ , whose elements are  $\{E, C_2, \sigma_v, \sigma'_v\}$ :

Such a table for symmetry operations can be read similar to the earlier case: for example, a  $C_2$  rotation followed by another  $C_2$  rotation amounts to a total of  $2\pi$  rotation, hence resulting

$C_{2v}$	$E$	$C_2$	$\sigma_v$	$\sigma'_v$
$E$	$E$	$C_2$	$\sigma_v$	$\sigma'_v$
$C_2$	$C_2$	$E$	$\sigma'_v$	$\sigma_v$
$\sigma_v$	$\sigma_v$	$\sigma'_v$	$E$	$C_2$
$\sigma'_v$	$\sigma'_v$	$\sigma_v$	$C_2$	$E$

**Table A.2** – Cayley table for the  $C_{2v}$  point group, under multiplication.

in the identity element. A reflection  $\sigma_v$  along a vertical axis followed by a  $C_2$  rotation of the axis is the same operation as a reflection  $\sigma'_v$  along the second vertical axis, and so on. Hence, needless to say, symmetry operations such as rotations and reflections follow the usual group axioms mentioned above.

## A.2 Representations of groups

In the previous section, we saw that the set all symmetries in a crystal can be expressed in the language of group theory. We also saw that these symmetry operations are defined with respect to a point or an axis. Hence, these operations are, in practice, represented as some linear transformations with respect to a coordinate system. Hence, every symmetry element in a point group, for example, those in Table A.2, is a matrix in itself. Under the group operation of multiplication, these matrices satisfy the relations defined in the respective point group's Cayley table. In other words, the matrix assigned to every symmetry operation is a *representation* of that symmetry group.

There is some flexibility in constructing matrix representations of a symmetry operation. The bottom line is that they have to satisfy the Cayley table of the point group. Hence, these matrices are not unique. Given a matrix representation  $\{D(e), D(a), D(b), \dots\}$  of elements  $\{e, a, b, c, \dots\} \in G$ , we can obtain a new set of matrix representations by some matrix transformation (for example a change of basis)  $\{BD(e)B^{-1}, BD(a)B^{-1}, BD(b)B^{-1}, \dots\}$ . New matrix representations can also be obtained as a sum of two or more representations. Let us say we have representations  $\{D(e), D(a), D(b), \dots\}$ , each of dimension  $m$ , and representations  $\{D'(e), D'(a), D'(b), \dots\}$ , each of dimension  $n$ . We can obtain representations of dimension  $m + n$  by constructing a block diagonal matrix corresponding to each element in the following way [230]:

$$\left\{ \begin{pmatrix} D(e) & 0 \\ 0 & D'(e) \end{pmatrix}, \begin{pmatrix} D(a) & 0 \\ 0 & D'(a) \end{pmatrix}, \begin{pmatrix} D(b) & 0 \\ 0 & D'(b) \end{pmatrix} \right\}. \quad (\text{A.1})$$

Each of the new matrices thus constructed is called as being a *direct sum* of the corresponding  $m$  and  $n$  dimensional matrices, and the new representation is written as [230]:

$$\{D(e) \oplus D'(e), D(a) \oplus D'(a), D(b) \oplus D'(b), \dots\}. \quad (\text{A.2})$$

There is also flexibility in such constructions: new representations can, in theory, be constructed out of such building units *ad infinitum*.

Conversely, given such a representation, it can be expressed as a direct sum of two or more representations of lower dimensionality. Hence, such a representation is called a *reducible representation*. Representations that cannot be expressed in terms of those with lower dimensionality are called *irreducible representations*.

### A.3 Characters of a representation

Given the non-uniqueness of all the different representations of symmetry group elements, it is important to note that there is one property that is unchanged, which is the trace of a representation [230]

$$\text{tr}(D(a)) = \sum_{i=1}^n D(a)_{ii}. \quad (\text{A.3})$$

The trace is invariant under a transformation of a representation:

$$\text{tr}(D(a)) = \text{tr}(BD(a)B^{-1}). \quad (\text{A.4})$$

In many applications of group theory, for example, in the context of crystallographic point groups, the details of the representations of symmetry operations are, very often, not required. This also makes sense because these matrices are not unique. However, we exploit the invariance of the trace, and use the trace to express the corresponding symmetry operation. The trace of a matrix representation is called the *character* of the operation. When using the symmetries of a crystal, what we use instead of a Cayley table of a point group, is the character table of the group. The general layout of a character table is given in Table A.3.

$G$	$C_1 = E$	$C_2$	$\cdots$	$C_j$	$\cdots$	$C_n$
$\Gamma^{(1)}$	$\chi^{(1)}(C_1)$	$\chi^{(1)}(C_2)$	$\cdots$	$\chi^{(1)}(C_j)$	$\cdots$	$\chi^{(1)}(C_n)$
$\Gamma^{(2)}$	$\chi^{(2)}(C_1)$	$\chi^{(2)}(C_2)$	$\cdots$	$\chi^{(2)}(C_j)$	$\cdots$	$\chi^{(2)}(C_n)$
$\vdots$	$\vdots$	$\vdots$	$\ddots$			$\vdots$
$\Gamma^{(i)}$	$\chi^{(i)}(C_1)$	$\chi^{(i)}(C_2)$		$\chi^{(i)}(C_j)$		$\chi^{(i)}(C_n)$
$\vdots$	$\vdots$	$\vdots$			$\ddots$	
$\Gamma^{(n)}$	$\chi^{(n)}(C_1)$	$\chi^{(n)}(C_2)$	$\cdots$	$\chi^{(n)}(C_j)$	$\cdots$	$\chi^{(n)}(C_n)$

**Table A.3** – General layout of a character table. The topmost row lists all the symmetry operations  $C_j$  in a point group  $G$ , whereas the leftmost column lists all the irreducible representations. Table adapted from [231].

In Table A.3, we see that the character table contains, at the outset, all the irreducible representations of the symmetry operations in a given point group.  $\Gamma^{(i)}$  denotes the  $i$ th irreducible representation,  $C_j$  denotes the  $j$ th symmetry operation. Hence, the character of the  $i$ th irreducible representation of  $C_j$  is given by  $\chi^{(i)}(C_j)$ .

### A.3.1 Nomenclature of irreducible representations: Mulliken notation

The leftmost column of any character table, as we saw in the last section, enumerates irreducible representations. Mulliken proposed a useful shorthand to denote an irreducible representation, using a notation which gave information on the dimension of the representation and how the representation transformed under certain symmetry operations. This shorthand, called the “Mulliken notation”, is now used as a standard part of writing character tables for any point group. The convention is as follows [232]:

- **Base/Main letter:** denotes the dimension of an irreducible representation.  $A$  (or  $B$ ) denotes singly degenerate representation, and  $E, T, G, H$  denote representations of dimensions 2, 3, 4, 5,  $\dots$  respectively. Note that the  $E$  here is used to denote a doubly degenerate representation, and appears on the leftmost column of a character table. This is different from the identity symmetry operation  $E$ , which appears in the topmost row of a character table, along with other symmetry operations.
- **Distinction between uni-dimensional representations:** The irreducible representation  $A$  transforms symmetrically around the principal axis, whereas  $B$  transforms asymmetrically.
- **Subscripts :** subscripts  $g$  and  $u$  are used to denote symmetry and anti-symmetry with respect to a center of inversion, respectively. Subscripts 1 and 2 denote symmetry/anti-symmetry with respect to rotation about a non-principal axis.
- **Superscripts:** single prime ( $'$ ) is used to denote symmetry with respect to  $\sigma_h$ , the horizontal plane of reflection. Similarly double prime ( $''$ ) denotes anti-symmetry with respect to  $\sigma_h$ .

## A.4 Character tables of point groups

We now have the prerequisites to read the character table of any point group. Though there are a total of 32 crystallographic point groups, we present here the character tables of only those point groups that appear in the main body of the thesis. In Fig. A.1, we present character tables for point groups we come across in Chapter 5 and Chapter 6. We have also marked the non-trivial ground states – that is, uni-dimensional representations that do not transform trivially under all symmetry operations, in red. In Fig. A.2, we present character tables of point groups we come across in Chapter 7, Chapter 8 and Chapter 9.

(a)

$C_i$	$E$	$i$
$A_g$	1	1
$A_u$	1	-1

(b)

$C_{2v}$	$E$	$C_2$	$\sigma_v$	$\sigma'_v$
$A_1$	1	1	1	1
$A_2$	1	1	-1	-1
$B_1$	1	-1	1	-1
$B_2$	1	-1	-1	1

(c)

$C_{3v}$	$E$	$2C_3$	$3\sigma_v$
$A_1$	1	1	1
$A_2$	1	1	-1
$E$	2	-1	0

(d)

$C_{4v}$	$E$	$C_2$	$2C_4$	$2\sigma_v$	$2\sigma_d$
$A_1$	1	1	1	1	1
$A_2$	1	1	1	-1	-1
$B_1$	1	1	-1	1	-1
$B_2$	1	1	-1	-1	1
$E$	2	-2	0	0	0

(e)

$T_d$	$E$	$8C_3$	$3C_2$	$6\sigma_d$	$6S_4$
$A_1$	1	1	1	1	1
$A_2$	1	1	1	-1	-1
$E$	2	-1	2	0	0
$T_1$	3	0	-1	-1	1
$T_2$	3	0	-1	1	-1

**Figure A.1** – Character tables of different point groups that we come across in Chapter 5 and Chapter 6. Here, we have shown tables for (a)  $C_i$ , (b)  $C_{2v}$ , (c)  $C_{3v}$ , (d)  $C_{4v}$  and (e)  $T_d$ . Singly degenerate, non-trivial degeneracies are highlighted using a red box. Tables adapted from [232].

(a)

$D_{3h}$	$E$	$\sigma_h$	$2C_3$	$2S_3$	$3C_2'$	$3\sigma_v$
$A_1'$	1	1	1	1	1	1
$A_2'$	1	1	1	1	-1	-1
$A_1''$	1	-1	1	-1	1	-1
$A_2''$	1	-1	1	-1	-1	1
$E'$	2	2	-1	-1	0	0
$E''$	2	-2	-1	1	0	0

(b)

$D_{3d}$	$E$	$2C_3$	$3C_2'$	$i$	$2iC_3$	$3iC_2'$
$A_{1g}$	1	1	1	1	1	1
$A_{2g}$	1	1	-1	1	1	-1
$E_g$	2	-1	0	2	-1	0
$A_{1u}$	1	1	1	-1	-1	-1
$A_{2u}$	1	1	-1	-1	-1	1
$E_u$	2	-1	0	-2	1	0

(c)

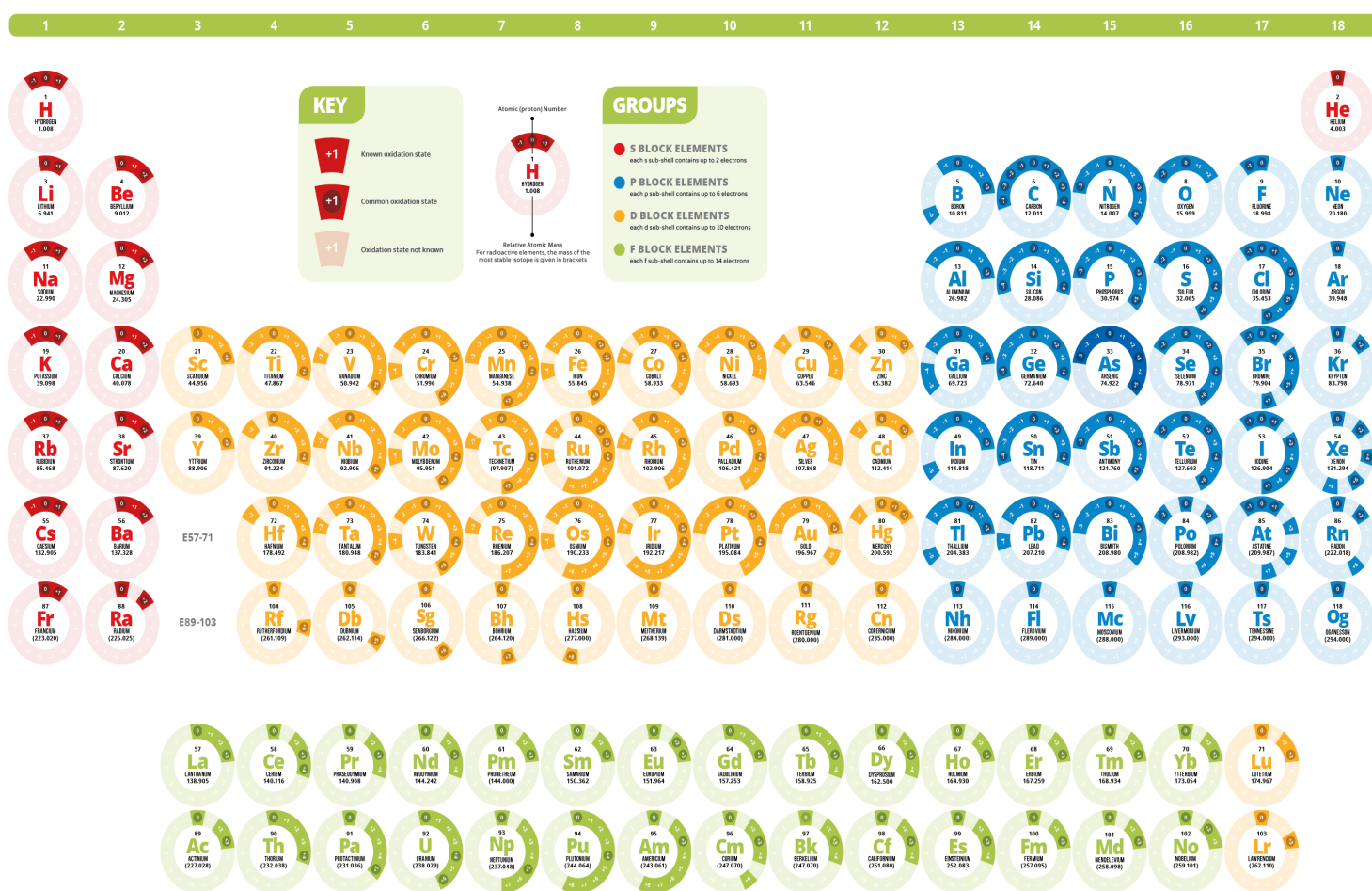
$O_h$	$E$	$3C_2$	$8C_3$	$6C_4$	$6C_2'$	$i$	$3\sigma$	$8S_6$	$6S_4$	$6\sigma_d$
$A_{1g}$	1	1	1	1	1	1	1	1	1	1
$A_{2g}$	1	1	1	-1	-1	1	1	1	-1	-1
$E_g$	2	2	-1	0	0	2	2	-1	0	0
$T_{1g}$	3	-1	0	1	-1	3	-1	0	1	-1
$T_{2g}$	3	-1	0	-1	1	3	-1	0	-1	1
$A_{1u}$	1	1	1	1	1	-1	-1	-1	-1	-1
$A_{2u}$	1	1	1	-1	-1	-1	-1	-1	1	1
$E_u$	2	2	-1	0	0	-2	-2	1	0	0
$T_{1u}$	3	-1	0	1	-1	-3	1	0	-1	1
$T_{2u}$	3	-1	0	-1	1	-3	1	0	1	-1

Figure A.2 – Character tables of different point groups that we come across in Chapter 7,8 and 9. Here, we have shown tables for (a)  $D_{3h}$ , (b)  $D_{3d}$ , and (c)  $O_h$ . Tables adapted from [183].



## The periodic table

## B



© COMPOUND INTEREST 2015 - WWW.COMPOUNDCHEM.COM | Twitter: @compoundchem | Facebook: www.facebook.com/compoundchem  
This graphic is shared under a Creative Commons Attribution-NonCommercial-NoDerivatives licence.



Figure B.1 – Periodic table of elements along with their known oxidation states.



# Bibliography

- [P1] **V. Jayakumar** and C. Hickey, Elementary building blocks for cluster Mott insulators, *under review at Phys. Rev. B*, 2023. arXiv: [2310.01060](https://arxiv.org/abs/2310.01060) [[cond-mat.str-el](#)].
- [U1] **V. Jayakumar** and C. Hickey, “M<sub>3</sub>O<sub>12</sub> Trimers in transition metal cluster Mott insulators,” *in preparation*, 2024.
- [1] P. W. Anderson, [Local moments and localized states](#), *Rev. Mod. Phys.* **50** (2), 191–201, 1978.
- [2] P. W. Anderson, [Absence of diffusion in certain random lattices](#), *Phys. Rev.* **109** (5), 1492–1505, 1958.
- [3] P. P. Poduval and S. Das Sarma, [Anderson localization in doped semiconductors](#), *Phys. Rev. B* **107** (17), 174204, 2023.
- [4] M. Cutler and N. F. Mott, [Observation of Anderson localization in an electron gas](#), *Phys. Rev.* **181** (3), 1336–1340, 1969.
- [5] C. L. Kane and E. J. Mele, [Quantum spin hall effect in graphene](#), *Phys. Rev. Lett.* **95** (22), 226801, 2005.
- [6] A. H. Castro Neto, F. Guinea, N. M. R. Peres, K. S. Novoselov, and A. K. Geim, [The electronic properties of graphene](#), *Rev. Mod. Phys.* **81** (1), 109–162, 2009.
- [7] F. Evers and A. D. Mirlin, [Anderson transitions](#), *Rev. Mod. Phys.* **80** (4), 1355–1417, 2008.
- [8] A. Furusaki, [Anderson localization due to a random magnetic field in two dimensions](#), *Phys. Rev. Lett.* **82** (3), 604–607, 1999.
- [9] J. Liao *et al.*, [Observation of Anderson localization in ultrathin films of three-dimensional topological insulators](#), *Phys. Rev. Lett.* **114** (21), 216601, 2015.
- [10] S. A. Gredeskul, Y. S. Kivshar, A. A. Asatryan, K. Y. Bliokh, Y. P. Bliokh, V. D. Freilikher, and I. V. Shadrivov, [Anderson localization in metamaterials and other complex media \(Review Article\)](#), *Low Temperature Physics* **38** (7), 570–602, 2012.
- [11] M. M. Wauters, A. Russomanno, R. Citro, G. E. Santoro, and L. Privitera, [Localization, topology, and quantized transport in disordered Floquet systems](#), *Phys. Rev. Lett.* **123** (26), 266601, 2019.

- [12] I. Vakulchyk, M. V. Fistul, P. Qin, and S. Flach, [Anderson localization in generalized discrete-time quantum walks](#), *Phys. Rev. B* **96** (14), 144204, 2017.
- [13] P. Titum, E. Berg, M. S. Rudner, G. Refael, and N. H. Lindner, [Anomalous Floquet-Anderson insulator as a nonadiabatic quantized charge pump](#), *Phys. Rev. X* **6** (2), 021013, 2016.
- [14] G. Roati, C. D’Errico, L. Fallani, M. Fattori, C. Fort, M. Zaccanti, G. Modugno, M. Modugno, and M. Inguscio, [Anderson localization of a non-interacting Bose-Einstein condensate](#), *Nature* **453** (7197), 895–898, 2008.
- [15] M. Segev, Y. Silberberg, and D. N. Christodoulides, [Anderson localization of light](#), *Nature Photonics* **7** (3), 197–204, 2013.
- [16] N. Mott, [On metal-insulator transitions](#), *Journal of Solid State Chemistry* **88** (1), 5–7, 1990.
- [17] J. H. Van Vleck, [The theory of electric and magnetic susceptibilities](#), *The Mathematical Gazette* **18** (231), 328–329, 1934.
- [18] P. W. Anderson, [More is different: Broken symmetry and the nature of the hierarchical structure of science](#). *Science* **177** (4047), 393–396, 1972.
- [19] A. Wietek, R. Rossi, F. Šimkovic, M. Klett, P. Hansmann, M. Ferrero, E. M. Stoudenmire, T. Schäfer, and A. Georges, [Mott insulating states with competing orders in the triangular lattice Hubbard model](#), *Physical Review X* **11** (4), 2021.
- [20] Z. Zhu, D. N. Sheng, and A. Vishwanath, [Doped Mott insulators in the triangular-lattice Hubbard model](#), *Phys. Rev. B* **105** (20), 205110, 2022.
- [21] M. Becker, M. Hermanns, B. Bauer, M. Garst, and S. Trebst, [Spin-orbit physics of  \$j = \frac{1}{2}\$  Mott insulators on the triangular lattice](#), *Phys. Rev. B* **91** (15), 155135, 2015.
- [22] Y. Shimizu, K. Miyagawa, K. Kanoda, M. Maesato, and G. Saito, [Spin liquid state in an organic Mott insulator with a triangular lattice](#), *Phys. Rev. Lett.* **91** (10), 107001, 2003.
- [23] C. Hotta, [Quantum electric dipoles in spin-liquid dimer Mott insulator  \$\kappa\$ -ET<sub>2</sub>Cu<sub>2</sub>\(CN\)<sub>3</sub>](#), *Phys. Rev. B* **82** (24), 241104, 2010.
- [24] Y. Shimizu, K. Miyagawa, K. Kanoda, M. Maesato, and G. Saito, [Emergence of inhomogeneous moments from spin liquid in the triangular-lattice Mott insulator  \$\kappa\$ -\(ET\)<sub>2</sub>Cu<sub>2</sub>\(CN\)<sub>3</sub>](#), *Phys. Rev. B* **73** (14), 140407, 2006.
- [25] K. W. Plumb, J. P. Clancy, L. J. Sandilands, V. V. Shankar, Y. F. Hu, K. S. Burch, H.-Y. Kee, and Y.-J. Kim,  [\$\alpha\$ -RuCl<sub>3</sub>: A spin-orbit assisted Mott insulator on a honeycomb lattice](#), *Phys. Rev. B* **90** (4), 041112, 2014.
- [26] B. Bauer, L. Cincio, B. P. Keller, M. Dolfi, G. Vidal, S. Trebst, and A. W. W. Ludwig, [Chiral spin liquid and emergent anyons in a kagome lattice Mott insulator](#), *Nature Communications* **5** (1), 5137, 2014.

- [27] P. A. Lee, N. Nagaosa, and X.-G. Wen, **Doping a Mott insulator: Physics of high-temperature superconductivity**, *Rev. Mod. Phys.* **78** (1), 17–85, 2006.
- [28] S. Hellmann *et al.*, **Ultrafast melting of a charge-density wave in the Mott insulator  $1T\text{-TaS}_2$** , *Phys. Rev. Lett.* **105** (18), 187401, 2010.
- [29] P. Chen, Y. H. Chan, X. Y. Fang, Y. Zhang, M. Y. Chou, S. K. Mo, Z. Hussain, A. V. Fedorov, and T. C. Chiang, **Charge density wave transition in single-layer titanium diselenide**, *Nature Communications* **6** (1), 8943, 2015.
- [30] T. Furukawa, K. Miyagawa, H. Taniguchi, R. Kato, and K. Kanoda, **Quantum criticality of Mott transition in organic materials**, *Nature Physics* **11** (3), 221–224, 2015.
- [31] S. Das, S. Voleti, T. Saha-Dasgupta, and A. Paramakanti, **XY magnetism, Kitaev exchange, and long-range frustration in the  $J_{\text{eff}} = \frac{1}{2}$  honeycomb cobaltates**, *Phys. Rev. B* **104** (13), 134425, 2021.
- [32] A. Revelli *et al.*, **Quasimolecular electronic structure of the spin-liquid candidate  $\text{Ba}_3\text{InIr}_2\text{O}_9$** , *Phys. Rev. B* **106** (15), 155107, 2022.
- [33] M. Magnaterra *et al.*, **RIXS Interferometry and the role of disorder in the quantum magnet  $\text{Ba}_3\text{Ti}_{3-x}\text{Ir}_x\text{O}_9$** , *Physical Review Research* **5** (1), 013167–, 2023.
- [34] J. Kim *et al.*, **Magnetic excitation spectra of  $\text{Sr}_2\text{IrO}_4$  probed by resonant inelastic X-ray scattering: Establishing links to cuprate superconductors**, *Phys. Rev. Lett.* **108** (17), 177003, 2012.
- [35] J. Hu, X. Zhang, C. Hu, J. Sun, X. Wang, H.-Q. Lin, and G. Li, **Correlated flat bands and quantum spin liquid state in a cluster Mott insulator**, *Communications Physics* **6** (1), 172, 2023.
- [36] T. Petersen, P. Bhattacharyya, U. K. Röbner, and L. Hozoi, **Resonating holes vs molecular spin-orbit coupled states in group-5 lacunar spinels**, *Nature Communications* **14** (1), 5218, 2023.
- [37] M. Querré, B. Corraze, E. Janod, M. P. Besland, J. Tranchant, M. Potel, S. Cordier, V. Bouquet, M. Guilloux-Viry, and L. Cario, **Electric pulse induced resistive switching in the narrow gap mott insulator  $\text{GaMo}_4\text{S}_8$** , *Key Engineering Materials* **617**, 135–140, 2014.
- [38] T.-H. Yang, T. Chang, Y.-S. Chen, and K. W. Plumb, **Jahn-Teller driven quadrupolar ordering and spin-orbital dimer formation in  $\text{GaNb}_4\text{Se}_8$** , *Phys. Rev. B* **109** (14), 144101, 2024.
- [39] Y. Zhang, Y. Gu, H. Weng, K. Jiang, and J. Hu, **Mottness in two-dimensional van der Waals  $\text{Nb}_3\text{X}_8$  monolayers ( $X = \text{Cl}, \text{Br}, \text{and I}$ )**, *Phys. Rev. B* **107** (3), 035126, 2023.
- [40] S. Regmi *et al.*, **Observation of flat and weakly dispersing bands in the van der Waals semiconductor  $\text{Nb}_3\text{Br}_8$  with breathing kagome lattice**, *Phys. Rev. B* **108** (12), L121404, 2023.
- [41] **The Hubbard model at half a century**, *Nature Physics* **9** (9), 523–523, 2013.

- [42] D. P. Arovas, E. Berg, S. A. Kivelson, and S. Raghu, [The Hubbard model](#), Annual Review of Condensed Matter Physics **13** (Volume 13, 2022), 239–274, 2022.
- [43] M. Qin, T. Schäfer, S. Andergassen, P. Corboz, and E. Gull, [The Hubbard model: A computational perspective](#), Annual Review of Condensed Matter Physics **13** (1), 275–302, 2022.
- [44] H. Bethe, [Zur theorie der metalle](#), Zeitschrift für Physik **71** (3), 205–226, 1931.
- [45] E. H. Lieb and F. Y. Wu, [Absence of Mott transition in an exact solution of the short-range, one-band model in one dimension](#), Phys. Rev. Lett. **20** (25), 1445–1448, 1968.
- [46] H. Ikeda, S. Shinkai, and K. Yamada, [Fourth-order perturbation expansion for Hubbard model on a two-dimensional square lattice](#), Journal of the Physical Society of Japan **77** (6), 064707, 2008.
- [47] K. A. Chao, J. Spałek, and A. M. Oleś, [Canonical perturbation expansion of the Hubbard model](#), Phys. Rev. B **18** (7), 3453–3464, 1978.
- [48] W. Metzner, [Hubbard model in high dimensions: A perturbation expansion about the atomic limit](#), Physica B: Condensed Matter **165-166**, 403–404, 1990, Proceedings of the 19th International Conference on Low Temperature Physics.
- [49] W. Metzner, [Linked-cluster expansion around the atomic limit of the Hubbard model](#), Phys. Rev. B **43** (10), 8549–8563, 1991.
- [50] T. S. R.D. Poshusta and D. Klein, [Heisenberg-model cluster expansion for half-filled Hubbard and ppp models](#), Molecular Physics **66** (2), 317–332, 1989.
- [51] E. Khatami, [Three-dimensional Hubbard model in the thermodynamic limit](#), Phys. Rev. B **94** (12), 125114, 2016.
- [52] D. Riegler, M. Klett, T. Neupert, R. Thomale, and P. Wölfle, [Slave-boson analysis of the two-dimensional Hubbard model](#), Phys. Rev. B **101** (23), 235137, 2020.
- [53] A. Rüegg, M. Indergand, S. Pilgram, and M. Sigrist, [Slave-boson mean-field theory of the Mott transition in the two-band Hubbard model](#), The European Physical Journal B **48** (1), 55–64, 2005.
- [54] J. O. Sofo and C. A. Balseiro, [Slave-boson mean-field theory for the negative- \$U\$  Hubbard model](#), Phys. Rev. B **45** (1), 377–382, 1992.
- [55] C. N. Varney, C.-R. Lee, Z. J. Bai, S. Chiesa, M. Jarrell, and R. T. Scalettar, [Quantum Monte Carlo study of the two-dimensional fermion Hubbard model](#), Physical Review B **80** (7), 2009.
- [56] A. W. Sandvik, [A generalization of Handscomb’s quantum Monte Carlo scheme-application to the 1d Hubbard model](#), Journal of Physics A: Mathematical and General **25** (13), 3667, 1992.
- [57] S. Sorella, [The phase diagram of the Hubbard model by variational auxiliary field quantum Monte Carlo](#), 2022. arXiv: [2101.07045 \[cond-mat.str-el\]](#).

- [58] X. Zhu, W. Han, S. Feng, and H. Guo, *Quantum Monte Carlo study of the attractive kagome-lattice Hubbard model*, Phys. Rev. Res. **5** (2), 023037, 2023.
- [59] M. Schneider, J. Ostmeyer, K. Jansen, T. Luu, and C. Urbach, *The Hubbard model with fermionic tensor networks*, Proceedings of Science / International School for Advanced Studies **Lattice2021**, 377, 2022.
- [60] R. Kaneko and I. Danshita, *Tensor-network study of correlation-spreading dynamics in the two-dimensional Bose-Hubbard model*, Communications Physics **5** (1), 65, 2022.
- [61] A. Sinha, M. M. Rams, P. Czarnik, and J. Dziarmaga, *Finite-temperature tensor network study of the Hubbard model on an infinite square lattice*, Phys. Rev. B **106** (19), 195105, 2022.
- [62] E. Gull, O. Parcollet, and A. J. Millis, *Superconductivity and the pseudogap in the two-dimensional Hubbard model*, Phys. Rev. Lett. **110** (21), 216405, 2013.
- [63] T. Maier, M. Jarrell, T. Pruschke, and J. Keller, *d-wave superconductivity in the Hubbard model*, Phys. Rev. Lett. **85** (7), 1524–1527, 2000.
- [64] S. Raghu, S. A. Kivelson, and D. J. Scalapino, *Superconductivity in the repulsive Hubbard model: An asymptotically exact weak-coupling solution*, Phys. Rev. B **81** (22), 224505, 2010.
- [65] J. Spalek, M. Fidrysiak, M. Zegrodnik, and A. Biborski, *Superconductivity in high- $T_c$  and related strongly correlated systems from variational perspective: Beyond mean field theory*, Physics Reports **959**, 1–117, 2022.
- [66] T. Misawa and M. Imada, *Origin of high- $T_c$  superconductivity in doped Hubbard models and their extensions: Roles of uniform charge fluctuations*, Phys. Rev. B **90** (11), 115137, 2014.
- [67] O. Dutta, M. Gajda, P. Hauke, M. Lewenstein, D.-S. Lühmann, B. A. Malomed, T. Sowiński, and J. Zakrzewski, *Non-standard Hubbard models in optical lattices: A review*, Reports on Progress in Physics **78** (6), 066001, 2015.
- [68] T. Esslinger, *Fermi-Hubbard physics with atoms in an optical lattice*, Annual Review of Condensed Matter Physics **1** (Volume 1, 2010), 129–152, 2010.
- [69] L. Tarruell and L. Sanchez-Palencia, *Quantum simulation of the Hubbard model with ultracold fermions in optical lattices*, Comptes Rendus Physique **19** (6), 365–393, 2018.
- [70] A. Walsh, A. A. Sokol, J. Buckeridge, D. O. Scanlon, and C. R. A. Catlow, *Oxidation states and ionicity*, Nature Materials **17** (11), 958–964, 2018.
- [71] S. Kettle, *Physical Inorganic Chemistry*. Springer, 2014.
- [72] C. Jorgensen, *Oxidation Numbers and Oxidation States*: Springer, 1969.
- [73] I. B. Bersuker, *Electronic Structure and Properties of Transition Metal Compounds: Introduction to the Theory*. John Wiley Sons, Inc., 2010.
- [74] F. A. Carey. “Benzene.” (2024), [Online]. Available: <https://www.britannica.com/science/benzene>.

- [75] J. Wilhelm, *Dynamic representation of organic chemical reaction mechanisms with animated lewis structures*, World Journal of Chemical Education **4** (1), 1–3, 2016.
- [76] M. B. Robin and P. Day, “Mixed valence chemistry—a survey and classification,” in *Advances in Inorganic Chemistry and Radiochemistry*, H. J. Emeléus and A. G. Sharpe, Eds. Academic Press, 1968, vol. 10, pp. 247–422.
- [77] C. Y. Liu and M. Meng, “Introduction and fundamentals of mixed-valence chemistry,” in *Mixed-Valence Systems*. 2023, pp. 1–43.
- [78] D.-S. Liu, Y. Sui, C.-H. Li, W.-T. Cheng, T.-W. Wang, and X.-Z. You, *Synthesis, structure and magnetic properties of a two-dimensional manganese(ii) complex with a maximum denticity of ethylenediaminetetraacetic ligand*, Inorganica Chimica Acta **376** (1), 112–117, 2011.
- [79] U.-C. Chung, J. Mesa, J. Pizarro, V. Jubera, L. Lezama, M. I. Arriortua, and T. Rojo, *Mn(HPO<sub>3</sub>): A new manganese (II) phosphite with a condensed structure*, Journal of Solid State Chemistry **178** (9), 2913–2921, 2005.
- [80] M. L. Agiorgousis, Y.-Y. Sun, D. West, and S. Zhang, *Intercalated Chevrel phase Mo<sub>6</sub>S<sub>8</sub> as a Janus material for energy generation and storage*, ACS Applied Energy Materials **1** (2), 440–446, 2018.
- [81] M. Zirnbauer, Lecture notes on advanced quantum mechanics, 2010.
- [82] B. Zweibach, Lecture notes on quantum physics III, 2018.
- [83] O. Krupin, *Dichroism and rashba effect at magnetic crystal surfaces of rare-earth metals*, Available at <https://refubium.fu-berlin.de/handle/fub188/7773?show=full>, PhD thesis, Freie Universität Berlin, 2004.
- [84] J. Kim, Lecture notes on quantum engineering with atoms, 2020.
- [85] M. G. Mayer, *Nuclear configurations in the spin-orbit coupling model. I. empirical evidence*, Phys. Rev. **78** (1), 16–21, 1950.
- [86] J. Hans, D. Jensen, and M. Goeppert-Mayer, *Electromagnetic effects due to spin-orbit coupling*, Phys. Rev. **85** (6), 1040–1041, 1952.
- [87] E. M. Pärschke and R. Ray, *Influence of the multiplet structure on the photoemission spectra of spin-orbit driven Mott insulators: Application to Sr<sub>2</sub>IrO<sub>4</sub>*, Phys. Rev. B **98** (6), 064422, 2018.
- [88] G. Racah, *Theory of complex spectra III*, Phys. Rev. **63**, 367–382, 9-10 1943.
- [89] J. M. Zhang and R. X. Dong, *Exact diagonalization: The Bose–Hubbard model as an example*, European Journal of Physics **31** (3), 591–602, 2010.
- [90] J.-H. Jung and J. D. Noh, *Guide to exact diagonalization study of quantum thermalization*, Journal of the Korean Physical Society **76** (8), 670–683, 2020.
- [91] G. B. Mbeng, A. Russomanno, and G. E. Santoro, *The quantum Ising chain for beginners*, 2020. arXiv: [2009.09208](https://arxiv.org/abs/2009.09208) [quant-ph].

- [92] “Simple examples of second quantization,” in *Introduction to Many-Body Physics*, P. Coleman, Ed. Cambridge University Press, 2015, pp. 71–94.
- [93] Y. Kaneda, H. Kawamura, and M. Sasai, Eds., *A Brief Introduction to Krylov Space Methods for Solving Linear Systems*, Springer Berlin Heidelberg, 2007, pp. 53–62.
- [94] G. M. D. Corso, O. Menchi, and F. Romani, “Krylov subspace methods for solving linear systems,” 2015.
- [95] P. Arbenz, “Lecture notes on solving large scale eigenvalue problems,” 2012.
- [96] E. Pavarini, E. Koch, and S. Zhang, Eds., *Many-Body Methods for Real Materials*, vol. 9, Autumn School on Correlated Electrons, Jülich (Germany), 16 Sep 2019 - 20 Sep 2019, Forschungszentrum Jülich GmbH Zentralbibliothek, Verlag, 16, 2019, getr. Zählung.
- [97] B. Tang, E. Khatami, and M. Rigol, *A short introduction to numerical linked-cluster expansions*, Computer Physics Communications **184** (3), 557–564, 2013.
- [98] N. M. Tubman, C. D. Freeman, D. S. Levine, D. Hait, M. Head-Gordon, and K. B. Whaley, *Modern approaches to exact diagonalization and selected configuration interaction with the adaptive sampling CI method*, Journal of Chemical Theory and Computation **16** (4), 2139–2159, 2020.
- [99] V. Waas, H. Fehske, and H. Büttner, *Exact diagonalization study of the  $t - J$  model in the low-density limit: Implications for phase separation*, Phys. Rev. B **48** (12), 9106–9109, 1993.
- [100] Y. Hasegawa and D. Poilblanc, *Hole dynamics in the  $t - J$  model: An exact diagonalization study*, Phys. Rev. B **40** (13), 9035–9043, 1989.
- [101] W. Fu and S. Sachdev, *Numerical study of fermion and boson models with infinite-range random interactions*, Physical Review B **94** (3), 2016.
- [102] A. M. García-García and J. J. M. Verbaarschot, *Spectral and thermodynamic properties of the Sachdev-Ye-Kitaev model*, Physical Review D **94** (12), 2016.
- [103] B. J. Kim *et al.*, *Novel  $J_{\text{eff}} = 1/2$  Mott state induced by relativistic spin-orbit coupling in  $\text{Sr}_2\text{IrO}_4$* , Phys. Rev. Lett. **101** (7), 076402, 2008.
- [104] *Properties of perovskites and other oxides*, doi:10.1142/7591, 2010.
- [105] A. Nag *et al.*, *Origin of the spin-orbital liquid state in a nearly  $J = 0$  iridate  $\text{Ba}_3\text{ZnIr}_2\text{O}_9$* , Phys. Rev. Lett. **116** (9), 097205, 2016.
- [106] D. Ziat, A. A. Aczel, R. Sinclair, Q. Chen, H. D. Zhou, T. J. Williams, M. B. Stone, A. Verrier, and J. A. Quilliam, *Frustrated spin- $\frac{1}{2}$  molecular magnetism in the mixed-valence antiferromagnets  $\text{Ba}_3M\text{Ru}_2\text{O}_9$  ( $M = \text{In}, \text{Y}, \text{Lu}$ )*, Phys. Rev. B **95** (18), 184424, 2017.
- [107] Q. Chen *et al.*, *Realization of the orbital-selective Mott state at the molecular level in  $\text{Ba}_3\text{LaRu}_2\text{O}_9$* , Phys. Rev. Mater. **4** (6), 064409, 2020.

- [108] Y. Li, A. A. Tsirlin, T. Dey, P. Gegenwart, R. Valentí, and S. M. Winter, **Soft and anisotropic local moments in 4d and 5d mixed-valence  $M_2O_9$  dimers**, Phys. Rev. B **102** (23), 235142, 2020.
- [109] Y. Li, S. M. Winter, D. A. S. Kaib, K. Riedl, and R. Valentí, **Modified Curie-Weiss law for  $j_{\text{eff}}$  magnets**, Phys. Rev. B **103** (22), L220408, 2021.
- [110] S. V. Streltsov and D. I. Khomskii, **Cluster magnetism of  $Ba_4NbMn_3O_{12}$ : Localized electrons or molecular orbitals?** JETP Letters **108** (10), 686–690, 2018.
- [111] L. T. Nguyen, T. Kong, and R. J. Cava, **Trimers of  $MnO_6$  octahedra and ferrimagnetism of  $Ba_4NbMn_3O_{12}$** , Materials Research Express **6** (5), 056108, 2019.
- [112] L. T. Nguyen and R. J. Cava, **Hexagonal perovskites as quantum materials**, Chemical Reviews **121** (5), 2935–2965, 2020.
- [113] S. Guo, H. E. Mitchell Warden, and R. J. Cava, **Structural diversity in oxoironates with 1D  $Ir_nO_{3(n+1)}$  chain fragments and flat bands**, Inorganic Chemistry **61** (26), 10043–10050, 2022.
- [114] S. A. Nikolaev, I. V. Solovyev, and S. V. Streltsov, **Quantum spin liquid and cluster Mott insulator phases in the  $Mo_3O_8$  magnets**, npj Quantum Materials **6** (1), 25, 2021.
- [115] J. P. Sheckelton, J. R. Neilson, D. G. Soltan, and T. M. McQueen, **Possible valence-bond condensation in the frustrated cluster magnet  $LiZn_2Mo_3O_8$** , Nature Materials **11** (6), 493–496, 2012.
- [116] R. Flint and P. A. Lee, **Emergent honeycomb lattice in  $LiZn_2Mo_3O_8$** , Phys. Rev. Lett. **111** (21), 217201, 2013.
- [117] G. Chen, H.-Y. Kee, and Y. B. Kim, **Cluster Mott insulators and two Curie-Weiss regimes on an anisotropic kagome lattice**, Phys. Rev. B **93** (24), 245134, 2016.
- [118] K. Iida *et al.*, **Quantum magnetisms in uniform triangular lattices  $Li_2AMo_3O_8$  ( $A = In, Sc$ )**, Scientific Reports **9** (1), 2019.
- [119] Y. Haraguchi, C. Michioka, M. Imai, H. Ueda, and K. Yoshimura, **Spin-liquid behavior in the spin-frustrated  $Mo_3$  cluster magnet  $Li_2ScMo_3O_8$  in contrast to magnetic ordering in isomorphic  $Li_2InMo_3O_8$** , Phys. Rev. B **92** (1), 014409, 2015.
- [120] A. Akbari-Sharbaf, R. Sinclair, A. Verrier, D. Ziat, H. D. Zhou, X. F. Sun, and J. A. Quilliam, **Tunable quantum spin liquidity in the  $1/6^{\text{th}}$ -filled breathing kagome lattice**, Phys. Rev. Lett. **120** (22), 227201, 2018.
- [121] **Formation of isomorphic  $Ir^{3+}$  and  $Ir^{4+}$  octamers and spin dimerization in the spinel  $CuIr_2S_4$** , Nature **416** (6877), 155–158, 2002.
- [122] D. I. Khomskii and T. Mizokawa, **Orbitally induced peierls state in spinels**, Phys. Rev. Lett. **94** (15), 156402, 2005.
- [123] K. M. Kojima, R. Kadono, M. Miyazaki, M. Hiraishi, I. Yamauchi, A. Koda, Y. Tsuchiya, H. S. Suzuki, and H. Kitazawa, **Magnetic frustration in iridium spinel compound  $CuIr_2S_4$** , Phys. Rev. Lett. **112** (8), 087203, 2014.

- [124] Y. Horibe, M. Shingu, K. Kurushima, H. Ishibashi, N. Ikeda, K. Kato, Y. Motome, N. Furukawa, S. Mori, and T. Katsufuji, *Spontaneous formation of vanadium “molecules” in a geometrically frustrated crystal:  $\text{AlV}_2\text{O}_4$* , *Phys. Rev. Lett.* **96** (8), 086406, 2006.
- [125] Y. Shimizu, M. Tanaka, M. Itoh, and T. Katsufuji, *Spin-singlet formation in the geometrically frustrated spinel oxide  $\text{AlV}_2\text{O}_4$ :  $^{51}\text{V}$  And  $^{27}\text{Al}$  NMR measurements*, *Phys. Rev. B* **78** (14), 144423, 2008.
- [126] A. J. Browne, S. A. J. Kimber, and J. P. Attfield, *Persistent three- and four-atom orbital molecules in the spinel  $\text{AlV}_2\text{O}_4$* , *Phys. Rev. Mater.* **1** (5), 052003, 2017.
- [127] T. Hikihara and Y. Motome, *Orbital and spin interplay in spin-gap formation in pyroxene  $\text{ATiSi}_2\text{O}_6$  ( $A = \text{Na}, \text{Li}$ )*, *Phys. Rev. B* **70** (21), 214404, 2004.
- [128] D. I. Khomskii and S. V. Streltsov, *Orbital effects in solids: Basics, recent progress, and opportunities*, *Chemical Reviews* **121** (5), 2992–3030, 2021.
- [129] M. Berovic, *Exploring Hund’s correlated metals: charge instabilities and effect of selective interactions*, Ph.D. dissertation, SISSA, 2018.
- [130] C. Noce and A. Romano, *Rotationally invariant parametrization of Coulomb interactions in multi-orbital Hubbard models*, *physica status solidi (b)* **251** (4), 907–911, 2014.
- [131] R. Frésard and G. Kotliar, *Interplay of Mott transition and ferromagnetism in the orbitally degenerate Hubbard model*, *Phys. Rev. B* **56** (20), 12909–12915, 1997.
- [132] A. Georges, L. de’Medici, and J. Mravlje, *Strong correlations from Hund’s coupling*, *Annual Review of Condensed Matter Physics* **4** (1), 137–178, 2013.
- [133] C. Noce and A. Romano, *Rotationally invariant parametrization of Coulomb interactions in multi-orbital Hubbard models*, *physica status solidi (b)* **251** (4), 907–911, 2014.
- [134] E. Dagotto, T. Hotta, and A. Moreo, *Colossal magnetoresistant materials: The key role of phase separation*, *Physics Reports* **344** (1), 1–153, 2001.
- [135] H. Tang, M. Plihal, and D. L. Mills, *Theory of the spin dynamics of bulk Fe and ultrathin  $\text{Fe}(100)$  films*, *Journal of Magnetism and Magnetic Materials* **187** (1), 23–46, 1998.
- [136] H. U. R. Strand, *Correlated Materials - Models & Methods*, Ph.D. dissertation, University of Gothenburg, 2013.
- [137] A. Subedi, O. E. Peil, and A. Georges, *Low-energy description of the metal-insulator transition in the rare-earth nickelates*, *Phys. Rev. B* **91** (7), 075128, 2015.
- [138] H. L. Nourse, R. H. McKenzie, and B. J. Powell, *Spin-0 Mott insulator to metal to spin-1 Mott insulator transition in the single-orbital Hubbard model on the decorated honeycomb lattice*, *Phys. Rev. B* **104** (7), 075104, 2021.
- [139] H. L. Nourse, R. H. McKenzie, and B. J. Powell, *Multiple insulating states due to the interplay of strong correlations and lattice geometry in a single-orbital hubbard model*, *Phys. Rev. B* **103** (8), L081114, 2021.

- [140] M. O. Soldini, N. Astrakhantsev, M. Iraola, A. Tiwari, M. H. Fischer, R. Valentí, M. G. Vergniory, G. Wagner, and T. Neupert, *Interacting topological quantum chemistry of Mott atomic limits*, Phys. Rev. B **107** (24), 245145, 2023.
- [141] Y. Haraguchi, C. Michioka, M. Ishikawa, Y. Nakano, H. Yamochi, H. Ueda, and K. Yoshimura, *Magnetic–nonmagnetic phase transition with interlayer charge disproportionation of Nb<sub>3</sub> trimers in the cluster compound Nb<sub>3</sub>Cl<sub>8</sub>*, Inorganic Chemistry **56** (6), 3483–3488, 2017.
- [142] C. M. Pasco, I. El Baggari, E. Bianco, L. F. Kourkoutis, and T. M. McQueen, *Tunable magnetic transition to a singlet ground state in a 2D van der Waals layered trimerized kagomé magnet*, ACS Nano **13** (8), 9457–9463, 2019.
- [143] R. Fumagalli *et al.*, *Mobile orbitons in Ca<sub>2</sub>CuO<sub>3</sub>: Crucial role of Hund’s exchange*, Phys. Rev. B **101** (20), 205117, 2020.
- [144] T. Kaneko, H. Sakakibara, M. Ochi, and K. Kuroki, *Pair correlations in the two-orbital Hubbard ladder: Implications for superconductivity in the bilayer nickelate La<sub>3</sub>Ni<sub>2</sub>O<sub>7</sub>*, Phys. Rev. B **109** (4), 045154, 2024.
- [145] V. Bilokon, E. Bilokon, M. C. Bañuls, A. Cichy, and A. Sotnikov, *Many-body correlations in one-dimensional optical lattices with alkaline-earth(-like) atoms*, Scientific Reports **13** (1), 2023.
- [146] J. Herbrych, J. Heverhagen, N. D. Patel, G. Alvarez, M. Daghofer, A. Moreo, and E. Dagotto, *Novel magnetic block states in low-dimensional iron-based superconductors*, Physical Review Letters **123** (2), 2019.
- [147] K. Sano and Y. Ōno, *Superconductivity in a two-orbital Hubbard model with electron and hole Fermi pockets: Application in iron oxypnictide superconductors*, Journal of the Physical Society of Japan **78** (12), 124706, 2009.
- [148] R. Peters and T. Pruschke, *Magnetic phases of the two orbital Hubbard model in dynamical mean field theory*, Journal of Physics: Conference Series **200** (1), 012158, 2010.
- [149] B. Pandey, G. Alvarez, and E. Dagotto, *Excitonic wave-packet evolution in a two-orbital Hubbard model chain: A real-time real-space study*, Physical Review B **104** (22), 2021.
- [150] A. Mukherjee, N. D. Patel, A. Moreo, and E. Dagotto, *Orbital selective directional conductor in the two-orbital Hubbard model*, Phys. Rev. B **93** (8), 085144, 2016.
- [151] K. Honkawa and S. Onari, *Orbital order in two-orbital Hubbard model*, Journal of the Physical Society of Japan **87** (3), 034703, 2018.
- [152] A. Romano, D. Guerra, F. Forte, and C. Noce, *Spin-orbital correlations in the two-orbital Hubbard model*, European Physical Journal Plus **138** (5) 480, 480, 2023.
- [153] Lemański and Matysiak, *Two-orbital Hubbard model vs spin  $S = 1$  Heisenberg model: Studies on clusters*, Condensed Matter Physics **21** (3), 33301, 2018.

- [154] R. Belford. “The shapes of atomic orbitals.” (2024), [Online]. Available: [https://chem.libretexts.org/Courses/University\\_of\\_Arkansas\\_Little\\_Rock/Chem\\_1402%3A\\_General\\_Chemistry\\_1\\_%28Belford%29/Text/6%3A\\_The\\_Structure\\_of\\_Atoms/6.6%3A\\_The\\_Shapes\\_of\\_Atomic\\_Orbitals](https://chem.libretexts.org/Courses/University_of_Arkansas_Little_Rock/Chem_1402%3A_General_Chemistry_1_%28Belford%29/Text/6%3A_The_Structure_of_Atoms/6.6%3A_The_Shapes_of_Atomic_Orbitals).
- [155] D. I. Khomskii, *Transition Metal Compounds*. Cambridge University Press, 2014.
- [156] H. Bethe, *Termaufspaltung in kristallen*, *Annalen der Physik* **395** (2), 133–208, 1929.
- [157] C. Ballhausen, *Introduction to Ligand Field Theory*. McGraw-Hill, 1962.
- [158] J. Goodenough, *Magnetism and the Chemical Bond*. Interscience Publishers, 1963.
- [159] G. L. Stamokostas and G. A. Fiete, *Mixing of  $t_{2g} - e_g$  orbitals in 4d and 5d transition metal oxides*, *Phys. Rev. B* **97** (8), 085150, 2018.
- [160] M. Reis, “Chapter 3 - angular momenta,” in *Fundamentals of Magnetism*, M. Reis, Ed. Academic Press, 2013, pp. 25–43.
- [161] C. Midwinter and M. Janssen, “Kuhn losses regained: Van vleck from spectra to <br/>susceptibilities,” in *Research and Pedagogy: A History of Quantum Physics through Its Textbooks*. Max-Planck-Gesellschaft zur Förderung der Wissenschaften, 2013.
- [162] J. H. Van Vleck, *On dielectric constants and magnetic susceptibilities in the new quantum mechanics Part II—application to dielectric constants*, *Phys. Rev.* **30** (1), 31–54, 1927.
- [163] J. H. Van Vleck, *On dielectric constants and magnetic susceptibilities in the new quantum mechanics Part III—application to dia- and paramagnetism*, *Phys. Rev.* **31** (4), 587–613, 1928.
- [164] N. Singh and A. M. Jayannavar, *A brief history of magnetism*, 2019. arXiv: [1903.07031](https://arxiv.org/abs/1903.07031) [physics.pop-ph].
- [165] B. Savoie, *On the atomic orbital magnetism: A rigorous derivation of the Larmor and Van Vleck contributions*, *Annales Henri Poincaré* **16** (1), 45–97, 2015.
- [166] *Tutorial: A beginner’s guide to interpreting magnetic susceptibility data with the Curie-Weiss law*, *Communications Physics* **5** (1), 95, 2022.
- [167] G. Cao, T. F. Qi, L. Li, J. Terzic, S. J. Yuan, L. E. DeLong, G. Murthy, and R. K. Kaul, *Novel magnetism of  $\text{Ir}^{5+}(5d^4)$  ions in the double perovskite  $\text{Sr}_2\text{YIrO}_6$* , *Phys. Rev. Lett.* **112** (5), 056402, 2014.
- [168] L. T. Corredor *et al.*, *Iridium double perovskite  $\text{Sr}_2\text{YIrO}_6$ : A combined structural and specific heat study*, *Phys. Rev. B* **95** (6), 064418, 2017.
- [169] Z. Y. Zhao, S. Calder, A. A. Aczel, M. A. McGuire, B. C. Sales, D. G. Mandrus, G. Chen, N. Trivedi, H. D. Zhou, and J.-Q. Yan, *Fragile singlet ground-state magnetism in the pyrochlore osmates  $R_2\text{Os}_2\text{O}_7$  ( $R = \text{Y}$  and  $\text{Ho}$ )*, *Phys. Rev. B* **93** (13), 134426, 2016.
- [170] S. Calder, Z. Y. Zhao, M. H. Upton, and J.-Q. Yan, *Local site behavior of the 5d and 4f ions in the frustrated pyrochlore  $\text{Ho}_2\text{Os}_2\text{O}_7$* , *Phys. Rev. B* **109** (5), 054408, 2024.

- [171] T. Dey *et al.*, **Ba<sub>2</sub>YIrO<sub>6</sub>: A cubic double perovskite material with Ir<sup>5+</sup> ions**, Phys. Rev. B **93** (1), 014434, 2016.
- [172] Q. Chen *et al.*, **Magnetism out of antisite disorder in the  $J = 0$  compound Ba<sub>2</sub>YIrO<sub>6</sub>**, Phys. Rev. B **96** (14), 144423, 2017.
- [173] Q. Chen, *Molecular orbital effects in heavy transition metal compounds*, Available at [https://trace.tennessee.edu/utk\\_graddiss/5847](https://trace.tennessee.edu/utk_graddiss/5847), PhD thesis, University of Tennessee, 2020.
- [174] H. A. Bethe, **Termaufspaltung in kristallen**, Annalen der Physik **395**, 133–208, 2006.
- [175] A. Le Paillier-Malécot and L. Couture, **Properties of the single and double  $D_{4d}$  groups and their isomorphisms with  $D_8$  and  $C_{8v}$  groups**, J. Phys. France (11), 1545–1552,
- [176] L. Elcoro, B. Bradlyn, Z. Wang, M. G. Vergniory, J. Cano, C. Felser, B. A. Bernevig, D. Orobengoa, G. de la Flor, and M. I. Aroyo, **Double crystallographic groups and their representations on the bilbao crystallographic server**, Journal of Applied Crystallography **50** (5), 1457–1477, 2017.
- [177] H. P. Fritzer, **Double groups: Some abstract properties and representations for the practitioner**, Physica A: Statistical Mechanics and its Applications **114** (1), 477–481, 1982.
- [178] G. Koster, *Properties of the Thirty-two Point Groups*. M.I.T. Press, 1963.
- [179] K. Foyevtsova, H. O. Jeschke, I. I. Mazin, D. I. Khomskii, and R. Valentí, **Ab-initio analysis of the tight-binding parameters and magnetic interactions in Na<sub>2</sub>IrO<sub>3</sub>**, Phys. Rev. B **88** (3), 035107, 2013.
- [180] P. E. R. Blanchard, K. W. Chapman, S. M. Heald, M. Zbiri, M. R. Johnson, B. J. Kennedy, and C. D. Ling, **Direct observation of pressure-driven valence electron transfer in Ba<sub>3</sub>BiRu<sub>2</sub>O<sub>9</sub>, Ba<sub>3</sub>BiIr<sub>2</sub>O<sub>9</sub>, and Ba<sub>4</sub>BiIr<sub>3</sub>O<sub>12</sub>**, Inorganic Chemistry **55** (11), 5649–5654, 2016.
- [181] E. V. Komleva, D. I. Khomskii, and S. V. Streltsov, **Three-site transition-metal clusters: Going from localized electrons to molecular orbitals**, Phys. Rev. B **102** (17), 174448, 2020.
- [182] J. G. Rau and M. J. Gingras, **Frustrated quantum rare-earth pyrochlores**, Annual Review of Condensed Matter Physics **10** (Volume 10, 2019), 357–386, 2019.
- [183] S. L. Altmann and P. M. Herzig, “Point-group theory tables,” 1994.
- [184] D. D. Maharaj, G. Sala, M. B. Stone, E. Kermarrec, C. Ritter, F. Fauth, C. A. Marjerrison, J. E. Greedan, A. Paramekanti, and B. D. Gaulin, **Octupolar versus néel order in cubic  $5d^2$  double perovskites**, Phys. Rev. Lett. **124** (8), 087206, 2020.
- [185] M. Liu, C.-E. Hu, and X.-R. Chen, **Electronic and magnetic properties of  $5d^1$ ,  $5d^2$ , and  $5d^3$  double perovskites Ba<sub>2</sub>MOsO<sub>6</sub> (M = K, Ca, and Sc): Ab-initio study**, Inorganic Chemistry **57** (8), 4441–4447, 2018.
- [186] A. Rayyan, X. Liu, and H.-Y. Kee, **Fate of multipolar physics in  $5d^2$  double perovskites**, Phys. Rev. B **108** (4), 045149, 2023.

- [187] A. J. Steele, P. J. Baker, T. Lancaster, F. L. Pratt, I. Franke, S. Ghannadzadeh, P. A. Goddard, W. Hayes, D. Prabhakaran, and S. J. Blundell, *Low-moment magnetism in the double perovskites  $\text{Ba}_2\text{MOsO}_6$  ( $M = \text{Li, Na}$ )*, Phys. Rev. B **84** (14), 144416, 2011.
- [188] K. Pradhan, A. Paramakanti, and T. Saha-Dasgupta, *Multipolar magnetism in  $5d^2$  vacancy-ordered halide double perovskites*, Phys. Rev. B **109** (18), 184416, 2024.
- [189] M. P. Hendrich and P. G. Debrunner, *Integer-spin electron paramagnetic resonance of iron proteins*. Biophys J **56** (3), 489–506, 1989.
- [190] K. A. Mueller, *Effective-spin hamiltonian for "non-Kramers" doublets*, Phys. Rev. **171** (2), 350–354, 1968.
- [191] D. R. Taylor and J. P. Harrison, *Cooperative Jahn-Teller ordering of electric dipoles in non-Kramers doublets*, Ferroelectrics **16** (1), 253–255, 1977.
- [192] G. Solt and P. Erdos, *Nearly non-magnetic Kramers doublet as crystal field ground state in  $\text{NpO}_2$* , Journal of Magnetism and Magnetic Materials **15-18**, 57–58, 1980.
- [193] *Radio frequency studies of  $\text{TmVO}_4$* , Proceedings of the Royal Society of London. Series A, Mathematical and Physical Sciences **370** (1741), 131–153, 1980.
- [194] A. M. Konic, R. B. Adhikari, D. L. Kunwar, A. A. Kirmani, A. Breindel, R. Sheng, M. B. Maple, M. Dzero, and C. C. Almasan, *Evolution of non-Kramers doublets in magnetic field in  $\text{PrNi}_2\text{Cd}_{20}$  and  $\text{PrPd}_2\text{Cd}_{20}$* , Phys. Rev. B **104** (20), 205139, 2021.
- [195] S. Lee, S. Trebst, Y. B. Kim, and A. Paramakanti, *Landau theory of multipolar orders in  $\text{Pr}(Y)_2X_{20}$  Kondo materials ( $Y = \text{Ti, V, Rh, Ir}$ ;  $X = \text{Al, Zn}$ )*, Phys. Rev. B **98** (13), 134447, 2018.
- [196] H. Kusunose, *Competing Kondo effects in non-kramers doublet systems*, Journal of the Physical Society of Japan **85** (6), 064708, 2016.
- [197] M. Amara, *Dynamical splitting of cubic crystal field levels in rare-earth cage compounds*, Phys. Rev. B **99** (17), 174405, 2019.
- [198] T. Onimaru *et al.*, *Quadrupole-driven non-Fermi liquid and magnetic-field-induced heavy fermion states in a non-Kramers doublet system*, Phys. Rev. B **94** (7), 075134, 2016.
- [199] Y. Li, S. Bachus, H. Deng, W. Schmidt, H. Thoma, V. Hutanu, Y. Tokiwa, A. A. Tsirlin, and P. Gegenwart, *Partial up-up-down order with the continuously distributed order parameter in the triangular antiferromagnet  $\text{TmMgGaO}_4$* , Phys. Rev. X **10** (1), 011007, 2020.
- [200] Z. Dun *et al.*, *Neutron scattering investigation of proposed Kosterlitz-Thouless transitions in the triangular-lattice Ising antiferromagnet  $\text{TmMgGaO}_4$* , Phys. Rev. B **103** (6), 064424, 2021.
- [201] S. Petit *et al.*, *Antiferroquadrupolar correlations in the quantum spin ice candidate  $\text{Pr}_2\text{Zr}_2\text{O}_7$* , Phys. Rev. B **94** (16), 165153, 2016.
- [202] S. Zheng *et al.*, *Exchange-renormalized crystal field excitations in the quantum Ising magnet  $\text{KTmSe}_2$* , Phys. Rev. B **108** (5), 054435, 2023.

- [203] O. Suzuki, H. S. Suzuki, H. Kitazawa, G. Kido, T. Ueno, T. Yamaguchi, Y. Nemoto, and T. Goto, **Quadrupolar Kondo effect in non-Kramers doublet system PrInAg<sub>2</sub>**, Journal of the Physical Society of Japan **75** (1), 013704, 2005.
- [204] Y. Shimoda, Y. Doi, Y. Hinatsu, and K. Ohoyama, **Synthesis, crystal structures, and magnetic properties of new 12L-perovskites Ba<sub>4</sub>LnRu<sub>3</sub>O<sub>12</sub> (Ln = Lanthanides)**, Chemistry of Materials **20** (13), 4512–4518, 2008.
- [205] Y. Shimoda, Y. Doi, M. Wakeshima, and Y. Hinatsu, **Crystal structures and characterizations of mixed valence 12-L perovskites Ba<sub>4</sub>EuM<sub>3</sub>O<sub>12</sub> (M = Ru and Ir)**, Inorganic Chemistry **48** (20), 9952–9957, 2009.
- [206] L. T. Nguyen, T. Halloran, W. Xie, T. Kong, C. L. Broholm, and R. J. Cava, **Geometrically frustrated trimer-based Mott insulator**, Phys. Rev. Mater. **2** (5), 054414, 2018.
- [207] W. Miiller, M. T. Dunstan, Z. Huang, Z. Mohamed, B. J. Kennedy, M. Avdeev, and C. D. Ling, **Complex 5d magnetism in a novel  $S = 1/2$  trimer system, the 12L hexagonal perovskite Ba<sub>4</sub>BiIr<sub>3</sub>O<sub>12</sub>**, Inorganic Chemistry **52** (21), 12461–12467, 2013.
- [208] G. S. Thakur, S. Chattopadhyay, T. Doert, T. Herrmannsdörfer, and C. Felser, **Crystal growth of spin-frustrated Ba<sub>4</sub>Nb<sub>0.8</sub>Ir<sub>3.2</sub>O<sub>12</sub>: A possible spin liquid material**, Crystal Growth and Design **20** (5), 2871–2876, 2020.
- [209] A. Bandyopadhyay *et al.*, **Novel quantum spin liquid ground state in the trimer rhodate Ba<sub>4</sub>NbRh<sub>3</sub>O<sub>12</sub>**, 2024. arXiv: [2403.06446](https://arxiv.org/abs/2403.06446) [`cond-mat.str-el`].
- [210] T. Basu, F. Y. Wei, Q. Zhang, Y. Fang, and X. Ke, **Complex magnetic structure in Ba<sub>5</sub>Ru<sub>3</sub>O<sub>12</sub> with isolated Ru<sub>3</sub>O<sub>12</sub> trimer**, Phys. Rev. Mater. **4** (11), 114401, 2020.
- [211] L. T. Nguyen and R. J. Cava, **Trimer-based spin liquid candidate Ba<sub>4</sub>NbIr<sub>3</sub>O<sub>12</sub>**, Phys. Rev. Mater. **3** (1), 014412, 2019.
- [212] Z. A. Kelly, M. J. Gallagher, and T. M. McQueen, **Electron doping a kagome spin liquid**, Phys. Rev. X **6** (4), 041007, 2016.
- [213] O. Mustonen, S. Vasala, E. Sadrollahi, K. P. Schmidt, C. Baines, H. C. Walker, I. Terasaki, F. J. Litterst, E. Baggio-Saitovitch, and M. Karppinen, **Spin-liquid-like state in a spin-1/2 square-lattice antiferromagnet perovskite induced by  $d^{10} - -d^0$  cation mixing**, Nature Communications **9** (1), 1085, 2018.
- [214] H. Zhao, Y. Zhang, P. Schlottmann, R. Nandkishore, and G. Cao, **Heavy-fermion strange metal and quantum spin liquid in a 4d-electron trimer lattice**, 2023. arXiv: [2305.01033](https://arxiv.org/abs/2305.01033) [`cond-mat.str-el`].
- [215] Y. HINATSU, **Diverse structures of mixed-metal oxides containing rare earths and their magnetic properties**, Journal of the Ceramic Society of Japan **123** (1441), 845–852, 2015.
- [216] Y. Shimoda, Y. Doi, M. Wakeshima, and Y. Hinatsu, **Synthesis and magnetic properties of 12L-perovskites Ba<sub>4</sub>LnIr<sub>3</sub>O<sub>12</sub> (Ln=lanthanides)**, Journal of Solid State Chemistry **182** (10), 2873–2879, 2009.

- [217] L. Holmlid, *Experimental studies and observations of clusters of Rydberg matter and its extreme forms*, Journal of Cluster Science **23** (1), 5–34, 2012.
- [218] T. H. Aasen, D. H. Zeiner-Gundersen, S. Zeiner-Gundersen, P. Ohlckers, and K. Wang, *A condensed excited (Rydberg) matter: Perspective and applications*, Journal of Cluster Science **33** (3), 839–852, 2022.
- [219] B. K. Teo, *A perspective on the science of clusters*, Journal of Cluster Science **25** (1), 5–28, 2014.
- [220] M. G. Hariprasad, P. Bandyopadhyay, G. Arora, and A. Sen, *Thermodynamics and self-organization of strongly coupled Coulomb clusters: An experimental study*, Physics of Plasmas **28** (7), 073702, 2021.
- [221] B. Spivak and S. A. Kivelson, *Phases intermediate between a two-dimensional electron liquid and Wigner crystal*, Phys. Rev. B **70** (15), 155114, 2004.
- [222] Y. Zhou *et al.*, *Bilayer Wigner crystals in a transition metal dichalcogenide heterostructure*, Nature **595** (7865), 48–52, 2021.
- [223] M. Knap, E. Berg, M. Ganahl, and E. Demler, *Clustered Wigner-crystal phases of cold polar molecules in arrays of one-dimensional tubes*, Phys. Rev. B **86** (6), 064501, 2012.
- [224] *Mapping charge excitations in generalized Wigner crystals*, Nature Nanotechnology **19** (5), 618–623, 2024.
- [225] D. Gotfryd, E. M. Pärshcke, J. ř. Chaloupka, A. M. Ole ś, and K. Wohlfeld, *How spin-orbital entanglement depends on the spin-orbit coupling in a Mott insulator*, Phys. Rev. Res. **2** (1), 013353, 2020.
- [226] T. Takayama, J. Chaloupka, A. Smerald, G. Khaliullin, and H. Takagi, *Spin-orbit-entangled electronic phases in 4d and 5d transition-metal compounds*, Journal of the Physical Society of Japan **90** (6), 062001, 2021.
- [227] Y. He, D. M. Kennes, C. Karrasch, and R. Rausch, *Terminable transitions in a topological fermionic ladder*, Phys. Rev. Lett. **132** (13), 136501, 2024.
- [228] A. Weichselbaum, W. Yin, and A. M. Tsvelik, *Dimerization and spin decoupling in a two-leg Heisenberg ladder with frustrated trimer rungs*, Phys. Rev. B **103** (12), 125120, 2021.
- [229] N. Chepiga and F. Mila, *DMRG investigation of constrained models: From quantum dimer and quantum loop ladders to hard-boson and Fibonacci anyon chains*, SciPost Physics **6** (3), 2019.
- [230] D. Vvdensky, *Lecture notes on groups*, 2001.
- [231] H. Jakob Wörner, *Lecture notes on spectroscopy*, 2023.
- [232] M. Dresselhaus, G. Dresselhaus, and A. Jorio, *Group Theory: Application to the Physics of Condensed Matter*. Springer Berlin, Heidelberg, 2007.



# Acknowledgements

At the outset, I would like to thank Prof. Simon Trebst for providing me the opportunity to pursue my doctoral studies in his group. Thank you for your encouragement through the years and for fostering an environment conducive to research. I also want to thank Prof. Ralf Bulla and Prof. Joachim Hemberger for kindly agreeing to being the second referee and the chair of the thesis committee, respectively.

I would like to extend my heartfelt gratitude to my supervisor, Ciarán Hickey. Your passion for research is contagious, and it is something I try to incorporate in my own approach to science. Your motivation, approachability, and most importantly, your empathy have been invaluable to me. Your absolutely steadfast support and faith in me helped me navigate a lot of curve-balls that life threw at me, and I am profoundly grateful to you for that. In the same spirit, a huge thank you and big hugs to Petra Neubauer-Guenther, who has seen me grow as a researcher and as an individual, since my early days at the admissions academy in Cologne. The innumerable conversations we have had over the years, and the guidance you have provided me about everything under the sun, are learnings that I will cherish and carry with me for a long time. In addition, special thanks to my mentor, Antonella Succurro, who offered clarity on many dilemmas on the career front and provided me with much-needed direction and resources for the same, especially during the tail-end of my doctoral studies.

None of the opportunities I have had would have been possible without the support of CRC1238. Not only did they employ me as a PhD student, but they also facilitated my travels to various conferences, enabling many fruitful scientific exchanges and collaborations. I extend my gratitude to everyone involved in the CRC1238 for the same. In addition, I am thankful to Dina and Mariela for administrative support. I would also like to thank Andreas Sindermann for his invaluable technical support, particularly during the pandemic when work went remote overnight.

I am also grateful to the RRZK in Cologne for facilitating data acquisition for parts of my thesis. Their provision of access to the CHEOPS cluster was instrumental in not only adding to the quality of research, but also in successfully completing the final project of my thesis.

The story of cluster Mott insulators woven in the thesis is also partly due to various people whose insights and ideas have enriched the projects I have worked on so far. Special thanks to Roser Valentí's group at Frankfurt, for clarifying many microscopic details of their work on cluster materials; I am also grateful to Maria Hermanns, whose enthusiasm for my work has significantly contributed to my own motivation. A big thanks to Qiang Chen, who, since meeting in 2022 at a conference in Paris, has not only provided many insights into various aspects of cluster Mott materials but also collaborated with me on the non-Kramers project.

All these years in Cologne would not have been memorable without friends and colleagues who enriched my stay in various ways. To begin with, the Office of Excellence – Christoph, Kai, and Carsten – thank you for making me feel truly welcome in the group and for all the light-hearted laughs and conversations. A heartfelt thank you and hugs to André, Baha and Simon, with whom I spent so many evenings jamming, making music, and visualizing how our band will one day break the indie music scene (this is still a work in progress – we should get around to this at some point. Hopefully!). You helped me keep my love for music alive even on days when I was overwhelmed with work.

I want to express my gratitude to everyone involved in the Association for Women in Physics, a passion project I pursued during my doctoral tenure, and which is very close to my heart. Thank you Andrea, for supporting my idea since the beginning and helping me establish this wonderful community in the department. You have been a patient listener to all my ramblings about women in STEM and community initiatives, sometimes for hours, and your calm demeanor has been very therapeutic to me. Special thanks to Prof. Diehl for helping me bring my ideas to fruition! Your faith in them have strengthened the association and helped me sustain and build it further. Thank you Bettina and Divita for lighting the atmosphere up with your presence! Special thanks to Roya and Maria for continuously bringing up new insights and issues to ponder about, and for helping me integrate them into the association.

I am also grateful to my colleagues Martin, Christoph and Sagar, for their meticulous proof-reading of my thesis. Your keen eyes and attention to detail have greatly improved the coherence of my writing. I am also grateful to Kai and Martin for putting up with my sudden barrage of questions at ungodly hours and patiently clarifying many bureaucratic subtleties I had to comply by, during the process of thesis writing and submission. Your repeated reassurances meant a lot.

Finally, I would like to thank my family for their unending support and encouragement, and without whom this achievement would not have been possible.

# Erklärung zur Dissertation

Hiermit versichere ich an Eides statt, dass ich die vorliegende Dissertation selbstständig und ohne die Benutzung anderer als der angegebenen Hilfsmittel und Literatur angefertigt habe. Alle Stellen, die wörtlich oder sinngemäß aus veröffentlichten und nicht veröffentlichten Werken dem Wortlaut oder dem Sinn nach entnommen wurden, sind als solche kenntlich gemacht. Ich versichere an Eides statt, dass diese Dissertation noch keiner anderen Fakultät oder Universität zur Prüfung vorgelegen hat; dass sie – abgesehen von unten angegebenen Teilpublikationen und eingebundenen Artikeln und Manuskripten – noch nicht veröffentlicht worden ist sowie, dass ich eine Veröffentlichung der Dissertation vor Abschluss der Promotion nicht ohne Genehmigung des Promotionsausschusses vornehmen werde. Die Bestimmungen dieser Ordnung sind mir bekannt. Darüber hinaus erkläre ich hiermit, dass ich die Ordnung zur Sicherung guter wissenschaftlicher Praxis und zum Umgang mit wissenschaftlichem Fehlverhalten der Universität zu Köln gelesen und sie bei der Durchführung der Dissertation zugrundeliegenden Arbeiten und der schriftlich verfassten Dissertation beachtet habe und verpflichte mich hiermit, die dort genannten Vorgaben bei allen wissenschaftlichen Tätigkeiten zu beachten und umzusetzen. Ich versichere, dass die eingereichte elektronische Fassung der eingereichten Druckfassung vollständig entspricht.

## Teilpublikationen:

- [P1] **V. Jayakumar** and C. Hickey, Elementary building blocks for cluster Mott insulators, *under review at Phys. Rev. B*, 2023. arXiv: [2310.01060](https://arxiv.org/abs/2310.01060) [[cond-mat.str-el](#)].
  
- [U1] **V. Jayakumar** and C. Hickey, “M<sub>3</sub>O<sub>12</sub> Trimers in transition metal cluster Mott insulators,” *in preparation*, 2024.

Köln, den 27. Mai 2025

---

(Vaishnavi Jayakumar)



The Hubbard model is a paradigmatic model in condensed matter physics, which provides a rich playground for investigating the physics of a wide range of strongly correlated electronic systems. The core principle of the Hubbard model is the competition between Coulomb repulsions and hoppings. An important limit in the model is the Mott insulating regime, which is realized in the strong interaction limit. As a result, electrons get localized on single atomic sites at half-filling. In this thesis, we investigate extensions of this idea to cluster Mott insulators. These are special materials where electrons are now localized on clusters of sites. We use the theoretical framework that we develop to explore the physics of real cluster Mott materials.

To that end, in a first study, we construct and study the cluster Hubbard model on a plethora of different clusters. We propose a new selection rule, called the cluster Hund's rule, which provides guidelines as to which states qualify as ground states in the pure interaction limit of the cluster Hubbard Hamiltonian. Using a combination of analytical insights and exact diagonalization, we conducted a comprehensive investigation of the emergent degrees of freedom in clusters of different geometries and fillings. This study helped us understand how these cluster Mott degrees of freedom respond to the interplay of strong correlations and hopping.

In a second study, we investigated the cause of the observed magnetic signatures in  $\text{Ba}_4\text{LiIr}_3\text{O}_{12}$ . This material hosts iridium dimers, and was expected to be non-magnetic since it possesses completely filled shells. Using insights from our previous study, we were able to detect non-trivial ground state degeneracies called non-Kramers doublets as the reason behind the observed magnetism of the material. Hence, we established  $\text{Ba}_4\text{LiIr}_3\text{O}_{12}$  as the first cluster Mott material whose physics is driven by non-Kramers doublets.

Having constructed this theoretical framework so far, we used it in our third study to investigate real materials which host trimer clusters – hexagonal perovskites of the form  $\text{A}_4\text{BM}_3\text{O}_{12}$ , and considered different fillings of  $3d$  to  $5d$  transition-metal “M” ions. Through a systematic treatment, we verified the observed magnetic moments for a wide variety of trimer materials. In addition, we also obtained the composition of magnetic moments in different directions. We use this study to propose ground state properties and phase diagrams for materials that are likely to be synthesized in the future.